CFD modelling of pipe erosion under multiphase flow regimes.

OGUNSESAN, O.A.

2020

CFD Modelling of Pipe Erosion under Multiphase Flow Regimes

OLUWADEMILADE ADEKUNLE OGUNSESAN

A thesis submitted in partial fulfillment of the
requirements of the
Robert Gordon University
for the degree of Doctor of Philosophy
(School of Engineering)

February 2020

CFD Modelling of Pipe Erosion under Multiphase Flow Regimes

OLUWADEMILADE ADEKUNLE OGUNSESAN

Supervisory Team:

Principal Supervisor: Dr Mamdud Hossain

Second Supervisor: Dr Mohamed Ghazi Droubi

School of Engineering, Robert Gordon University,

The Sir Ian Wood Building, Riverside East,

Garthdee Road, AB10 7GJ,

Aberdeen,

United Kingdom.

Dedication

This thesis is dedicated to my amiable and supportive parents, Mr. and Mrs. Adekunle Abdulrahman Ogunsesan.

Acknowledgement

I express my profound and unending gratitude to Almighty God for His grace and mercy towards me ever since, and through the course of this project.

My unreserved appreciation goes to my principal supervisor, Dr Mamdud Hossain for the invaluable advice, amiable guidance and words of encouragement during the course of this research. I remain everly grateful. And the other members of my supervisory team in persons of Dr Mohamed Ghazi Droubi and Dr Draco Iyi, thank you for your time, words and kind support!!

I am also grateful to the staff of the School of Engineering and the Library, Robert Gordon University for their support always. My colleagues in the Flow Modelling and Heat Transfer Research Group and the School of Engineering Research Hub, Nkemjika Asiegbu, Russein Mahon, Haider Al-Mashhadanie and David Alaita amongst others, your support and words of encouragement kept me going. I say thank you all!

My sisters, Yetunde, Oluwadamilola and Ayomide Ogunsesan thank you for your perseverance, invaluable support and encouragement. My uncles, Engr. Kola and Mr. Adedamola Ogunsesan and other extended family members, your support and encouragement in varying ways are well appreciated. My sweetheart, Oluwatoyin Adewole, thank you for your support and understanding. Finally, my friends, Akintola Aremu, Idowu Adewusi, Abdullateef Jimoh, Ahmed Adebayo, Abass Busari and Abdullateef Adepoju to mention a few, I say a big thanks to you all for the support and encouragement every time I needed to clear my head. May we all attain success in our chosen endeavours.

Oluwademilade Ogunsesan

August 2019

Abstract

Pipe erosion due to sand transport can have an adverse effect on the production efficiency of pipe lines and other related flow systems. Proper knowledge of the flow characteristics, particle behaviour and geometric effects is very important in the accurate prediction of erosion rates and location. This study focuses on predicting erosion under complex multiphase flow conditions with emphasis on double bend geometries. The Eulerian Multifluid-VOF coupled with the Lagrangian Discrete Phase Model (DPM) has been employed to account for the flow and particle behaviour, RNG $k - \varepsilon$ model for the effects of turbulence and erosion rate was calculated using the Oka et al. model. A pseudo single phase model was also evaluated in order to reduce the simulation resources to predict erosion in elbows mounted in series. Results from both modelling techniques were compared.

Results show that phase distribution plays a vital role in estimating erosion in complex multiphase flows. The presence of a separation distance results in a change in phase distribution before the first and second elbows, and an increase in the separation distance aides the flow development towards the second elbow. The presence of the second bend has a significant influence on the erosion rate of the first bend compared to a single bend geometry. Furthermore, Elbow 2 is subjected to more erosion than Elbow 1 in churn flow while Elbow 1 is more erosive in slug flow. The reverse of these were predicted with the pseudo single-phase approach for both flow conditions. Although the pseudo approach reduces computational time, it ignores vital flow features and predicts erosion rates higher than the Eulerian Multifluid-VOF approach in both elbows and flow condition. And irrespective of modelling technique, the best double bend operating conditions predicted for both flow conditions are the same.

Key words: Erosion, Churn, Slug, Elbows, Double bends, Separation distance

Table of Contents

List of Figures

List of Tables

Nomenclature

Notation

A Area

API American Petroleum Institute

C_D Drag coefficient

C_l Empirical constant

CFD Computational Fluid Dynamics

D Diameter

d_p Particle diameter

DNV Det Norske Veritas

$E(\alpha)$ Erosion damage

ER Erosion rate

f drag function

F_D Drag force

F_d Drag Force

F_e Specific erosion factor

F_G Force due to gravity

F_P Force due to pressure gradient

F_V Force due to Virtual mass

F_{int} Interphase momentum force

F_{vm} Virtual mass force

g Gravitational constant

$g(\alpha)$ impact angle dependence of normalized erosion

G_b Turbulence kinetic energy due to buoyancy

G_k Turbulence kinetic energy due to mean velocity gradient

H_L Liquid hold up

Hv Material hardness

I Unit tensor

IAC Interfacial Area Concentration

$IATE$ Interfacial Area Transport Equation

K_s Fitting erosion constant

K_{gl} Interphase momentum exchange coefficient

L Length

m Mass

m mass

P Material hardness

p Pressure

r_c Radius of curvature

R_e Reynolds number

RNG Renormalization Group

S_m Geometry dependant constant

S_{α_g} Source term

S_{RC} Sink term due to random collision

S_{TI} Source term due to turbulent impact

S_{WE} Sink term due to wake entrainment

U_P Particle velocity

V velocity

V_e Erosional velocity

V_{sg} Superficial gas velocity

V_{sl} Superficial liquid velocity

W_e Webber number

W_p Sand flow rate

WR Wear rate

X_p Interfacial Area Concentration

Subscripts and Superscripts

a Air

cr Critical

eff Effective

G Gravity

g, l Gas, Liquid

i, j Phases

int Interface

L	Lift
m	Mixture
n	Number of phases
$norm$	Normal
p	Particulate phase
q	Continuous phase
sm	Sauter mean
tan	Tangential
vm	Virtual mass
w	Water

Greek Letters

α	Volume fraction
ζ	Distributed random number
μ	Viscosity
$\overline{\overline{\tau}}$	stress tensor
$\overrightarrow{F}_{gl}$	Interaction force
ρ	Density
τ	Stress
τ_g	Particle relaxation time
τ_p	Particulate relaxation time
ε	Dissipation rate
k	Kinetic energy

Chapter 1

Introduction

1.1 Overview

Ever growing demand for oil and gas due to the increasing world population pushes the oil and gas industry to increase the production and supply of hydrocarbon, according to the International Energy Agency world energy outlook report in 2015, this demand is set to grow by 30-40% by 2040 (Tebowei, 2016). Hence, there is a need to explore in extreme environments where access to crude is very challenging with associated problems of sand production. One of the oldest challenges in the oil field is sand production and a number of potentially dangerous problems can occur due to the production of formation sand with oil and gas (Al-Rawahi, 2009).

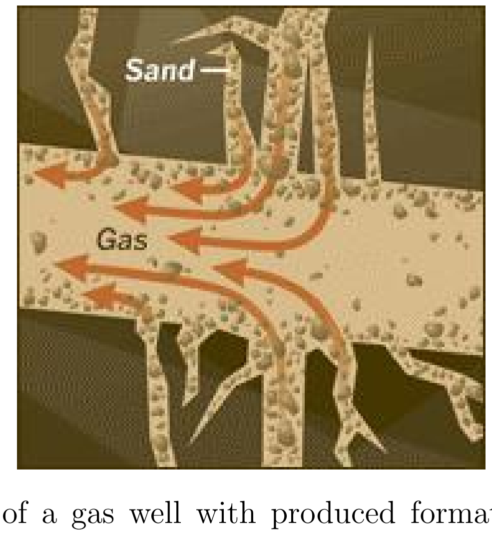

Figure 1.1: Schematics of a gas well with produced formation sand (United States Department of Labour, 2016)

Although technology advancement has led to the design of various sand control mechanism, they are not 100% efficient. Sand particles which come in different sizes and shapes are still being produced and transported along side fossil fuel, leading to problems of blockage, pressure drop and erosion in pipelines and other facilities on the flow line. Table 1.1 shows the effects of sand production in the oil and gas field.

Table 1.1: Effects of sand production (Al-Rawahi, 2009)

Area	**Problem(s)**	**Effects**
Reservoir	Wellbore fill	Restricted access to production interval Loss of productivity Loss of reserve
Subsurface Equipment	Sand fouling	Difficult wire line operation
	Erosion	Equipment replacement Equipment failure
Surface Installation	Sand Accumulation	Malfunctioning of control equipment Unscheduled shut down
	Erosion	Deferred production Sand separation and disposal

From Table 1.1, erosion can be seen as a major drawback of sand production in the oil and gas field, it strongly affects the subsurface and surface facilities. Due to this, erosion assessment while designing flow facilities is of utmost importance. Pipelines are one of the most important infrastructure in the oil and gas field, for example pipelines link the production field to the processing field or sub-sea facilities to the surface. Most prolific hydrocarbon reservoirs are prone to produce sand, therefore oil and gas pipelines will mostly contain streams of liquid, gas and solid particles. Hence, understanding the complex interaction between the sand particles, fluid and pipe wall is very important in order to get a know of the effects of the sand particles impinging on the internal pipe wall causing erosion, while being transported.

1.2 Sand erosion in pipelines and its challenges

In the oil and gas industry, predicting erosion is very important because many wells around the world produce a significant amount of formation sand alongside the fluid (either oil, gas or both), and this produced sand can cause erosion damage to pipelines and other facilities (Sedrez et al., 2018). Erosion is described as the gradual removal of the internal pipe wall material by repeated deformation and cutting action (Salama et al., 1983). This is due to the impact of solid or sand particles being transported through the pipe along with the fluid. It is a very complex mechanical process, it is influenced by a large number of parameters all of which contribute to its severity, these include fluid properties (i.e density, viscosity, number of phases), particle behaviour, pipe orientation, particle size and turbulence (Parsi, 2015). Repeated impact of the suspended solid particles on the inner wall of pipelines and pipe fittings removes material from the metal surface as shown in Figure 1.2. The reduced wall thickness due to particle impact overtime fails to withstand the operating pressure and condition the pipe system was initially designed for, hence resulting in premature failure. This failure leads to delay or drop in production as well as environmental and safety hazards with huge loss to the industry and economy (Mazumder et al., 2008a). Therefore predicting pipe erosion rate due to the transport of produced formation sand is a helpful tool in designing and selecting equipment to prevent failures (Shoham, 2006).

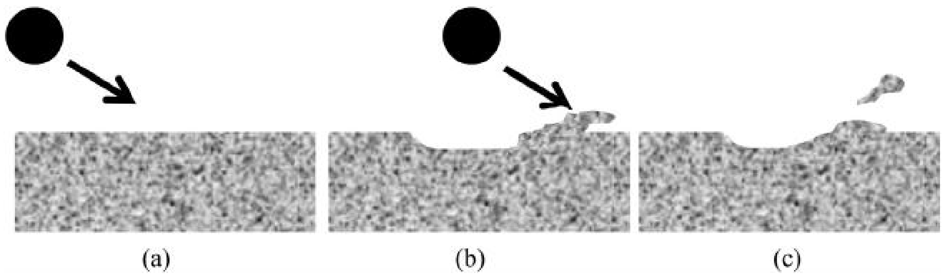

Figure 1.2: Schematics of erosion damage on pipe walls

Erosion damage occurs more at pipe sections that result in change in flow direction, and amongst these elbows have broad applications in the oil and gas industry (Parsi, 2015) (see Figures 1.3 and 1.4), therefore predicting erosion in elbows takes the centre stage.

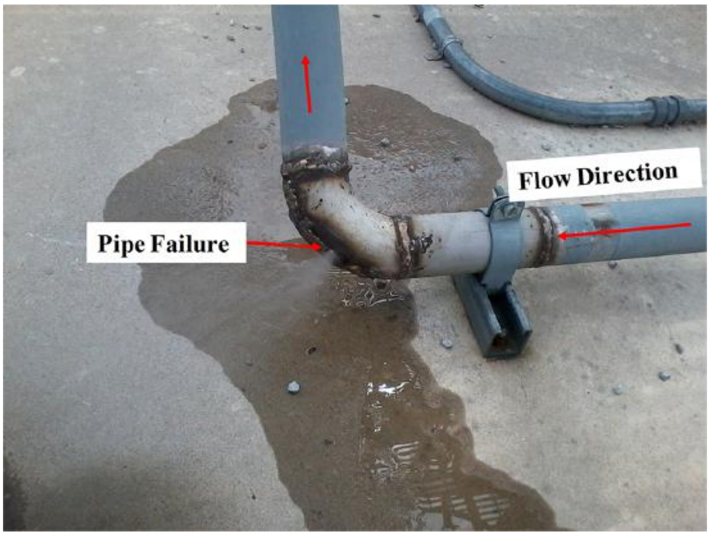

Figure 1.3: Pipe bend failure

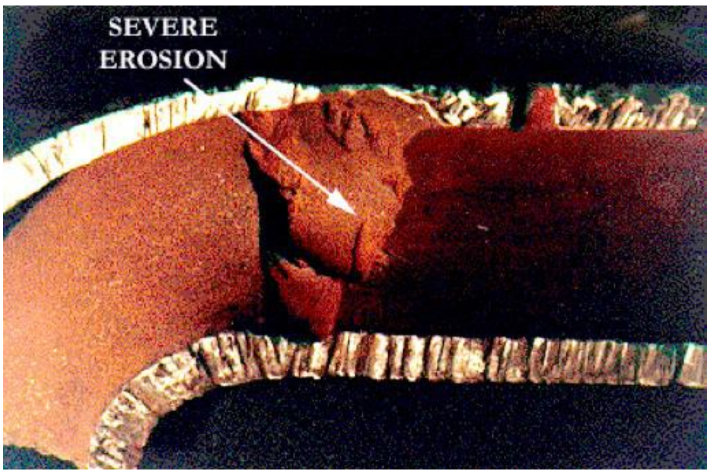

Figure 1.4: Pipe elbow damaged due to sand erosion

Many models and approaches have been proposed by researchers for predicting erosion in pipelines. Most of these models are categorised into empirical, mechanistic and CFD-based models, and due to the complexity of erosion, it could also be a combination of all three. While a lot of these erosion models are applicable to flow conditions where the carrier fluid is single phase, the actual fluid flow in many industries is in multiphase gas-liquid flow (Parsi et al., 2016a). Sand erosion in multiphase flow is not widely understood due to the complex interaction between the individual fluid phases and particles. When a mixture of liquid and gas flows through a pipe, the mixture tends to separate out with time and distance, and eventually form a definite configuration at steady state known as flow pattern. Various flow patterns occur in gas-liquid flow, and the individual phase behaviour and distributions vary among them (Parsi et al., 2016a). Flow regimes are also different based on different pipe orientation, in vertical pipes, annular, churn, slug and bubble flows are observed, while dispersed bubble, slug, stratified and annular flows are seen in horizontal (Parsi, 2015) (See Figure 1.5). Increasing gas superficial velocity at a constant liquid superficial velocity brings about transitions from one flow pattern to another.

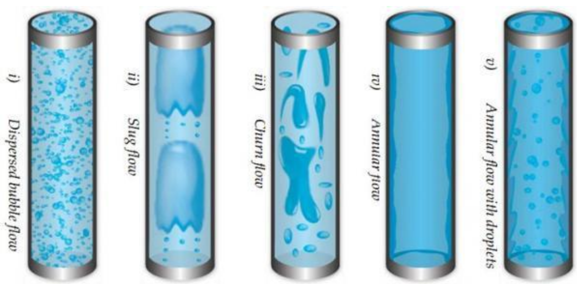

(a) vertical pipes

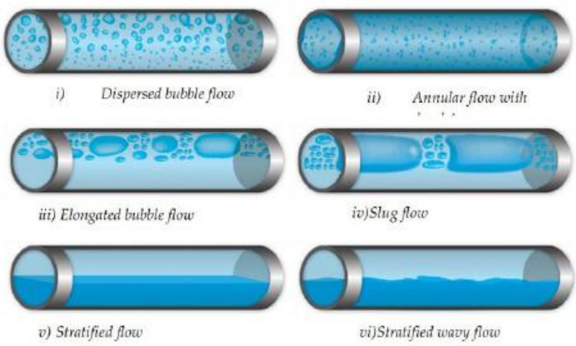

(b) horizontal pipes

Figure 1.5: Typical flow patterns (Bratland, 2010)

Multiphase flows exhibit complex physical behaviours which are more pronounced in complex flows such as churn and slug flows, and with erosion already being a complex phenomenal, accurate prediction of pipe erosion in multiphase flows becomes a very challenging area of study. This study remains of significant importance in the quest to make pipeline maintenance and design more economical as well as prevent environmental pollution and hazards as a result of pipe failures (Sedrez et al., 2018).

1.3 Motivation / Justification of Present Study

Despite all the resources that have been spent to investigate and study erosion in pipelines, the solid particle erosion mechanism is still not fully understood. Most previous studies on erosion in pipelines due to sand transport have also considered a pipe bend for which the upstream length is long enough for the flow to get fully developed before it reaches the elbow, however in recent times due to the exploration of oil and gas in extreme conditions, there is need for the use of complex pipe systems such as jumpers and other complex pipe networks to transport oil and gas from subsea level to the surface facilities. In these types of conditions where there is more than one elbow mounted at different sections of the pipe network with little or no distance for flow development between them, there is a paucity of research in erosion. Furthermore, there are still notable challenges in the study of erosion under two-phase flows. Due to this, it is highly desirable to analyse erosion damage due to sand particle impact in double bend pipe configurations where the carrier fluid is in multiphase. This study therefore uses the Computational Fluid Dynamics (CFD) approach to obtain fundamental information on sand erosion in pipes with double bends.

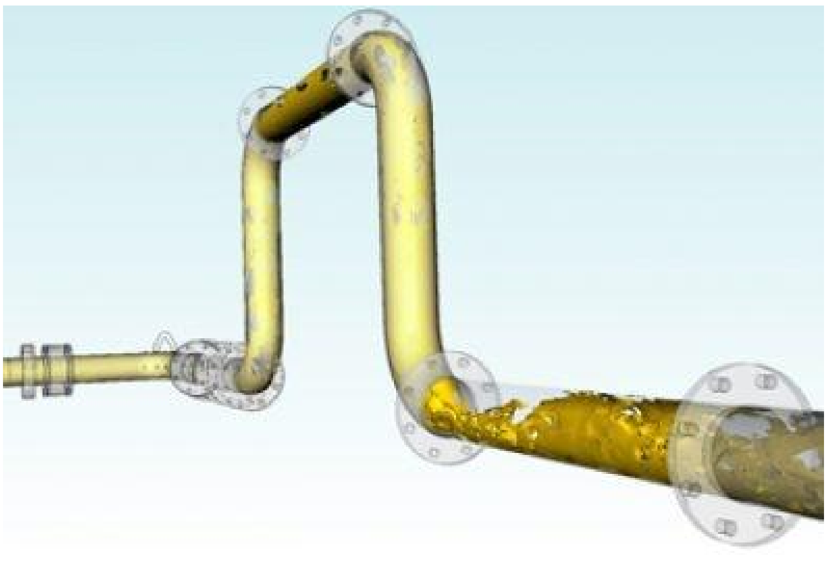

Figure 1.6: Typical pipe network with more than one bend (Oil and Gas Drill, 2015)

CFD is a numerical method for analysing engineering process systems involving fluid flow, heat transfer and related phenomena such as chemical reactions by means of computer-based simulation (Versteeg and Malalasekera, 2007). Numerical modelling based on Computational Fluid Dynamics (CFD), has attracted the attention of scientists and engineers from a wide range of backgrounds over recent decades during which these models have been extensively developed, analysed and applied to many practical applications. CFD investigation has become a vital component in the design of industrial products and processes, such as pipelines for transporting multiphase fluids. Although the CFD prediction will not completely replace experimental investigation for obtaining information for design purposes, but it is believed that computational methods play a vital role in providing insight into complex flow phenomenon (Pletcher et al., 2012). One major advantage of this approach is that it provides useful local and temporal information which are often difficult to obtain via experimental route (Kaushal et al., 2012; Ekambara et al., 2009; Syamlal et al., 1993).

1.4 Research aim and objectives

1.4.1 Aim

The aim of this study is to predict erosion at pipe bends under two-phase flow regimes in order to provide a better design consideration and pipe failure probability using CFD techniques.

1.4.2 Objectives

- To investigate and validate the CFD multiphase framework to determine its capability to model different multiphase flow conditions, and study the effects of change in flow patterns / conditions on the erosion at the pipe bend.
- To investigate the effects of separation ratio between two elbows mounted in series on their erosion rate due to sand particle impact, with particular emphasis on the multiphase flow pattern after the first elbow, sand concentration and particle

tracks.

- To investigate the effects of change in elbow orientation on erosion rate and location in the downstream elbow, highlighting the critical influence of the flow interaction between the upstream and downstream elbows.
- To investigate the effects of change in flow regime and conditions on erosion in double bends mounted in series by comparing erosion rate and location in different complex multiphase flow conditions and pseudo single phase flow conditions.
- To investigate the applicability of pseudo-single phase modelling for erosion prediction in order to reduce computational time.

1.5 Thesis Outline

This thesis is outlined as follows;

- Chapter 1 gives an overview of sand production and its effects in the oil and gas field, erosion in pipelines due to sand transport and the challenges with erosion estimation was also discussed. Justification and relevance of this study was explained, the research aim and objectives were stated.
- Chapter 2 presents a critical review of literature. This chapter concludes by revealing the gap in knowledge in the subject area under investigation.
- Chapter 3 presents the CFD methodology employed for this research. This includes detailed explanations of the necessary governing equations and models employed in the present study.
- Chapter 4 covers the solution procedure and validation to obtain the realistic results in this study as well as the numerical schemes employed. It also gives detailed explanation of the mesh sensitivity study as well as the model validation.
- Chapter 5 presents results of the numerical predictions of the multiphase flow patterns in double bends, flow patterns before the second elbow and erosion

in standard elbows mounted in series when the carrier fluid is in multiphase. This also reveals the implications of the separation ratio as well as varying flow interactions and parameters between the upstream and downstream elbows.

- Chapter 6 presents results of the numerical predictions of erosion in standard elbows mounted in series when the carrier fluid is in pseudo single phase (mixture properties employed). This reveals the implications of the separation ratio as well as varying flow interactions and parameters between the upstream and downstream elbows. It also presents the comparison of the erosion rates predicted using the multiphase and pseudo single-phase models.

- Chapter 7 summarizes the outcomes of this study, shows the conclusions drawn and the recommendations for future studies.

Chapter 2

Literature Review

2.1 Overview

2.1.1 Pipe Erosion Due to Sand Transport

Erosion due to solid particle impact at pipe bends has been studied using experimental, analytic and computational fluid dynamics (CFD) techniques, and due to the complex and complicated nature of erosion, most proposed erosion prediction technique are a combination of all three categories. Sand production remains one of the major problems while exploring fuel in mature fields. The broad applications of elbows (pipe bends) in the oil and gas and process industries has motivated the considerable amount of research in this area over the years. Furthermore, most researches have focused on erosion in elbows with upstream length long enough for flow development, however there is need for the analysis and exploration of erosion in complex geometries with more than one pipe elbows within close proximity of each other. Also, erosion prediction in multiphase flows still remain a challenging area of research.

2.1.2 Mechanism of solid particle erosion

As sand particles impinge on the a metal surface, a portion of metal is removed. When a particle hits a surface, scars are generated, these scars have been studied by many researchers to explain the mechanism of erosion damage (Parsi, 2015). The rate of erosion is primarily governed by the ductility of the metal, solid particle impact angle and velocity. Brittle materials are said to be eroded by a chipping and cracking mechanism while ductile materials are eroded by a scraping mechanism or plastic deformation (Figure 2.1) (Finnie, 1960; Jordan et al., 1998). According to Finnie (1960), the amount of surface material eroded by solid particles in a fluid stream depends on the conditions of fluid flow and on the mechanism of material removal. For ductile materials, it is possible to predict the mechanism with which material removal varies with change in the velocity and direction of impinging particles.

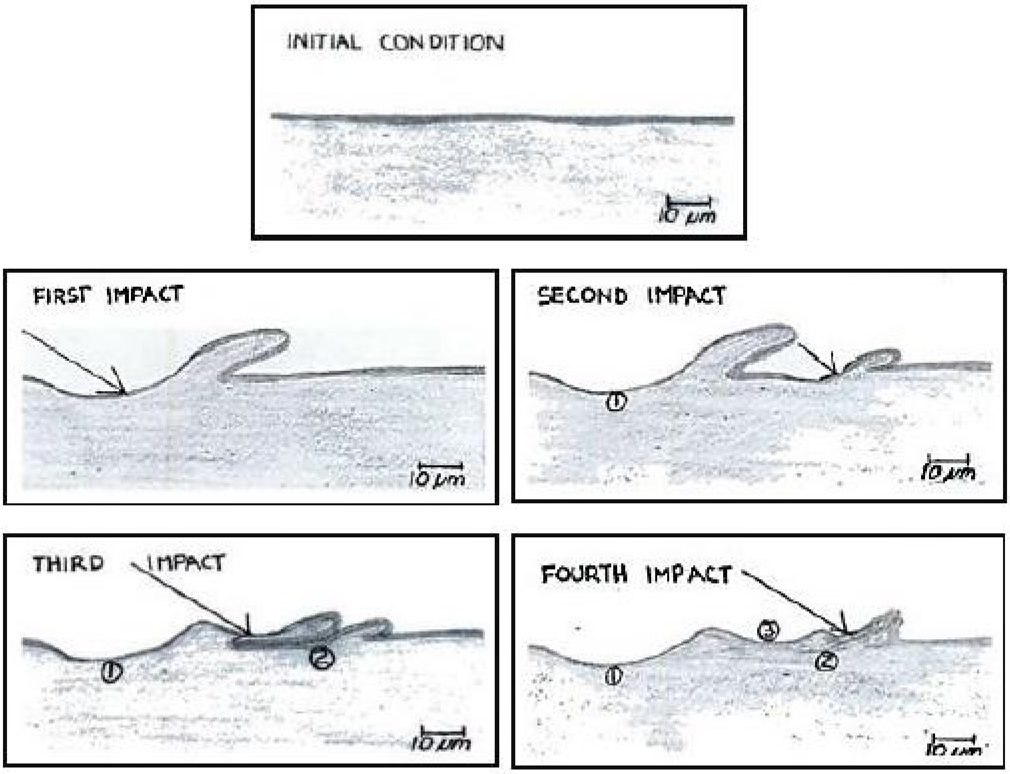

Figure 2.1: Schematics of erosion mechanism in ductile materials: (Levy, 1986)

Finnie (1958) suggested micro-cutting is the cause of erosion in ductile materials and proposed a micro-geometry model for ductile material. A particle creates a crater when it impinges on a ductile surface, subsequent particles pile up around the crater and their impacts make it bigger. Continued impacts eventually removes the piled up material. The model however under-predicts the magnitude of erosion for particles with high impact angles when compared with experimental data. This limitation was later addressed by Finnie (1960). More solid particle erosion mechanism for ductile materials can be found in the works of Hutchings and Winter (1974), Hutchings et al.

(1976), Hutchings (1977) and Andrews (1981) amongst others.

Unlike ductile materials, solid particle erosion mechanism for brittle materials is widely understood. Erosion in brittle materials is suggested to be due to crack formation (Parsi, 2015). When a brittle surface is hit by a particle, lateral and radial cracks are created, subsequent impacts on this surface causes the cracks to grow. These cracks split the target surface into small debris which are later removed as the particles impact the surface further. Formation and propagation of cracks remain the leading mechanism of erosion in brittle materials (Levy, 1995; Mansouri, 2016). Figure 2.2 shows the schematic of erosion mechanism in a brittle material, and Figure 2.3 is the plots of erosion rate against the impact angle for brittle and ductile materials.

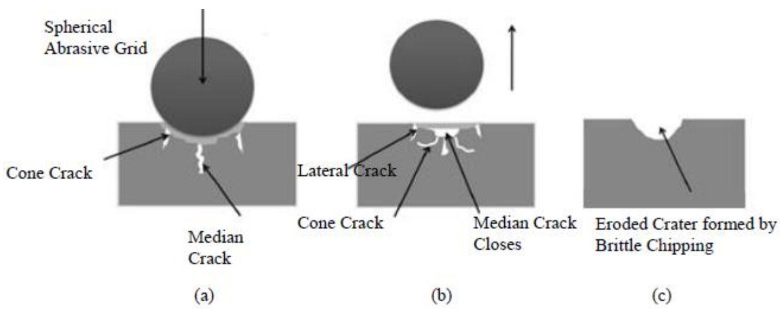

Figure 2.2: Schematics of erosion mechanism in brittle materials: (a) growth of cracks; (b) closure and median of lateral cracks; (c) eroded crater formed (Sooraj and Radhakrishnan, 2013; Parsi, 2015)

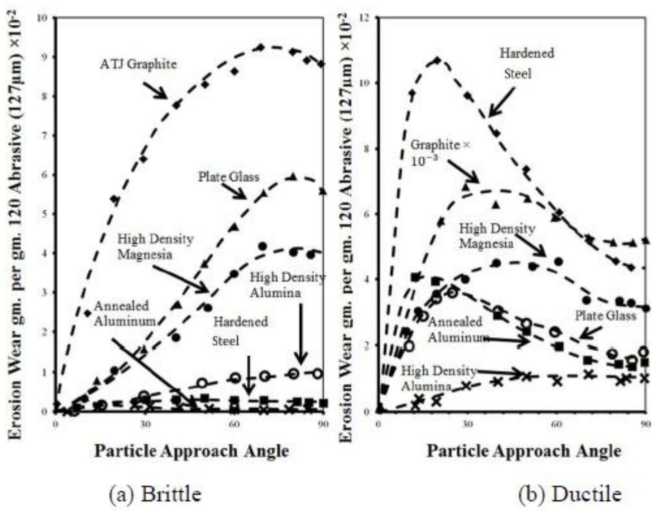

Figure 2.3: Erosion rate of ductile and brittle materials versus the impact angle (Sheldon, 1970; Parsi, 2015)

2.1.3 Parameters in predicting solid particle erosion

Solid particle erosion mechanism is influenced by varying parameters, all of which act in tandem. To develop an accurate erosion model or accurately predict erosion, the pertinent parameters in the erosion process has to be identified (Mansouri, 2016). Based on these parameters, many models for predicting erosion in pipelines have been proposed. Meng and Ludema (1995) listed 33 different parameters which are mostly mentioned in different erosion correlation available in literature. Most of them are however not independent. Clark (2002) however highlighted the following parameters to be the most important in erosion due to solid particle impact; particle properties (shape, size and material), particle impact speed, particle impact angle, carrier fluid properties, target wall properties and particle concentration amongst others. More reviews of important parameters in predicting sand particle erosion can be found in Levy et al. (1986), Jordan et al. (1998), Parsi (2015) and Mansouri (2016).

2.2 Empirical erosion prediction in pipelines

The American Petroleum Institute Recommended Practice 14E, API RE 14E is one of the earliest empirical equations used in the oil and gas industry for estimating erosional velocity. This was published in 1975, however, its basis and source remains a subject of speculation (API, 1981; Salama et al., 1983; McLaury et al., 1997; Salama et al., 2000; McLaury and Shirazi, 2000; Parsi, 2015). According to McLaury and Shirazi (2000), the procedure states that erosional velocity can be used where no specific information as to the erosive /corrosive properties of the fluid is available. In other words, the procedure determines the production velocity below which only a tolerable amount of erosion will occur (McLaury et al., 1997). The erosion velocity is determined based on the correlation given in Equation (2.1).

$$V_e = \frac{C_1}{\sqrt{\rho_m}} \tag{2.1}$$

where; V_e is the erosional velocity in ft/s, C_1 is an empirical constant and ρ_m is the fluid mixture density in lb/ft^3.

The use of this practice resulted from its ease of application and the lack of other available methods (McLaury and Shirazi, 2000; McLaury et al., 2011). However, the correlation is unsuitable in a system where production of sand and other solid particles is anticipated because it suggests that when the fluid density is low, the limiting velocity could be high. Meanwhile, sand in liquids with higher densities results in higher erosion than gas with low density (McLaury and Shirazi, 2000). Constant Values for C_1 are given as 100 and 125 for continuous and intermittent services respectively in a solid-free fluid system. Where solids and / or corrosive conditions are present, API RE 14E recommends that the C factor is reduced, but no guideline is provided on how to apply this reduction (Shirazi et al., 1995b; McLaury and Shirazi, 2000; Salama et al., 2000; Parsi, 2015). Different values were recommended for the C factor in Equation (2.1) by different researchers and based on this they showed that the equation is easy to use and too conservative for clean service such as liquid droplet. In a non-clean service, many important factors such as solid particle size and shape, sand production rate and multi-phase characteristics are not considered in the correlation. The equation also predicts higher values of erosional velocity as fluid mixture density decreases, this is not physical. By reducing the fluid density, the drag force exerted on the particle also decreases, hence causing the particle to impact at a higher velocity which results in more erosion (Parsi, 2015). The limitations of this erosion equation led researchers to the development of more sophisticated correlations for erosion prediction.

To account for the limitations of the recommendations of API RP14E, Salama et al. (1983) proposed a method for calculating erosion damage as a function of fluid and flow characteristics. The authors employed the experimental data of Rabinowicz (1979) which showed results of the erosive damage of ductile metals due to solid particle impingement.

$$ER = 1.86 \times 10^5 \frac{W_p}{P} \frac{V_f^2}{D^2} \tag{2.2}$$

Where; ER is the erosion rate in mils per year (mpy), W_p is the sand flow rate in bbl/month, V_f is the fluid flow velocity in ft/s, D is the pipe diameter in inches and P is the material hardness in psi.

Erosion rate predicted using equation (2.2) although overestimated by a factor of 1.44, the validity of the correlation was established when compared to available experimental data. Results presented in Salama et al. (1983) also showed that for flow in elbows and tees, erosion rates in tees are about 50% lower than that in elbows. Equation (2.2) is therefore rewritten for taking into account variations in bends or joints in the form in Equation (2.3);

$$ER = S_m \frac{W_p}{V_f^2} D^2 \tag{2.3}$$

Where S_m is a geometry dependant constant. The values suggested for S_m are; $S_m = 0.038$ for pipe bends, and $S_m = 0.019$ for tees.

Equation (2.3) predicts erosion rate more accurately for gas flow systems because it was developed based on erosion data in air-sand flow (Salama et al., 1983).

Bourgoyne Jr et al. (1989) conducted an experimental study to measure erosion rate for various field conditions. The author measured erosion rate in gas-solid, liquid-solid and mist-solid flows in diverter systems, and proposed a correlation for predicting wear rate in dry gas flows.

For gas continuous phase (Dry gas or mist flow);

$$ER = F_e \frac{\rho_p}{\rho_t} \frac{W_p}{A_{pipe}} (\frac{V_{SG}}{100\alpha_g})^2 \tag{2.4}$$

For liquid continuous phase;

$$ER = F_e \frac{\rho_p}{\rho_t} \frac{W_p}{A_{pipe}} (\frac{V_{SL}}{100H_L})^2 \tag{2.5}$$

Where; ER is the erosion rate in m/s, F_e is the specific erosion factor, ρ_p and ρ_t are the densities of the particle and wall in kg/m^3 respectively, W_p is the sand flow rate in m^3/s, A_{pipe} is the cross-sectional area in m^2, V_{SG} and V_{SL} are the superficial gas and liquid velocities in m/s respectively, α_g is the gas volume fraction and H_L is the liquid hold up.

Equations (2.4) and (2.5) were developed based on experimental data obtained at high flow rates that can be observed in diverter systems. Hence, under low concentration, their applications to oil and gas production systems is questionable. The study reports a 29% percent error in erosion prediction, and an order of magnitude decrease was observed in the erosion rate when the elbow was changed to a tee or vortice elbow (Bourgoyne Jr et al., 1989).

Svedeman and Arnold (1993) investigated the applicability of Bourgoyne Jr et al. (1989)'s method of predicting wear rate to lower flow velocities. An average over-prediction of 25% was observed when a comparison was made with erosion data from Weiner and Tolle (1976). Because different wear mechanism have varying controlling parameter, the authors rearranged Bourgoyne Jr et al. (1989)'s equation and recommended the correlation shown in Equation (2.6) for erosional velocity for erosive service based on an acceptable wear rate of 5 mils/year.

$$V_e = K_s \frac{D}{\sqrt{W_p}} \tag{2.6}$$

Where V_e is the erosional velocity in ft/s, D is the pipe diameter in inches and W_p is the sand flow rate in ft^3/day. K_s is fitting erosion constant derived from Bourgoyne's specific wear factors, it depends on the flow conditions as well as fitting material and geometry. K_s is 1.34 and 7.04 for long radius elbows and plugged tees respectively. The erosional velocity is the mixture velocity, that is; summation of superficial liquid and gas velocities (Parsi, 2015).

Svendeman and Arnold (1994) also recommended a similar correlation to that of Salama et al. (1983), the authors reported that a different set of parameters must be accounted for to limit erosion damage in pipes. Criteria for determining appropriate pipe sizes for sizing multiphase flowlines where erosion and corrosion are expected was presented, and different values were reported for S_m; 0.017 for long radius elbows and 0.0006 for plugged tees.

Jordan et al. (1998) proposed a new method of calculating erosion limits in multiphase oil and gas pipelines. The author employed the data from Bourgoyne Jr et al.

(1989) and made assumptions on the particle size and rate of production. It was proposed that the rate of material volume loss should vary directly with the square of the particle velocity and linearly with the volumetric rate at which the target wall is impinged by particles. The correlation developed is shown in equation (2.7).

$$ER = 10^{C_1} V_{SG}^{2.349} W_p^{0.9535} (1 - (1 + \frac{1}{2r_c})^{-2})^{\frac{1.8885}{2}} \tag{2.7}$$

Where r_c is the bend radius of curvature. The parameters also have similar units as to the equation of Bourgoyne Jr et al. (1989). C_1 is equal to -4.9619 and -5.4355 for cast and seamless materials respectively.

Salama (1998) and Salama et al. (2000) carried out a study to investigate the basis of the recommendations of API RP14E, the authors found out that alternative approaches have been proposed for establishing erosional velocity in particle laden flows. But none of these have been put to use due to their complexity. Based on the findings, the author proposed a new simplified model for erosional velocity in particle laden fluids. This new correlation incorporates the effects of pipe diameter, fluid density and sand flow rate in the previously developed correlation by Salama et al. (1983) but the influence of elbow radius of curvature was not considered. The results did not show any concrete difference between erosion in bends with radius of curvatures (RC) of 1.5 and 5. The equation is also applicable to multiphase flow.

$$ER = \frac{1}{S_m} \frac{W_p V_m^2 d_p}{D^2 \rho_m} \tag{2.8}$$

Where; ER, W_p and D are in mm/year, kg/day and mm respectively. d_p is the particle diameter in microns, V_m is the mixture velocity in m/s and ρ_m is the density of the fluid mixture in kg/m^3. S_m is a geometry dependent constant.

Empirical erosion equations are easy to use but can only be applied to operating conditions similar to the experimental conditions for which they have been developed (Mazumder et al., 2003), but erosion mechanism could change with the slightest change in conditions. Due to this, researchers developed mechanistic models to aid erosion prediction in a comprehensive and complex scenario. Mechanistic models incorporate various parameters that could influence erosion phenomenon, they were developed based on the physics and mechanisms of erosion (Parsi, 2015).

2.3 Mechanistic erosion prediction

Shirazi et al. (1995b) and Shirazi et al. (1995) proposed a preliminary guideline to overcome the demerits of recommendations of API RP14E. The guideline contains a procedure for predicting a characteristic threshold velocity and / or particle size below which only a minimal amount of erosion occurs. The model incorporates the effects of a number of variables, including sand particle size, flow geometry, pipe size, material type, sand density, sand sharpness, flow stream velocity, fluid viscosity, and fluid density on erosion rate. The authors proposed a mechanistic correlation for computing penetration rates in single phase flow in elbows and tees. The procedure assumes that in a direct impingement situation, for every geometry, before impact, particles penetrate a fluid layer called stagnation zone (Figure 2.4); to capture the effect of geometry type and size, the equivalent stagnation length concept was also introduced (Figure 2.5).

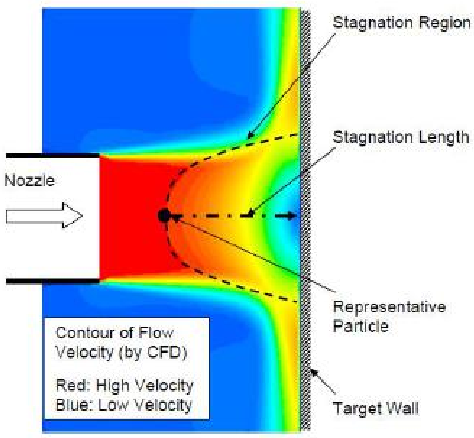

Figure 2.4: Schematic of stagnation region in direct impingement geometry (Zhang et al., 2010)

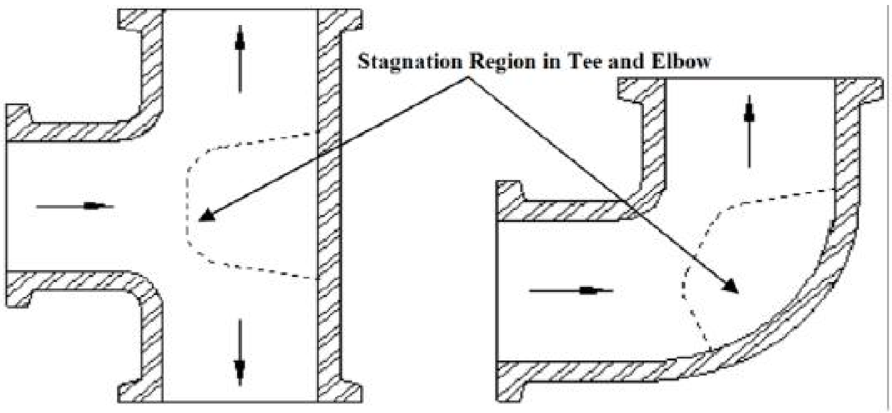

Figure 2.5: Schematic of stagnation region in tee and elbow (Parsi, 2015; Mansouri, 2016)

Depending on the type of geometry, the stagnation length is obtained from Equation (2.9) or Equation (2.10).
For elbows, the length of the region of stagnation is obtained from;

$$\frac{L_{stag}}{L_{ref}} = 1 - 1.27tan^{-1}(1.01D^{-1.89}) + D^{0.129} \tag{2.9}$$

For tees, the length of the region of stagnation is obtained from;

$$\frac{L_{stag}}{L_{ref}} = 1.35 - 1.32tan^{-1}(1.63D^{-2.96}) + D^{0.247} \tag{2.10}$$

Where D is the pipe diameter, L_{stag} is the length of stagnation region and L_{ref} is the reference length (1.18 and 1.06 inches for elbows and tees respectively). For small pipe diameters, L_{stag} is a strong function of pipe diameter while for pipe diameters larger than about 6 inches, pipe diameter has little influence on L_{stag} (Parsi, 2015).
Flow velocity is calculated from Equation (2.11). The characteristics velocity of the flow is set equal to the average velocity of the flow.

$$V_f = V_{char}(1 - \frac{x}{L_{stag}}) \tag{2.11}$$

Where V_f is the fluid velocity and V_{char} is the flow characteristic velocity. The particle impact velocity is obtained by solving the particle equation of motion as shown in

Equation (2.12).

$$m_p V_p \frac{dV_p}{dX} = 0.5\rho_f (V_f - V_p)|V_f - V_p| C_D \frac{\pi d_p^2}{4} \tag{2.12}$$

Where m_p is the mass of particle, V_p is the particle velocity, V_f is the fluid velocity at the particle location, ρ_f is the fluid density and C_D is the drag coefficient.

As an initial boundary condition, the particle equation of motion needs the particle velocity (V_p) at $X = 0$. Initial particle velocity is also assumed to be the same as V_{char}. Particle tracking is stopped and particle velocity at that location is considered as the impact velocity when the distance between the particle and the wall is equal to the radius of the particle (Parsi, 2015).

The drag coefficient is expressed as;

$$C_D = \frac{24}{Re_p} + 0.5 \tag{2.13}$$

where Re_p is the particle Reynolds number and it is expressed as;

$$Re_p = \frac{\rho_f |V_f - V_p| d_p}{\mu_f} \tag{2.14}$$

μ_f is the fluid viscosity.

The erosion ratio is finally obtained from Equation (2.15).

$$ER = 1.73 \times 10^{-6} V_L^{1.623} \tag{2.15}$$

Where ER is the erosion ratio of the mass of the target material removed to mass of particle, and V_L is the particle impact velocity. The particle impact velocity, V_L, is calculated from a simple 1-D particle tracking approach along the stagnation length. Here the particle equation of motion is numerically solved.

Equation (2.15) was developed based on erosion data for low carbon steels. Results obtained showed that threshold velocity for single phase liquid is higher than that of gas. This was in good agreement with the experimental data obtained from Bourgoyne Jr et al. (1989) and Clark (1991), however, the procedure assumes that particle trajectory to be a straight line and does not incorporate the effects of turbulence on the particle trajectory. The model was originally developed for single phase flows and was later extended to multiphase by McLaury and Shirazi (2000), this formed the basis for many subsequent mechanistic models. Furthermore, Mazumder et al. (2005) at the Erosion / Corrosion Research Centre (E/CRC) of the University of Tulsa improved the previous mechanistic models by considering the distribution and characteristic behavior of the liquid and gas phases in multiphase flows.

The limitations of Shirazi et al. (1995b), Shirazi et al. (1995) Shirazi et al.'s (1995a,b,c) model was identified by Zhang et al. (2010), the author found that the model predicts erosion by calculating particle impact velocity based on 1-Dimensional particle tracking. This limits its application to sand particle sizes of between 50 and 100 microns or flow conditions which has gas as the carrier fluid. It was discovered that both normal and tangential particle impact velocity components as well as turbulence have significant impacts on erosion prediction. They suggested a 2-D mechanistic approach to capture these particle characteristics. The procedure has three main steps; firstly, 2-D flow field information was obtained from CFD simulations focused on the flow in the stagnation region. Secondly, the flow field information obtained is used to compute particle information such as impact speed, angle and location. Unlike the 1-D where a single representative particle is tracked, in 2-D models many particles are tracked. The impact information are finally entered into the erosion equation developed by Zhang et al. (2007) to calculate the erosion rate. To account for the particle impact velocity and the effect of turbulence, the 2-D model provides more representative particle impact information and therefore predicts erosion behavior much better than the 1-D model. These improvements are of high significance for cases with liquid carrying small sand particles.

Arabnejad et al. (2015) proposed a semi-mechanistic model for predicting erosion of different target materials due to solid particle impact. The model is based on experimental data from a direct impingement testing that accounts for particle and target material properties, and it assumes that solid particle erosion is caused by two different mechanisms; cutting and deformation. Hence, the erosion equation has two parts; cutting and deformation erosion. Particle velocity was measured by Particle Image Velocimeter (PIV), and the model predictions were compared with various cases for validation purposes. The correlation pointed out that particle impact angle changes with particle shape and velocity.

Parsi et al. (2018) developed a correlation for estimating solid particle erosion under gas-sand flow conditions in standard elbows. The approach has three steps; a dimensional analysis was performed to obtain dimensionless groups such as Reynolds number, diameter ratio and density ratio that control flow and particle behaviour in elbows. Investigation of the effect of target wall material on erosion was conducted and lastly, an empirical factor was included in the correlation to account for sand particle shape. The correlation is an effective tool that estimates erosion under gas-sand flow conditions with minimal computational efforts. The predictions of using the correlation showed good agreement with experimental data. It was however developed based on limited experimental data and it accounts for all particle and flow parameters.

Erosion prediction even in single phase flow is complex, and this complexity increases significantly in multiphase flows due to its nature of occurrence. Particle tracking also becomes more complex when entrained in multiphase flows. In multiphase flows, the spatial distribution of the liquid and gas phases and their corresponding velocities changes continuously (Mazumder et al., 2005). McLaury et al. (1999) and McLaury and Shirazi (2000) developed a mechanistic model to predict erosion rate in elbows, tees and direct impingement geometries. They extended the single phase erosion model of Shirazi et al. (1995b) to multiphase flow conditions. The new model was developed to account for many physical variables such as solid flow rate, mixture viscosity, particle impact velocity, pipe diameter, fluid density, elbow radius and particle material. In this model, the density and viscosity of the fluid in the stagnation length is computed based on the volume of the liquid and gas at flowing conditions. It was noted that in elbows, more erosion occurs when the exchange of momentum between the fluid and particles is low because of the inability of the fluid to direct the particles as they travel through the bend. Hence, any factor that increases the rate of momentum exchange will decrease the erosion rate. Results compared to data from the recommendations of API 14RE showed the empirical procedure to be too conservative at high superficial flow rates of liquid.

Mazumder (2004), Mazumder et al. (2005), Mazumder (2007) and Mazumder et al. (2008a) proposed a mechanistic model to predict sand erosion in multiphase flow in elbows downstream of vertical pipes. The influence of particle velocities on erosion rate in gas and liquid flows was studied. The model employs the entrainment correlation proposed by Ishii and Mishima (1989) to calculate the entrained liquid fraction in the gas core because of its accuracy over a wide range of flow conditions. Liquid droplet velocity was observed to have a significant effect on particle impact velocity, hence causing large erosion damage. Accurate prediction of droplet is therefore recommended so as to determine the sand particle velocity before it reaches the stagnation zone. Particles could also be trapped in the liquid droplets moving at a velocity similar to the gas velocity, these particles therefore have significant effects on the erosion damage when compared to particles in the liquid film moving at a slower speed near the pipe wall. Although there are discrepancies, predicted erosion shows good estimate of erosion in multiphase flow when compared with data from erosion experiments conducted for multiphase flow. The authors also observed erosion damage to be much higher in vertical annular flows with high gas velocity and low liquid velocities. The model predictions are 2.9 to 6.8 times more at lower liquid rates and 4.2 to 8.2 times more at higher liquid rates when compared to experimental data. For bubble, slug and churn flows, the erosion predictions are higher and conservative when compared with experiments. Based on this, further verification and modification of the model is recommended.

Furthermore, Zhang et al. (2011) proposed a two-dimensional mechanistic model for predicting sand erosion in slug flows. All mechanistic models prior to this are based on 1-D approach. A 2-D method is therefore extended to solving erosion in multiphase flows. The model assumes particles are uniformly distributed in the liquid phase and do not contribute to the erosion due to their low velocities. The slug body was also simplified into a representative single phase. Erosion rate was successfully predicted at different locations in the elbow geometry. At 45° into the elbow, predicted erosion agrees very well with available data while at 90°, there is more scattered prediction. This was attributed to the influence of secondary flow in the elbow. Overall, the 2-D has a better accuracy compared to the 1-D approach.

Shirazi et al. (2016) developed a semi-mechanistic model for predicting sand erosion threshold velocities in gas and multiphase flow productions. Unlike the API RP 14E, this model can be applied in two ways; one to provide maximum penetration rate for a particular operating condition, and two, it can be employed to determine threshold superficial liquid and gas velocities if an allowable maximum penetration rate is specified. The model shows a significant improvement on previous mechanistic models for situations involving small particles flowing in compressed gases with high densities and those in liquid streams. It is also applicable to single phase conditions. The model's ability to include the effects of various parameters such as particle diameter and shape, fluid density and viscosity and flow velocity was verified by comparing with available experimental data in literature and the Tulsa Erosion / Corrosion Research Centre (E/CRC). The results show good agreement over a broad range of operating conditions for both single and multiphase flows, however, some discrepancies were observed for annular flow. The threshold superficial velocity predicted by the model was also compared with that from API RP 14E for multiphase flow conditions, the latter shows to be highly conservative at high superficial liquid velocities.

Recently, Kang and Liu (2019*a*) developed a mathematical model to predict solid particle erosion on the symmetry plane of elbows for annular flows. The model tracks particle as they impact the pipe wall and accounts for particle motion in both the gas core and liquid film. The model assumes the gas core to be a homogeneous flow and the liquid film velocity and thickness to stay uniform along the pipe bend. The entrance length is assumed to be long enough for the particles to mix with the carrier fluid before accessing the elbow. The authors also studied the effects of different macroscopic parameters on penetration ratios. The accuracy of the model is poor at low gas superficial velocities but better in higher velocities. The results show that increasing the particle diameters and gas superficial velocity leads to an increase in penetration ratios. The effect of superficial liquid velocity on erosion ratios however varies with liquid loading conditions. Results presented showed an average deviation of 26.15% when compared to available experimental data. The model however lacks the capability to present a more robust flow field information and is limited to annular flows. Kang and Liu (2019*b*) also developed a probability model for predicting sand erosion in elbows for annular flow. The authors estimated erosion caused by a group of sand particles by calculating the erosional damage as a result of a single particle. The probability models of the first and second collisions were based on the works of Liu et al. (2015). Results presented show good agreement with available data for annular flow regime. The authors concluded the second collisions of particles has huge influence on magnitudes and locations of erosion under annular flow conditions. However, its application to other multiphase flow patterns still remains a subject of discussion.

2.4 Experimental analyses of sand erosion in pipelines

Mazumder et al. (2008b) performed experimental investigation to determine the location of maximum erosive wear damage in single-phase, multiphase horizontal and vertical flows. Aluminum elbow specimens were used due to its lower density to obtain more precise thickness loss measurements and erosion damages were accessed using electrical resistance probes. Single-phase erosion experiments was performed at superficial gas velocity of 34.1 m/s in vertical flow, in multiphase flow, 33.5, 27.4, 18.9 and 9.8 m/s superficial gas velocity while liquid velocities are 0.03 and 0.3 m/s in the vertical and horizontal pipes. Results showed a maximum thickness loss of 42.5 μm at 55° from the elbow inlet in the single-phase flow, and in multiphase flow at superficial gas velocity of 9.8, 27.4 and 34.1 m/s the average thickness losses are 10.2, 17.6 and

22.3 μm respectively in vertical pipes. The thickness loss increased with an increase in gas velocity for the same superficial liquid velocity. Furthermore, in both vertical and horizontal pipes for multiphase flows, maximum thickness loss was observed at 55° and between 35° and 55° from elbow inlet respectively. Further studies are recommended to study the effects of liquid rates on erosion. Graham et al. (2009) measured erosion in slurry flows with the use of coordinate measuring machines (CMM). The pipe network diameter was 53 mm ID and the experimental setup was designed so that a vertical flow was achievable. The elbow was also made of aluminum blocks. Maximum erosion was observed towards the exit of the elbow. The CMM results were compared qualitatively with paint modelling and visual inspection, and good agreement was observed.

Kesana et al. (2012) and Kesana et al. (2013a) used a novel non-intrusive ultrasonic device to measure erosion at 16 different locations in a standard elbow. The experiments were initially performed with a single-phase carrier (gas-sand) before they were extended to multiphase flow conditions. The influence of particle diameter and liquid viscosity was studied, and results showed acceptable agreement with available experimental data. While performing the Ultrasonic Technique (UT) experiments, erosion was simultaneously measured in the straight pipe section using an intrusive Electrical Resistance (ER) probe. The erosion pattern at the bend was successfully identified and the location of maximum erosion in the gas-sand flow was observed around 45° into the bend while it is at the top end of the bend for multiphase condition. An increase in particle size also led to a corresponding increase in erosion, at 10 cp viscous liquid, erosion slightly increased when compared to 1 cp, while it decreased after the viscosity was increased to 40 cp. Results from the Ultrasonic Technique (UT) and Electrical Resistance (ER) probes are both similar.

Kesana et al. (2013b) conducted experiments with superficial gas velocities ranging between 9.1 m/s and 35 m/s with a constant liquid velocity of 0.76 m/s to investigate sand erosion in multiphase slug flow. Three liquid viscosities of 1cp, 10cp and 40cp were also employed. The test section is made up of a standard 76.2 mm elbow. The authors observed that the entrainment of sand particles in pseudo slugs (highly aerated slugs) are very high compared to that in slug flow regimes because the mixing region in pseudo slugs lasts the entire length of the slug and pseudo slugs travel at lower velocities. Also, as a result of turbulence, particles may be suspended across the entire cross-section of the pipe in pseudo slugs, hence, the number of particles impinging on the pipe wall for pseudo slugs is higher compared to slug regimes. Kesana et al. (2014) extended the same procedure to study the effects of particle size and liquid viscosity on erosion in annular and slug flows. Three different sand sizes (20, 150 and 300 μm) were employed for the test, and erosion in straight pipes and bends were measured using the Electrical Resistance (ER) probes. Erosion measurements taken in the bend at 45° and 90° and in the straight section show that for any operating condition, larger particles create more erosion than the smaller ones and a change in liquid viscosity has no influence on the effect of particle size on erosion. Erosion rate in annular flow was also observed to be higher than slug flow irrespective of location and liquid viscosity because the sand causing erosion damage to the pipe is in the gas core region with a lower density in annular flow whereas for slug flow, the particles travel in the liquid slugs.

Parsi et al. (2015a) also used the Ultrasonic Technique (UT) to measure sand particle erosion in gas dominant multiphase churn flow in vertical pipes and compared their results to the erosion data from Kesana et al. (2013a)'s horizontal-horizontal flow analyses. The experiments were carried out in a 76.2mm ID standard vertical-horizontal (V-H) elbow made of stainless steel and erosion was measured, effects of superficial gas and liquid velocities, particle size and liquid viscosity on erosion rate were investigated. Sand particle sizes 20, 150 and 300 μm were employed, and liquid viscosities were 1 cp and 10cp. Superficial gas velocity ranged between 9.8 and 49 m/s and superficial liquid velocity ranged between 0.1 and 0.55 m/s. It was observed that erosion rates in the vertical-horizontal elbow are significantly higher than those measured in the horizontal-horizontal elbow for all flow conditions. Results also showed that as far as the flow regime does not change, a change in superficial liquid velocity has no significant effect on the erosion rate, and in churn flow, the inlet area of the elbow up to 45° was more prone to erosion damage.

Vieira et al. (2017a) measured solid particle erosion in multiphase annular flow using the electrical resistance probe, the study focused on collecting experimental data in a large scale multiphase flow loop with 76.6 mm standard elbow. Superficial gas and liquid velocities ranged from 11 m/s to 48 m/s and 0.004 m/s to 0.27 m/s respectively. Liquid viscosities of 1cp and 10cp were also used as well as 3 different sand sizes (20, 150 and 300μm). The influence of ER probe location, flow orientation, sand size and liquid flow rate and viscosity was examined. They observed that a change of the carrier fluid from gas-sand to low-liquid annular flow decreased the measured erosion by a factor of 4 in the vertical elbow orientation. An increase in the viscosity of the fluid surrounding the bend also led to a reduction in the particle impact on the wall. Furthermore, irrespective of the operating conditions, the higher metal loss was recorded at the probe at 45°. In the horizontal orientation on the other hand, as liquid film becomes thicker at the bottom of the pipe, a decrease in erosion was observed.

The effects of superficial gas and liquid velocities, and particle size on erosion rates and patterns was further experimentally studied by Vieira et al. (2017b) and Vieira et al. (2017c). Instead of the electrical resistance probe, the authors employed the non-intrusive ultrasonic measurement technique to analyze erosion under multiphase annular flow conditions in a vertical-horizontal bend. It was observed that for higher superficial gas velocities, erosion first decreased and then increased again after reaching a minimum. It was however generally observed that erosion increased when particle size and / or gas flow rate increased.

2.5 CFD modelling of pipe erosion

2.5.1 CFD modelling of pipe erosion in single phase flows

Zhang et al. (2009) used CFD based method to study erosion predictions. The authors examined the particle motion in the near-wall region, and compared calculated solid particle erosion patterns with experimental data to investigate the accuracy of the models employed in calculating particle motions. The effects of turbulent velocity profile at the near wall region was considered and its effect on particle impact velocity was investigated. A comparison was made when standard wall functions have been applied in the near-wall particle tracking and rebounding the particles at a radius from the wall. Flow was modelled by solving the continuity and momentum equations, particle trajectory determined by integrating the force balance on the sand particle via the Discrete Phase Model (DPM) and the effects of turbulence on the particle motion was accounted for by applying a Discrete Random Walk (DRW) Model. The near-wall region was resolved using the RSM turbulence model with standard wall function and erosion was calculated using the erosion equation proposed by Zhang et al. (2007). Solid particle erosion predicted before and after introducing the near wall rebound modification and turbulence effects shows that the modification has a significant effect on the erosion results when compared with experimental data. For a turbulent flow through a standard 90° bend, it was observed that accounting for rebound helps to avoid non-physical impacts and reduces the number of impacts by more than one order of magnitude for small particle ($25\mu m$) due to turbulent velocity fluctuations while non-physical impacts are not observed for large particles ($256\mu m$), hence reducing the corresponding erosion. Applying standard wall functions in the near wall particle tracking also reduces the predicted erosion for the larger particles slightly and by a factor of 2 for the small particles. Erosion results from the small particle show better agreement with experimental data. Small sand particles cause a more uniformly distributed erosion pattern compared to large particles.

Zhang et al. (2012) also conducted a numerical investigation of the location of maximum erosive wear damage in elbows. The length of the elbow is about 0.628 m and diameter is 0.1m. The authors studied the effects of slurry velocity, bend orientation and angle of elbow. Particle trajectory and effects of particle-particle interactions were calculated with the Discrete Element Model while fluid characteristics were modelled with the Reynolds Averaged Navier Stokes equations. It was observed that location of erosion damage is influenced by the slurry velocity because the location of maximum erosion moves downstream when slurry velocity increases. Bend orientation also shows a significant influence on the wear damage, in the horizontal to vertical pipe, particles settle on the bottom of the horizontal pipe which results in most particle moving away from the central axis and this movement makes the impact point move deeper into the bend. For a U-shaped bend, maximum erosion location was observed at two different peaks; about 43°, this is similar to that of the 90° elbow, and approximately 160° due to the centripetal force.

The effects of wall roughness on erosion rate in gas-solid horizontal turbulent annular pipe flow was numerically studied by Jafari et al. (2015) in a 30 cm diameter pipe with a length of 100cm, and the results were compared with earlier studies. The gas phase was modeled by resolving the Reynolds averaged Navier Stokes (RANS) equations coupled with the standard $k-\varepsilon$ model and particles were tracked in using the Discrete Element Method (DEM). Turbulent dispersion was accounted for with the Discrete Random Walk Model (DRW). Sand particle size employed are 100 and 200 μm. The results generated showed that erosion rates at both inner and outer walls increase as wall roughness increases, the erosion rates are also much higher when compared with that of smooth walls irrespective of the sand particle size. This is because when roughness increases, particle concentration is enhanced near the inner wall of the elbow and this lead to more frequent particle-wall collisions which results in increased erosion rates. Also, the authors reported that the outer wall of the annular pipe bend is more erosive when compared with a simple circular pipe with the same outer radius and the erosion rate increases as the radius ratio increases.

Chen et al. (2015) proposed a CFD-DEM based liquid-particle two-phase flow erosion prediction method for pipeline elbows. The interactions of liquid-particle, particle-particle and particle-wall were considered. Water was used as the continuous phase, sand particle diameter of $150\mu m$ and maximum erosion rate and location were predicted in 90, 60 and 45° elbows of 40 mm diameter. The continous phase was modeled by solving the Reynolds Averaged Navier Stoke's equations, the standard $k - \varepsilon$ model accounted for the flow turbulence in the elbow and sand particle motion was modeled using the Discrete Element Model (DEM) to further capture the fluid-particle interactions. Maximum erosion rates were observed to be different for the 3 elbows with 90° elbow being the most erosive. Locations with maximum erosive damage is at or near the exit of the elbows. The authors further recommend wide bend-angle elbows such as 90° be replaced with small bend angle elbows (45° and 60°) to reduce erosive damage.

Zahedi et al. (2016) conducted a parametric analysis of erosion in standard 90° (r/D = 1.5) and long radius elbows, the effects of the particle size, fluid velocity, pipe diameter and radius on maximum erosion in a gas-sand flow system were investigated. The internal diameters investigated are 2, 3, and 6 inches, and superficial gas velocity of between 11 and 27 m/s. Conservation of mass and momentum equations were resolved for the fluid flow, turbulence was accounted for using the Reynolds Stress Model (RSM) with scalable wall functions and the particles were tracked in the Lagrangian Discrete Phase Model. Erosion rates were calculated with the correlation developed by Vieira (2014) for the Erosion / Corrosion Research Centre (E/CRC) and particle-wall rebound was accounted for with the model by Grant and Tabakoff (1975). Results presented showed good agreement with the experimental data in Vieira (2014). It was observed that for single phase gas-sand flow at low pressure condition, location of highest erosion is at about 45° into the elbow. It was observed that particles of 300 μm in size causes about two times the erosion caused by 150 μm particles. Increase in superficial gas velocity also caused an in increase in erosion rate, erosion ratios were however reduced exponentially with an increase in pipe diameter at constant flow conditions and particle properties. Maximum erosion magnitude in long radius elbow is also less than that in a standard elbow.

Mahdavi et al. (2016) studied erosion due to highly concentrated slurries. The authors investigated the effects of particle size and velocity on erosion ratio for different sand concentrations. Liquid inlet velocity was set at 45 ft/s and sand concentrations of 1, 6, 10 and 15% were employed, sand particle size is 300 μm. Flow solution was obtained by resolving the Reynolds averaged Navier Stokes (RANS) equations using the Eulerian approach while the particles were tracked in the Lagrangian and Granular scheme for the sake of making comprison between the results, erosion ratio was calculated with the correlation developed by Vieira (2014). Both the Eulerian-Lagrangian and Eulerian-Granular approaches under-predicted the experimental data, however, the erosion predictions of the Eulerian-Granular scheme decreases slightly as sand concentration increases while in the Eulerian-Lagrangian case, erosion ratio is constant for various sand concentrations. It was also observed that an increase in the sand concentration leads to a corresponding increase in the metal loss, also at high sand concentrations for all cases investigated, the depth of erosion could affect the fluid flow hence, altering the trajectory of particles. The difference in the results of the two approaches was concluded to be due to the consideration of the two-way interaction of particles and fluid in the Eulerian-Granular technique.

Xu et al. (2016) numerically studied the effects of particle concentration, friction coefficient, coefficient of restitution and spring stiffness coefficient on erosion in elbows, and compared their results to available experimental data. A two-way CFD-DEM simulation was conducted to account for the flow physics, particle motion was calculated using the Discrete Element Method (DEM) and the flow field resolved by solving the Reynolds averaged Navier Stokes (RANS) equations. Erosion rate was accounted for by employing a particle-scale erosion model based on the direct impingement study of Ashrafizadeh and Ashrafizadeh (2012). Pipe diameter is 25.4 mm with a vertical length of 1200 mm before a standard 90° elbow, the coefficient of friction employed are from 0.1 to 0.6 and sand particle diameter is 150 μm. The inlet velocity is 45.72 m/s, coefficient of restitution was varied four times between 0.8 and 0.95, and the sand mass flow rate employed were 0.000208, 0.00208, 0.0208 and 0.208 kg/s. Their results show that particle concentration plays a dominant role in the erosion of elbows because an increase in particle flow rate significantly increased the wear rate on the inner wall of the elbow extrados. While the coefficient of friction, coefficient of restitution and spring stiffness has little or no effect on elbow erosion rate.

To study the effects of bend orientation and flow direction on erosion rate, Peng and Cao (2016) performed a numerical simulation to study solid particle erosion in pipe bends for liquid-solid flow. The authors considered five different erosion correlations and selected the most accurate for this investigation. The relationship between stokes number and maximum erosion was also analyzed. It was observed that all the erosion equations generate similar erosion patterns, no significant difference was however observed in the erosion rate when bend orientation changes and the maximum location of wear damage all occur at about 85°.

Vieira et al. (2016) carried out a study to validate and improve CFD based erosion modeling predictions with focus on flow conditions with low sand concentration and small sizes. Hence ignoring the influence of interactions between particles. Experiments were conducted to measure erosion rates for 76.2 mm ID stainless steel 316 standard elbow caused by 300 μm and 150 μm sand particles with air in a direct impingement geometry. Gas and sand velocities were measured using a pitot tube and PIV respectively. And the erosion measured with a non-intrusive ultrasonic transducer. The fluid phase accounted for by resolving the averaged Navier-Stokes equation, Discrete Random Walk (DRW) Model for interaction between particles and turbulent eddies, coefficient of restitution model used was the one proposed by Grant and Tabakoff (1975). The authors predicted CFD erosion magnitudes using four empirical correlations proposed by Oka et al. (2005a); DNV (2007); Neilson and Gilchrist (1968); Zhang et al. (2007) and their proposed model. All these are compared with present and previous data from Ultrasonic (UT) erosion experiments in elbows. CFD predictions with the proposed model slightly over predict results generated from the Ultrasonic (UT) single-phase erosion experiment by a factor of 2 while the four models from literature under predict the Ultrasonic (UT) data. The profiles of the predicted erosion rates are also in agreement with those of the measured. Although erosion was over-predicted with

CFD in air-sand flow, it displayed its capability at highlighting locations of maximum erosion rates in the elbow.

Al-Khayat et al. (2018) developed a 3-D CFD model to investigate different parameters that affect erosion of pipe walls when transporting crude oil with entrained sand particles. The model describes the turbulent transport of sand particles under various transport parameters of crude oil such as viscosity, density, velocity and temperature. Three different erosion equations, Finnie model, Erosion / Corrosion Research Centre (E/CRC) and the DNV model were employed (more details on these models can be found in Al-Khayat et al. (2018)). Conservation and continuity equations were solved to account for the fluid phase and the effect of turbulence was modeled using the $k-\omega$ model. Particle motion were tracked in the Lagrangian Disrete Phase Model (DPM). The pipe and sand diameter are 0.2 m and 170 μm respectively, and flow velocity was set at 0.3 m/s. Results generated show good agreement with available experimental data. It was further observed that as the friction between the oil and pipe wall increases, erosion also increases. Erosion rate increased by about 100% with increase in viscosity from 1 mPa.s to 20 mPa.s, hence oil viscosity has a significant influence on erosion rate. The erosion rate is however not affected by the change in oil density, temperature or mass flow rate of sand.

2.5.2 CFD modelling of pipe erosion in multiphase flows

Due to the complex interactions between the fluid and particles in multiphase flows, many researchers are now employing Computation Fluid Dynamics (CFD) technique for erosion prediction and analyses. CFD has the advantage of predicting erosion rate, location of the maximum erosion, hence identifying possible leakage locations as well as temporal evolution of erosion. It can also be employed for complex geometries and complex fluids.

Peng Jr et al. (2013) carried out a CFD erosion assessment and compared the results of the erosion equation in a commercial CFD code with that of empirical equations.

The geometry is a 1 inch elbow made from 316 stainless steel with estimated Brinell Hardness of 230 BHN. Carrier fluid is air-water mixture in the annular flow regime with superficial gas and liquid velocities of 34.1376 m/s and 0.3048 m/s respectively. Sand particle diameter is 150 μm and mass flow rate is 0.006 kg/s. The SST (Shear Stress Transport) Model was employed to account for turbulence near the pipe, flow was modeled with the Eulerian-Eulerian multiphase techniques and particles were tracked in the Lagrangian framework. Erosion rate was calculated using the equation proposed by Finnie Erosion available in the commercial CFD package, CFX, and compared to the results of empirical correlations developed by Salama (1998), DNV (2007), Tulsa Erosion Corrosion Research Center (Peng Jr et al., 2013), API (1981). The results obtained showed a promising agreement between the erosion rate and the empirical predictions of Salama et al. (2000) and DNV (2007) methods. However, when the fluid flow is from horizontal to vertical downwards (H-VD), the erosion rate is over-predicted by at least a factor of 20. The best prediction is observed in the erosion correlation by Tulsa Erosion / Corrosion Research Centre (E/CRC) (Peng Jr et al., 2013).

Nguyen et al. (2014) performed a combined numerical and experimental study to understand how evolution of material surface induced by erosion can affect the erosion mechanism in multiphase water-sand flow. The water-sand flow was simulated using the Eulerian-Lagrangian approach. Water was treated as a continuum phase governed by Navier-Stokes equations and sand particles treated in the Lagrangian discrete phase framework. Furthermore, turbulence was captured by the $k - \omega$ turbulent model and particle rebound velocity at the wall determined by the Forder's rebound model (Zhang et al., 2007). Erosion rate and pattern were evaluated using the erosion model by Oka et al. (2005a) and Oka and Yoshida (2005b). Surface profiles obtained after 5, 15 and 30 minutes of the experiment were used to create geometry models for numerical simulations for direct particle impingement. It was observed that erosion rate is highest in the profile created after 15 minutes because erosion is caused by the cutting action and high impact velocity of the particles at this stage unlike the indenting and rebound actions at 5 and 30 minutes respectively. Lowest erosion rate is recorded in the surface profile after 30 minutes. It was also observed that erosion rates from both experimental data and numerical results have the same trend, both also have a linear relationship with the impact velocity; increasing impact velocity increases the erosion rate. However, at the same flow velocity, numerical simulations over-predict the erosion rates compared to the experiments and this could be due to the effects of particle-particle interactions not considered in the simulations.

Zhu et al. (2015) using CFD technique investigated the factors influencing erosion at pipe bends. A 3-D elbow pipe is considered for investigation and the trajectory of discrete solid particles are calculated using the Discrete Phase Model (DPM). The characteristics of the continuous phase were obtained based on the Reynolds Averaged Navier Stokes (RANS) equations, and empirical correlation given by Zhu et al. (2012) and Zhu et al. (2014) was employed to calculate the erosion rate. Sand particle size employed was 0.01 mm. Severe erosion zone was observed at about 30° downstream the angular bisector of the elbow. Results presented also show that the increase in the liquid content has less effect on flow erosion as against the same amount of increase in sand particle content. Meanwhile an increase in the sand concentration from 1 to 2 to 3% resulted in a corresponding increase in the erosion rate. Erosion rate is 54.4% and 2.11 times higher at 3% and 5% sand concentration than at 1%.

Liu et al. (2015) also proposed a simplified CFD-based procedure to calculate erosion rates in elbows for annular flow, this method overcomes the current limitations of current empirical and semi-empirical models. In the flow field analysis, the gas-liquid annular flow interface is regarded as the actual pipe wall and the lagrangian method was adopted to account for particle tracks in the core area, the velocity decay of the sand particles across the liquid film is calculated with the liquid film correlation. The turbulent flow field is modeled using the $k-\varepsilon$ model and erosion correlation by Oka and Yoshida (2005b) was introduced to calculate the erosion rates. Sand particle sizes used are 150 and 250 μm and the rebound of particles at the wall was captured by adopting the model proposed by Grant and Tabakoff (1975). Erosion results from this method were compared with those from the experimental cases of Kvernvold and Sandberg (1993), Birchenough et al. (1995) Mazumder (2004), and the method was also used to investigate erosion in elbows with curvatures (r/D) 1.5 and 5. The proposed model performed better when compared to the experimental data from Kvernvold and Sandberg (1993) and Birchenough et al. (1995) while it recorded a poor agreement with data from Mazumder (2004). The average erosion ratio from the three data are 1.12, 1.84 and 1.95 respectively. Although the proposed method recorded higher erosion rates than the experiments, the results are still said to be in good agreement with the available data for annular flow condition. A better agreement is recorded with the works of Kvernvold and Sandberg (1993) because the radius of curvature (5) of the elbow in this case is greater than the other experiments, hence making a relatively stable flow possible. Neglecting the sand particle entrained in the liquid film around the elbow and the turbulent dispersion of particles resulted in the poor agreement observed when compared to Mazumder (2004).

Parsi et al. (2015b) used CFD to study sand particle erosion in gas-dominant multiphase flows in a standard vertical-horizontal elbow of diameter 76.2 mm. ANSYS Multifluid-VOF model was used to simulate air-water multiphase flow at superficial gas velocities 10.1, 18.3 and 27.1 m/s while the liquid velocity remained constant at 0.3 m/s. Sand particles of 150 and 300 μm were considered and tracked within the Lagrangian Discrete Phase Model. Turbulence effects were captured using the RNG $k-\varepsilon$ model. A User Defined (UDF) Algorithm was coupled into the DPM model to account for the forces on the particles at specific locations in the multiphase flows. The algorithm allows for forces on particles at locations where liquid phase is 100% to be calculated based on the properties of water and particles where the gas phase is 100% based on the properties of air. Where the volume fraction of both gas and liquid is 50% each, forces on the particles will be calculated using the flow mixture properties. Erosion equations by Neilson and Gilchrist (1968), Grant and Tabakoff (1975), Oka et al. (2005a), DNV (2007), Zhang et al. (2007) and Mansouri (2016) were employed to calculate the erosion rate to discover which provides the best predictions at all flow conditions simulated. Results obtained showed good agreement when compared with experimental from an Ultrasonic erosion prediction technique. The authors observed that erosion equation developed by Mansouri (2016) provided the best predictions while that of Grant and Tabakoff (1975) over-predicted the maximum erosion rates significantly for all cases examined. The ratios of the CFD predictions to experimental data are 2.14, 0.99, 1.06 for all cases respectively. Erosion ratio also dropped as superficial gas velocity increased and the location of the maximum erosion is 45° on the elbow extrados and an increase in the liquid phase at the elbow resulted in a corresponding increase in the sand concentration at the elbow. In this analysis, particle loading was however assumed to be sufficiently low and the effects of particle-particle interaction was ignored.

Zahedi et al. (2017) conducted a CFD simulation of multiphase flows and erosion predictions under annular flow and low liquid loading conditions, the impact of annular flow behaviour and particle impact characteristics was investigated. The air-water multiphase flows were simulated with both the VOF and Eulerian-Eulerian Multifluid VOF approach and the results were compared. Turbulence was accounted for using the RSM turbulence model with Scalable Wall Function and SST $k-\omega$ turbulent model in the VOF and Multifluid-VOF respectively. Sand particles were tracked in the Lagrangian - DPM model and erosion rate was calculated using the model proposed by Mansouri (2016) based on the results of Parsi et al. (2015b) and particle-wall rebound accounted for using the model proposed by Grant and Tabakoff (1975). CFD results showed good agreement when compared with the experimental data from Vieira (2014). It was concluded that the multifluid-VOF method is able to accurately capture the air-water interfaces under annular flow conditions, but does not accurately simulate the liquid droplet entrainment from the liquid film to the gas core. Since particles moving in the gas core have to penetrate the liquid film to impact the wall to cause erosion damage, this will therefore have significant effects on the erosion prediction. The authors reported an increase in liquid flow rate will result in an increase in the liquid film thickness around the elbow and hence, a corresponding drop in particle impact velocity and the erosion rate. At a constant superficial gas velocity (Vsg) of 41 m/s, increasing the superficial liquid velocity from 0.02 m/s to 0.1 m/s resulted in a decrease in the erosion ratio from 1.31×10^{-3} to 2.15×10^{-3} mm/kg.

2.6 Erosion Modeling in Elbows Mounted In Series

While most previous studies have focused on solid particle erosion in simplified geometries with single elbows and an upstream length long enough for flow development (as seen in the previous sections), there has been arguably little or no focus when there are elbows mounted in series and the potential impact of this complex flow geometry on the solid particle erosion for a succession of elbows. The recent influx of oil and gas exploration in extreme conditions has called for the use of more complex piping systems where elbows are mounted in series but there is little or no comprehensive data as well as limited understanding to predict erosional damage in such a scenario. This necessitates more understanding of solid particle erosion in such conditions.

Deng et al. (2005) carried out experiments with four bends (vertical upwards to horizontal, horizontal to horizontal, horizontal to vertical downwards and horizontal to vertical upwards) to study the puncture point location most influenced by bend orientations in a pneumatic conveying system. Air was employed as the carrier fluid and high concentration of Olivine sand as particles. Steel tube with 60.3 mm outer diameter with 3.9 mm wall thickness and average particle size of 294 μm were employed. Their results showed that puncture point location is most influenced by the bend orientations due to biased particle distribution and particle flux distribution. The horizontal-to-vertically downward orientated bends were observed to have the shortest life to puncture and the deepest penetration point location at about 25°, the horizontal-to-vertically upward orientated bend has the nearest puncture point location at about 8° from the entrance of the pipe bend and a slightly longer life than the downward bend, while the other bend orientations showed no significant differences of the puncture point locations. Potential flow interaction between consecutive elbows was however neglected as the shortest distance between two successive elbows in the flow path employed was in excess of 300 times the pipe diameter.

Zhang et al. (2012) numerically studied the transportation of slurry in a U-shaped bend for a large radius of curvature, their focus was to ascertain the puncture point location in the pipe. Slurry velocity was 18 m/s and there was no gravity effect incorporated. Reynolds Averaged Navier Stokes Equations were resolved to account for the fluid flow and particles were tracked using the Discrete Element Method. Results presented show that the location of maximum erosion in the first elbow is observed at approximately 43° due to the direct impingement of the particles from the horizontal pipe in the first elbow and 160° in the second bend due to the centripetal force. The location in the first bend is similar to that of the standard 90° elbow when the same slurry velocity is adopted. There was however no insight on the harshness of the erosion in the second elbow.

Mazumder (2014) conducted a CFD simulation of diluted gas-solid and liquid-solid flows to study the location of maximum erosion in S-bend. The fluid phase was treated by solving time averaged Navier-Stokes, sand particles were tracked in the Lagrangian framework by the Discrete Phase Model (DPM) and erosion was calculated using default erosion model in ANSYS Fluent. Turbulence was modeled using the Realizable $k - \varepsilon$ model. Results were presented for sand particle sizes 50 and 200 μm at three different superficial air and water velocities. Gas inlet velocity were set at 15.24, 30.48 and 45.72 m/s while the liquid velocities were 0.1, 1.0 and 10.0 m/s. The maximum erosive wear was observed in two different locations in the S-bend. In bend 1 it was at 20° and 50°, and in bend 2, was at 43° and 161.3° for particle size 50 μm at Vsg 15.24 m/s. For 200 μm, the location of maximum erosion was found at 20° and 145° for bend 1, and 43 and 161.3 for bend 2 from the inlet. The locations of maximum erosion was also observed to be similar in bend 1 as the superficial gas velocity increased, but different in bend 2. The location of erosion for water also differs from that of air for all cases studied, erosion location moves further away from the inlet as sand sizes increase.

To highlight and study the effects of the flow interaction between the elbows mounted in series, Sedrez et al. (2018) conducted experiments and CFD analyses for two elbows in series; one in vertical upward to horizontal and the other in horizontal-vertical downward orientation. The distance between the elbows was fixed at 6 times the pipe diameter ($L = 6D$). Erosion experiments were carried with liquid-sand and liquid-gas-sand flow conditions using ultrasonic wall thickness measurements. The erosion test section in the experimental setup was made with 50.8 mm diameter pipes and sand particles are of 300 μm average diameter. In the CFD simulations, the continous flow flow field was resolved by solving the time-averaged Navier Stokes (RANS) equations with the RSM model to capture turbulence, particles were tracked in using the DPM model neglecting the particle-particle interactions and the dispersion of particles due to the turbulence of the continous phase was captured by the Discrete Random Walk (DRW) model. Erosion calculations were performed by employing the correlation proposed by Arabnejad et al. (2015). For the single-phase analysis, the water velocity was 6.3 m/s and the superficial water and air velocities for the multiphase were 5.3 and 10 m/s respectively. The authors presented results for the second elbow only and erosion was observed in the experiment that it took approximately 16 minutes to have a considerable amount of material removal in the liquid-sand flow while it took 3 minutes in the liquid-gas-sand flow. The erosion pattern was however very similar occurring at about 90° of the elbow outer radii in both cases. It was also observed that erosion rate is 7.8 times higher in multiphase flow than liquid-sand flow. In the CFD analysis, the authors observed a similar erosion pattern in the multiphase and liquid-sand flow when compared to the experiment, however erosion in the second elbow of the multiphase appeared more distributed. The maximum relative erosion ratio in the liquid-sand flow was over-predicted by 60%.

Asgharpour et al. (2017) also carried out experimental and numerical studies on erosion in elbows mounted in series to investigate erosion in the second elbow. The experimental facility is made up of 4-inch pipe elbows and the two elbows are separated by a distance 10 times the pipe diameter (10D). Experiments were conducted in the single and two-phase flow conditions, diameter of sand particles employed is 300 μm, and gas velocities 15, 23 and 31 m/s were considered. In the multiphase test, liquid velocities 0.016 , 0.02, 0.055 and 0.1 m/s were considered with gas velocity held constant at 31 m/s (all in the range of annular flow). For the CFD analysis, simulations were performed for the single-phase air-sand flow and the RANS equations with the Reynolds Stress models with non-equilibrium wall function was employed. The sand particles were tracked using the Discrete Phase Model (DPM) and the Discrete Random Walk model accounted for the particle dispersion at the wall. Erosion was calculated using the correlation proposed by Arabnejad et al. (2015). The wall material was stainless steel 316. The results showed an obvious decrease in the erosion rate as velocity reduced from 31 to 15 m/s in the single-phase flow, and the maximum erosion in the first bend is about 30% higher than the second. Also for all gas velocities, maximum erosion location is at 45° from the elbow inlet on the extrados of the first elbow while the location varies in the second elbow. Furthermore, in the gas-liquid flow, for all liquid velocities, erosion ratio in the first bend was observed to be higher than the second. Based on their experimental results, the authors concluded that the location of maximum erosion is similar in the first and second elbows for both the single- and two-phase flows, but maximum erosion is higher in single-phase flow than gas-liquid flow by one order of magnitude. Erosion rates predicted by the CFD analysis also showed good agreement with single-phase experimental data with a maximum error of 25% and 24% for the first and second elbows respectively at a gas velocity of 23 m/s. The location of maximum erosion in the first elbow was well predicted but not well captured for the second elbow.

Zhang et al. (2018) applied a comprehensive CFD-based erosion prediction to study erosion in two elbows mounted in series. The analyses was based on the erosion data from Kumar et al. (2014) for two horizontal-horizontal 2 inches short radius elbows mounted in series. The authors studied the effects of turbulence models to ascertain the most appropriate model combination for running erosion simulation. Turbulence models Standard $k - \varepsilon$, RNG $k - \varepsilon$, Realizable $k - \varepsilon$, SST $k - \omega$ and RSM were assessed. Air flowing at a uniform velocity of 32 m/s was simulated by solving the RANS equations and the sand particles were tracked in the Langragian Discrete Phase Model. Four-equation RSM model was found to be the most appropriate because when in use, erosion rate and location in the first and second elbows were better predicted than the two equation models when compared to the measured experimental data. It over predicted the maximum erosion rates in the first and second elbows by 46% and 17% respectively. All the two-equation models showed similar performances in the second bend, the standard $k-\varepsilon$ over predicts the erosion rate in the first elbow by 47% and under-predicts the second elbow by 100 to 300% when compared to experimental data, RNG $k-\varepsilon$ model predicted similar erosion rate to the former in the first elbow and overpredicted maximum erosion in the second bend by 300 to 400%. Realizable $k-\varepsilon$ and SST $k-\omega$ prediction's were similar to RNG and standard $k-\varepsilon$ respectively. The authors concluded that turbulence modeling is vital in sand fines erosion prediction.

Farokhipour et al. (2018) numerically modelled sand particle erosion at return bends in gas-particle two-phase flow and the authors evaluated erosion rates at four different vertical return bends. Sharp return, standard (r/D = 1.5), long radius (r/D = 3) and 180° bends were studied. The distance between the two elbows was 20D. The Oka et al. (2005a) model was used to calculate the erosion rate, RANS equations with the $k-\omega$ SST turbulence model was employed to resolve the continuous gas phase and the sand particles were tracked in the Lagrangian DPM framework with the Discrete Random Walk model accounting for the dispersion of particles. Sand particles of diameters 150 and 300 μm were considered. The particle flow rate was also varied (1, 3, 5, 10, 15, 20 kg/day). Fluid velocity remained constant at 20 m/s. It was found that the 180° pipe elbow had better erosion performance than other geometries did and experienced lower erosion rates by 67, 64, and 52% when compared to the sharp bend, standard, and long elbows, respectively. Erosion rates was also discovered to have a linear relationship with the mass flow rate of the particles in all cases studied but the 180° pipe bend was less sensitive to the increase of particle mass flow rate, the maximum erosion caused by 300 μm particles is about one third of the standard elbow. The pattern of erosion caused by both particle sizes were reported to be similar.

Recently, Sedrez et al. (2018, 2019) investigated erosion wear of elbows in series using commercial CFD code ANSYS Fluent. Eulerian and Mixture multiphase models with discrete and erosion models were used to predict erosion in the multiphase flows. Reynolds Stress Turbulence model and standard wall function were used to account for the turbulence in the system and the spherical and non-spherical particle drag laws were considered in the Lagrangian particle tracking frame. Erosion was calculated in the CFD simulations with the model by Arabnejad et al. (2015) and compared to that of models by (Oka et al., 2005a; Oka and Yoshida, 2005b), DNV (2007) and Zhang et al. (2007). Pipe diameter employed is 50.8 mm with standard elbows (r/D = 1.5), the distance between the elbows is 3 diameters (3D) and there is a 42 diameters (42D) upstream length before the first elbow. Erosion in two different gas bubble sizes 0.01 mm and 1 mm were also analysed. Liquid and gas velocities are 6.31 m/s and 5.46 m/s respectively, particle size is 300 μm. Their results showed that even though Eulerian model does not consider the secondary phase for particle tracking, it showed better erosion results in the second bend compared to the first when compared to experimental data. Maximum erosion was overpredicted using the spherical drag law compared to the non-spherical drag law. A higher maximum erosion ratio of the second to the first elbow was also observed compared to the experimental data. 1 mm gas bubble size also presented the better results for fluid separation. Maximum erosion rate was very high compared to experimental data using the model by Arabnejad et al. (2015) but the maximum erosion ratio of the second to the first elbow was in good agreement. Furthermore, it was observed that the models by Oka et al. (2005a); Oka and Yoshida (2005b) and Zhang et al. (2007) give better agreements with experimental data. The best model for operational condition was observed in Zhang et al. (2007) which overpredicted erosion in the first and second elbows by 37% and 70%. Maximum erosion was observed at 88° after the entrance of the first and second elbows, this is similar to the 90° observed in the experiment. DNV (2007) model under-predicted erosion by 26% and 22% in the first and second elbows respectively. In all cases investigated, Elbow 2 is observed to be subjected to more erosion than Elbow 1.

In summary, critical review of literature has shown that majority of studies in CFD erosion analysis in pipelines have employed the Eulerian-Lagrangian modelling technique with more focus on conditions with single phase flows as the continuous phase. Various modelling techniques have also been employed in multiphase flow erosion studies to account for turbulence and other interface parameters. The two-equation turbulence models have been used in modeling erosion by many researchers over the years due to their ease of application and extensive level of validation. They are also less computational intensive when compared to models like Large Eddy Simulation (LES) or the four-equation models. According to Zhang et al. (2018) two-equation turbulence models showed similar performance when employed for erosion prediction in elbows and they are less computationally intensive when compared to the four-equation models or other complex turbulence models. Amongst these two-equation models, based on literature, the $k-\varepsilon$ is the most widely employed for research and industrial applications both in single- and multi-phase flow modelling.

To account for the particle tracks, the Discrete Phase Model (DPM) is the most widely used technique. Although this model comes with its limitations as it does not account for the effects of particles on the carrier fluid and the complex interactions between particles compared to the Discrete Element Method (DEM), its requirement of lower computing power makes it the best short for researchers. Also considering the fact that particle tracking frameworks such as the Discrete Element Method (DEM) are most appropriate where the sand particle concentration is expected to be over 10%, DPM is best employed in scenarios with lower percentage of sand concentration. Furthermore, various erosion models have been developed and employed for erosion prediction, however according to literature erosion model developed by Oka et al. (2005a); Oka and Yoshida (2005b) has been widely used and validated with different erosion data (both multiphase and single phase) over the years. The recent study by Parsi et al. (2015b) showed that erosion model by Oka et al. (2005a); Oka and Yoshida (2005b) gave the best erosion prediction in complex multiphase flows after the model developed in-house at the Erosion / Corrosion Research Centre (E/CRC) of the University of Tulsa, USA.

Previous studies have also shown that erosion has been studied in single bends and simple geometries with long enough upstream length for flow development hence the need for more exploration in double bend and more complex geometries. In double bends analysis on the other hand, based on literature, erosion analysis has been limited to single phase flows and geometries with a fixed separation distance between the elbows. Although there is a rule of thumb in the industry which states "if the distance between the elbows is more than 10 times the pipe diameter, the erosion of the second elbow is comparable to that of the first", but this contradicts the findings of researchers such as Uzi et al. (2017) and Asgharpour et al. (2017) amongst others. It is therefore of pertinent importance to carry out further investigation on sand erosion in elbows mounted in series and the effects key parameters such as the separation distance between elbows and bend orientation will have on their respective erosion rates. The purpose of this study is to investigate erosion due to sand transport in complex multiphase flows and elbows mounted in series using Computational Fluid Dynamics (CFD) approach. This numerical investigation will provide improved understanding in designing complex pipe geometries with more than one elbow where carrier fluid is in multiphase. It will also provide more information on the effects of the separation distance between the elbows in double bend geometries on the erosion rates in both elbows. If properly construed, CFD modelling approaches will provide more detailed information on the local flow and particle parameters that can be difficult obtain experimentally.

Chapter 3

CFD Methodology

3.1 Overview

Analysing the complex nature of sand erosion in gas-liquid multiphase flows requires a comprehensive computational framework. Computational Fluid Dynamics, CFD, is the analysis of systems involving fluid flow, heat transfer and associated phenomena by means of computer-based simulation (Versteeg and Malalasekera, 2007). To obtain the basic equations of fluid motion, the appropriate fundamental basic physical principle is chosen, they are applied to a suitable model of flow and the mathematical statement which embodies such physical phenomenal extracted (Anderson and Wendt, 1995; Wendt and Anderson, 2009).

Obtaining numerical solutions in CFD is generally in two stages, the first stage involves formulation of the Partial Differential Equations (PDE) that govern the flow based on the conservation laws, and the second has to do with creating the geometry and mesh structure of the computational domain, specifying the boundary conditions for the computational domain and finally application of appropriate numerical method to obtain solutions of the conservation equations (Oliveira and Issa, 2003; Xu and Subramaniam, 2010).

Furthermore, Computational Fluid Dynamics (CFD) analysis of sand erosion involves 3 submodels; Flow Modelling, Particle Tracking and Erosion Modelling and Estimation. Figure 3.1 shows a schematic of the 3 submodels in erosion analysis.

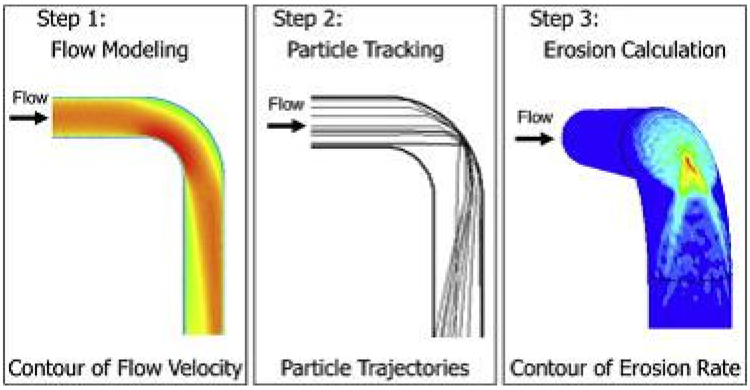

Figure 3.1: CFD steps for sand erosion analysis

3.2 Flow Modelling

In nature, fluid flow exits in two different forms; single phase and multiphase. The word 'phase' in multiphase flow refers to the three physical state that a matter can exist and the prefix 'multi' means multiple, which implies two or more (Tebowei, 2016). A flow that consists of a mixture of liquid and solid, gas and liquid, gas and solid or liquid, gas and solid phases is called multiphase flow. The flow may be laminar or turbulent depending on how random its properties are. Most flows encountered in nature and engineering applications are however turbulent, and the highly random and chaotic nature is a key feature. The numerical solution of laminar flows is relatively easy to obtain, and the accuracy of the solutions are reliable while that of multiphase is more complex and challenging due to its random form of occurrence (Tebowei, 2016; Andersson et al., 2011; Ogunsesan et al., 2018).

CFD can be employed as a tool to analyze the random and chaotic nature of turbulent multiphase flows by solving the instantaneous equations that govern such flow. This is achieved by a method called the Direct Numerical Simulation (DNS) which involves resolving the entire scales of velocity fluctuations (Elghobashi, 1991; Tebowei, 2016). However, it is not always necessary to predict the detailed flow and instantaneous information of the entire turbulence scale in most engineering applications

(Drew, 1983), as this will be computationally expensive in terms of simulation time. Moreover, with advancement in technology, the average of the instantaneous equations that describe the flow are obtained by suitable averaging procedures as a solution to the mean properties of the flow. This method is called the Reynolds-averaged Navier-Stokes (RANS) approach for flow modelling. This is a computational less expensive approach compared to the DNS.

3.2.1 Governing Equations

A detailed description of the derivation and the various averaging procedures of the conservation equations can be found in Drew (1983), Ma and Ahmadi (1990), Enwald et al. (1996), Versteeg and Malalasekera (2007), Ishii and Hibiki (2010) and Jakobsen (2014).

Assuming no mass transfer between the fluid phases, the continuity and momentum equations are as follows;

Continuity Equation

The mass conservation equation for the continuous phase is;

$$\frac{\partial \rho_i \alpha_i}{\partial t} + \nabla.(\alpha_i \rho_i \overrightarrow{v}_i) = 0 \tag{3.1}$$

Where α_i, ρ_i and $\overrightarrow{v}_i$ are the volume fraction, density and velocity of the continuous fluid phase.

$$\sum_i^n \alpha_i = 1 \tag{3.2}$$

Momentum Equation

The momentum equation is given as;

$$\frac{\partial(\alpha_i \rho_i \overrightarrow{v}_i)}{\partial t} + \nabla.(\alpha_i \rho_i \overrightarrow{v}_i \overrightarrow{v}_i) = -\alpha_i \nabla P + \nabla.\tau_i + \alpha_i \rho_i \overrightarrow{g} + \overrightarrow{F}_{ij} \tag{3.3}$$

Where P is the pressure, g is acceleration due to gravity and $\overrightarrow{F}_{ij}$ is the interfacial force between the continuous phases. τ_i is the stress-strain tensor and it is expressed as;

$$\tau_i = \alpha_i \mu_i (\nabla \overrightarrow{v}_i + \nabla \overrightarrow{v}_i^T) + \alpha_i (\lambda_i - \frac{2}{3}\mu_i) \nabla . \overrightarrow{v}_i I \tag{3.4}$$

Where μ_i is the molecular viscosity and I is the unit tensor.

3.2.2 Multiphase Flow Modeling

Numerical modelling of turbulent multiphase flow is much more challenging than single phase flow because there are lots of varying parameters influencing the flow interaction and behavior. Accurate solution of the full RANS equations and accounting for the interfacial interaction is a major problem in multiphase flow modelling (Tryggvason et al., 2001). Many multiphase flow correlations have been developed for industrial and environmental applications in order to predict two-phase flow based on a Eulerian approach. These approaches are classified into two reference frames, these are the Euler-Lagrangian model and the Euler-Euler model approach.

In the Euler-Lagrangian approach, assuming a liquid-solid multiphase flow, the liquid phase is treated as a continuum by solving the Navier-Stokes equations, while the dispersed solid phase is modelled by tracking a large number of solid particles as they move through the computational domain (Sommerfeld, 2003; Sommerfeld and Kussin, 2003). The solid particles trajectories are computed for each parcel of particles that follow the same trajectory by solving equation of motion. This approach is mainly applicable when the volume fraction of the solids phase is relatively low. Momentum exchange between the primary phase (liquid) to the secondary (solid) phase occurs, this is termed one- or two-way coupling, while accounting for particle-particle interaction as in four-way coupling may not be possible (Tebowei, 2016). However, in the Euler-Euler model for flow modelling, the primary and secondary phases are treated as interpenetrating continuum. This approach is referred to as the two-fluid model and it is considered to be the most general form of the partial differential equations describing the flow of a mixture containing two or more fluids of different physical properties (Alhajraf, 2000). The model is derived by volume or ensemble averaging of the instantaneous continuity and momentum equations for each phase. The averaging introduces a volume fraction function which defines the probability of occurrence of a phase in a fixed control volume in space and time, and their sum is equal to one (Enwald et al., 1996). Detailed derivations and discussions on the two and multi-phase flow numerical models have been widely covered in the last few decades (Ma and Ahmadi, 1990; Gidaspow, 1994; Ishii and Hibiki, 2010, 2011; Drew, 1983). There is however no general numerical framework applicable for modelling all types of multiphase flows encountered in engineering applications (Tebowei, 2016).

The available multiphase models within the Euler-Euler framework are the volume of fluid (VOF) model, mixture model and Eulerian model. The mixture model is a simplification of the Euler-Euler model which assumes the phases interact strongly and a single momentum equation is used for the phases using mixture properties of the phases. The VOF model involves interface surface tracking technique where the interface between different phases is tracked. VOF model is suitable for separated flow of two immiscible fluids. The Eulerian model is applicable for a wide range of complex multiphase flows. It can be applied for modelling flow with multiple phases. There is also the hybrid multifluid-VOF model, and this has been employed in the course of this research.

The hybrid Multifluid-VOF model is a combination of the Eulerian-Eulerian model which solves separate mass and momentum equations for the individual phases, and uses the VOF to capture the evolution of the interfaces between them. In this model, a single pressure field is shared between the two fluid phases (Ogunsesan et al., 2018). The Eulerian Multifluid-VOF framework resolves the separate forms of the RANS equations in Equations (3.1) and (3.3) for the individual fluid phases of the continuous flow. According to Cerne et al. (2001) coupling of the Eulerian-Eulerian and VOF approaches results in preventing interface numerical diffusion and also removes some closure correlations required by the Eulerian-Eulerian model (Parsi et al., 2016a,b). Another advantage of using this hybrid model is that individual velocity information of the phases can be extracted and employed for analyzing the behavior of sand particles within that particular phase.

3.2.3 Transport Equations and Closure Models for Multiphase Flow Modeling

The governing equations of mass and momentum for the isothermal incompressible multiphase liquid-gas flow and the closure models formulated in the Eulerian-Multifluid-VOF multiphase model framework applied in this study are presented in this section. A comprehensive description of the derivation and various averaging procedures of the conservation equations can be found in Gidaspow (1994), Ishii and Hibiki (2010), Ishii and Hibiki (2011) and Versteeg and Malalasekera (2007) amongst others.

Volume Fraction Parameter

To account for the volume fraction in a two-phase flow of immiscible fluids, the tracking of the interface(s) between the phases is achieved by the solution of a continuity equation for the volume fraction of one (or more) of the phases. For a two-phase gas-liquid flow, the volume fraction formulation for the secondary phase (gas) is given as;

$$\frac{1}{\rho_g}[\frac{\partial}{\partial t}(\alpha_g \rho_g) + \nabla.(\alpha_g \rho_g \overrightarrow{v}_g)] = S_{\alpha_g} + \textstyle\sum_{\rho=1}^{n}(m_{lg} - m_{gl}) \tag{3.5}$$

Where m_{gl} is the mass transfer from the primary (liquid) to the secondary (gas) phases. S_{α_g} is the source term and this is zero by default.

The volume fraction of the primary(liquid) phase is not solved but computed based on the expression below;

$$\textstyle\sum_{l=1}^{n} \alpha_l = 1 \tag{3.6}$$

Equation (3.6) can be calculated within the implicit or explicit scheme. A detailed discussion on these schemes can be found in Kolev and Kolev (2005) and Versteeg and Malalasekera (2007). According to the works of Parsi et al. (2015b), Parsi (2015) and

Parsi et al. (2016a), the implicit scheme has been employed for the volume fraction formulation in the present study. This scheme is more stable compared to the explicit and allows for larger time step size, hence reducing the overall computational time. It can also be used for both time-dependent and steady state calculations.

Interfacial Forces

Interfacial forces such as lift, virtual mass force, wall lubrication and turbulent dispersion were neglected in this study, only the drag force which is the dominant interfacial force was considered.

The general form of the interfacial force F_{gl} from Equation (3.3) is expressed as;

$$\overrightarrow{F}_{gl} = K_{gl}(\overrightarrow{V}_g - \overrightarrow{V}_l) \tag{3.7}$$

Where K_{gl} is the interface momentum exchange coefficient, and it is expressed as;

$$K_{gl} = \frac{\alpha_g \alpha_l \rho_g}{\tau_g} f \tag{3.8}$$

Where f is the drag function and τ_g is the particulate relaxation time.

- Drag Force

This force accounts for the drag of one phase on the other. Researchers have developed various drag correlations to account for the interfacial interaction between two phases in multiphase flow modelling. Some of these include the drag force model by Schiller and Naumann (1935), Wen and Yu (1966), Morsi and Alexander (1972), Grace et al. (1978), Ishii (1979), Syamlal and O'Brien (1989), Gidaspow (1994) and Tomiyama (1998) to mention a few. The approach in the formulation of the momentum exchange or drag coefficient, C_D, is the major difference in the various drag force models. The drag force model based on the formulation of Schiller and Naumann (1935) was employed for this study as this is acceptable for all fluid-fluid pair of phases.

The drag function, f, from Equation (3.8) is obtained from;

$$f = \frac{C_D Re}{24} \tag{3.9}$$

Where C_D is the drag or momentum exchange coefficient and Re is the Reynolds number.

The drag or momentum exchange coefficient is given by;

$$C_D = \frac{24}{Re}(1 + 0.15Re^{0.687}) \tag{3.10}$$

Where Re is the relative Reynolds Number.

The relative Reynolds number of the liquid and gas phases is obtained from;

$$Re = \frac{\rho_l |\overrightarrow{v}_g - \overrightarrow{v}_l| d_g}{\mu_l} \tag{3.11}$$

Where d_g is the diameter of the gas bubble.

Interfacial Momentum Exchange

To account for a reliable calculation of the momentum transfer of the total interfacial force, an accurate calculation of the interfacial area between the fluid phases is of utmost importance. The interfacial transfer terms in Equation (3.3) are proportional to a geometric parameter called the Interfacial Area Concentration (IAC). IAC is defined as the total interfacial area per unit two-phase flow mixture volume (Pellacani et al., 2011). It is an important parameter for predicting mass, momentum and energy transfers through the interface between the phases. The IAC captures the bubble breakage and coalescence within the flow, and uses a single transport equation per secondary phase. For the present study, to account for the momentum and energy transfers via the interface between the liquid and gas phases, the IAC was evaluated by incorporating the Interfacial Area Transport Equation, IATE, into the hybrid multiphase model. This correlation was developed by Ishii and Grolmes (1975).

Assuming no mass transfer between the two phases, the transport equation for IAC in a gas-liquid multiphase flow system can be written as;

$$\frac{\partial(\rho_g X_p)}{\partial t} + \nabla.(\rho_g \overrightarrow{u}_g X_p) = \frac{1}{3}\frac{D\rho_g}{Dt}X_p + \frac{2}{3}\frac{m_g}{\alpha_g}X_p + \rho_g(S_{RC} + S_{WE} + S_{TI}) \tag{3.12}$$

Where X_p is the interfacial area concentration and α_g is the gas volume fraction. The first two terms on the right hand are the gas bubble expansions due to compressibility and mass transfer, m_g is the mass transfer rate into the gas phase per unit mixture volume. S_{RC} and S_{WE} are coalescence sink terms due to random collision and wake entrainment respectively. S_{TI} is the breakage source term due to turbulent impact.
The IATE in Equation (3.12) represents the transport and evolution in the interfacial area between the phases, one considered continuous (liquid) and the other considered dispersed (gas). As identified by Kim et al. (1997), Wu et al. (1998) and Hibiki and Ishii (2000), the changes in this interfacial area are due to several interaction mechanisms which include;

- Coalescence due to random collision driven by turbulence.
- Coalescence due to wake entrainment.
- Breakup due to the impact of turbulent eddies.
- Shearing-off of small bubbles from larger cap bubbles.
- Breakup of large cap bubbles due to interfacial instabilities.

The source and sink terms are accounted for with the Hibiki and Ishii (2000) model. The correlations for these are presented in Equations (3.13), (3.14) and (3.15).

- Coalescence sink terms, S_{RC} and S_{WE}

$$\begin{aligned} S_{RC} &= -\frac{1}{3\phi}(\frac{\alpha_g}{X_P})^2 C_{RC}[\frac{n_b^2 u_t d_b^2}{\alpha_{gmax}^{\frac{1}{3}}(\alpha_{gmax}^{\frac{1}{3}} - \alpha_g^{\frac{1}{3}})}][1 - exp(-C\frac{\alpha_{gmax}^{\frac{1}{3}}\alpha_g^{\frac{1}{3}}}{\alpha_{gmax}^{\frac{1}{3}} - \alpha_g^{\frac{1}{3}}})] \\ &= -\frac{1}{3\pi}C_{RC}u_t X_p^2[\frac{n_b^2 u_t d_b^2}{\alpha_{gmax}^{\frac{1}{3}}(\alpha_{gmax}^{\frac{1}{3}} - \alpha_g^{\frac{1}{3}})}][1 - exp(-C\frac{\alpha_{gmax}^{\frac{1}{3}}\alpha_g^{\frac{1}{3}}}{\alpha_{gmax}^{\frac{1}{3}} - \alpha_g^{\frac{1}{3}}})] \end{aligned} \tag{3.13}$$

$$S_{WE} = -\frac{1}{3\phi}(\frac{\alpha_g}{X_P})^2 n_b^2 d_b^2 u_r C_D^{\frac{1}{3}} = -\frac{1}{3}\pi C_{WE} u_r X_p^2 C_D^{\frac{1}{3}} \tag{3.14}$$

- Breakage source term, S_{TI}

$$\begin{aligned} S_{TI} &= \frac{1}{3\phi}(\frac{\alpha_g}{X_P})^2 C_{TI}(\frac{n_b u_t}{d_b})(1-\frac{We_{cr}}{We})^{\frac{1}{2}} exp(-\frac{We_{cr}}{We}) \\ &= \frac{1}{18} C_{TI} u_t \frac{X_P^2}{\alpha_g}(1-\frac{We_{cr}}{We})^{\frac{1}{2}} exp(-\frac{We_{cr}}{We}) \end{aligned} \tag{3.15}$$

Where, u_t is the mean bubble velocity and it is expressed as;

$$u_t = \varepsilon^{\frac{1}{3}} d_b^{\frac{1}{3}} \tag{3.16}$$

u_r is the bubble terminal velocity, and it is a function of bubble diameter and local time-averaged void fraction. It is expressed as;

$$u_r = (\frac{d_b g \Delta\rho}{3 C_D \rho_f})^{\frac{1}{2}} \tag{3.17}$$

where;

$$C_D = 24 \frac{(1 + 0.1 Re_D^{0.75})}{Re_D} \tag{3.18}$$

and;

$$Re_D = \frac{\rho_f u_r d_b}{\mu_f}(1-\alpha_g) \tag{3.19}$$

and;

$$We = \frac{\rho_f u_t^2 d_b}{\sigma} \tag{3.20}$$

Where We is the Webber number, and it is less than the critical Webber number We_{cr}. μ_f is the molecular viscosity of the fluid phase, g is the gravitational acceleration and σ is the interfacial tension. The values of the coefficients in these models are 0.004, 0.002, 0.085, 3.0, 6.0 and 0.75 for C_{RC}, C_{WE}, C_{TI}, C, We_{cr} and α_{gmax} respectively. More details on this can be found in the work of Ishii and Hibiki (2011).

It is important to note that the local average bubble diameter in this study is calculated based on the Sauter mean diameter, D_{sm}, by using Equation (3.21).

$$D_{sm} = \frac{6\alpha}{a_i} \tag{3.21}$$

The Sauter mean diameter is the diameter of a sphere that has the same volume or surface area ratio as a particle of interest. It is not a fixed constant value but dependant on the flow conditions through the modification applied by the sources and sink terms.

3.2.4 Turbulence Modeling

It is of utmost importance to account for turbulence in multiphase flow modelling as it is an essential feature of gas-liquid flows. In these types of flows fluid velocities varies significantly and irregularly in both position and time (Pope, 2001). Over the years, many different techniques have been proposed and adopted to answer many different questions about turbulence and model turbulent flows, some of these are analytic, experimental or numerical modelling. In numerical modelling approach, there are many turbulence models available in CFD codes for the closure of the momentum equations (in the form of Equation 3.3). These include Spalart-Allmaras, Mixing length, Two-equation($k-\varepsilon$, $k-\omega$ and $k-kl$), Reynolds stress, Detached Eddy Simulation and Large Eddy Simulation models. These models are classified based on the number of additional transport equations to be solved, the RSM has the highest number of additional transport equations (Versteeg and Malalasekera, 2007; Tebowei, 2016). Majority of the turbulence models are however originally developed based on single-phase turbulence flow but considerable efforts have been put in place by researchers to extend their use to multiphase flow modelling (Versteeg and Malalasekera, 2007; Tebowei, 2016).

A good turbulence closure model should be simple to apply and have vast applicability (Launder and Spalding, 1974). The standard $k-\varepsilon$ model developed by Launder and Spalding (1974) amongst other two-equation turbulence models have been reported to have extensive and successful practical applicability for various engineering purposes. It is also the most validated and simplest turbulence model (Pope, 2001). However, over the years, many modifications have been proposed to remedy its poor performance and application to a wider class of flows, notable amongst these is Renormalization Group (RNG) method (Orszag et al., 1993; Smith and Reynolds, 1992; Smith and Woodruff, 1998; Pope, 2001) which is similar to the standard $k-\varepsilon$ model but more accurate and reliable for a wider class of flows. It is also more responsive to the effects of rapid strain and streamline curvature. In the present study, the RNG $k-\varepsilon$ turbulence model was employed.

- **RNG $k-\varepsilon$ Turbulence Model**

This is derived from the instantaneous Navier-Stokes equations, using a mathematical technique called "Renormalization Group" (RNG) methods. It was derived using a statistical technique called Renormalization Group theory. It is similar in form to the standard model, but includes refinements for its ε equation. A more comprehensive description of the RNG theory and its application to turbulence can be found in Orszag et al. (1993) and Orszag et al. (1996).

The transport equations for the turbulence kinetic energy, k, and rate of dissipation, ε in the RNG $k-\varepsilon$ turbulence model are;

Turbulence kinetic energy, k

$$\frac{\partial}{\partial t}(\rho k) + \frac{\partial}{\partial x_i}(\rho k u_i) = \frac{\partial}{\partial x_j}(\alpha_k \mu_{eff} \frac{\partial k}{\partial x_j}) + G_k + G_b - \rho\varepsilon - Y_M + S_k \tag{3.22}$$

Rate of dissipation, ε

$$\frac{\partial}{\partial t}(\rho \varepsilon) + \frac{\partial}{\partial x_i}(\rho \varepsilon u_i) = \frac{\partial}{\partial x_j}(\alpha_\varepsilon \mu_{eff} \frac{\partial \varepsilon}{\partial x_j}) + C_{1\varepsilon}\frac{\varepsilon}{k}(G_k + C_{3\varepsilon}G_b) - C_{2\varepsilon}\rho\frac{\varepsilon^2}{k} - R_\varepsilon + S_\varepsilon \tag{3.23}$$

Where, G_k and G_b are the generation of turbulence kinetic energy due to the mean velocity gradients and the generation of turbulence kinetic energy due to buoyancy respectively. Y_M is the contribution of the fluctuating dilatation in compressible turbulence to the overall dissipation rate, α_k and α_ε are the inverse effective Prandtl numbers for k and ε respectively. S_k and S_ε are source terms, C_1, C_2 and C_3 are model constants and μ_{eff} is the effective viscosity.

The effective viscosity, μ_{eff}, is obtained by differentiating the turbulent viscosity as shown in Equation (3.24).

$$d(\frac{\rho^2 k}{\sqrt{\varepsilon\mu}}) = 1.72\frac{v}{\sqrt{v^3 - 1 + C_v}} \tag{3.24}$$

Where $C_v \approx 100$ and;

$$v = \frac{\mu_{eff}}{\mu} \tag{3.25}$$

Equation (3.25) is applicable for flows with low Reynolds number while in the case of high Reynolds number, the turbulent viscosity is obtained from Equation (3.26).

$$\mu_t = \rho C_\mu \frac{k^2}{\varepsilon} \tag{3.26}$$

Where $C_\mu = 0.0845$. The inverse effective Prandtl numbers α_k and α_ε are computed based on;

$$\left|\frac{\alpha - 1.3929}{\alpha_0 - 1.3929}\right|^{0.6321}\left|\frac{\alpha + 2.3929}{\alpha_0 + 2.3929}\right|^{0.3679} = \frac{\mu_{mol}}{\mu_{eff}} \tag{3.27}$$

Where $\alpha_0 = 1.0$, and in high Reynolds number limit, $(\frac{\mu_{mol}}{\mu_{eff}} \ll 1)$, $\alpha_k = \alpha_\varepsilon \approx 1.393$. The major difference between the standard $k - \varepsilon$ and the RNG $k - \varepsilon$ models is the addition of the R_ε to the equation for the rate of dissipation. This term is accounted for with Equation (3.28).

$$R_\varepsilon = \frac{C_\mu \rho \eta^3 (1 - \frac{\eta}{\eta_0})}{1 + \beta\eta^3}\frac{\varepsilon^2}{k} \tag{3.28}$$

Where $\eta \equiv \frac{S_k}{\varepsilon}$, $\eta_0 = 4.38$ and $\beta = 0.012$

The model constants $C_{1\varepsilon} = 1.42$ and $C_{2\varepsilon} = 1.68$.

3.3 Particle Tracking

Multiphase flow either in two or more phases, such as liquid or gas and dispersed phase or a mixture of all three, can be found in many engineering industries. To model any of these phenomena, two approaches can be considered, these are the Eulerian - Eulerian (two - fluid model) and the Eulerian - Lagrangian (also known as Lagrangian model) approaches (Chiesa et al., 2005; Vegendla et al., 2011; Mahdavimanesh et al., 2013). In both methods, the carrier phase is considered as a continuous phase, however, in the Eulerian - Eulerian approach, the particle phase is treated as another continuum phase and fully inter-penetrating. Although physical characteristics of the solid particles such as shape and size are included in the continuum representation through empirical relations, this model does not recognize the discrete character of the solid phase (Chiesa et al., 2005), governing equations resolved from the mass conservation condition are solved to account for the particle concentration field. More details on the Eulerian - Eulerian approach can be found in Gidaspow (1994) and Benyahia et al. (2005) amongst others.

In the Lagrangian approach on the other hand, the dynamics of a single particle is treated by the trajectory method. Under this framework, the flow field is obtained by applying the RANS turbulence models and equations of motion resulting from the various forces exerting on individual particles are solved to generate as single particle trajectory (Vegendla et al., 2011). The Lagrangian particle tracking is a numerical technique for tracking Lagrangian particles within an Eulerian phase. It is also commonly referred to as Discrete Particle Simulation (Alhajraf, 2000). It is the natural frame for treating particles (Shirolkar et al., 1996). Unlike the eulerian models, Lagrangian models have the potential to account for all the forces acting on a particle.

The Lagrangian approach was used in this study, and the correlations for the particle equations of motion in the Lagrangian framework employed to predict the particle trajectories are discussed in this section. The effect of particle-particle interaction was however assumed negligible.

3.3.1 Particle Equation of Motion

In the Lagrangian approach, individual particles are tracked as they are driven by the flow of the continuous phase. The particle trajectory can be determined by solving its equation of motion, which can be deduced from Newton's Second Law (Salem 2000). The Lagrangian reference frame of ANSYS Fluent predicts the trajectory of a discrete particle by integrating the force balance on the particle and this force balance equates the particle inertia with forces acting on the particle. It is referred to as the Discrete Phase Model (DPM) (Deen et al., 2007; Vegendla et al., 2011). The particle equation of motion was first derived by Basset, Boussinesq and Oseen, and is commonly known as the B-B-O equation (Shirolkar et al., 1996) and it can be written as;

$$\frac{d\overrightarrow{U}_P}{dt} = \sum F \tag{3.29}$$

Where the RHS is the summation of all the forces acting on a particle along its trajectory. These summed forces are made up of drag, lift, virtual, gravity and a host of others as shown in Equation (3.30).

$$\frac{d\overrightarrow{U}_P}{dt} = F_D + F_P + F_V + F_G + F_L + F_{other} \tag{3.30}$$

Where F_D is the drag force, F_P is the force due to pressure gradient, F_V is the virtual mass (this is the force required to accelerate the fluid surrounding the particles), F_L is the lift force and F_G is the force due to gravity. F_{other} accounts for forces such as the particle – wall interaction force amongst others.

The separation of the total sum of forces as a result of Equation (3.30) is not always valid, as there can be non-linear interactions between these various forces. Such interactions are not well understood but within negligible range for many flow applications (Durst et al., 1984; Shirolkar et al., 1996; Crowe et al., 1996; Alhajraf, 2000). Assuming the particles are spherical in shape the forces acting on them can be summarized as follows;

Drag Force, F_D

This is the main force affecting the motion of the particle(s). The interaction between the particle and fluid induce forces at the particle-fluid interface. For a spherical particle this results in a normal and shear stress, the normal stress is a result of the pressure applied on the surface referred to as the pressure drag force while the shear stress is a result of the fluid viscosity known as the viscous drag force (Alhajraf, 2000). The general equation for describing the drag force acting on a spherical particle is shown in Equation (3.31).

$$F_D = \frac{1}{2}\rho C_D \frac{1}{\tau_p} \mid \overrightarrow{U}_{rel} \mid \overrightarrow{U}_{rel} \tag{3.31}$$

where C_D is the coefficient of drag, τ_p is the particle relaxation time and $\overrightarrow{U}_{rel}$ is the particle-fluid relative velocity.

Particle Relaxation Time, τ_p:

This is the rate of response of the particle acceleration to the relative velocity between the particle and the carrier fluid (Shirolkar et al., 1996). When tracking particles in turbulent flow, this is a very important parameter. It is expressed as;

$$\tau_p = \frac{24\rho_p d_p^2}{18\mu_f C_D Re_p} \tag{3.32}$$

where ρ_p, d_p and Re_p are the particle density, diameter and Reynolds number respectively, μ_f is the fluid viscosity, and C_D is the drag coefficient.
The particle relative Reynolds number is given as;

$$Re_p = \frac{\rho_f \mid \overrightarrow{U}_p - \overrightarrow{U}_f \mid d_p}{\mu_f} \tag{3.33}$$

where $\overrightarrow{U}_p$ and $\overrightarrow{U}_f$ are particle and fluid velocity vectors respectively.
Particles smaller than the eddy size remain inside an eddy for a certain time before jumping to another. The maximum time that a particle can remain under the influence of a particular eddy is known as the eddy lifetime. A common approximation in the particle/turbulent interaction models is the assumption that the eddy properties remain constant for the entire eddy lifetime and therefore, particles trapped by an eddy can experience constant turbulent properties (Alhajraf, 2000).

In this study, the turbulence properties were predicted using the two-equation RNG $k - \varepsilon$ turbulence model and details of the interaction between the particle relaxation time.

Forces Due To Pressure Gradient, F_P

This force is associated with the threshold condition of the particle. It has a significant effect if the ratio of particle density to fluid density is close to unity; for example, particle in water; otherwise it is negligible (Alhajraf, 2000). It is expressed as shown below;

$$F_p = -\frac{\pi D^3}{6}\frac{\partial P}{\partial X} \tag{3.34}$$

Virtual Mass Force, F_V

This is the kinetic energy required to accelerate the particle. It is divided between the particle itself and the surrounding fluid attached to the particle surfaces.This force is required to accelerate the fluid surrounding the particles, and it is very important when the density of the particle is much lower than that of the carrier fluid.The relative velocity between the fluid and particle affects the fluid momentum boundary layer around the particle. Thus, if the particle is faster than the fluid then the particle can accelerate the surrounded fluid, i. e. more mass is accelerated than the mass of the particle itself. Therefore, the work done to accelerate the particle is in fact greater than the work required to accelerate the particle alone (Alhajraf, 2000). The Virtual mass force is defined by Equation (3.35). For multiphase flows, the virtual mass effect that occurs when a secondary phase p accelerates relative to the primary phase q is included and the inertia of the primary-phase mass encountered by the accelerating particles (or droplets or bubbles) exerts a “virtual mass force” on the particles (Drew, 1983).

$$\overrightarrow{F}_{vm} = 0.5\alpha_p\rho_q(\frac{d_q\overrightarrow{\vartheta}_q}{dt} - \frac{d_p\overrightarrow{\vartheta}_p}{dt}) \tag{3.35}$$

The term $\frac{d_q}{dt}$ is the phase time derivative of the form;

$$\frac{d_q(\phi)}{dt} = \frac{\partial(\phi)}{\partial t} + (\overrightarrow{\vartheta}_q.\nabla)\phi \tag{3.36}$$

Force Due To Gravity, F_G

The gravitational force is directly proportional to the mass of the particle and it is defined based on the difference between the density of the particle and the surrounding fluid. The force is applied in the negative vertical direction. It is accounted for based on the expression below;

$$F_G = (\rho_p - \rho_f) \tag{3.37}$$

Where ρ_p and ρ_f are the particle and fluid densities respectively.

Lift Force, F_L

This force acts perpendicular to the drag force. It is influenced by factors such as the particle shape, size and density. It is due to shear stress. The force employed is from Li and Ahmadi (1992), this is a general expression for lift force provided by Saffman (1968). This is applicable to mainly spherical solid particles.

$$\overrightarrow{F} = \frac{2Kv^{1/2}\rho d_{ij}}{\rho_p d_p (d_{lk} d_{kl})^{1/4}} (\overrightarrow{u} - \overrightarrow{u}_p) \tag{3.38}$$

where K = 2.594 and d_{ij} is the tensor deformation.

Particle - Wall Interaction

It is very important that the particle-wall interaction is properly accounted. In view of this to predict the particle – wall collision, a rebound model was employed. The rebound model is also referred to as the restitution coefficient, because when the particle impacts the wall momentum loss occurs. In other words, the particle velocity after impact is less than before impact. This can be modelled as a function of impact angle for normal and tangential velocities (Zahedi et al., 2016). In this study, the normal and tangential coefficients of restitution proposed by Grant and Tabakoff (1975) were used. This model has been widely used by many researchers such as Chen et al. (2004), Parsi (2015), Peng and Cao (2016) and Duarte et al. (2017) amongst others, and has showed good agreement with relevant experimental findings. The normal and tangential components of the model are;

Normal Component;

$$e_{norm} = 0.933 - 1.76\alpha - 1.56\alpha^2 - 0.49\alpha^3 \tag{3.39}$$

Tangential Component;

$$e_{tan} = 0.998 - 1.66\alpha + 2.11\alpha^2 - 0.67\alpha^3 \tag{3.40}$$

where α is the particle impact angle.

3.3.2 Turbulent Dispersion of Particles

This is usually used to describe the transport phenomena of particles that can be distinguished from the carrier fluid. Dispersion of particles due to turbulence in the fluid phase can be predicted by employing either of two models, the stochastic tracking model or the particle cloud model. The stochastic tracking (random walk) model includes the effect of instantaneous turbulent velocity fluctuations on the particle trajectories through the use of stochastic methods while the particle cloud model tracks the statistical evolution of a cloud of particles about a mean trajectory. The concentration of particles within the cloud is represented by a Gaussian probability density function (PDF) about the mean trajectory, however, the stochastic tracking model accounts for the generation or dissipation of turbulence in the continuous phase (Fluent, 2013). In the present study, the stochastic tracking model has been employed and it's explained below.

Stochastic Discrete Random Walk (DRW) Model

In this model, the fluctuating velocity components are discrete piecewise constant functions of time. Their random value is kept constant over an interval of time given by the characteristic lifetime of the eddies. Furthermore, the interaction of a particle with a succession of discrete stylized fluid phase turbulent eddies is simulated (Gosman and Loannides, 1983; Fluent, 2013). Each eddy is characterised by a Gaussian distributed random velocity fluctuation, u', v', w', and a time scale, τ_e. The random velocities are assumed to have obeyed the Guassian probabilty distribution to satisfy Equation (3.41).

$$u' = \zeta \sqrt{\overline{u'^2}} \tag{3.41}$$

Where ζ is a normally distributed random number and the other terms on the right hand side of Equation (3.41) represents the local RMS value of the velocity fluctuations. Assuming isotropy, for the RNG $k-\varepsilon$ turbulence model employed in this present study, the values of the RMS fluctuating components is obtained from Equation (3.42).

$$\sqrt{\overline{u'^2}} = \sqrt{\overline{v'^2}} = \sqrt{\overline{w'^2}} = \sqrt{\frac{2k}{3}} \tag{3.42}$$

3.4 Erosion Modelling / Estimation

Many researchers have proposed various erosion correlations to account for pipe erosion due to sand particle impact. Some of these are Finnie (1960), Bitter (1963), Bitter (1963b), Neilson and Gilchrist (1968), Finnie (1972), Sheldon and Kanhere (1972), Tilly (1973), Jennings et al. (1976), Hutchings et al. (1976), Evans et al. (1978), Tabakoff et al. (1979), Hutchings (1981), Salama et al. (1983), Sundararajan and Shewmon (1983), Johansson et al. (1987), Shirazi et al. (1995), DNV (2007b), Chen et al. (1997), Oka et al. (2005a), Huang et al. (2008) and Zhang et al. (2010) to mention a few.

In this study, the erosion model proposed by Oka et al. (2005a) and Oka and Yoshida (2005b) was employed to predict the pipe erosion rate. This model considers more influencing parameters than many other available models and it is based on a wide variety of particle diameters, velocities, impact angles and material properties from empirical results, in other words, it is a predictive erosion equation that can be applied under any velocity, impact angle, particle size and material type (Oka et al., 2005a; Duarte et al., 2017). The Oka et al. (2005a) model was found to agree well when compared with experimental data. The erosion correlation is shown in Equation (3.43).

$$E(\alpha) = g(\alpha)E_{90} \tag{3.43}$$

where $E(\alpha)$ is the erosion damage at an arbitrary impact angle in mm^3kg^{-1}, $g(\alpha)$ is the impact angle dependence of the normalized erosion and E_{90} is the erosion damage at a normal impact angle in mm^3kg^{-1}.

The impact angle dependence of normalized erosion, $g(\alpha)$, is expressed by two trigonometric functions and by the initial material hardness Hv in GPa as shown in Equation (3.44).

$$g(\alpha) = (sin\alpha)^{n_1}(1 + Hv(1 - sin\alpha))^{n_2} \tag{3.44}$$

where n_1 and n_2 are exponents (empirical constants) determined by the material hardness and other impact conditions such as particle properties such as particle shape (Oka et al., 2005a).

The Empirical constants n_1 and n_2 are expressed in the form;

$$n_1 = S_1(Hv)^{q_1} \tag{3.45}$$

$$n_2 = S_2(Hv)^{q_2} \tag{3.46}$$

where S_1, S_2, q_1 and q_2 are all empirical constants.

In this model, the impact angle $g(\alpha)$ is the ratio of the erosion damage at the arbitrary angle $E(\alpha)$ to the damage at the normal angle. $g(\alpha)$ is further defined in the works of Oka et al. (1997). Equation (3.44) is a combination of two terms, the first one is repeated plastic deformation or brittle characteristics, the value of this term increases with increase in particle impact angle (Abdulla, 2011). While the second term accounts for the cutting action which is relative and more effective at shallower impact angles. The relative cutting action at an arbitrary angle to the normal angle has its maximum value at 0^o. $g(\alpha)$ is a useful term which reflects complicated erosion mechanism as a function of the type of material and this concept is supported by the measurements of plastic strain around indentations (Oka et al., 1997, 2005a; Oka and Yoshida, 2005b). The general overview of the plastic deformation and cutting action is shown in Figure 3.2.

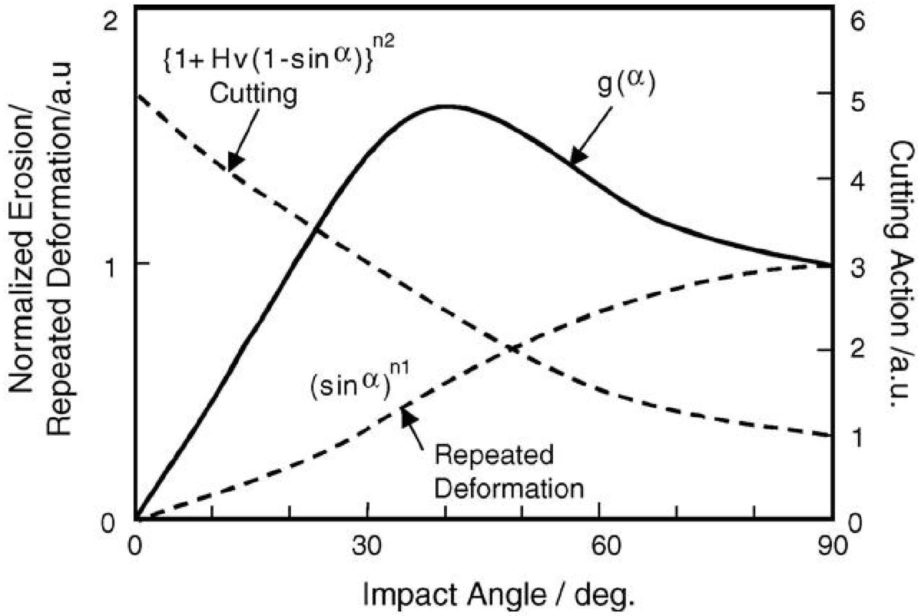

Figure 3.2: Concept of erosion arising from repeated plastic deformation and cutting action Oka and Yoshida (2005b)

The erosion damage at a normal impact angle, E_{90}, is expressed as shown in Equation (3.47).

$$E_{90} = K(Hv)^{k_1}(\frac{V}{V^*})^{k_2}(\frac{D}{D^*})^{k_3} \tag{3.47}$$

Where K is an empirical exponent that denotes a particle property factor such as particle shape (angularity) and particle hardness which has no correlation among different types of particles and other factors, V is the particle impact velocity and D is the particle diameter. V^* and D^* are the standard impact velocity and particle diameter used in the experiments for the correlations of erosion damage while k_1 and k_3 are exponents determined by properties of the particle (type of particle). k_2 is an exponent determined both by material hardness and by particle properties.
k_2 is expressed as;

$$k_2 = 2.3(Hv)^{0.038} \tag{3.48}$$

The values of the empirical constants of the model are shown on the Table 3.1.

Table 3.1: Values of empirical parameters in Oka et al. (2005a) model

Empirical Parameters	**Values**
K	60
k_1	-0.12
k_3	0.19
S_1	0.71
S_2	2.4
q_1	0.14
q_2	-0.94
V^* (m/s)	10.4
D^* (μm)	326

Erosion rate is converted to wear rate using the expression in Equation (3.49). The wear rate in the of mm/yr provides a better understanding of the magnitude of erosion.

$$WR = ER(\frac{kg}{m^2 s}) \times \frac{1}{\rho}(\frac{m^3}{kg}) \times \frac{39370 mils}{1m} \times \frac{3.1557e07}{1year} \tag{3.49}$$

Where WR is the wear rate in $mils/yr$, ER is the erosion rate and ρ_w is the pipe wall density.
The target wall is SS 316 wall with a density of $7900 kg/m^3$ (Parsi et al., 2015b).

3.5 Numerical Procedure

Computational Fluid Dynamics (CFD) solver, Ansys FLUENT 17.0 have been used to numerically obtain solutions for the governing and closure equations for multiphase air-water-sand flow. The transport of sand particles in pipelines is said to be turbulent in nature, hence, appropriate modelling approaches for specific interactions between solid particles and other fluid phases have been employed in order to account for the erosion of the pipe wall due to sand particle impact. The FLUENT code provides four different models for erosion estimation amongst which the Oka et al. (2005a) erosion model was employed for this study due to its capabilities in estimating erosion rates as observed by other researchers.

3.5.1 Numerical Schemes

In this scheme, for time discretization, standard finite-difference interpolation schemes such as QUICK, Second and Fisrt Order Upwind, and the Modified HRIC schemes, are used to obtain the face fluxes for all cells, including those near the interface between the phases. The volume fraction is computed based on Equation (3.50).

$$\frac{\alpha_g^{n+1}.\rho_g^{n+1} - \alpha_g^n \rho_g^n}{\Delta t} V + \Sigma_f(\rho_g^{n+1} U_f^{n+1} \alpha_{g,f}^{n+1}.f) = \left[S_{\alpha_g} + \sum_{\rho=1}^{n}(m_{lg} - m_{gl})\right] V \tag{3.50}$$

The solution methods employed are summarized on Table 3.2.

Table 3.2: Numerical Schemes

Variable	**Settings**
Pressure - Velocity Coupling	Phase - Coupled SIMPLE
Momentum	First Order Upwind
Volume Fraction	Compressive
Turbulent Kinetic Energy	First Order Upwind
Turbulent Dissipation Rate	First Order Upwind
Interfacial Area Concentration	First Order Upwind
Transient Formulation	First Order Implicit
Turbulence Model	RNG $k - \varepsilon$
Particle Treatment	Discrete Phase Model
Erosion Estimation	Oka et al. (2005) Model

Chapter 4

Solution Procedure and Validation Study

4.1 Overview

This chapter presents the solution procedure as well as validation of the model framework employed in the present study. The solution procedure shows the details of the model setup used in achieving the desired result, while validation of study involves comparing the predictions of the numerical frame investigated in the present study to appropriate published data. This study was born out of the lack of available data obtained from analyses of pipe erosion in conditions where multiphase flow transition could occur as well as in double bends or elbows mounted in series when the carrier fluid is in multiphase air-water flow. An ideal validation test case should have pipe geometry and solids parameters similar to the case of interest in the present study, and in view of this, the comprehensive experimental and numerical data from the works carried out on a single bend by Parsi (2015), Parsi et al. (2015c), Parsi et al. (2015a), Parsi et al. (2015b) and Parsi et al. (2016a) were identified as the most suitable for the purpose of validating the model setup before it was extended to the actual investigation of interest.

4.2 Solution Procedure

4.2.1 Computational Domain

The computational geometry from Parsi et al. (2015b) consists of 3m vertical and 1.9m horizontal pipes, upstream and downstream a standard 90 degree elbow respectively. Flow of fluid is from upward vertical to horizontal as shown in Figure 4.1. Pipe diameter and elbow radius of curvature are 76.2mm and 1.5 respectively. A monitoring surface was created 1m before the elbow from where Void Fraction data was extracted and compared with appropriate published data.

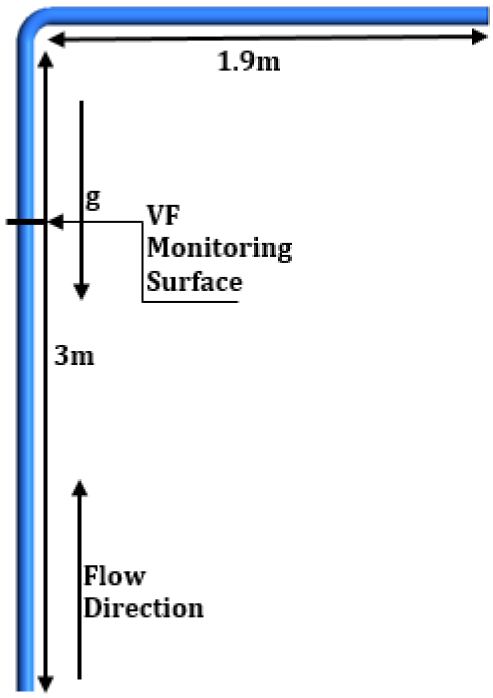

Figure 4.1: Computational vertical - horizontal geometry with a standard 90 degree elbow

4.2.2 Flow Conditions

Two different air-water flow conditions were considered for the model validation in this study. These data points were obtained from the flow map employed in the works of Parsi et al. (2016a) and are within the slug/churn region. According to Parsi (2015) and Parsi et al. (2016a), the flow pattern map was generated by the FLOPATN computer code developed by Pereyra and Torres (2005). The code is based on the model of

Barnea (1987) for the transition criteria between different multiphase flow regimes. The operating points employed for the validation of this study are also highlighted as shown on Figure 4.2.

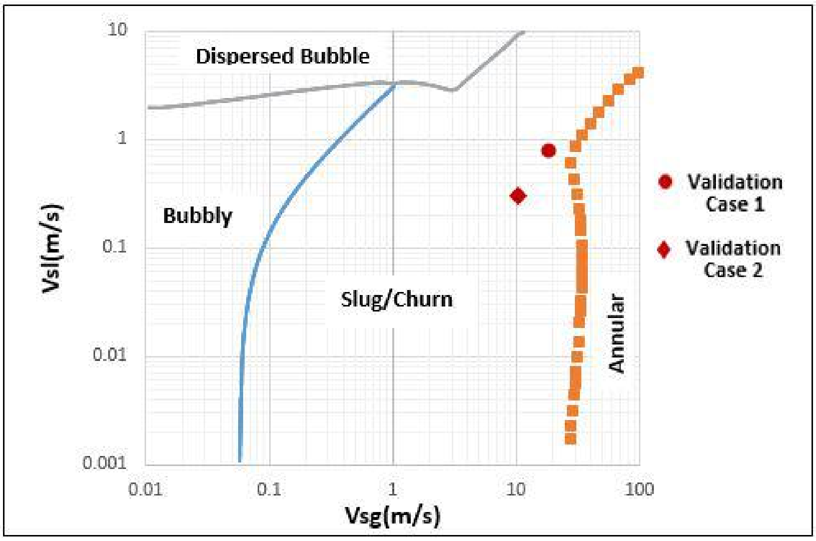

Figure 4.2: Validation points on flow regime map

Table 4.1: Flow Conditions

Case No.	$V_{sl}(m/s)$	$V_{sg}(m/s)$
Validation case 1	**0.3**	**10.3**
Validation case 2	**0.79**	**18.4**

4.2.3 Grid Generation

The pipe geometry was exported to ICEM CFD 17.0 meshing package for discretization, here a structured grid was generated across the flow domain to enable a smooth refinement of the mesh spacing and clustering in the pipe wall-region (Figure 4.3). The computational mesh is then imported to FLUENT solver where all the simulation calculations have been performed.

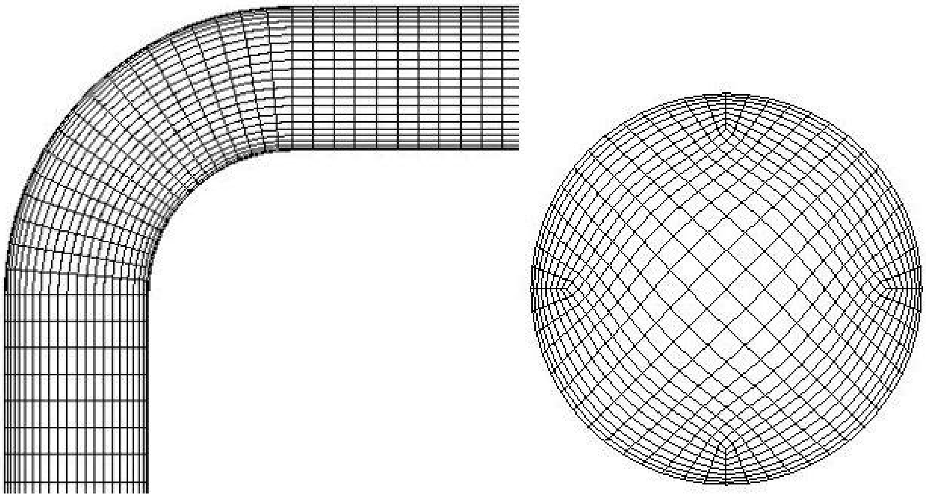

Figure 4.3: Sectional slice of meshed computational domain

4.2.4 Boundary Conditions

Specification of boundary conditions of a computational domain is a very important step in numerical simulation, this aides the direction of the fluid flow and prescribes information of flow variables at the domain boundaries. In this study, as shown in Figure 4.4 inlet, outlet and wall boundaries are specified for the computational domain.

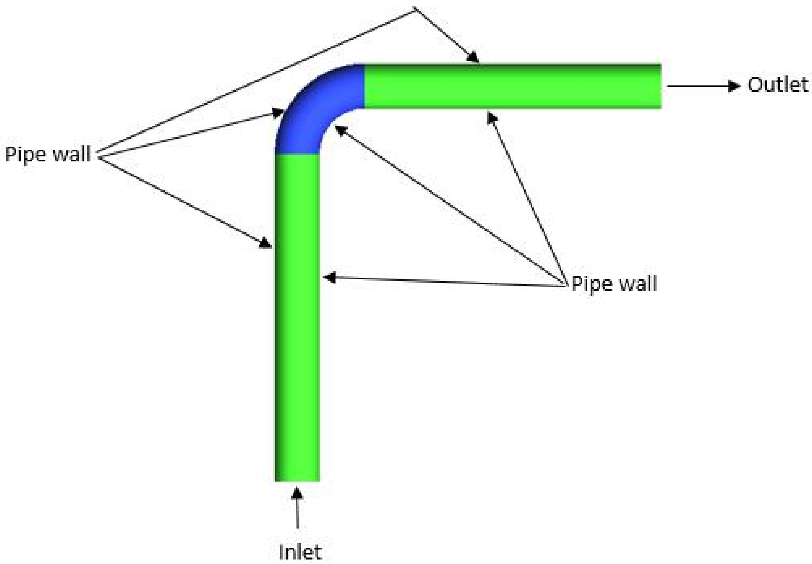

Figure 4.4: Boundaries of computational domain

Inlet and Outlet Boundary Conditions

Velocity inlet boundary condition was set at the pipe inlet, here the initial velocities of the gas and liquid were specified assuming no slip condition. The gas volume fraction was also appropriately specified. Turbulence intensity imposed and hydraulic diameter at the pipe inlet were 5% and 0.0762m respectively. The outlet boundary condition was set as pressure outlet, and the outlet pressure was set as zero. The gravitational effect on the flow was accounted for by specifying acceleration due to gravity to be $-9.81m/s^2$.

To ensure that the mass flow rates in the simulations are identical to those employed in the experimental data, as well as aide early flow development, the pipe inlet surface was split into two as shown in Figure (4.5). The liquid and gas phases were introduced into the domain based on the velocities obtained from Equation (4.1) and Equation (4.2) respectively. These equations and inlet splitting format are similar to those employed in the works of Parsi et al. (2015b). Gas was introduced into the domain via the middle of the inlet (red patch) while the liquid was introduced circumstantially (blue patch). The whole domain was initially filled with the liquid phase at zero velocity.

$$V_{inlet-Gas} = \frac{V_{SG} \times A_p}{A_G} \tag{4.1}$$

$$V_{inlet-Liquid} = \frac{V_{SL} \times A_p}{A_L} \tag{4.2}$$

Where $V_{inlet-Gas}$ and $V_{inlet-Liquid}$ are the gas and liquid velocities imposed at the inlet respectively. V_{SG} and V_{SL} are superficial gas and liquid velocities, A_p is the pipe cross-sectional area, A_G is the gas injection area (red patch in Figure 4.5) and A_L is the liquid injection area (blue patch in Figure 4.5).

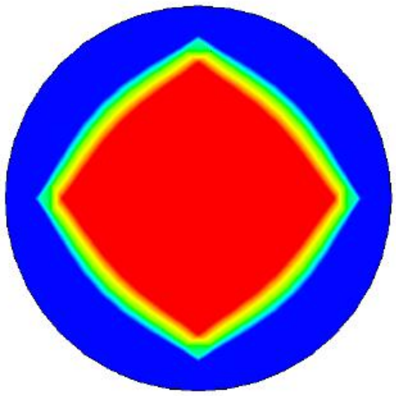

Figure 4.5: Injection of the phases via the inlet – red and blue indicates air and water respectively

Wall Boundary Condition

Appropriate treatment of the wall boundary condition is important in order to obtain a realistic solution of the flow in the pipe wall region as the flow could be affected by the conditions near the wall. The two-equation turbulence model employed in this study is mostly valid in the pipe-core region, where the effect of turbulence is dominant. To resolve the near wall viscous effect, it is required to model the entire flow boundary layers with the appropriate turbulence model. This approach however requires high number of mesh cells at the pipe wall region, hence becoming computationally more expensive. That is, it may also result in much slower solution convergence and divergence issue could occur due to high aspect ratio mesh cells. In view of this, semi-empirical correlations known as wall functions are applied to resolve the near wall treatment in the vicinity dominated by the viscous effects. Near wall functions allows for the use of a reasonable number of mesh cells while resolving the flow in question.

Wall functions consist of 'wall laws' for mean velocity and temperature and formulas for turbulent quantities. The standard wall function proposed by Launder and Spalding (1974) was employed in this study to resolve the behaviour of the flow at the pipe wall region. The standard wall function introduces additional velocity scales into the wall laws to account for the near wall treatment of the flow. The mean velocity in near wall region is then given as;

- For $y^* < y_v^*$

$$U^* = y^* \tag{4.3}$$

- For $y^* > y_v^*$

$$U^* = \frac{1}{k} In(Ey^*) \tag{4.4}$$

Where;

$$U^* \equiv \frac{U_P C_\mu^{\frac{1}{4}} k_P^{\frac{1}{2}}}{\frac{\tau_w}{\rho}} \tag{4.5}$$

$$y^* \equiv \frac{\rho C_\mu^{\frac{1}{4}} k_P^{\frac{1}{2}} y_P}{\mu} \tag{4.6}$$

Where subscript P refers to the first node point from the wall, μ is the dynamic viscosity of the fluid, U_P, is the mean velocity at the near-wall node distance, y_P is the log-layer constant given as 9.743, k is the von-karman constant given as 0.4187 and k_P is the turbulent kinetic energy at the near wall node P. The k_P and ε_P of the fluid at the near-wall node, P are accounted for by Equations 4.7 and 4.8. y^* is the dimensionless distance of the adjacent mesh node from the wall.

$$k_P = \frac{{U^*}^2}{\sqrt{C_\mu}} \tag{4.7}$$

$$\varepsilon_P = \frac{{U^*}^2}{k y_P} \tag{4.8}$$

The standard wall function formulation employs a logarithmic relation for the fluid in the near-wall region, which requires the the dimensionless distance of the adjacent mesh node from the wall, y^* to be within the range $30 < y^+ < 200$.

The present study also considered the effects of sand particle impacts on the internal pipe wall, hence the wall boundary treatment while considering the particle behaviour at the wall was accounted for using the normal and tangential coefficients of restitution proposed by Grant and Tabakoff (1975) explained in Section (3.3.1).

4.2.5 Solver Control

In this study, three dimensional (3-D) transient simulations were performed with the assumption that the liquid and gas phases were incompressible with no mass transfer between them. The effect of gravity was also incorporated. This is a time-dependent numerical solution scheme and an appropriate size of 0.001s was assigned to the time-step which is a critical controlling factor in transient simulations. The maximum number of iterations per time-step was set at 60. This is of utmost importance, in order to have smooth convergence of the required solutions. The convergence and stability of the solution is further controlled by setting appropriate values for the under-relaxation factors, values set for these are shown on Table 4.2. The maximum residual for all parameters was set at 0.001.

Table 4.2: Under-Relaxation Factors

Parameters	**Values**
Pressure	0.3
Density	1
Momentum	0.3
Volume Fraction	0.5
Turbulent Kinetic Energy	0.6
Turbulent Dissipation Rate	0.6
Turbulent Viscosity	0.5
Interfacial Area Concentration	0.3

4.3 Validation Study

A model set up validation study was carried out based on the validation cases highlighted in Figure 4.3. Simulations were conducted to analyse the flow regimes obtainable from these flow conditions and the results obtained were appropriately compared to experimental and CFD data of Parsi et al. (2016a), Parsi et al. (2015b), Parsi et al. (2015a) and Parsi et al. (2015c). Other published data were also used to underpin the validity of these results. The details of the test cases employed for this validation are shown on Table 4.4.

Table 4.3: Test Cases For Validation (Experiment (Parsi et al., 2015a,c), Numerical (Parsi et al., 2016a, 2015b))

Parameters	**Experimental Study**	**Numerical Study**
Pipe Diameter(mm)	76.2	76.2
Elbow Radius of curvature	1.5	1.5
Gas Velocity(m/s)	9.8, 18.3	10.3, 18.4
Liquid Velocity(m/s)	0.58, 0.76	0.3, 0.79
Sand Diameter(μm)	300	300
Sand Density(kgm^{-3})	2650	2650
Sand Flow Rate(kg/s)	0.0256	0.0256

4.3.1 Mesh Sensitivity Study

Three structured grids were considered for the mesh sensitivity study of this work. Figure 4.6 displays their cross-sectional slices while their details can be seen on Table 4.5. The mesh independence study was carried out to ascertain the consistency of results, and the flow condition with Gas Superficial Velocity, V_{sg} of 10.3m/s and Liquid Superficial Velocity, V_{sl} of 0.3m/s as shown on the flow regime map in Figure 4.3 was employed for this purpose.

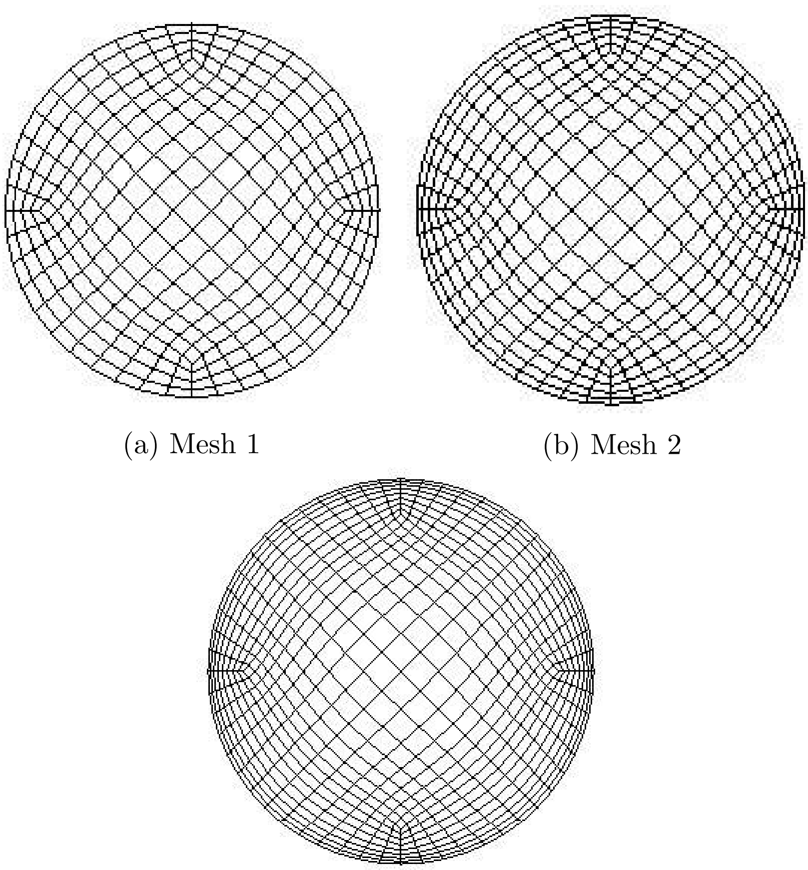

(a) Mesh 1 (b) Mesh 2

(c) Mesh 3

Figure 4.6: Cross-sectional slices of the different grids considered in this study

Table 4.4: Mesh refinement parameters

Mesh	Height of first cell	Height Ratio	Number of cells
1	0.0015	1.2	80,000
2	0.001	1.2	105,600
3	0.0005	1.2	181,608

The optimum mesh that produced the most realistic results was determined by comparing the predicted mean and standard deviation of the void fraction time series of the air-water validation case based on the change in grid size with that of the experimental and CFD data of Parsi et al. (2015a) and Parsi et al. (2016a) respectively. From the results presented on Table 4.5 and Figure 4.7, Mesh 2 was employed for the purpose of this study. The mesh specification gives an appropriate result which displays no quantitative change in the data generated. It will also reduce the computational time for running simulations compared to Mesh 3. Figure 4.7 shows the effect of grid size on the cross-sectional averaged void fraction time series of the validation case.

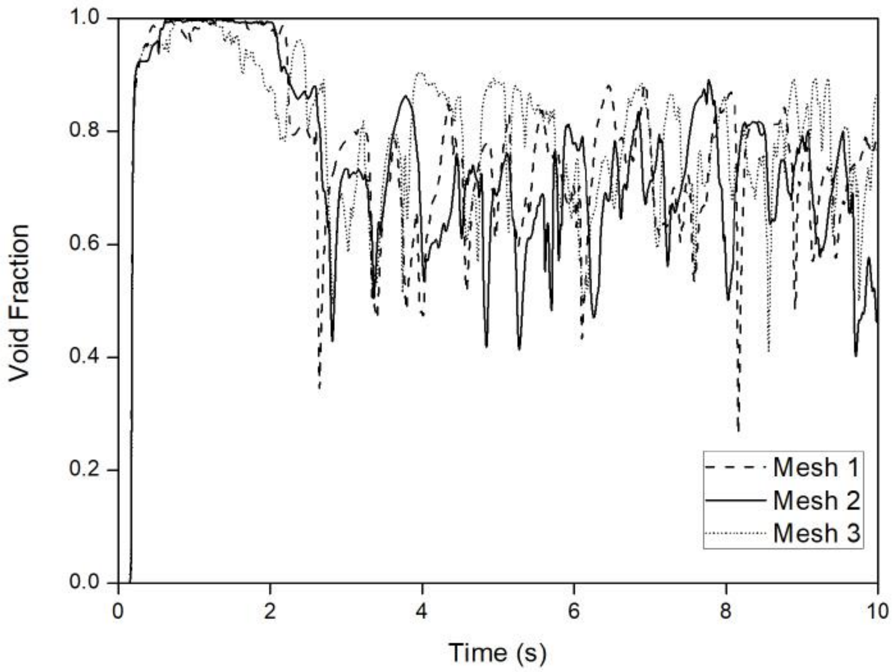

Figure 4.7: Effect of grid size on the cross-sectional averaged void fraction time-series

Table 4.5: Mean and Standard Deviation of Void Fraction (Experimental and CFD Data from Parsi et al. 2015a and 2016)

	Experiment	**CFD**	**Mesh 1**	**Mesh 2**	**Mesh 3**
Mean	0.74	0.72	0.72	0.72	0.76
SD	0.1	0.1	0.12	0.11	0.12

4.3.2 Results and Discussion of Validation Study

Air-water multiphase simulations were conducted employing the two set of flow velocities shown on Figure 4.3 as validation data points, and their profiles of Time Series of Cross-Sectional Averaged Void Fraction are presented in Figures 4.8 and 4.9. Figure 4.8 shows the profile of the flow condition with gas velocity 10.3m/s and liquid velocity 0.3m/s while Figure 4.9 shows that of 18.4m/s and 0.79m/s gas and liquid velocities respectively. These results were compared with the experimental data of Parsi et al.

(2015c) supplied by the Wire Mesh Sensor (WMS) and the numerical data of Parsi et al. (2016a) and Parsi et al. (2015b) as can be seen in the same figures mentioned earlier, however the profile of the Time Series of Cross-Sectional Averaged Void Fraction for flow condition with gas velocity 18.4m/s and liquid velocity 0.79m/s could not be obtained but other established post processing data such as the probability density function (PDF), mean void fraction and erosion rate presented by Parsi et al. (2016a) were used to ascertain the validity of the results generated. The air-water flow conditions used for the simulation for which the profiles presented in Figures 4.8 and 4.9 were generated are expected to produce a complex multiphase flow called churn flow, and the time series profiles of this type of flow exhibit the cyclic fluctuations which represents the sudden increase or drop in cross-sectional average void fraction across a monitoring surface as can be observed in different multiphase flows. The monitoring surface in this case was created 1m before the elbow as was in the works of Parsi et al. (2016a). Both profiles clearly show this behaviour and Figure 4.8 shows that there is appropriate agreement between the experimental and numerical data of Parsi et al. (2015c) and Parsi et al. (2015b) between the times of about 2.5 and 10s.

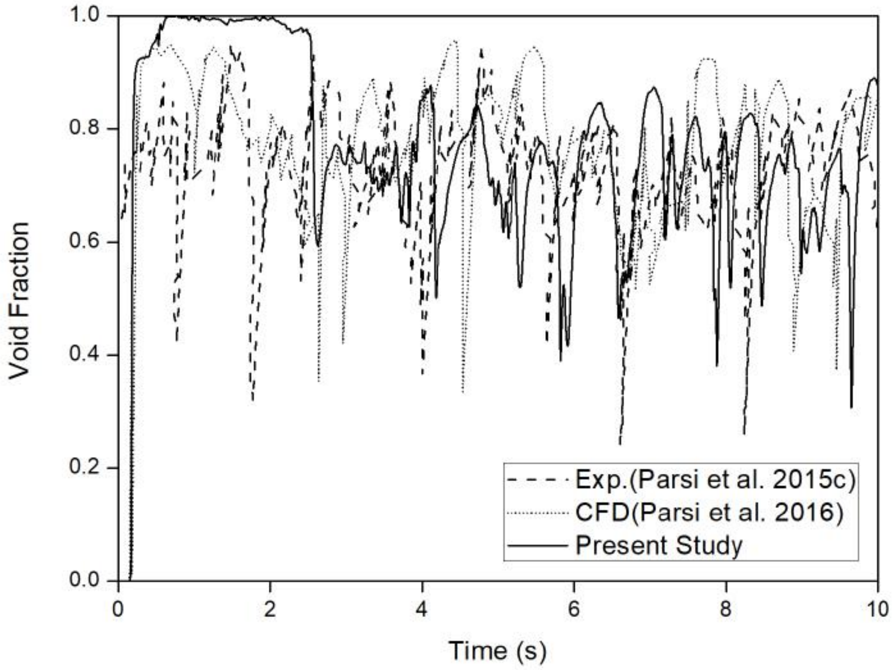

Figure 4.8: Cross-sectional averaged void fraction time series of V_{sg} 10.3m/s and V_{sl} 0.3m/s

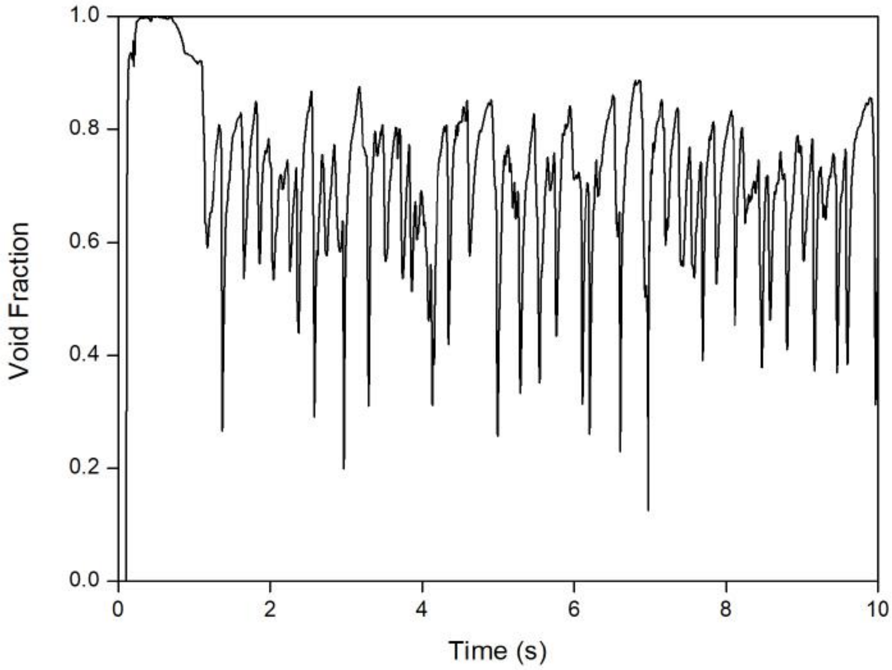

Figure 4.9: Cross-sectional averaged void fraction time series of V_{sg} 18.4m/s and V_{sl} 0.79m/s

In Figure 4.8, a clear disagreement can be observed between the present study and the data from Parsi et al. between 0 and 2.5 s, this is an indication of the flow behaviour before expected interaction to push the flow development began to occur in the flow domain, this is due to how the model was set up. The lowest volume fraction after 2.5s in the experimental and numerical data of Parsi et al. (2015c) and Parsi et al. (2015b) are 0.24 and 0.33 respectively, while the lowest volume fraction drop in the present study is 0.37. While the lowest drop in the volume fraction in numerical data of Parsi et al. (2016a) shows a difference of 37.5% from that experimental data of Parsi et al. (2015c), the present study displayed a percentage difference of 54% from it. However more information to ascertain the result of the present study are inferred from the mean void fraction.

The mean void fraction is computed from the time averaging of the cross-sectional averaged void fraction time series. The comparisons between the mean void fraction of the present study and the experimental and numerical studies of Parsi et al. for both validation cases are shown on Table 4.6 and Table 4.7. Validation case 1 has a difference of 2.7% and 0% from the WMS experimental data of Parsi et al. (2015c) and numerical data of Parsi et al. (2016a) respectively, and validation case 2 has 8.6% and 0.4% from the experimental and numerical data respectively. These discrepancies hence show that the CFD mean void fraction results of the present study are in appropriate agreement with those of the WMS and CFD of Parsi et al. (2015c) and Parsi et al. (2016a). The standard deviation of the cross-sectional averaged void fraction time series of validation case 1 was also compared to those of the WMS and CFD of Parsi et al. (2015c) and Parsi et al. (2016a), a difference of 10% was observed here between the present study and both published data.

Table 4.6: Comparison of mean void fraction and standard deviation of Validation Case 1

	Experiment	**CFD**	**Present Study**	**% diff(Exp)**	**% diff(CFD)**
Mean	0.74	0.72	0.72	2.7	0
SD	0.1	0.1	0.12	10	10

Table 4.7: Comparison of mean void fraction and standard deviation of Validation Case 2

	Experiment	**CFD**	**Present Study**	**% diff(Exp)**	**% diff(CFD)**
Mean	0.78	0.71	0.713	8.6	0.4

A qualitative agreement was also observed with the experimental and numerical data of Parsi et al. (2015b). Figure 4.10 shows a comparison between the contour plots of the present study and Parsi et al. (2015b) on a cross-sectional slice of the flow domain and the monitoring surface 1 m before the elbow. The contour plots in this study were extracted after 10 s of simulation time. Although the time averaged contour plots displayed some characteristics of annular flow instead of the expected churn flow as mentioned earlier, in the actual sense, there is the presence of periodic large waves of different liquid volumes and film changing direction of motion in the flow domain as can be seen in Figure 4.10(b).

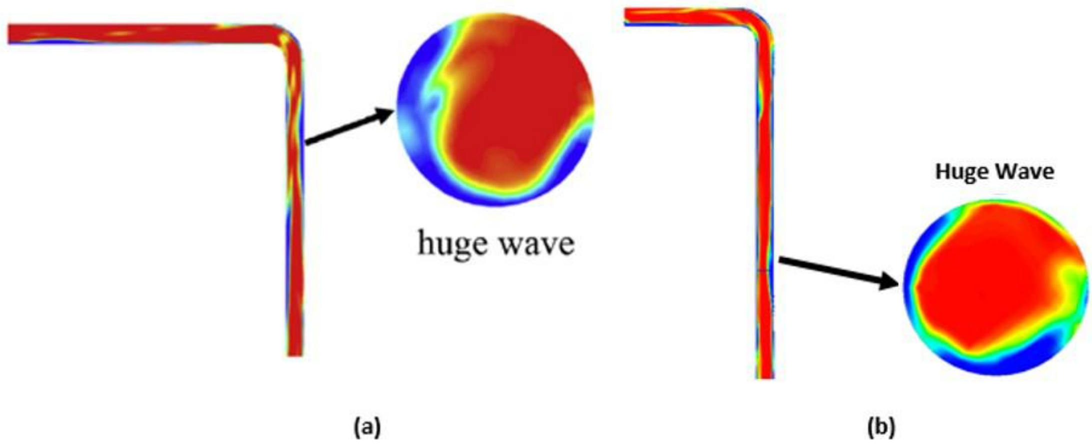

Figure 4.10: Contour plots showing presence of huge wave within the flow; (a) Parsi et al(2015), (b) Validation Case 1

Figures 4.11 and 4.12 show the comparison of the Probability Density Function (PDF) of the validation cases to the numerical and WMS data of Parsi et al. (2016a). The probability Density Function (PDF) shows the probability that a continuous random variable acquires a specific value. Statistical analysis of the behaviour of void fraction is one method that can also be used to further ascertain flow patterns under normal gravity conditions. It reveals the probability of each void occurring in the fluid.

According to Costigan and Whalley (1997), every flow pattern exhibit a specific PDF signature based on the fluctuation of its fluid phases. The ksdensity function of MATLAB was used to generate the PDF curves of average void fraction time series in this study.

Churn flow is characterized by high a void fraction with random dips and lows with no clear boundaries between the phases. The low dips are very short lived, hence the unstable nature of the slug. Churn flow is characterized by a PDF curve with a single peak at high void fractions and a broad tail at the low void fractions, the single peak at high void fraction is indicative of the flow's proximity to annular flow and the broad tail represents the passage of unstable slugs. According to Lowe and Rezkallah (1999), a typical PDF curve of churn flow is between an average VF of 0.6 and 0.9. This behaviour and those described by Costigan and Whalley (1997) can be observed in the PDF profiles of both validation cases (Figures 4.11 and 4.12). Appropriate agreement is also observed between the PDF profiles of Validation Case 1 and 2 and the experimental and numerical data of Parsi (2015) and Parsi et al. (2016a). Although there are noticeable discrepancies, the peaks of the PDF profiles of the validation cases, WMS and CFD data occurring at different void fractions. The difference between the experiment and the validation cases could be attributed to the fact that the experiment was performed over a period of 60 s while the CFD simulations of the present study were conducted for 10 s. This could further be due to the effect of the entrance length before the elbow which is 18 m in the experiment and 3 m in the present CFD study. The difference between the results of the Validation Cases and CFD data of Parsi et al. (2016a) could also be due to the differences in grid specifications as well as the time-step specifications of the iterative process which affects the rate of void fraction fluctuations. Difference in computing power will also lead to a notable difference.

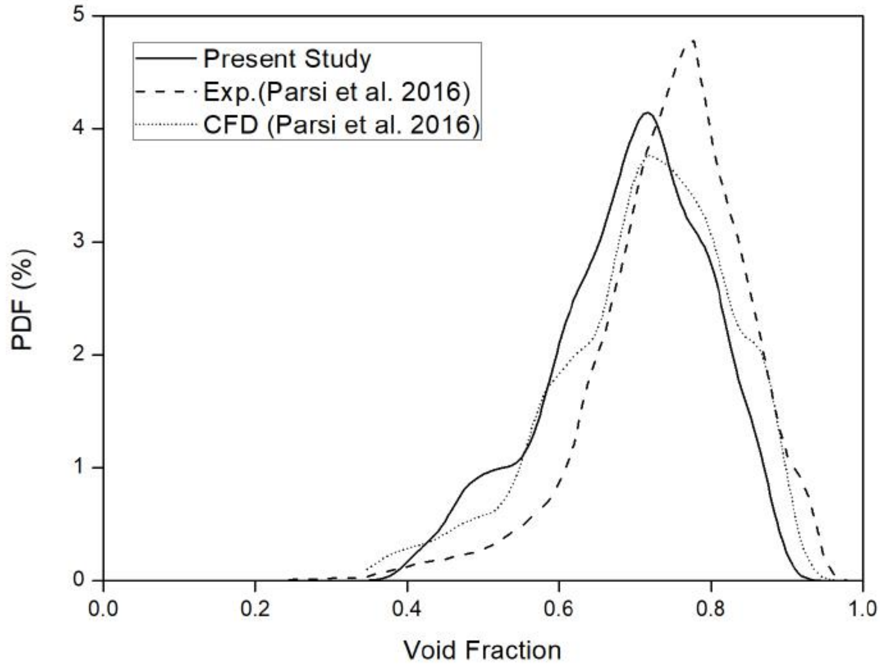

Figure 4.11: Comparison of PDF profiles - Validation Case 1

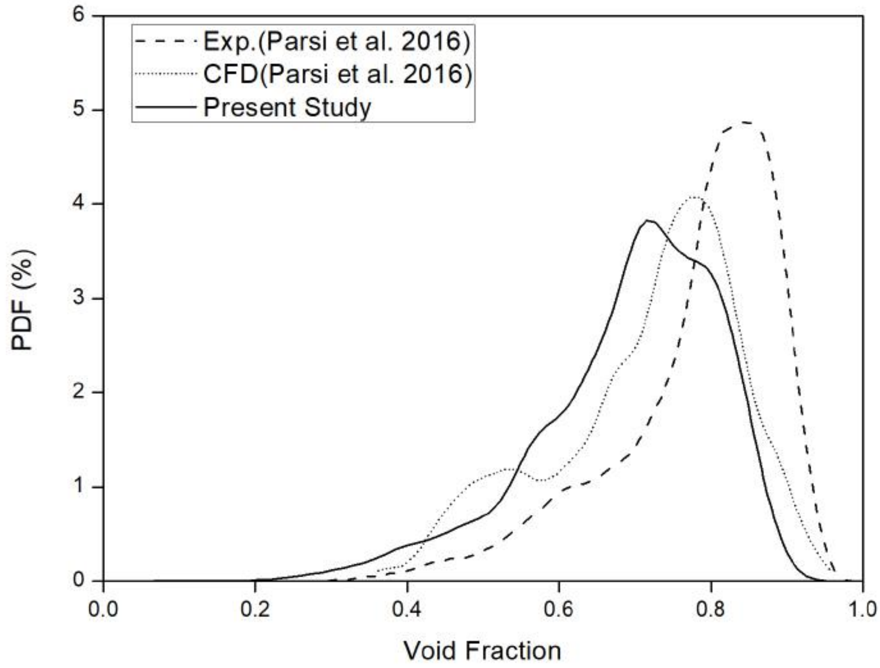

Figure 4.12: Comparison of PDF profiles - Validation Case 2

Figure 4.13 shows the profile of the overall frequency data achieved from the presently study compared to the data presented by Parsi et al. (2015d). The overall frequency is calculated by the Power Spectral Density (PSD). Power Spectral Density (PSD) shows the strength of the variations as a function of frequency. It is computed to know frequencies and amplitudes of signals in a time series data and can also extract the maximum power in a time series data. In this study, the Fast Fourier Transform tool in the ANSYS post-processing software CFDPost was used to analyze the power signal in the random cross-sectional averaged void fraction (VF) data generated to produce the frequency signals shown in Figure 4.13. As can be seen in Figure 4.13, the frequency with the maximum power in the PSD of the present study is 0.54Hz while that of the CFD data from Parsi et al. (2015d) is 0.3Hz. The maximum power in the PSD of the WMS experimental data is reported to be 0.68Hz.

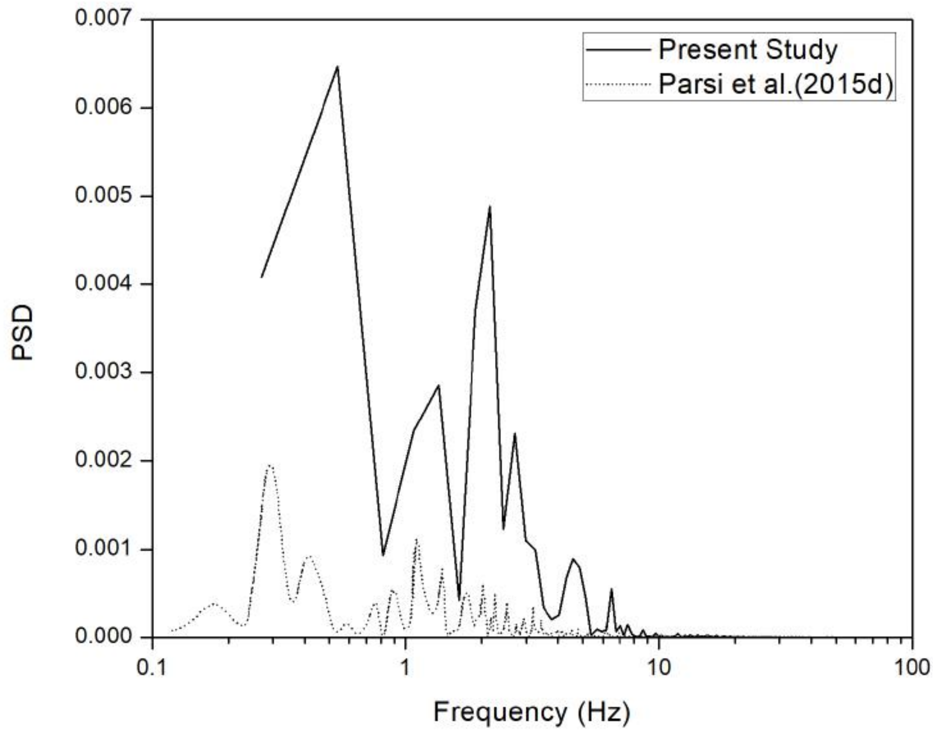

Figure 4.13: Comparison of PSD profiles of averaged void fraction time series - Validation Case 1

Table 4.8: Comparison of PSD Data - Parsi et al.(2015b) and Validation Case 1

	WMS Experiment	**CFD**	**Present Study**
Frequency (Hz)	0.68	0.3	0.54

Furthermore, for the present study, erosion analyses were conducted for Validation Case 1 and compared to the results generated by Parsi et al. (2015a) and Parsi et al. (2015b). Parsi et al. (2015a) conducted experiments to determine the erosion pattern in a standard elbow while flow regime is churn flow using non-intrusive ultrasonic devices and a CFD analysis was also presented. These have been used to further benchmark the present study. In the CFD analysis, sand particles were injected into the flow domain and tracked with the DPM model, pipe erosion rate at the elbow was then accounted for with the erosion model developed by Oka et al. (2005a). Figure 4.14 shows the schematics of transducer positions in the experiment and Figure 4.15 shows the erosion pattern at the elbow in the present study compared to CFD data of Parsi et al. (2015b).

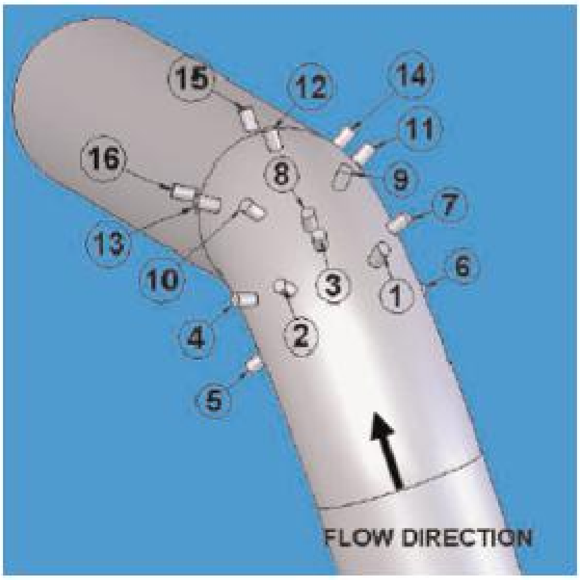

Figure 4.14: Schematics of Transducer positions (Parsi et al., 2015a)

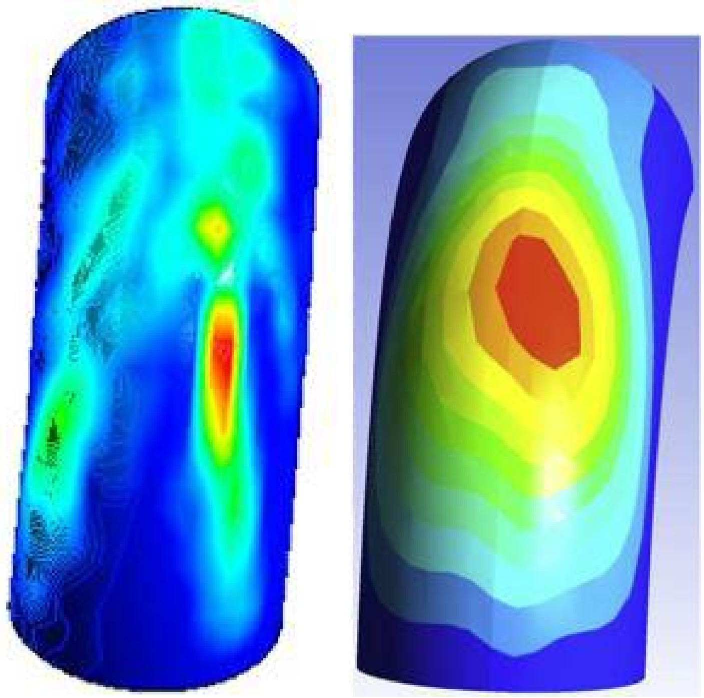

(a) Present Study (Validation case 1) (b) Parsi et al. (2015b)

Figure 4.15: Comparison of erosion contours

Parsi et al. (2015a) reported transducer numbers 1 to 3 and 8 as the areas most susceptible to erosion damage for the vertical churn flow case analyzed. This is up to 45°on the inlet area of the outer radius of the elbow. CFD data of Parsi et al. (2015b) also showed that the maximum erosion of the elbow occurred at 45°on the outer bend spreading towards the elbow sides as can be seen in Figure 4.15(a). These same behaviours and patterns have been observed in the present study, see Figure 4.15(a). The maximum erosion location is the patch in color red and the erosion location could also be observed spreading towards the sides of the elbow. All of these show the capability of the current model set-up to reproduce similar results to the works of Parsi et al. (2015a), Parsi et al. (2015b) and Parsi (2015). The discrepancies in the erosion pattern could be due to some numerical differences such as mesh refinement, in order to produce a finer result, the simulations could be conducted using a finer mesh specification, this will further ensure that erosion patterns are independent of the mesh size. It could also be due to the simulation run time. Furthermore, the erosion rate obtained for validation case 1 was compared with that of the CFD and experimental data of Parsi (2015), this is presented on Table 4.10. Erosion rate from the CFD analyses was converted to mils/year using Equation (3.51)(Chapter 3).

Table 4.9: Comparison of Erosion Rate - Parsi (2015) and Validation Case 1

	ER(kg/m^s)	**ER(mpy)**	**%diff(Exp)**	**%diff(CFD)**
Exp	-	587	-	-
CFD	4.0E-06	629	-	-
Present Study	3.4E-06	540	8	14

Results from the present study show appropriate agreement with the experimental data of Parsi et al. (2015a). The maximum erosion rate at the elbow is predicted to be 540 mpy as against 587 mpy presented by Parsi et al. (2015a) and Parsi et al. (2015b). This is an under-prediction of 8%, and could be as a result of the assumptions of the present study in terms of the negligible particle-particle interaction, the turbulence model employed, as well as the computer simulation run time against the actual time taken to conduct the experiment.

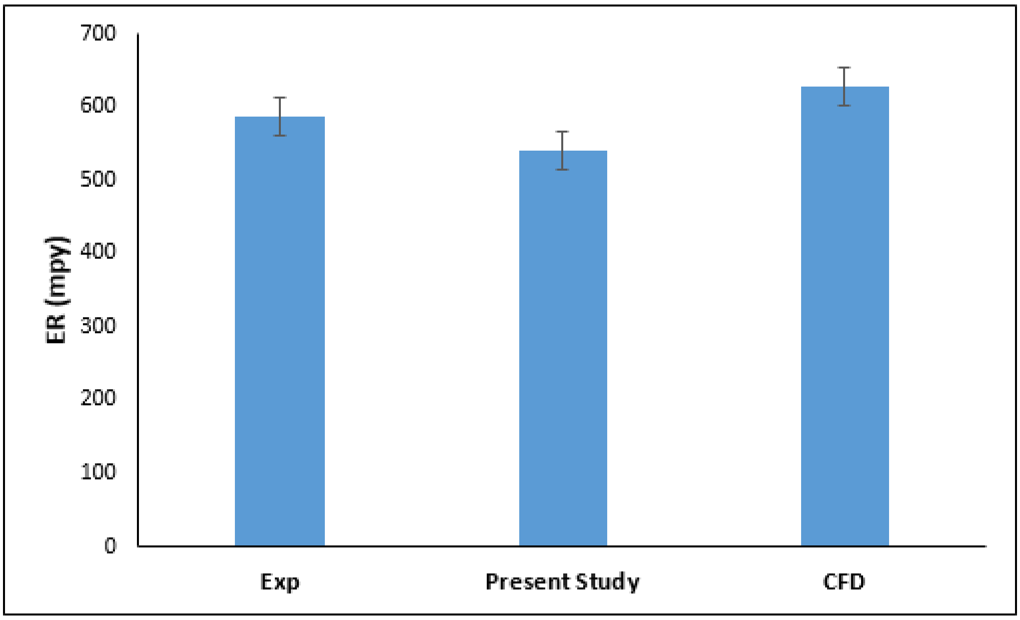

Figure 4.16: Comparison of erosion rates

In a nutshell, the model framework has shown great capability of modeling and capturing the features of complex multiphase flows like Churn flow, it also displayed great ability at generating the erosion rate due to sand particle transport and pattern. Although there are few discrepancies in the results generated, an appropriate agreement has been observed between these results and the experimental and numerical analyses carried out by Parsi et al. (2015a), Parsi et al. (2015b), Parsi (2015) and Parsi et al. (2016a). Based on these findings and due to the limited availability of data in the study of erosion in double bends, this model was employed and extended to investigate sand erosion in double bends or elbows mounted in series.

Chapter 5

Erosion In Elbows Mounted In Series Using Multiphase Modelling Technique

5.1 Description of geometries and Flow conditions

5.1.1 Geometry

The single bend geometry described in the previous chapter was modified to accommodate a second elbow as shown in Figure 5.1 and fluid flow simulation was appropriately conducted. Sand particles were injected via the pipe inlet and erosion analysis was carried out. The normalized separation distance (L/D) between the two elbows mounted in series were 0, 5, 10, 15 and 20, and the orientation of the second elbow was varied as shown (the orientations hereafter are referred to as Geometry 1, 2 and 3). The mesh specification employed is identical to that used for the validation effort discussed in the previous chapter.

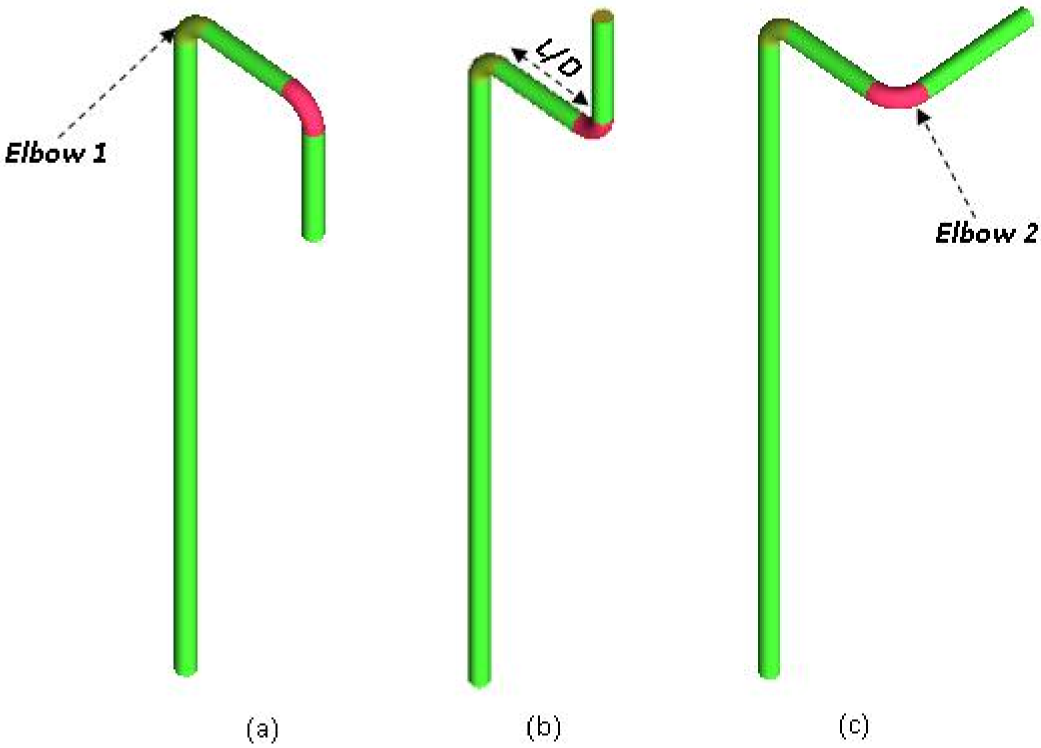

Figure 5.1: Double Bend Geometries; a) Geometry 1; b) Geometry 2; c) Geometry 3

5.1.2 Flow conditions

Two air-water flow conditions in the slug/churn region were considered in this study. For both conditions, the superficial liquid velocity, V_{sl}, was kept constant while the superficial gas velocity, V_{sg}, was varied. The superficial gas velocities are at low and high velocities intended to produce complex multiphase flows - slug and churn (See Figure 5.2). The data point at the high gas velocity is similar to that employed for the validation of this study (Validation case 1) and it is based on the works of Parsi et al. (2016a), Parsi (2015) and Parsi et al. (2015b). While the data point with the lower superficial gas velocity was selected for the purpose of comparison of erosion in two different complex multiphase flows. The air-water flows have been simulated in the double bend geometries using the validated Eulerian-Multifluid VOF model setup and on obtaining a considerably developed flow, sand particles where injected into the flow domain via the pipe inlet surface. The erosion damage(s) the pipe wall is subjected to were obtained and appropriately analyzed. The sand properties remained the same as that used in the previous chapter (see Table 5.1).

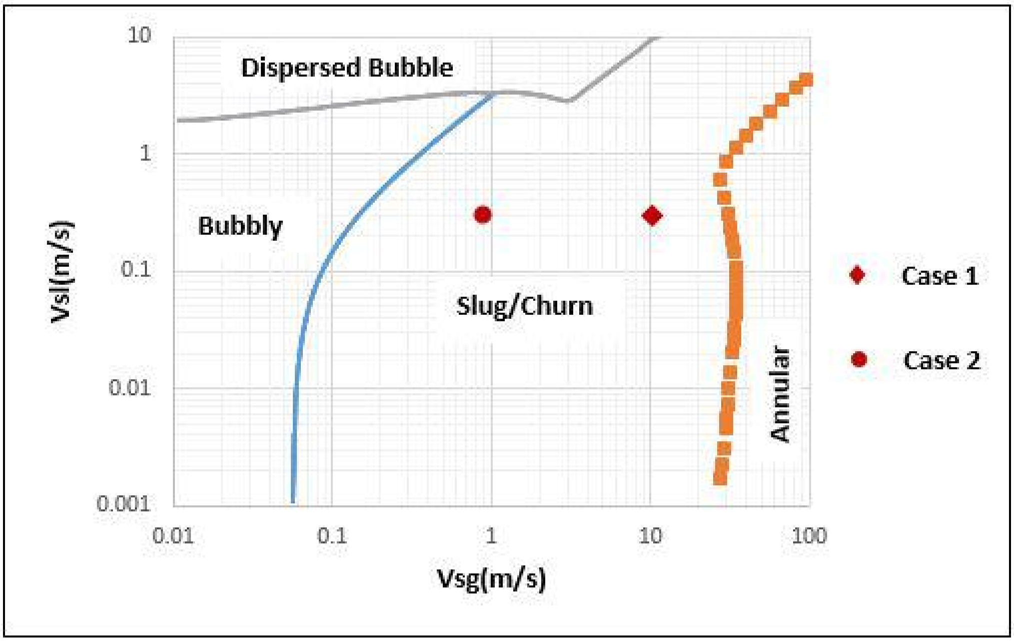

Figure 5.2: Flow conditions on flow regime map

Table 5.1: Flow Conditions and sand properties

	V_{sl}(m/s)	V_{sg}(m/s)	Sand flow rate (kgm^{-3})	Sand diameter (μm)
Case 1	0.3	10.3	0.0256	300
Case 2	0.3	0.9	0.0256	300

5.2 Results Analysis

5.2.1 Contour Plots and Cross-sectional Time Series of Averaged Void Fraction

Contour Plots

Figures 5.3 and 5.4 show the contour plots of the cases studied at 10 s. Case 1 shows the same features shown in Validation case 1 which is Churn flow. And as already highlighted in Chapter 4, churn flow is characterized with the attributes of both slug and annular flows. There are no clear boundaries between the liquid and gas phases, and there is the presence of waves and discontinuous gas cores. Huge waves in the churn flow was also observed by Parsi et al. (2015b) and Parsi et al. (2016a). Some authors however consider this type of flow to be fundamentally annular flow in nature with large disturbance waves carried by the gas flow (Costigan and Whalley, 1997).

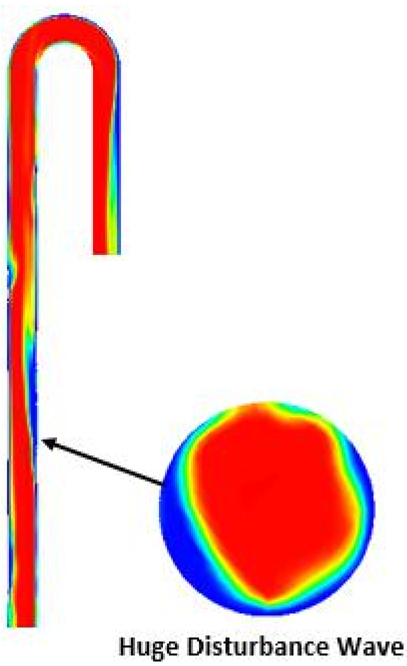

Figure 5.3: Contour plot of Churn flow at 10 s - Case 1

Unlike the churn flow, there are clear and defined boundaries between the liquid and gas phases in Case 2. The fluid flow data extracted across a monitoring surface positioned 1 m before the elbow shows the presence of alternating gas pockets of varying lengths separating the continuous liquid flow stream. These gas pockets are referred to as Taylor Bubbles while the discontinuous liquid streams are called the liquid slugs. The small bubbles between the two Taylor Bubbles in Figure 5.4 are as a result of the slip between the liquid and gas, these are induced at higher gas velocities. These characteristics and features are of slug flow. Similar features have also been observed and described in the previous works of Costigan and Whalley (1997), Lowe and Rezkallah (1999) and Parsi et al. (2014) amongst others.

The more prominent gas core in the contour plot of the churn flow shows the high presence of gas due to its higher velocity when compared to slug flow.

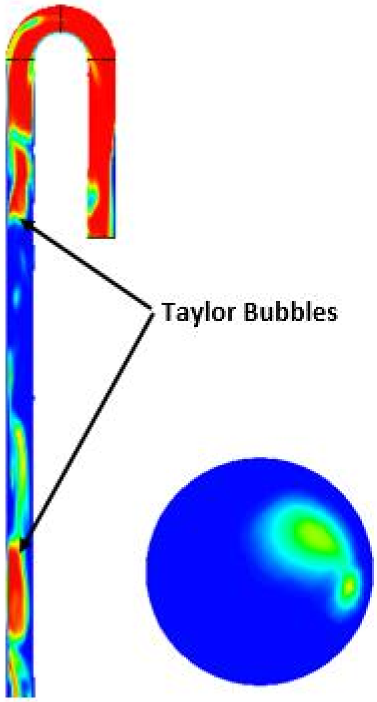

Figure 5.4: Contour plot of Slug flow at 10 s - Case 2

Cross-sectional Time Series of Averaged Void Fraction

Time series contain vital information concerning the liquid and gas behaviours within a particular flow. Cross-sectional time series of the averaged void fraction have distinct nature of occurrence in different flow patterns. There are however some main features irrespective of the flow pattern. These are; they all exhibit cyclic fluctuations that depict a sudden increase or drop in cross-sectional averaged void fraction across a monitoring surface; as the superficial gas velocity (V_{sg}) increases, there is a drop in the amplitude of the fluctuations.

In this section, the time series at both flow conditions studied in the double bend geometries are presented. Just as in the case of the single bend geometry, the monitoring surface is placed 1m before Elbow 1. Figure 5.5 and 5.6 show the cross-sectional averaged void fraction times series for both the churn and slug flow conditions respectively. In Figure 5.5, the unstable nature and undefined pattern of the cyclic fluctuations observed are attributed to the complex nature / interactions of the liquid and gas phases at these flow conditions. As liquid structures passes through the monitoring surface, drops in the time series are observed; the higher the volume of liquid in the fluid structure passing through the monitoring surface, the higher the amplitude of the drops experienced. On the other hand, as superficial gas velocity increases, the liquid structures become aerated forming huge and disturbance waves as seen on the contour plot (Figure 5.3). As the flow becomes more aerated, the amplitude of the time series rises accordingly. These are typical attributes of the intermittent or churn flow, which occurs between the slug and annular flow region, observed in this study.

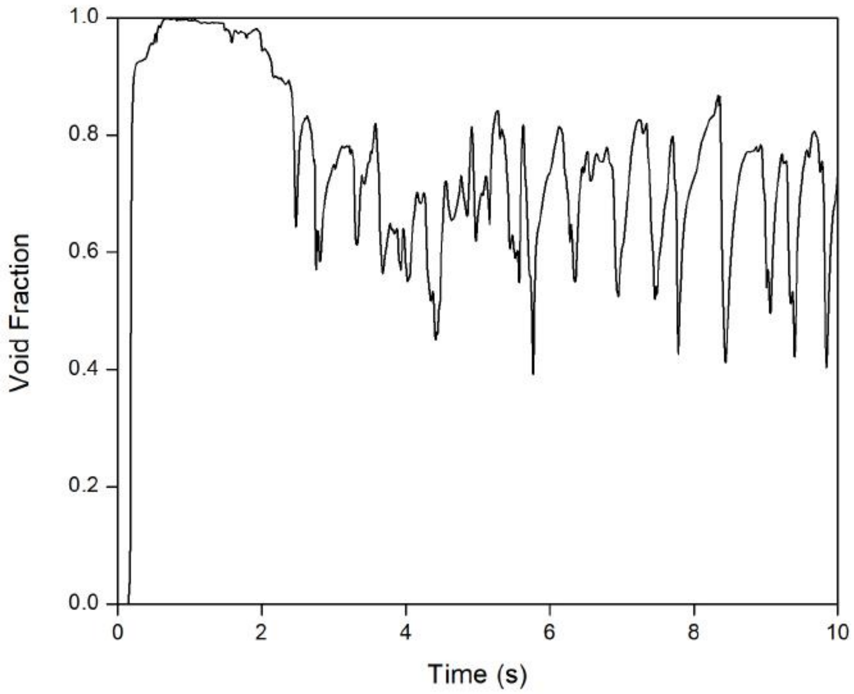

Figure 5.5: Cross-sectional averaged void fraction time series of Churn flow

Figure 5.6 shows the time series averaged void fraction at the low superficial gas velocity. Here, there is a more defined pattern of the cyclic fluctuations. Across the monitoring plane, the profile shows the intermittent passage of the gas and liquid phases as explained in the characteristics of the contour plots of slug flow. The high void fraction values indicates the passage of a high volume of air, this occurs when the Taylor Bubbles described above cuts across the monitoring surface. The low void fractions on the other hand indicates the passage of liquid slugs.

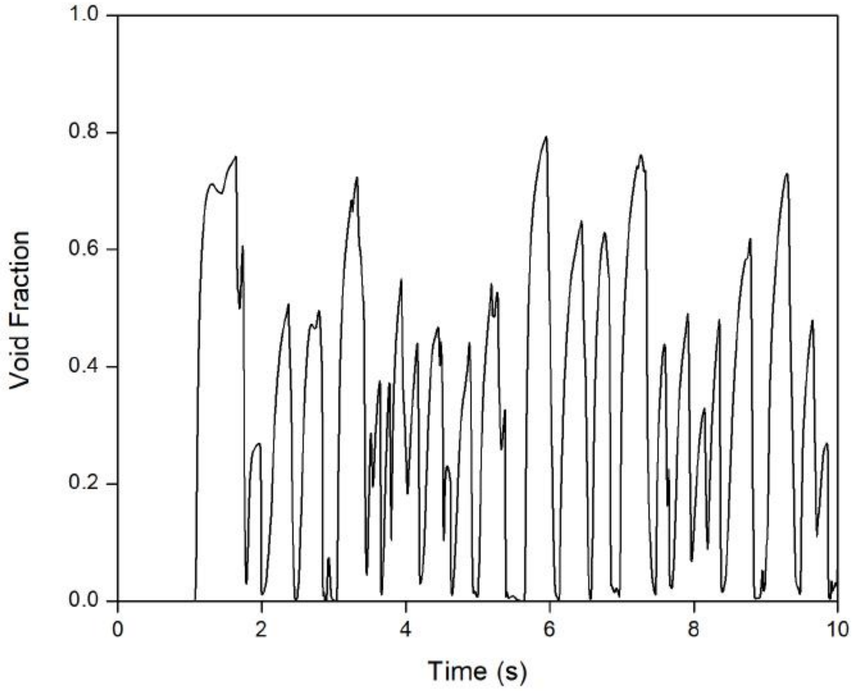

Figure 5.6: Cross-sectional averaged void fraction time series of Slug flow

The cross-sectional averaged void fraction of the churn flow when elbows are mounted in series was also compared with that of the single bend flow domain. It was observed that the flow pattern upstream of Elbow 1 in the case of a double bend geometry is the same as that observed in the single bend. This is shown in Figure 5.7. The contour plots are also compared to ascertain that the fluid development in the single and double bend geometries is not altered. Figure 5.8 is the comparison of the contour plots of the flow in the single and double bend geometries.

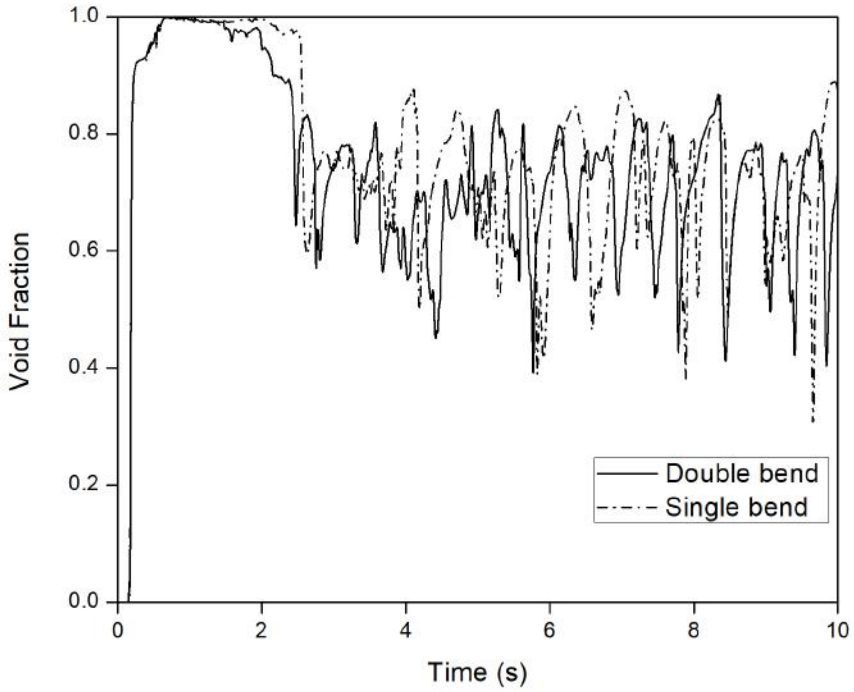

Figure 5.7: Comparison of Cross-sectional averaged time series of churn flow in single and double bend geometries at L/D of 0

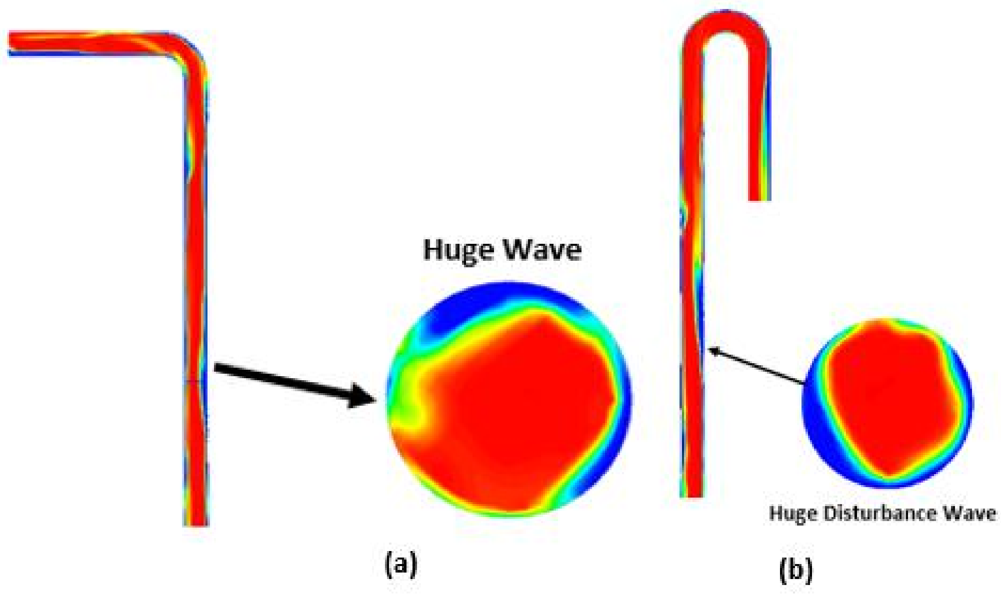

Figure 5.8: Comparison of the contour plots of churn flow in single and double bend geometries at 10 s

5.2.2 Mean Void Fraction

In this study, the mean void fraction is computed from the time averaging of the time series of the cross-sectional average void fraction. Table 5.2 shows the mean void fractions resulting from the data of the churn and slug flow conditions. The mean void fractions observed are within the range reported in previous studies by Costigan and Whalley (1997) and Lowe and Rezkallah (1999) for churn and slug flow conditions. The mean void fractions of churn and slug flows are between 0.7 - 0.9 and 0.3 - 0.42 respectively (Costigan and Whalley, 1997) and (Lowe and Rezkallah, 1999).

Table 5.2: Mean Void Fraction

Flow	V_{sg}**(m/s)**	V_{sl}**(m/s)**	**Mean VF**
Churn	10.3	0.3	0.71
Slug	0.9	0.3	0.32

5.2.3 Probability Density Function 'PDF'

The probability Density Function (PDF) shows the probability that a continuous random variable acquires a specific value at a given observation space. Statistical analysis of the behaviour of the void fraction is one method that can be used to further ascertain flow patterns under normal gravity conditions. It reveals the probability of each void occurring in the fluid. According to Costigan and Whalley (1997) and Lowe and Rezkallah (1999) the void fraction of every flow pattern exhibit a specific PDF signature based on the fluctuation of its fluid phases. In this study, the ksdensity function of MATLAB was used to generate the Probability Density Function (PDF) profiles of the times series of average void fractions of the flow investigated.

Churn flow is characterized by high void fraction with random dips and lows with no clear boundaries between the phases. The low dips are very short lived, hence the unstable nature of the frothy slug. It is therefore characterized by a PDF curve with a single broad peak at high void fractions and a broad tail at the low void fractions. The single peak at high void fraction is indicative of the flow's proximity to annular flow and the broad tail represents the passage of unstable slugs. According to Lowe and Rezkallah (1999), a typical PDF curve of churn flow is between an average void fraction of 0.7 and 0.9. Lowe and Rezkallah (1999) also described this type of flow as transitional flow while it was referred to as fundamentally annular with large disturbance waves by Costigan and Whalley (1997). Figure 5.9a shows the PDF profile of the churn flow condition in this study.

In slug flow on the other hand, the PDF of time series average void fraction has two peaks, one at the low void fractions and another at higher ones. These peaks represents the periodic passage of the two specific features of slug flows; the Taylor bubble at high void fractions and liquid slug at low void fractions. Flow data is distributed in the two peaks of the PDF as movement occurs from predominantly slug at low gas flows to Taylor bubble as the flow gets aerated, and as this happens, the void fraction in both the liquid slug and Taylor bubble rises. PDF profile data generated conforms with the previous study by Ye and Guo (2013). Figure 5.9b shows the PDF profile of the slug flow condition in this study.

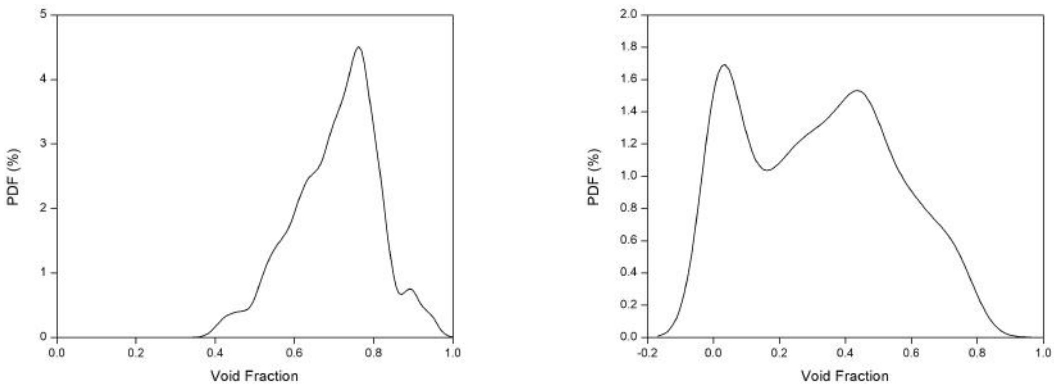

(a) Churn flow

(b) Slug flow

Figure 5.9: PDF profiles

Although results generated conform to standard signatures of PDF for both churn and slug flows as can be found in literature, the PDF profile of the churn flow in double bend is compared with that of the single bend which is the benchmark of this study in Figure 5.10 for confidence purpose as well as highlight if there is any major change to the flow properties before Elbow 1 due to the second Elbow and a good agreement was observed.

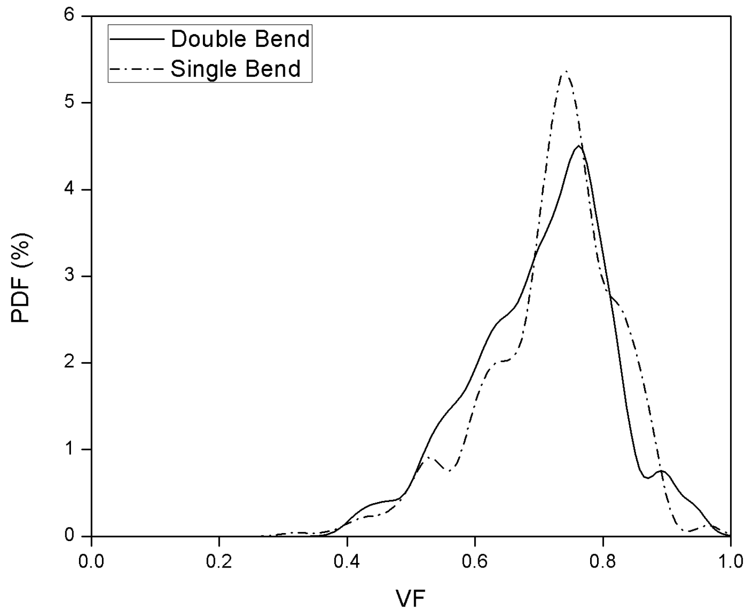

Figure 5.10: Comparison of the PDF profiles of Churn flow in single and double bend geometries before Elbow 1

5.2.4 Power Spectral Density 'PSD'

Averaged spectral coefficients that are independent of time are produced with the Fourier transform in the ANSYS Post-Processing Software, CFD-Post, this is useful to identify the dominant frequency in a signal in various flow regimes. The time domain signals of the cross-sectional averaged void fractions are converted into a frequency domain from which magnitude and PSD of the dominant frequencies are identified. When the PSD displays more than one peak, the frequency with the highest peak is said to be the dominant frequency (Hanafizadeh et al., 2016). PSD has also been used to identify different flow regimes by researchers such as Franca et al. (1991), Liu et al. (2012), Ye and Guo (2013) and Hanafizadeh et al. (2016) amongst others.

Figure 5.11 shows the PSD of the cross-sectional times series of averaged void fraction of the cases studied. The power spectral density of churn flow shows a dominant frequency of between 1.5 and 4Hz as shown in Figure 5.11a, and the maximum amplitude is 0.0063.

According to Ye and Guo (2013), in the case of severe slugging, the PSD of slug flow displays a low and dominant frequency. In this study, at the slug flow condition, the dominant frequency is of between 2 to 3Hz with a maximum amplitude of 0.073. Figure 6.11b shows the PSD of the cross-sectional times series of averaged void fraction in the slug flow condition studied.

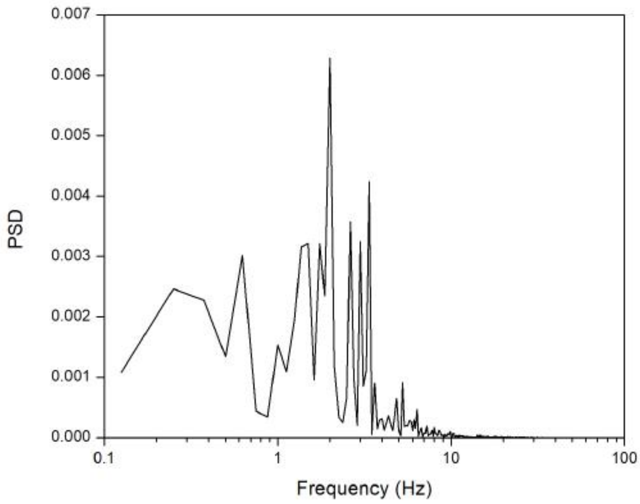

(a) Churn flow

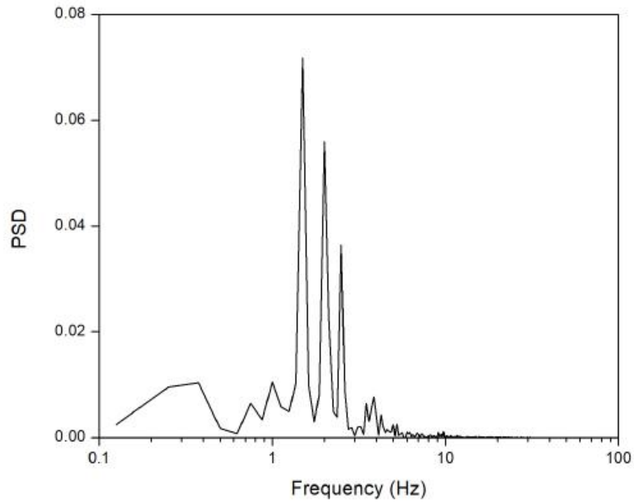

(b) Slug flow

Figure 5.11: PSD profiles

Furthermore, the PSD or magnitude of energy with the dominant frequencies of slug flow is observed to be higher than that of churn flow. The Peak PSD of churn flow is an order of magnitude smaller than that of the slug flow as shown in Figure 5.12. This is in agreement with the studies of Liu et al. (2012) where the time domain signals and power spectrum densities (PSD) of various flow regimes were compared.

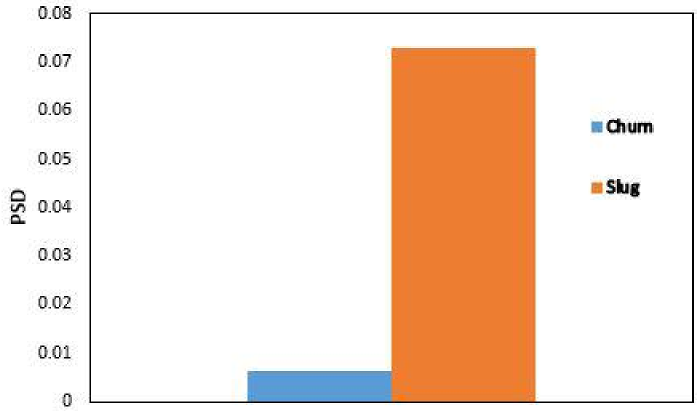

Figure 5.12: Comparison of the highest PSDs of churn and slug flows

The PSD of churn flow in both the single and double bend geometries are also compared in Figure 5.13 to study if the presence of possible variation in the fluctuating signals would have significant on the profile and dominant frequencies. A good agreement is observed in the PSD profile and dominant frequencies are between 1.5 and 4Hz.

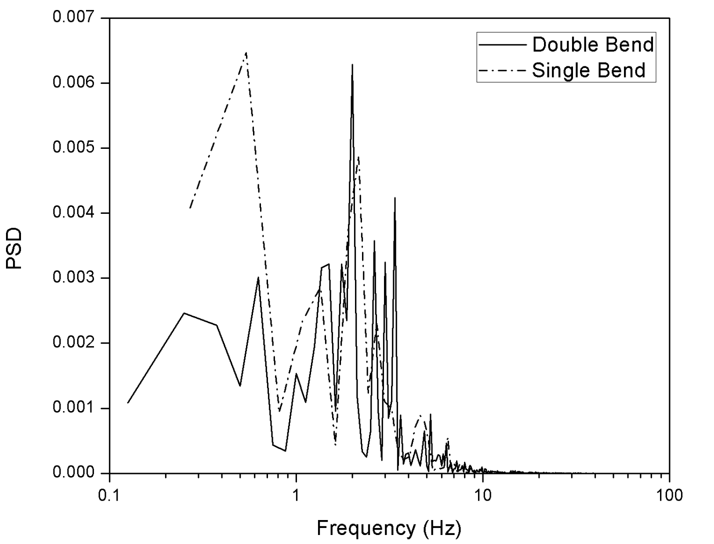

Figure 5.13: Comparison of PSD of Churn flow in single and double bend geometries

5.2.5 Flow Development in Double Bends

Churn Flow

The multiphase flow after Elbow 1 (in the horizontal section) was analyzed to study the flow development towards the second bend. In churn flow, it is observed that most of the liquids fall in the bottom of the horizontal pipe while the gas flows just at the top occupying the remaining space in the pipe. This is due to the effects of gravity and the difference in densities; the density of water is higher than that of air. The contour plots of the cross-sectional averaged void fraction of the flow at 10.5 s is shown in Figure 5.14. The flow pattern observed shows characteristics of wavy stratified flow. As the flow develops, highly aerated bubbles can be seen within the flow. These are liquid waves accumulating in the flow domain but not enough to form liquid slugs. Such characteristics is a sign of the transition state between churn and annular flows. Similar observation was also reported in the works of Asgharpour et al. (2018). Furthermore, as the normalized separation distance increases, a slight but notable difference is observed in the flow development within the horizontal section in all the geometries studied. In Geometry 1 (Figure 5.14a), when L/D is 0 it can be observed that the liquid phase flows through the elbows more as a thin film pushed towards the elbow extrados of elbow 2 and as as the normalized separation distance increased 5, the presence of the liquid phase becomes more pronounced in the horizontal section between Elbows 1 and 2. This can be attributed to the effects of gravity on the flow phases with the flow with the higher density moving at the bottom of the pipe and the lighter gas phase (red patch) moving at the top of the liquid phase. In Geometries 10, 15 and 20, after a distance of about L/D of 5, the liquid phase (blue patch) is observed to be settled and flowing at the bottom of the horizontal pipe. A similar observation and trend is seen in Geometries 2 and 3 (Figures 5.14b and 5.14c).

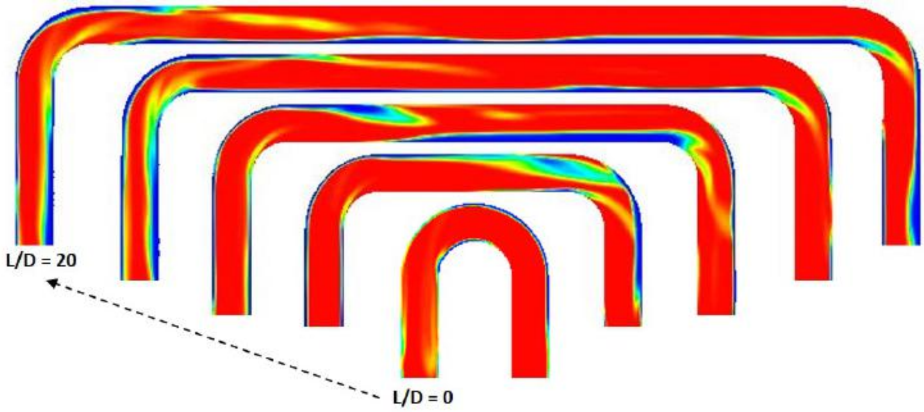

(a) Geometry 1

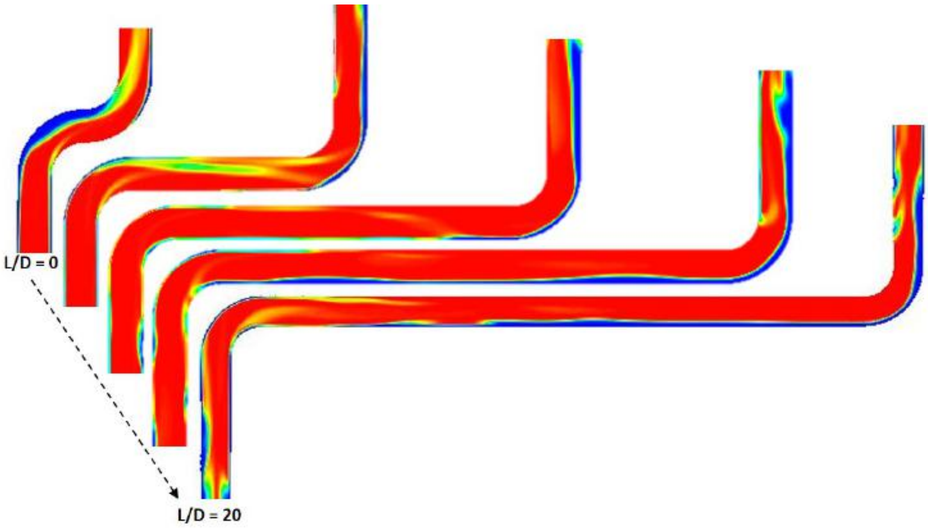

(b) Geometry 2

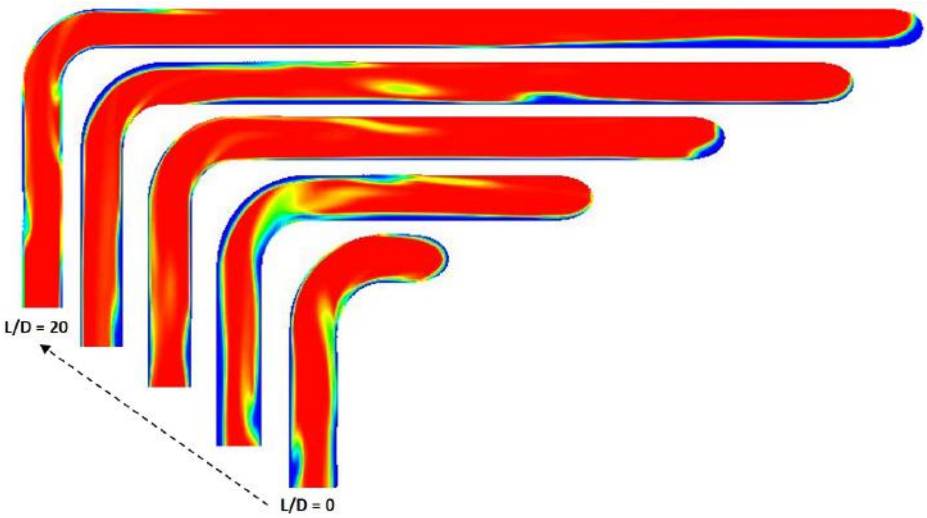

(c) Geometry 3

Figure 5.14: Contour plots of flow in horizontal section in Churn Flow at 10.5 s

Figures 5.15 shows the time series of cross-sectional averaged void fraction of the flow before Elbows 1 and 2 in Geometries 1, 2 and 3. In these plots, the sudden drop in volume fraction can be observed. This indicates the passage of liquid waves as observed in the contour plots above. Some of these waves occupy a large fraction of the pipe section and this is evident when the volume fraction drops as low as 0.2 and 0.45 before Elbows 1 and 2 respectively, at a normalized separation distance of 5 in Geometry 1 (see Figure 5.15). In Geometry 2, the highest drop in volume fraction of about 0.55 was observed when the normalized separation distance is 0 (see Figure 5.16b) while before Elbow 1 the highest drop of about 0.2 is observed at L/D of 10 and 20. In Geometry 3, the highest drop is about 0.45 and can be seen when the normalized separation distance is 10 and 15, before Elbow 1, it is about 0.23 observed at L/D of 10 (see Figure 5.17). It is important to note that at no normalized separation distance and geometry within the time frame investigated is the drop in volume fraction before Elbow 2 equal to or lower than the drop before Elbow 1. Before Elbow 2, the gas volume fractions at every L/D has increased compared to before Elbow 1. This can attributed to the fact that after Elbow 1, there is a more defined interface between the liquid and gas phases due to the change in flow pattern from churn, where the flow is distorted, to wavy stratified flow. Also gravity effects aides the separation of the flow in the horizontal section as L/D increases thereby increasing the gas volume fraction at about every time step.

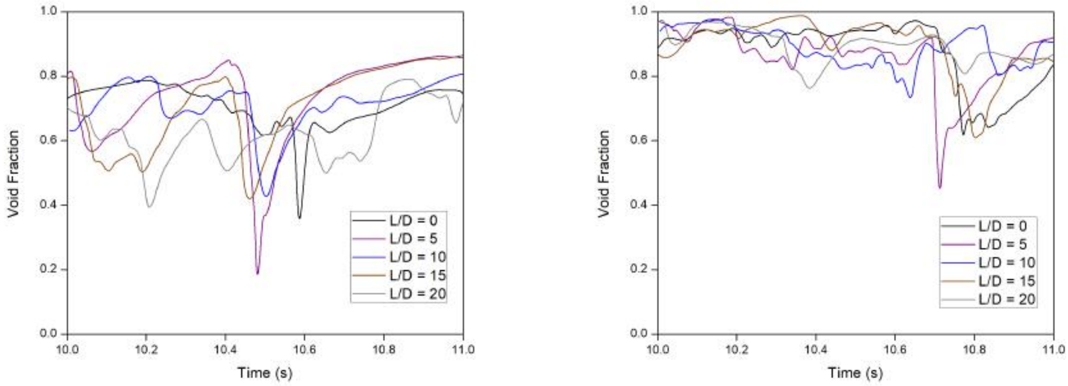

(a) Elbow 1

(b) Elbow 2

Figure 5.15: Comparison of cross-sectional averaged void fraction time series Before Elbow 1 and Elbow 2 in Geometry 1 for Churn flow

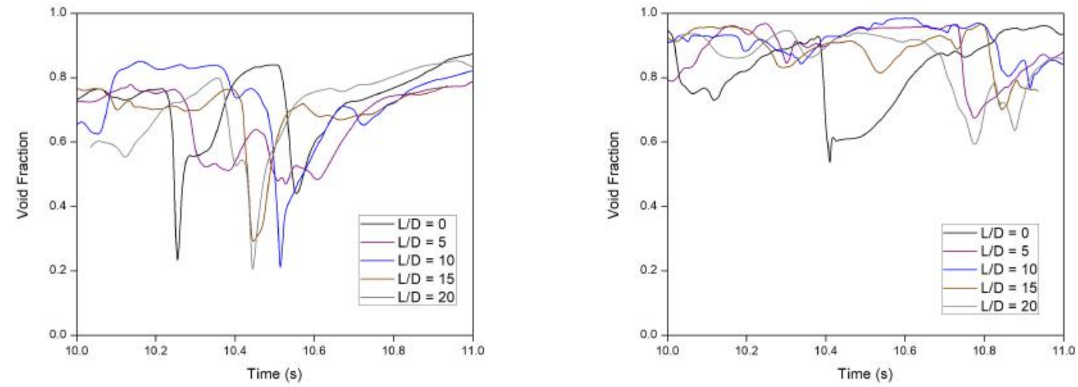

(a) Elbow 1 (b) Elbow 2

Figure 5.16: Comparison of cross-sectional averaged void fraction time series Before Elbow 1 and Elbow 2 in Geometry 2 for Churn flow

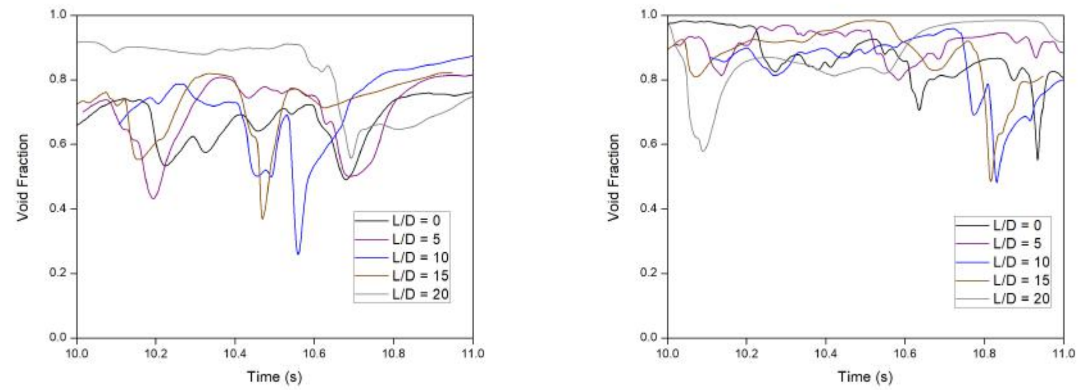

(a) Elbow 1 (b) Elbow 2

Figure 5.17: Comparison of cross-sectional averaged void fraction time series Before Elbow 1 and Elbow 2 in Geometry 3 for Churn flow

The Probability Density Function (PDF) of the cross-sectional averaged times series of the volume fraction are shown in Figures 5.18 to 5.20. Most of these profiles show a curve with relatively broad tails and double peaks; the low one indicative of the high volume fraction of liquid and the highest peak representing the dominant / highest void fraction. Exhibiting two peaks further ascertains the presence of liquid waves or aerated bubbles which indicates the flow is showing some features of slug flow. The broad tail on the other hand is indicative of churn flow and the high peak is the flow's annular flow characteristics. It is therefore safe to conclude that the observed wavy stratified flow exhibits features of the slug/churn - annular transition state. Increasing the normalized separation distance could be a step to further establish this conclusion.

The PDFs of the flows before Elbow 2 was further compared to that before Elbow 1. The peak of the PDF before Elbow 1 appears at about 0.75 while those of before Elbow 2 irrespective of the normalized separation distance and geometry are between 0.85 and 0.95. This further ascertains the claim that the flow is behaving more like annular flow in the horizontal section as the normalized separation distance increases.

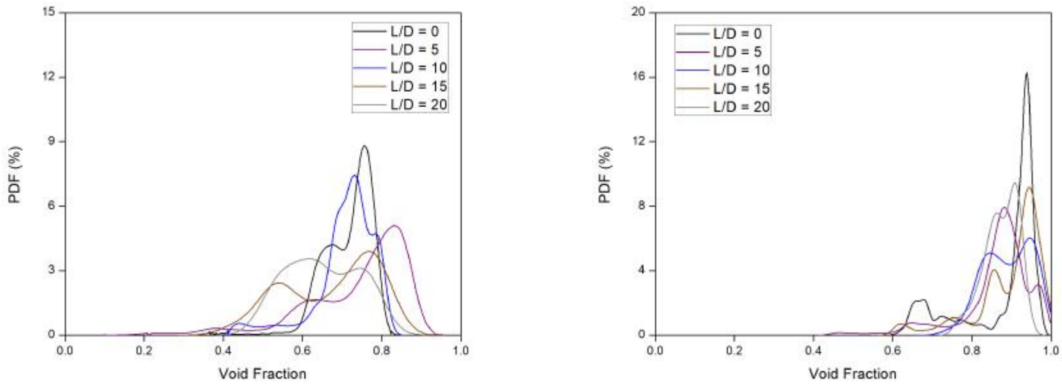

(a) Before Elbow 1 (b) Before Elbow 2

Figure 5.18: PDF of churn flow in Geometry 1

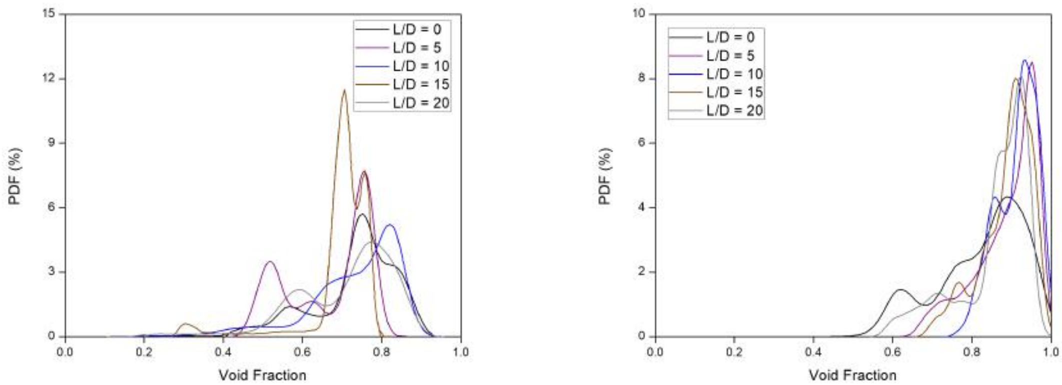

(a) Before Elbow 1 (b) Before Elbow 2

Figure 5.19: PDF of churn flow in Geometry 2

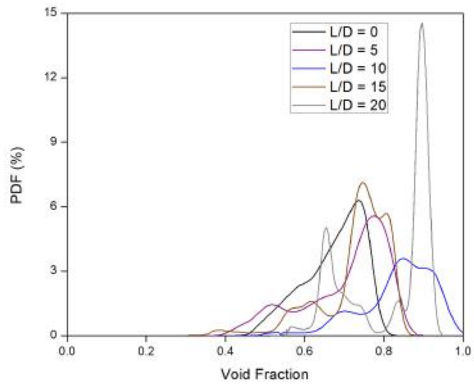

(a) Before Elbow 1

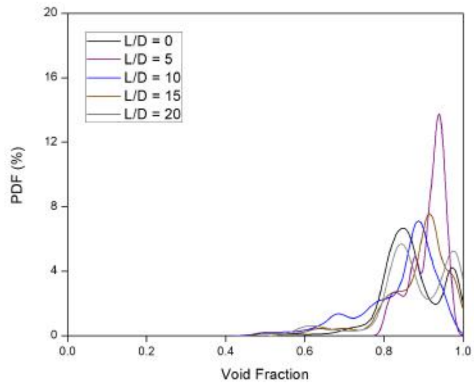

(b) Before Elbow 2

Figure 5.20: PDF of churn flow in Geometry 3

Slug Flow

Similar observation as in churn flow was made in the slug flow, the flow development in the horizontal section seems to differ from that in the vertical section before Elbow 1. However, unlike in churn flow, the features of slug flow such as the Taylor bubbles and liquid slug are still visible in the horizontal section after Elbow 1. Figure 5.21 shows the contour plots of the cross-sectional averaged void fraction of the flow in Geometries 1, 2 and 3. As observed in churn flow earlier, most of the liquid phase (blue patch) occupies the bottom section of the pipe while the gas phase (red patch) remained at the top of the liquid. This is the effect of gravity acting on the fluids, the fluid with the higher density will flow at the bottom of the one with the lesser density. This type of flow can be mistaken for stratified flow, however, the liquid content at different sections of the pipe occupies more than 50% of the flow domain and completely cuts through the gas phase in some parts. These features are indicative of typical slug flows in horizontal pipes where the liquid slug at the bottom of the pipe cuts through the gas phase at different sections to form gas pockets known as the Taylor Bubbles just as in the vertical section before Elbow 1, although these are bigger gas bubbles. These observations are similar to that of researchers such as Kesana et al. (2013b) and Kesana et al. (2013a) who modelled slug flow in horizontal pipes. An increase in the normalized separation distance aides better development and separation of the flow, in Figure 5.17, it is seen that after L/D of 5, the presence of the liquid slug and Taylor bubble becomes obvious. Figure 5.21 is the contour plots of the flow in all cases studied after 10.5 s.

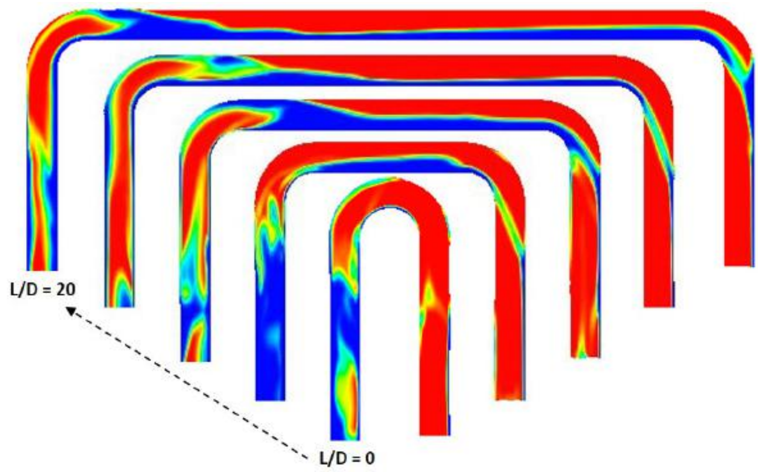

(a) Geometry 1

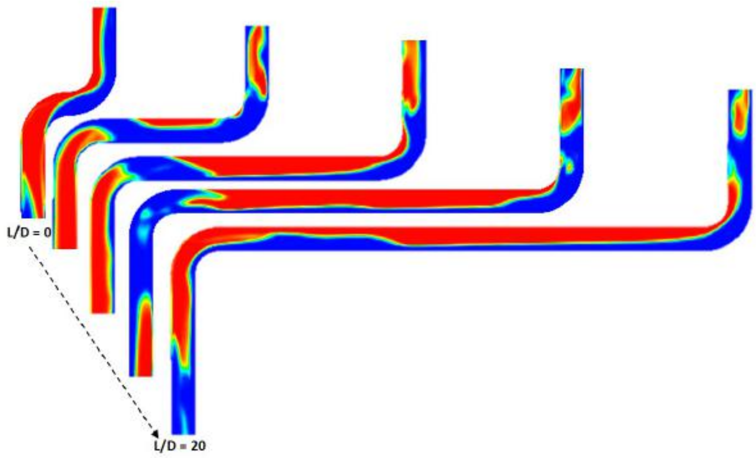

(b) Geometry 2

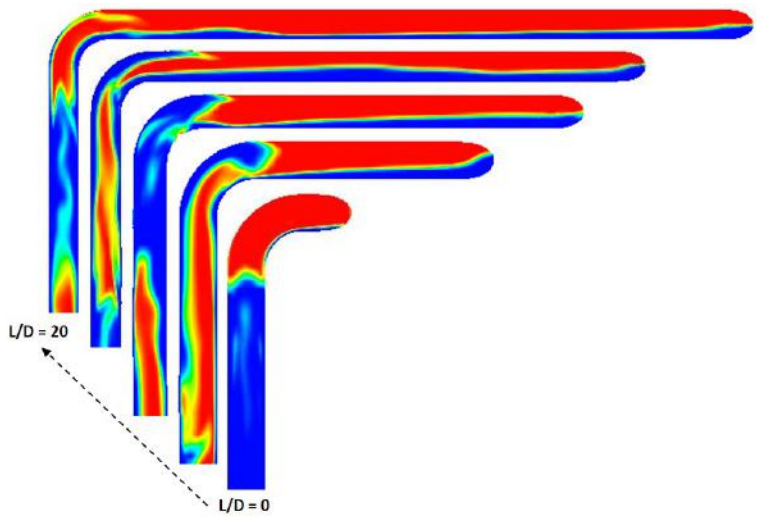

(c) Geometry 3

Figure 5.21: Contour plots of flow in horizontal section in Slug Flow at 10.5 s

The time series of cross-sectional averaged void fraction for slug flow are shown in Figures 5.22 to 5.24. The drop in the volume fraction to zero or almost zero indicates the passage of the liquid slugs while the high volume fraction represents the passage of the alternating gas pockets across the monitoring surface. In Geometry 1, when the normalized separation distance is 5, 15 or 20 the horizontal pipe section (Before Elbow 2) is occupied by about 50% of each of the two phases. While in L/D of 10, the volume fraction drops to as low as 0.3. It can be seen that there are more drops in the volume fraction in the vertical section (Before Elbow 1) within the reference time compared to the horizontal section, this indicates that the Taylor bubbles in the vertical section are smaller in size compared to those in the horizontal pipe between Elbows 1 and 2. Hence, the average void fractions in the horizontal section (Before Elbow 2) are higher than the vertical(Before Elbow 1). Similar observations can be made in Geometries 2 and 3 as shown in Figures 5.23 and 5.24. Just as observed in churn flow, gravity effects make the larger percentage of the liquid phase with the higher density to settle and separate out at the bottom of the pipe thereby increasing the liquid volume fraction at about every time step before Elbow 2 as L/D increases compared to the vertical flow domain before Elbow 1.

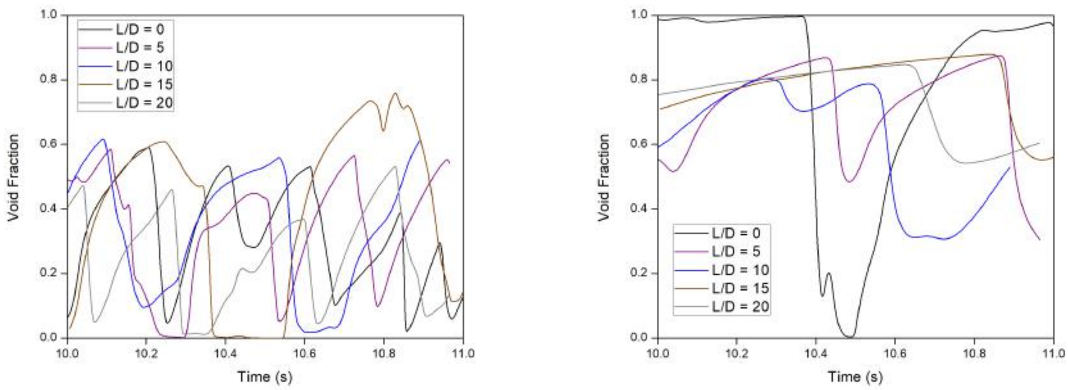

(a) Elbow 1

(b) Elbow 2

Figure 5.22: Comparison of cross-sectional averaged void fraction time series Before Elbow 1 and Elbow 2 in Geometry 1 for Slug flow

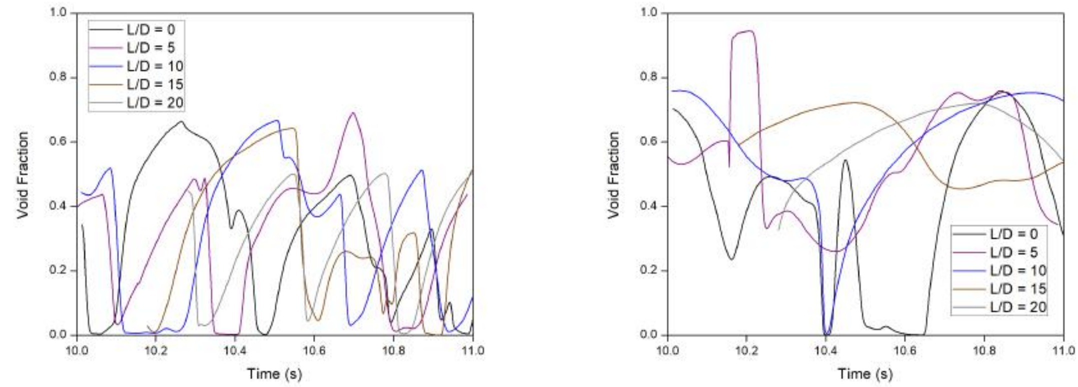

(a) Elbow 1 (b) Elbow 2

Figure 5.23: Comparison of cross-sectional averaged void fraction time series Before Elbow 1 and Elbow 2 in Geometry 2 for Slug flow

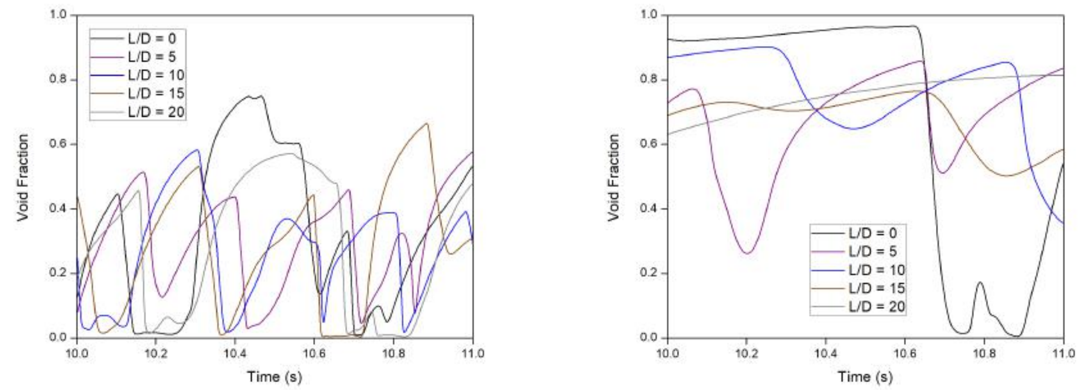

(a) Elbow 1 (b) Elbow 2

Figure 5.24: Comparison of cross-sectional averaged void fraction time series Before Elbow 1 and Elbow 2 in Geometry 3 for Slug flow

The PDF of the flow in the horizontal pipe section shows the typical features observed in that of slug flow with two peaks, one at the low and high void fractions respectively. Figure 5.25 to 5.27 show the PDF profiles of slug before Elbow 2 in all geometries studied compared to the PDF of the flow before Elbow 1. In Geometry 1, the peaks of the curve changes as the normalized separation distance (L/D) changes, the flow pattern however remained the same. As L/D increases, the flow develops better. This is more obvious in the noticeable shift in the PDF peak at the low void fractions from 0.01 to 0.3 at normalized separation distances of 0, 5 and 10, and finally to 0.55 at L/D of 15 and 20. The peak of the high void fraction fluctuates between 0.76 and

0.82 as the flow tends towards attaining equilibrium between normalized separation distances of 5 and 20. There is little or no shift in the low and high void fractions before Elbow 1 compared to before Elbow 2. In Geometry 2 on the other hand, the flow is more distorted before Elbow 2 compared to Elbow 1 as the normalized separation distance increases. At L/D of 20, the flow is already behaving more like churn flow with the profile showing a broad tail and a single void fraction peak at 0.7 as described in the works of Costigan and Whalley (1997), Lowe and Rezkallah (1999) and Parsi et al. (2016a) amongst others. However, between the L/D 0 and 15, the slug flow development can be tracked as both the low and high void fraction peaks move from 0.01 and 0.45 at L/D of 0 to 0.5 and about 0.76 at L/Ds of 10 and 15 respectively. It is also seen that the PDF curve at the normalized separation distance of 0 unlike other L/Ds is similar to that obtained before Elbow 1. In Geometry 3, a similar behaviour to that of Geometry 2 at a normalized separation distance of 20 is observed, the PDF profile has a broad tail and a single peak which is the feature of a typical churn flow. The peaks of both the low and high void fractions are also different in the horizontal section compared to the vertical section before Elbow 1. This is indicative of the transition taking place in the flow development as it navigates the bend into the horizontal section and as the normalized separation distance increased from 0 to 20. The peaks of the PDF profiles at normalized separation distance of 0 in geometries 1 and 3 before Elbow 2 are also similar. The peak PDF at the high and low void fractions are higher before Elbow 2 compared to before Elbow 1, this is due to the increase in the volume fraction of the gas phase before Elbow 2.

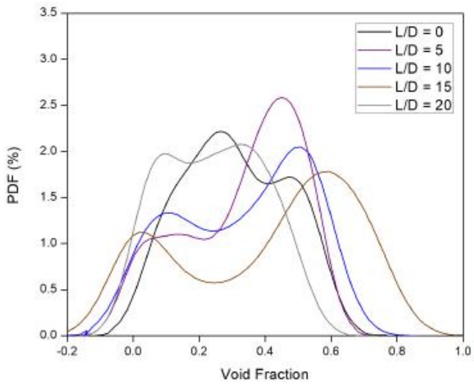

(a) Before Elbow 1

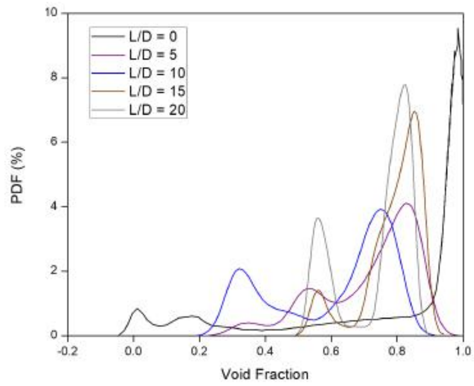

(b) Before Elbow 2

Figure 5.25: PDF of slug flow in Geometry 1

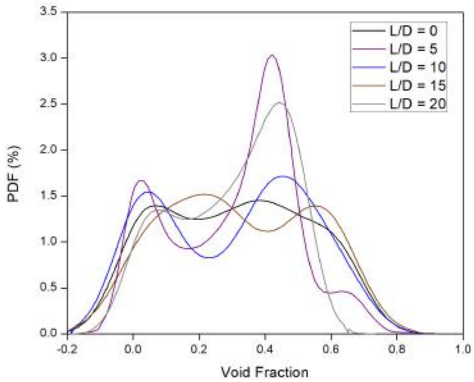

(a) Before Elbow 1

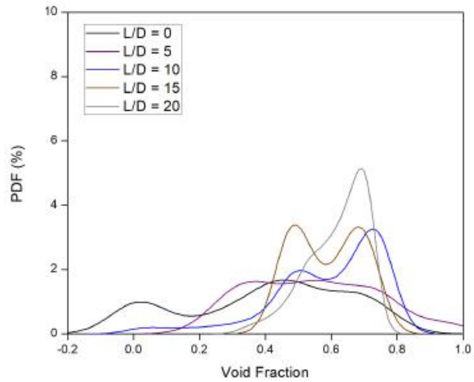

(b) Before Elbow 2

Figure 5.26: PDF of slug flow in Geometry 2

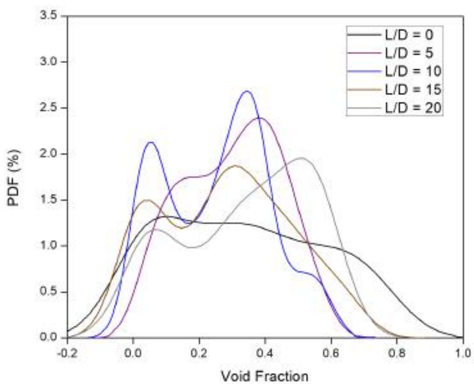

(a) Before Elbow 1

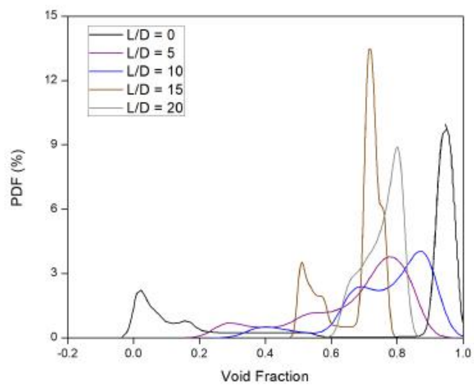

(b) Before Elbow 2

Figure 5.27: PDF of slug flow in Geometry 3

Mean Void Fraction Before Elbow 1 and Elbow 2

Table 5.3 and 5.4 show the mean void fractions before Elbow 1 compared to before Elbow 1 in churn and slug flow respectively. It can be observed from Table 5.3 that the average void fraction of the churn flow increased from 0.71 before Elbow 1 to between 0.82 and 0.91 after Elbow 1 (before Elbow 2), this is due to the separation and effects of gravity becoming more prominent in the horizontal pipe section compared to the vertical upstream pipe. Also, it is important to note that there is very minimal difference in the mean void fraction across all normalized separation distances and geometries. This means in the downstream horizontal pipe after Elbow 1 (before Elbow 2), churn flow separates into an almost stable flow pattern. In Table 5.4, the mean void fraction in slug flow shows different peaks in different geometries. In Geometry 1, the mean void fraction increased from 0.31 to between 0.74 and 0.79, in Geometry 2 it increased to between 0.41 and 0.62 while in Geometry 3, it increased to between 0.67 and 0.75. Unlike churn flow, the stability of slug flow after Elbow 1 (before Elbow 2), differs with geometry. The mean void fraction is highest in Geometry 1 and lowest in Geometry 2, Geometry 3 is in-between.

In a nut shell, there is a massive increase in the mean void fraction of slug flow compared to churn flow before Elbow 2. In churn flow, an increase of about 28% in is observed in all the cases studied while in slug flow there is an increase of between 87.5% and 147%, 28% and 94% and 109% and 134% in Geometries 1, 2 and 3 respectively.

Table 5.3: Comparison of Mean Void Fraction in churn flow Before Elbow 1 (E1) and Before Elbow 2 (E2)

	Geometry 1		**Geometry 2**		**Geometry 3**	
	E1	**E2**	**E1**	**E2**	**E1**	**E2**
L/D = 0	0.71	0.88	0.72	0.82	0.70	0.87
L/D = 5	0.73	0.86	0.67	0.89	0.70	0.91
L/D = 10	0.71	0.89	0.72	0.91	0.72	0.84
L/D = 15	0.71	0.89	0.70	0.88	0.72	0.88
L/D = 20	0.65	0.87	0.71	0.86	0.81	0.88

Table 5.4: Comparison of Mean Void Fraction in Slug flow Before Elbow 1 (E1) and Before Elbow 2 (E2)

	Geometry 1		**Geometry 2**		**Geometry 3**	
	E1	**E2**	**E1**	**E2**	**E1**	**E2**
L/D = 0	0.32	0.78	0.31	0.41	0.33	0.67
L/D = 5	0.33	0.72	0.31	0.55	0.30	0.67
L/D = 10	0.33	0.60	0.31	0.59	0.26	0.74
L/D = 15	0.40	0.79	0.32	0.59	0.28	0.68
L/D = 20	0.25	0.74	0.20	0.62	0.28	0.75

5.3 Erosion in Double Bends

5.3.1 Comparison of Erosion in Single Bend and Elbow 1 in Churn Flow

Figure 5.28 shows the comparison of the erosion contour in single bend analysis, when the carrier fluid is churn, with Elbow 1 of the double bend Geometries in the present study with the same flow condition. Elbow 1 at a normalized separation distance of 0 in each geometry has been selected for this comparison. It is seen that the elbow extrados is subjected to the most erosion. This further ascertains the capability of the model employed for this study. However there are discrepancies in the location of maximum erosion. Although concentrated on the elbow extrados as stated earlier, in Geometry 1, maximum erosion location is observed at about 45° into the elbow, this is similar to that observed in the single bend analysis but does not spread to the sides of the bend as much. In Geometry 2, maximum erosion location is observed towards the elbow outlet with erosion spreading from about 45° into the elbow. In Geometry 3, maximum erosion location is at about 50° into the elbow.

The erosion patterns over time in the other normalized separation distances are better analysed in the next section under double bends.

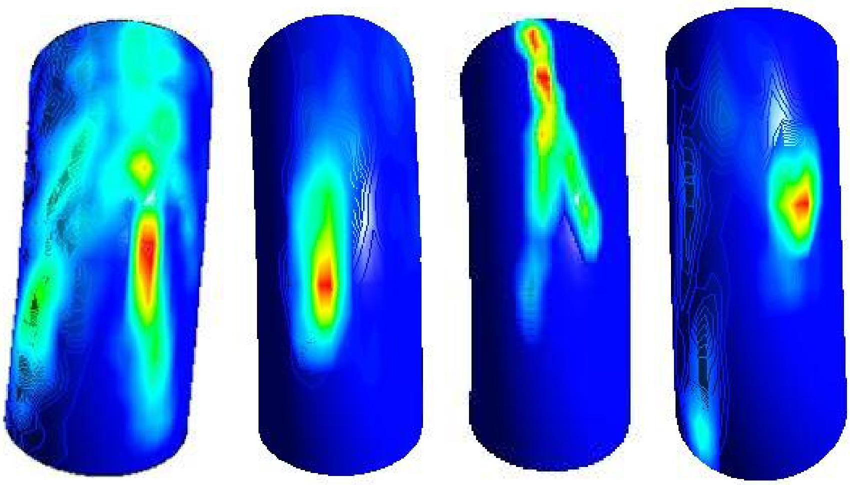

(a) Single Bend (b) Geometry 1 (c) Geometry 2 (d) Geometry 3

Figure 5.28: Comparison of erosion contour in single bend with Elbow 1 in churn flow

Figure 5.29 is the comparison of the average erosion rates in Elbow 1 of Geometries 1, 2 and 3 compared to that of the single bend analysis. In Geometry 1 and 3, the peak erosion rate in the single bend is similar to when L/D is 5, and in Geometry 2, it is similar to that of L/D of 15. Erosion peaks at other normalized separation distances are observed to be higher. The presence of a second bend and normalized separation distance has a significant effect on the erosion rates in Elbow 1 in double bend compared to the single bend analysis. The average peak erosion rate in Elbow 1 is about 115%, 50% and 88% higher in Geometries 1, 2 and 3 than the peak erosion rate in the single bend geometry.

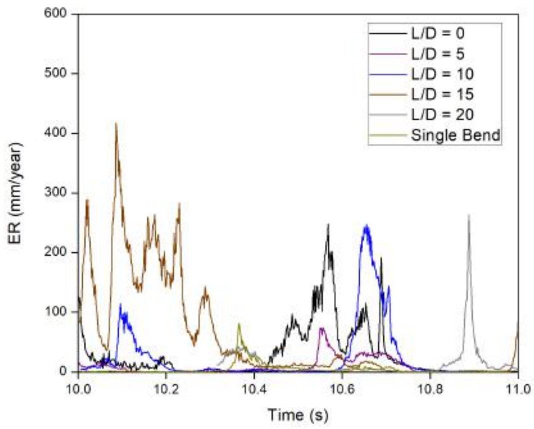

(a) Geometry 1

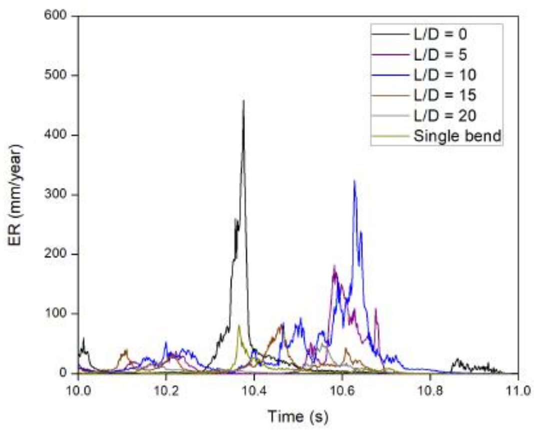

(b) Geometry 2

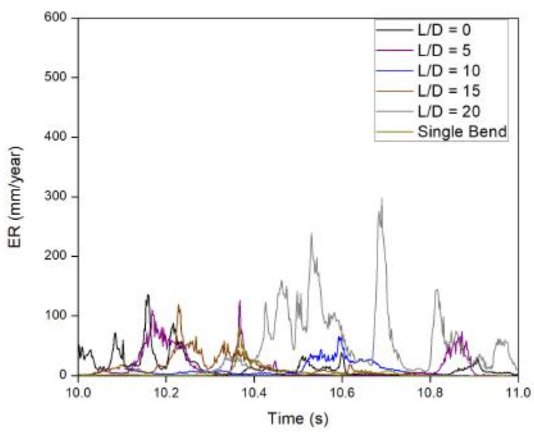

(c) Geometry 3

Figure 5.29: Comparison of erosion rates in single bend with Elbow 1 in churn flow

5.3.2 Erosion Patterns in Double bends

Due to the transient nature of the flow, the erosion pattern in the elbow is observed to equally change with time. Figures 5.30 to 5.32 show the erosion contour in churn flow for all geometries under investigation. The erosion pattern in each group (group of 3) of the contour plots (either Elbow 1 or Elbow 2) is taken at intervals of 0.5 s between 10 s and 11 s respectively. The red patch(es) of the contour plot is the maximum erosion location and the arrows indicate the direction of flow. In all cases studied, the erosion location and pattern though concentrated at the elbow extrados changes as the flow time changes. For the flow times highlighted, similar erosion pattern can be observed in Elbow 1 across all geometries and the changes with time also remained within the same range. In Elbow 1 of Geometry 1, at 10 s, erosion occurred more at about 45° on the elbow extrados and spreads towards the elbow outlet except for L/D of 15 in which the elbow inlet till about 45° into the elbow is subjected to most erosion. Similar patterns are observed at a flow time of 10.5 s but at 11 s, the erosion location becomes concentrated between 45° and 50° into the elbow at all normalized separation distances with the maximum erosion location occurring at the 45° mark except for L/D of 20 where the maximum erosion is towards the elbow outlet. This is an indication that irrespective of the change in L/D, Elbow 1 will be subjected to the most erosion between 45° and 50°. This is in agreement with the results presented by Parsi et al. (2015b) where the maximum erosion location was observed 45° into the elbow at the extrados. A similar observation is made in the Elbow 1 of Geometries 2 and 3 as well.

The erosion pattern and behaviour in Elbow 2 on the other hand differs with Geometry, normalized separation distance as well as time. Although just like Elbow 1, the elbow extrados is also subjected to the most erosion. In Geometry 1, at L/D of 0, the maximum erosion is observed at the elbow inlet with the erosion spreading across the elbow extrados towards the outlet. As L/D increased to 5, the erosion pattern becomes more concentrated and maximum erosion location is observed at about 40° into the elbow at 10 s. The location moves towards the elbow outlet at flow times of 10.5 s and 11 s. At L/D of 10, 15 and 20, maximum erosion location is observed half way into the elbow and spreads towards the elbow outlet. In a nutshell, after L/D of 5 Elbow 2 will be subjected to the most erosion damage towards the elbow outlet from about 45° into the bend. In Geometry 2, unlike the Geometry 1, at L/D of 0, the elbow outlet is subjected to the most damage due to sand erosion. As L/D increases, erosion becomes more prominent at the both sides of the elbow. This becomes more concentrated at the left side of the elbow extrados with the maximum erosion occurring about 45° to 50° into the elbow, and at L/D of 20, erosion is observed to spread across the elbow extrados and the maximum erosion location has moved towards the elbow inlet. Hence, with an increase in the normalized separation distance, erosion location behaviour in Elbow 2 behaves in contrast to that of Geometry 1. Just like the two other geometries, erosion occurs at the extrados of Elbow 2 in Geometry 3. And erosion location changes with every corresponding change in the normalized separation distance. At L/D of 0, due to the orientation of the elbow, erosion occurs at the bottom section of the bend but maximum erosion is observed at the top end of the elbow outlet. At L/D of 5, erosion location becomes more concentrated on the elbow extrados and maximum erosion location is also observed at about 45° into the elbow at 11 s. At L/D of 10 when the flow times are 10 s and 10.5 s, the erosion location is observed about half way into the elbow with the region of maximum erosion spreading to the sides of the top and bottom of the elbow. At 11 s, erosion is concentrated at the bottom of the elbow and maximum erosion occurred towards the elbow outlet. Furthermore, at L/D of 15 and 20, the elbow inlet is subjected to the most erosion, it spreads from the inlet to about 35° into the elbow at 10 s and 10.5 s and at 11 s, it becomes more prominent across the elbow extrados from bottom to top.

In churn flow, it is observed that erosion occurred more at the extrados of both Elbows 1 and 2, although it also spreads towards both sides of the elbows, especially in Elbow 1. Furthermore, irrespective of the instantaneous change in flow properties, the maximum erosion remained at the extrados of both elbows. In Elbow 2, as the normalized separation distance (L/D) increases, the maximum erosion location moves towards the elbow outlet in Geometry 1. In Geometry 2, erosion cuts across the whole elbow extrados and in Geometry 3, a similar shift in the erosion pattern at the extrados of Geometry 1 was observed. The longer the flow time, the more concentrated the erosion location becomes in both elbows across all geometries.

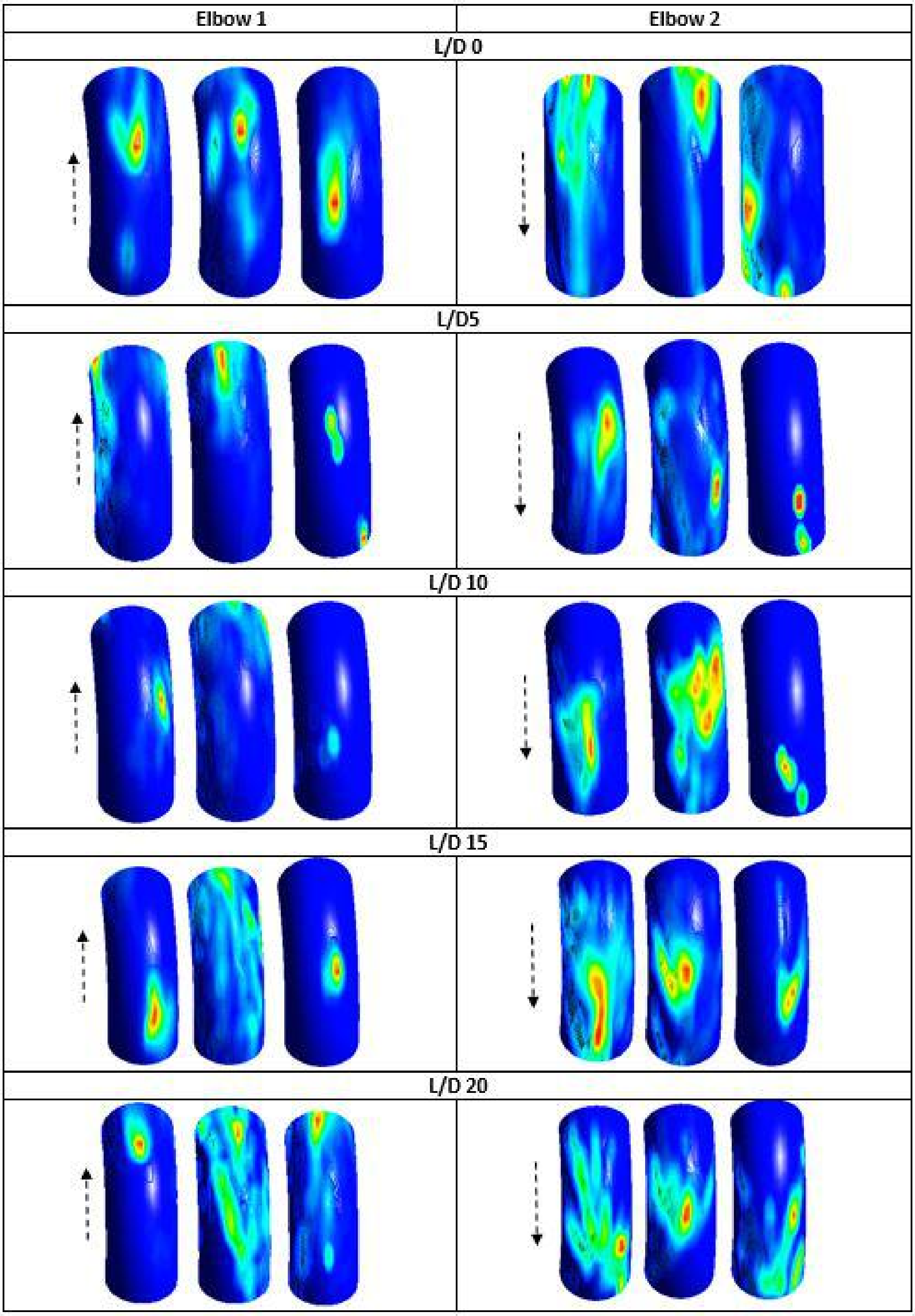

Figure 5.30: Erosion Pattern in Churn flow Geometry 1 (Each group at intervals of 0.5 s from 10 s to 11 s)

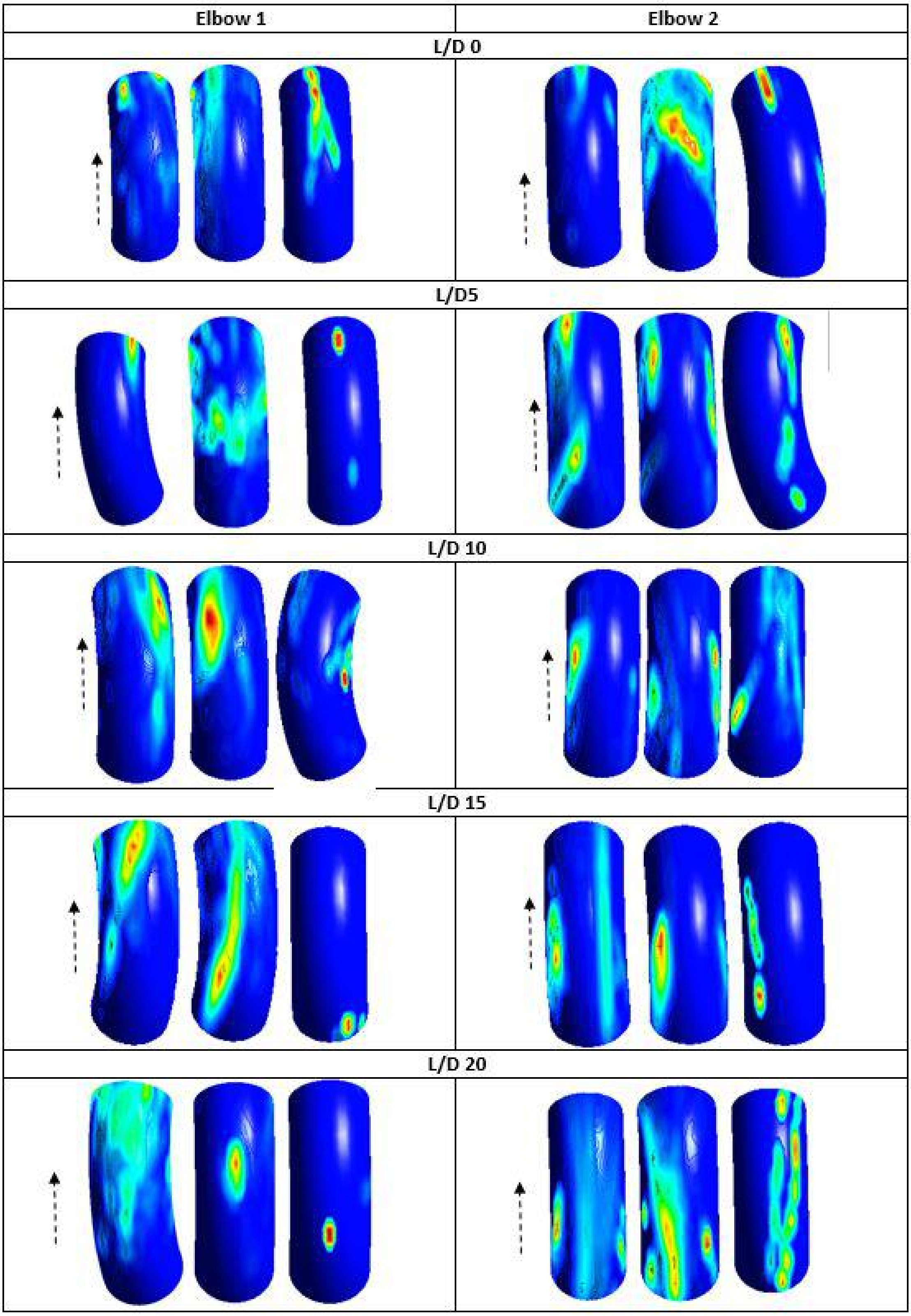

Figure 5.31: Erosion Pattern in Churn flow Geometry 2 (Each group at intervals of 0.5 s from 10 s to 11 s)

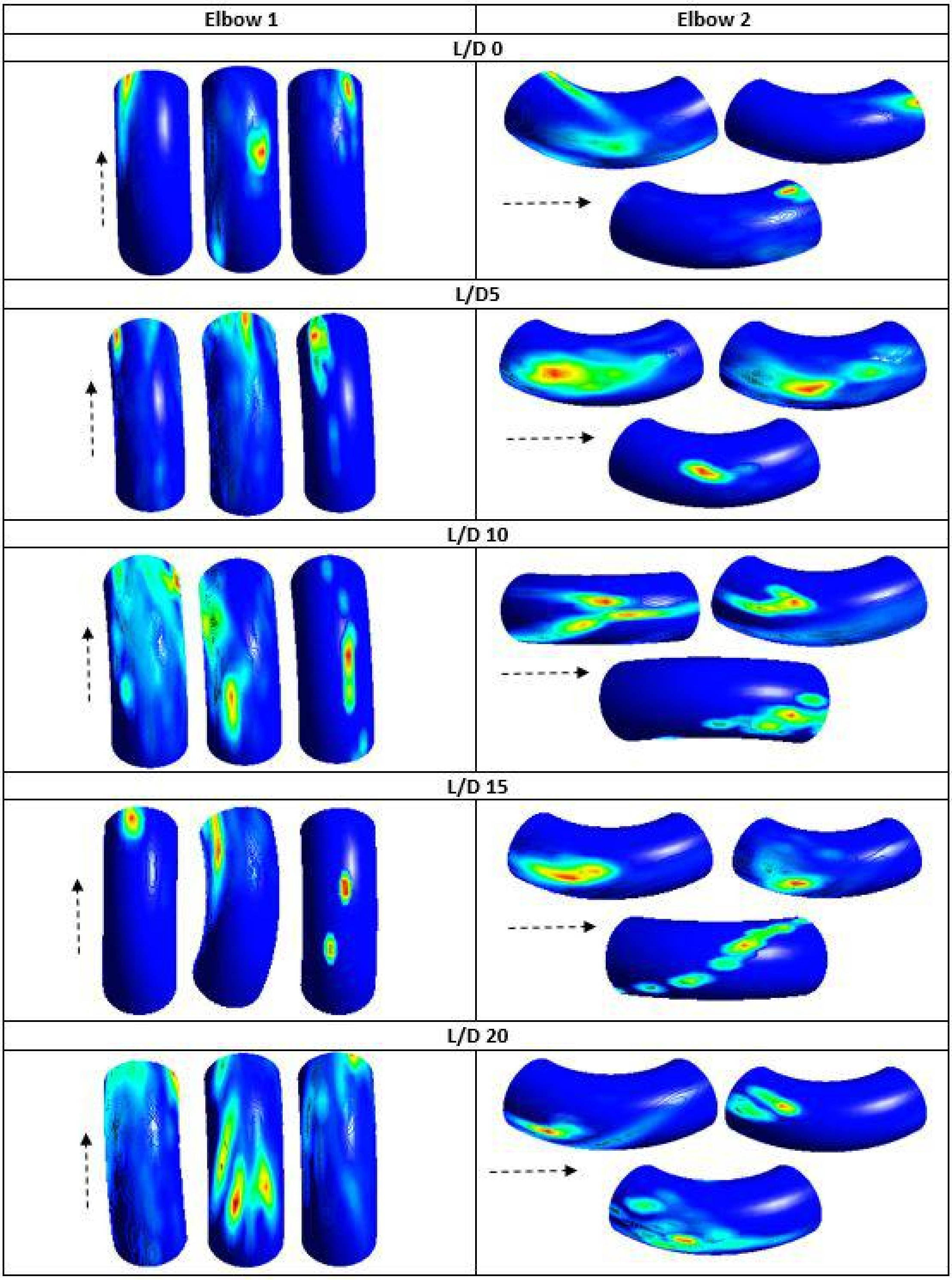

Figure 5.32: Erosion Pattern in Churn flow Geometry 3 (Each group at intervals of 0.5 s from 10 s to 11 s)

Erosion pattern is observed to behave differently in slug flow to churn flow, erosion occurs more in the elbow intrados with little or no spread to the sides of both Elbows 1 and 2 in slug flow. Figures 5.33 to 5.35 show erosion contours in slug flow for all geometries studied. The contour plots have the same time intervals as those of churn flow. In Geometry 1 (Figure 5.33), the intrados of Elbow 1 is subjected to the most erosion damage with the maximum erosion occurring at more than one location. At L/D of 0, maximum erosion location is observed at both the elbow inlet and outlet when flow time is 10 s. This becomes concentrated towards the elbow outlet at 10.5 s and spreads to the side of the elbow from the elbow inlet to about 45° into the elbow at 11 s. Same fluctuation is observed as the normalized separation distance increased with the erosion location remaining in the elbow intrados, maximum erosion location moved to the sides and concentrated towards the elbow inlet at 11 s. In Elbow 2, erosion occurs more at the elbow intrados. At L/D of 0, erosion is observed to spread from the elbow inlet till about 45° just across the intrados. Similar behaviour is observed at L/D of 10 however the maximum erosion location has become more concentrated at the elbow inlet with few other locations within the intrados. As L/D increased further, the location subjected to erosion damage remain at the elbow inlet spreading to about 40° into the elbow and the maximum erosion location is at the elbow inlet.

In Geometry 2 (Figure 5.34) on the other hand, although the erosion location does not seem to be as stable as that of Geometry 1, it could be inferred that the intrados of Elbow 1 is also subjected to the most erosion damage. In Elbow 2 on the other hand, erosion occurs more at the sides of the elbow and gets more concentrated towards the elbow inlet as the normalized separation distance increased. When L/D is 0, erosion occurs more on the sides at about half way into the elbow, this location moved towards the elbow inlet as time increased from 10 s to 11 s. At L/D of 5, the erosion location spreads from the side of the elbow across the extrados, this becomes concentrated at the side of the elbow at 11 s and the maximum erosion location is observed at about 20° from the elbow inlet. Similar behaviour and location is observed at L/D of 10 and 15, and at L/D of 20, at flow times 10 s and 10.5 s the erosion location is concentrated at the sides of the elbow and it is seen to spread across the elbow in patches at 11 s almost becoming independent of time.

Furthermore, in Geometry 3 (Figure 5.35), just like Geometries 1 and 2, the intrados of Elbow 1 remained subjected to the most erosion damage. While in Elbow 2, erosion location is dependent on the change in the normalized separation distance and time. At L/D of 0, when the flow time is 10 s, erosion occurs at bottom section of the bend towards the elbow outlet. The location of maximum erosion moved to about half way into the elbow at 11 s with erosion spreading towards the elbow extrados. At L/D of 5, the erosion location remained at the bottom of elbow but has moved towards the elbow inlet and maximum location observed at about 30° from the inlet. The erosion location becomes more prominent and spreads towards the elbow outlet as time increased to 11 s. At 11 s, it is already almost spreading across the whole elbow length and location of maximum erosion is about 60° from the elbow inlet. When L/D is 10, erosion had spread across the whole elbow length, though remaining at the bottom of the elbow but spreading towards the elbow intrados towards the outlet and the maximum erosion location is at the elbow inlet. Similar behaviour is however seen when the normalized separation distance is 15, maximum erosion location now spreads from the elbow inlet to about 50° into the elbow. Maximum erosion location is observed to spread from about 30° into the elbow to the elbow outlet and the erosion location remains more defined at the bottom of the elbow. This could be as a result of the effects of gravity having more influence on the particles in the orientation of Elbow 2 in Geometry 3. Most of the particles tend to settle at the bottom of the elbow and are dragged through by the fluid.

In summary, it is observed that unlike churn flow, with an increase in the normalized separation distance erosion in slug flow occurred more at the intrados of Elbows 1 and 2 in Geometry 1 with the maximum erosion location remaining towards the inlet of Elbow 2. While in Geometry 2 it occurs more on the sides of the elbows, here the maximum erosion location is also more or less at the inlet region of Elbow 2. In Geometry 3, erosion occurs more at the intrados of Elbow 1 but the extrados and bottom section of Elbow 2, maximum erosion location spreading towards the elbow outlet.

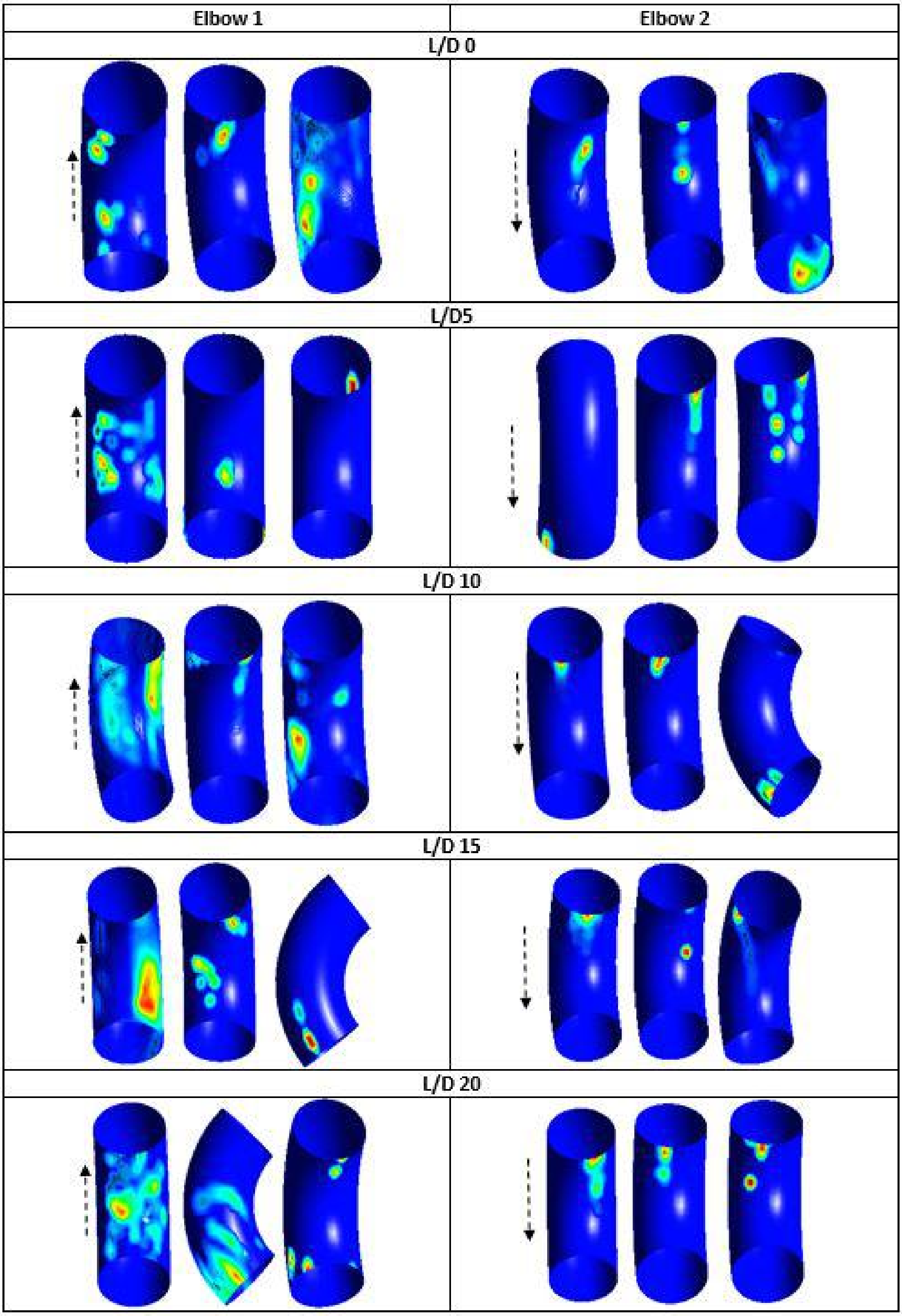

Figure 5.33: Erosion Pattern in Slug flow Geometry 1 (Each group at intervals of 0.5 s from 10 s to 11 s)

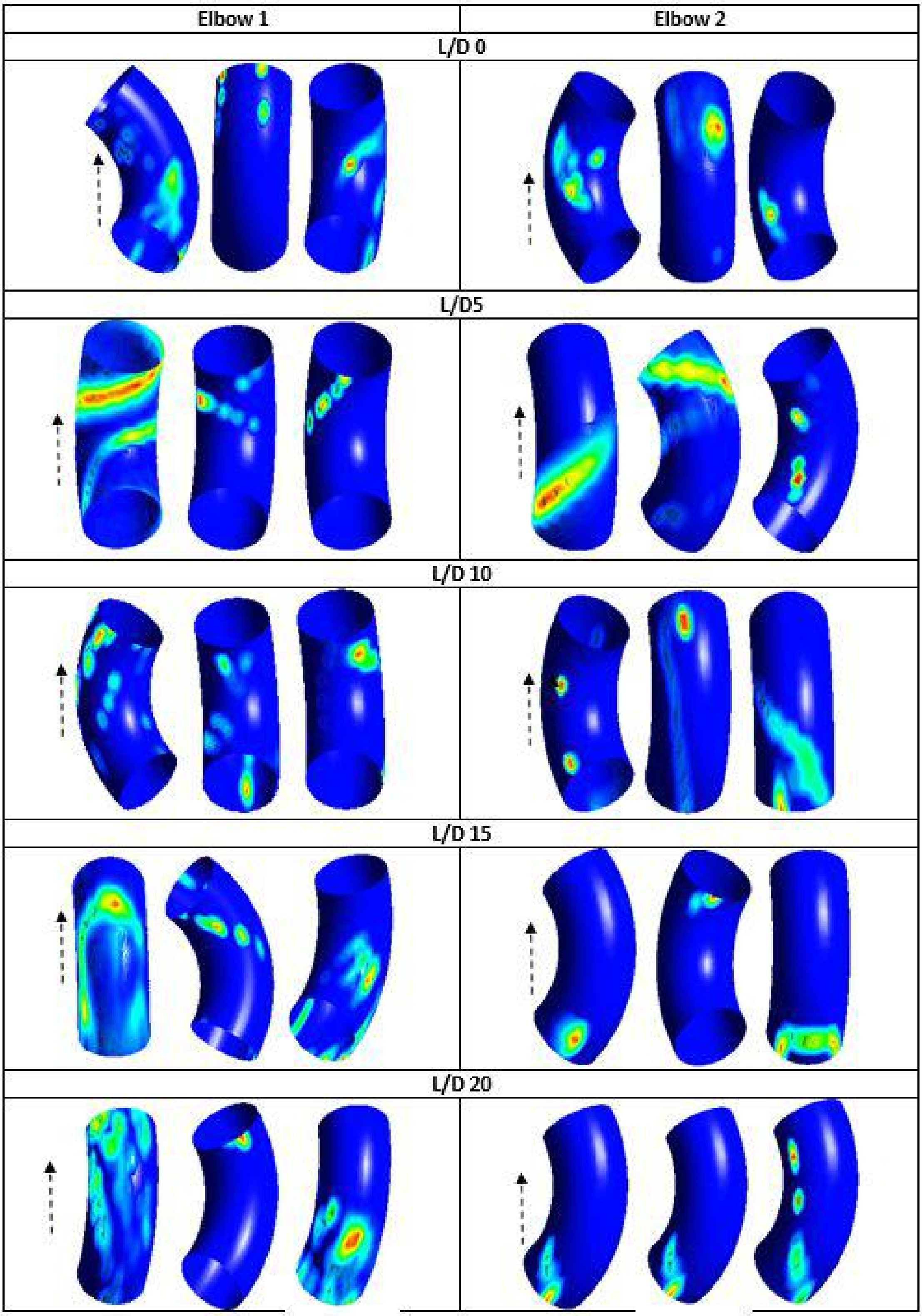

Figure 5.34: Erosion Pattern in Slug flow Geometry 2 (Each group at intervals of 0.5 s from 10 s to 11 s)

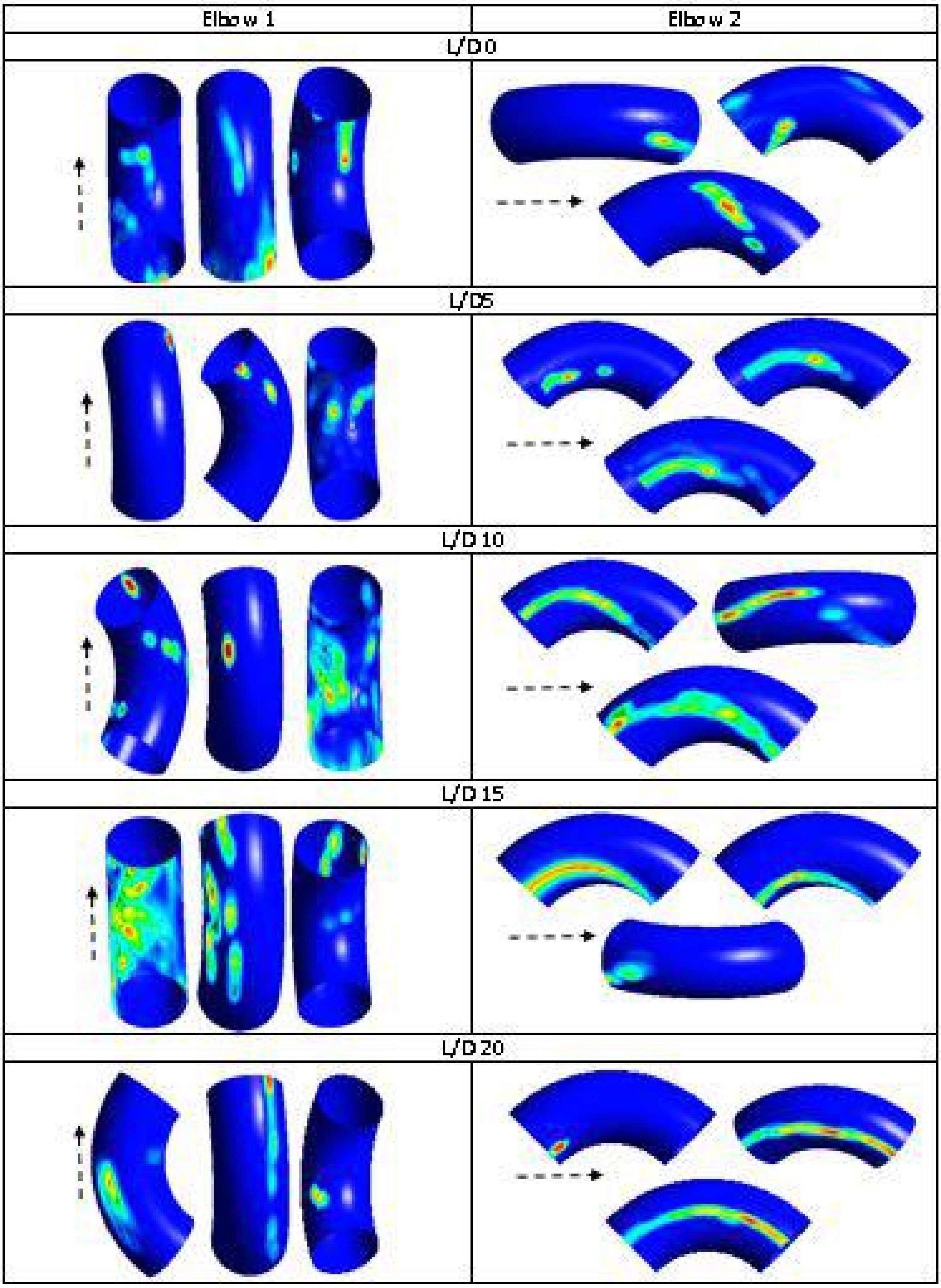

Figure 5.35: Erosion Pattern in Slug flow Geometry 3 (Each group at intervals of 0.5 s from 10 s to 11 s)

5.3.3 Sand Particle Concentration

Below is the contour of the predicted sand particle concentration in each of the bends. It can be seen in Figures 5.36 and 5.37 that the concentration of sand particles has some sort of relationship with the erosion rates at the pipe bends. This is because the erosion location and areas of the elbows where the sand particles get concentrated are similar. And according to previous studies and literature search, sand particle concentration is one of the determining factors in pipe erosion. In the figures below, the erosion pattern and the corresponding sand particle concentration contours are placed side by side at a particular flow time. The flow time shown here is 10 s for both flow conditions (churn and slug). An obvious similarity is observed between the locations of both erosion in both elbows and where most of the sand particles are concentrated. In Figures 5.36 and 5.37, E represents Erosion while PCn is the particle concentration and the contour plots when L/D is 20 has been employed to represent all cases studied .

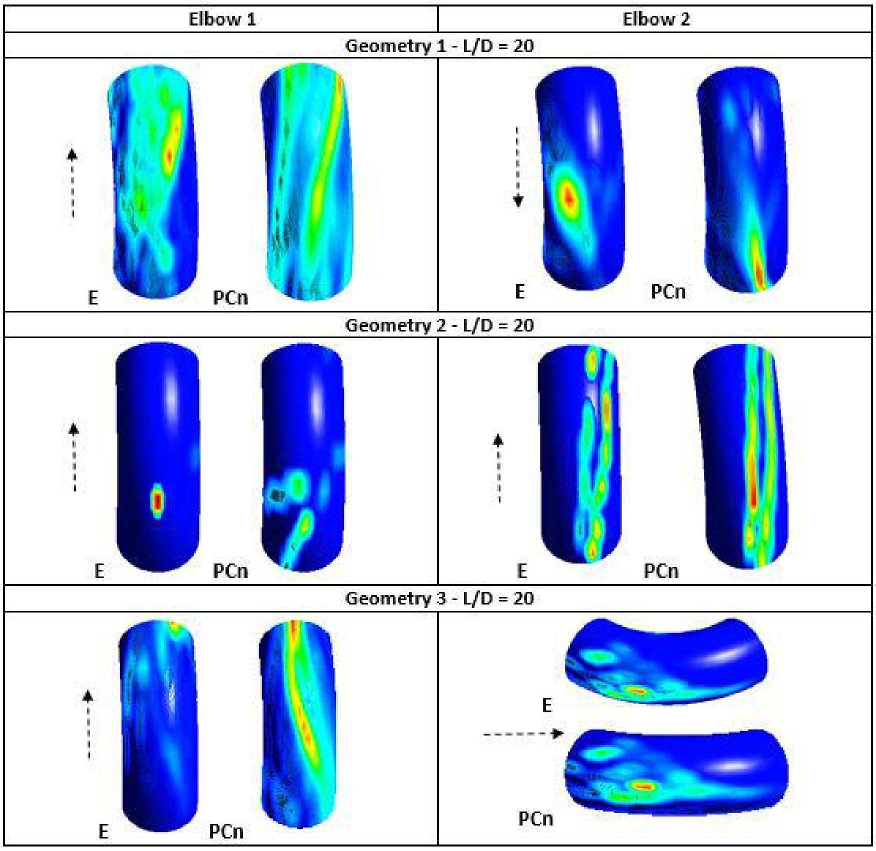

Figure 5.36: Comparison of Sand particle concentration and Erosion pattern in churn flow at 10 s

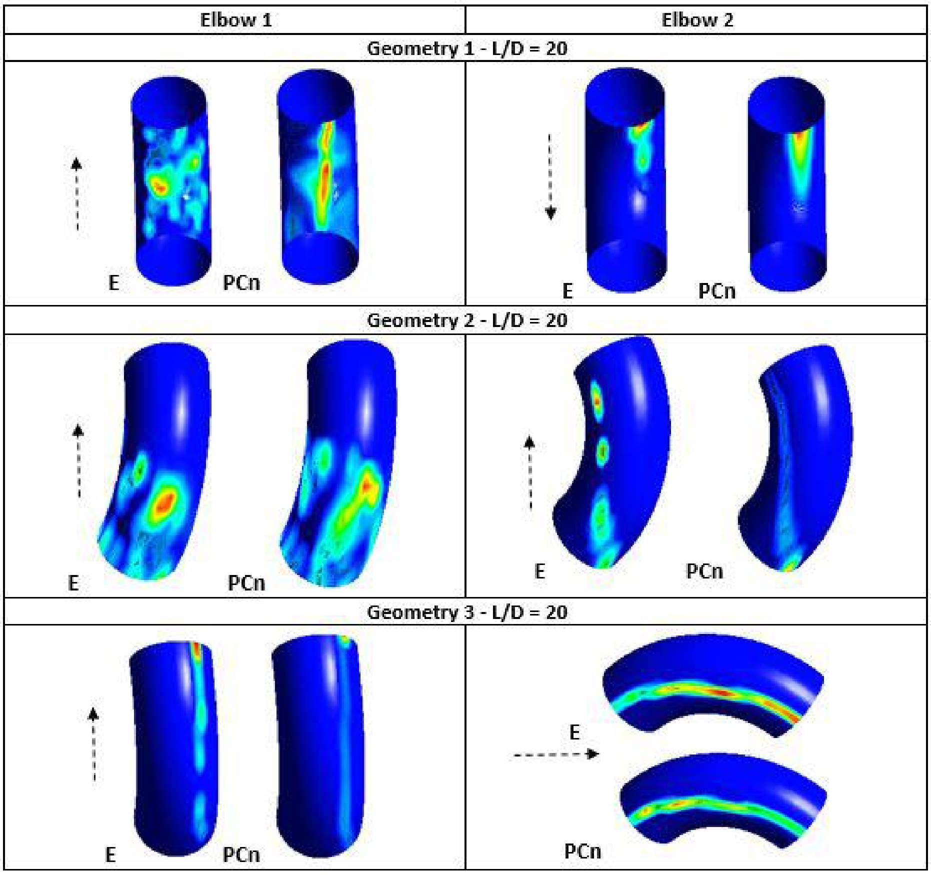

Figure 5.37: Comparison of Sand particle concentration and Erosion pattern in Slug flow at 10 s

5.4 Erosion rates in Pipe Bends and Influencing Parameters

Understandably, it is of paramount importance to state that in multiphase flows, as the flow dynamics vary from one instance to another, the erosion rates as well as the volume of sand particles at the elbows also vary as seen in the contours of erosion damage and sand concentration. Noticeably, there seem to be a significant relationship between the erosion rates and the sand particle concentration at the elbows. The instantaneous maximum and average erosion rates have been compared to the sand particle concentration to investigate the influence the particle concentration have on erosion rates at the bends. Also the influence of the impact velocities of the particles is highlighted.

The volume of particles dragged into the pipe bend is highly influenced by the particular phase of the multiphase flow navigating the elbow at a particular instance. In Figure 5.38 it can be seen that sand particles are transported by either the liquid or gas phase. When there is more of the liquid phase at the bend, the sand concentration at the elbow will be highly influenced by the liquid phase and vice versa. Therefore, it can be concluded that, if there is a higher volume of liquid at the elbow there will be a corresponding increase in the volume of sand particles dragged along the pipe bend at a particular instance and this in the end leads to higher erosion damage. This observation is more pronounced at lower gas velocities under slug flow conditions than in churn flows and more importantly towards Elbow 2. There is a higher volume fraction of liquid in slug compared to churn flow (See Figures 5.14 and 5.21). This is because slug flow is a more segregated flow compared to churn flows and there is a more defined interface between the liquid slugs and the Taylor bubbles, hence a higher volume of the liquid is dragged into the elbow at every a particular instance. Churn flow on the other hand is more distorted with no clear interface between the liquid and gas phases, it is also more aerated. Hence at a particular flow time, the elbow could be occupied with a mixture of both with a higher presence of the gas phase.

Drops in particle impact velocity could be as a result of different flow dynamics, however a significant one is the flow phase present in the elbow at the time of impact. The particle trajectory shown in Figure 5.38 shows that particles in the gas phase accelerate faster than the ones in the liquid phase in both churn and slug flow, therefore if at a particular instance there is more of gas than liquid at the elbows, higher erosion damage should be expected because of the higher momentum of the sand particles in the gas phase. And a reverse will be the case if otherwise. Furthermore, in complex multiphase flows like slug and churn where there is the occurrence of liquid slugs and waves, while navigating the pipe bend, higher volume of the liquid phase due to its higher density during or after separation tends to flow along the pipe wall thereby forming a cushion referred to as the liquid film. In this kind of instance, particles need to cut through this cushion before impinging on the pipe wall to cause erosion. In the process, with the presence of the liquid film and the sand particles dragged by the liquid phase, the impact velocity is reduced by the viscous forces in the liquid film and the sand concentration shielding the walls of the elbows before it impinges the wall.

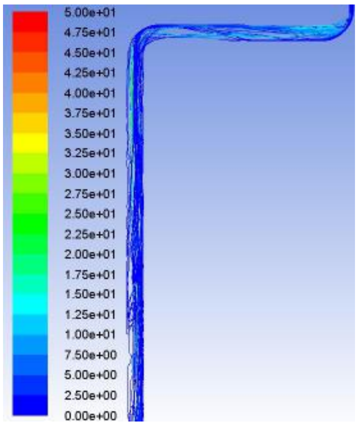

(a) Particle Tracks in churn flow

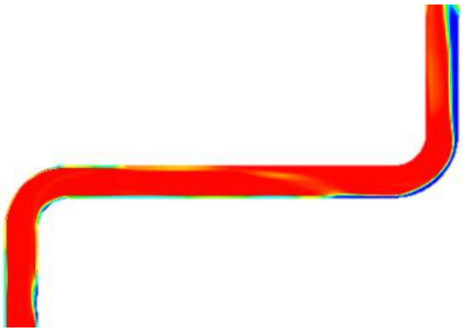

(b) Churn flow

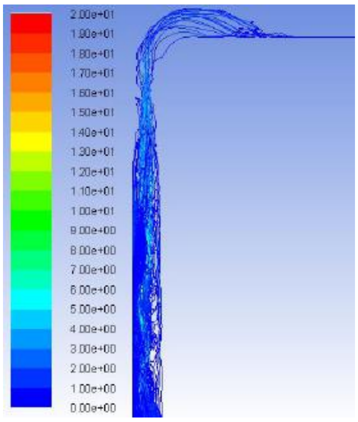

(c) Particle tracks in slug flow

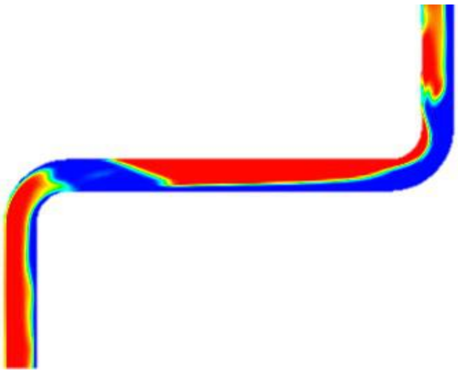

(d) Slug flow

Figure 5.38: Particle Tracks and Cross-sectional volume fraction at L/D of 10 in Geometry 2

The profiles of the instantaneous change in average and maximum erosion rates in Elbows 1 and 2 within a specific time frame, and the corresponding sand concentration and particle impact velocity for both churn and slug flows are shown in Figures 5.39 to 5.44. The time-frame employed in this study is 1 s (10 s to 11 s). It can be seen that at a high peak in the sand concentration, there is a corresponding high peak in the erosion rates in Elbows 1 and 2. And also at the highest volume of sand concentration, there is an obvious rise in the erosion rates in Elbows 1 and 2. This is observed at every normalized separation distance investigated. This can be related to the fact that when there is high sand concentration irrespective of the fluid phase dragging the particles through the elbows, there will repeated particle impingement on the pipe walls hence resulting in higher erosion rates of the elbows.

Previous studies on sand erosion in pipelines such as Islam and Farhat (2014) has also shown that particle impact velocity has a significant influence on the erosion rates at the bends. And it can also be inferred from the erosion model developed by Oka et al. (2005a) and Oka and Yoshida (2005b) that apart from the empirical constants and other fixed parameters, the parameter which could result in instantaneous changes to the pipe erosion rates is the velocity of the particles at the time of impinging the pipe walls. Talia et al. (1999) reported that a change in the particle impact velocity will lead to a corresponding change in the erosion rate at a particular instance, that is an increase in impact velocity leads to an increase in the erosion rate and vice versa. In view of this, the average impact velocities of the sand particles at Elbows 1 and 2 have also been pitched against the predicted erosion rates at Elbows 1 and 2 (See Figures 5.39 to 5.44).

From the profiles of the particle impact velocities within the time frame of analysis and the erosion rates for all cases studied, just as the case with the volume of sand particles at the elbows, it can also be seen that the velocity of the particles impacting the pipe wall has a significant influence on the erosion damage. A drop in particle velocity at impact results in a corresponding drop in the erosion rate at that instance and vice versa. Figures 5.39 to 5.44 also show the comparisons of the erosion rates, sand concentration and impact velocities in both churn and slug flows. Similar behaviours to the churn flow is however seen in the in slug flow.

In Geometry 1 (Figure 5.39) when the flow condition is churn flow, the peak average erosion rate at the normalized separation distances are observed to be between 50 mm/year at L/D of 5 and 400 mm/year at L/D of 15 and 150 mm/year at L/D of 0 and 550 mm/year at L/D of 10 in Elbows 1 and 2 respectively. Maximum erosion rates are predicted between 10000 mm/year at L/D of 5 and 25000mm/year when the normalized separation distance is 15 in Elbow 1. In Elbow 2, it is predicted to be between 7500 mm/year when L/D is 5 and 22500 mm/year at L/D of 20. In Geometry 2, the peak average erosion rates in Elbows 1 and 2 are between 50 mm/year at L/D of 20 and 450 mm/year at L/D of 0 and 120 mm/year at L/D of 50 and 680 mm/year at L/D of 10 respectively. While the maximum erosion rates in Elbow 1 are between 5000 mm/year at L/D of 15 and 17000 mm/year at L/D of 10, and in Elbow 2 between 5000 mm/year at L/D of 5 and 18000 mm/year at L/D of 15 (see Figure 5.40). In Geometry 3 (Figure 5.41), the peak average erosion rates in Elbows 1 and 2 are between 150 mm/year at L/D of 15 and 350 mm/year at L/D of 20 and 120 mm/year at L/D of 15 and 300 mm/year at L/D of 5 respectively. While the maximum erosion rates are between 5000 mm/year at L/D of 10 and 33000 mm/year at L/D of 0 in Elbow 1. In Elbow 2, the erosion rates are between 10,000 mm/year at L/D of 5 and 65,000 mm/year when L/D is 20.

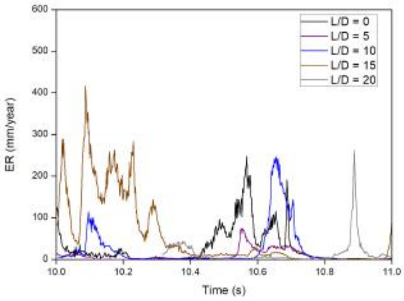

(a) Av. Erosion Rate in Elbow 1

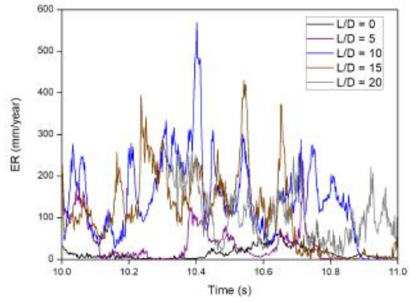

(b) Av. Erosion Rate in Elbow 2

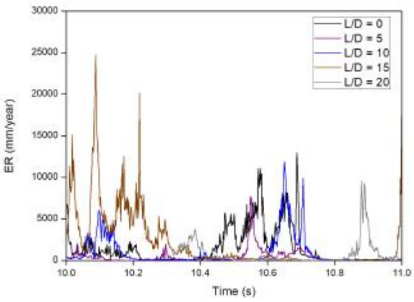

(c) Max. Erosion Rate in Elbow 1

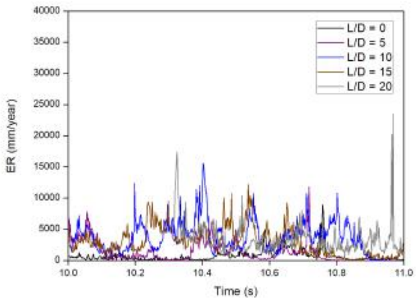

(d) Max. Erosion Rate in Elbow 2

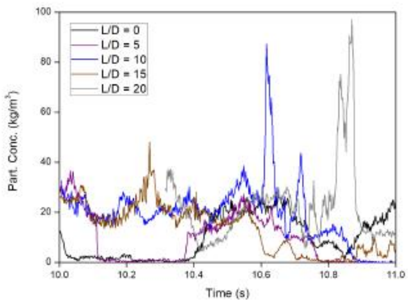

(e) Sand Concentration in Elbow 1

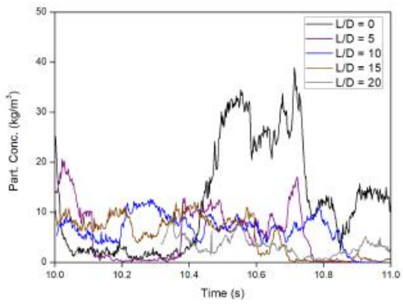

(f) Sand Concentration in Elbow 2

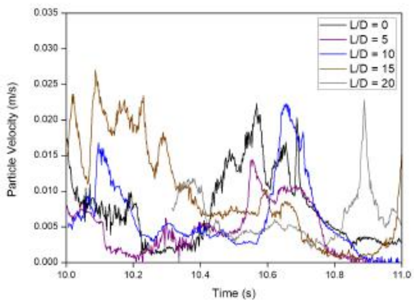

(g) Particle Impact Vel. in Elbow 1

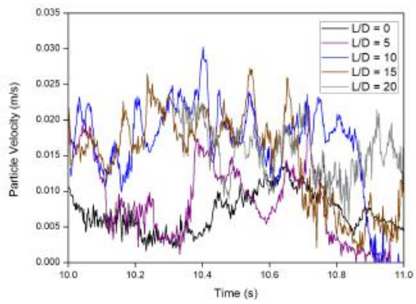

(h) Particle Impact Vel. in Elbow 2

Figure 5.39: Erosion rates, sand concentration and particle impact velocity in Churn Flow - Geometry 1

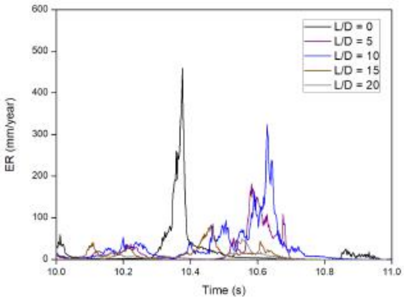

(a) Av. Erosion Rate in Elbow 1

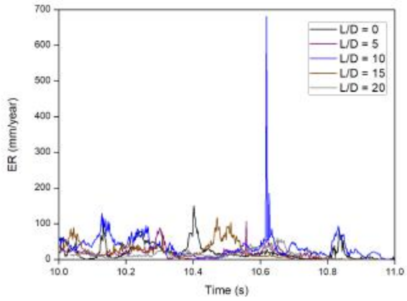

(b) Av. Erosion Rate in Elbow 2

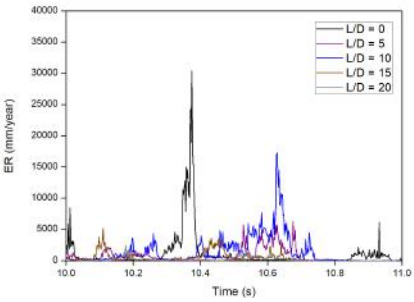

(c) Max. Erosion Rate in Elbow 1

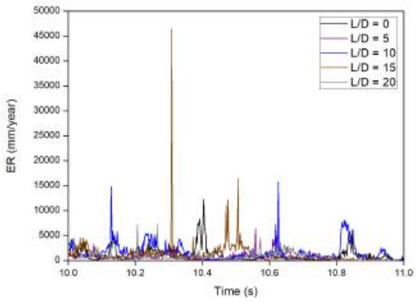

(d) Max. Erosion Rate in Elbow 2

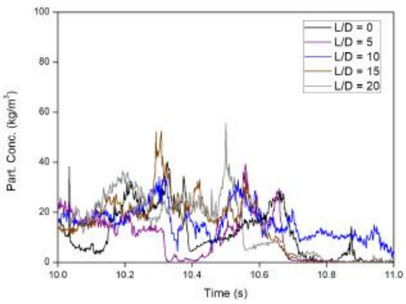

(e) Sand Concentration in Elbow 1

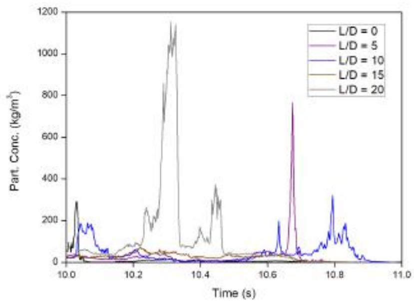

(f) Sand Concentration in Elbow 2

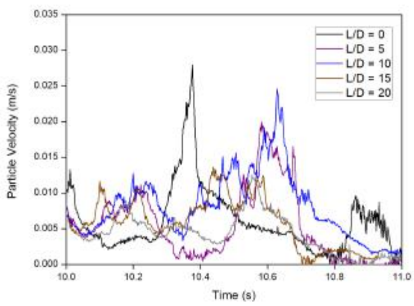

(g) Particle Impact Vel. in Elbow 1

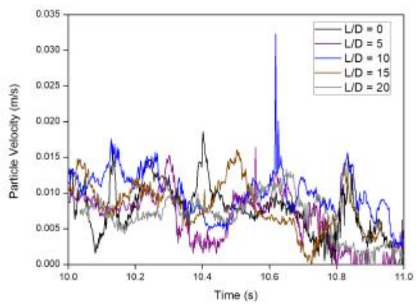

(h) Particle Impact Vel. in Elbow 2

Figure 5.40: Erosion rates, sand concentration and particle impact velocity in Churn Flow - Geometry 2

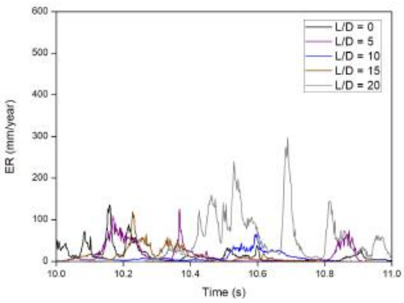

(a) Av. Erosion Rate in Elbow 1

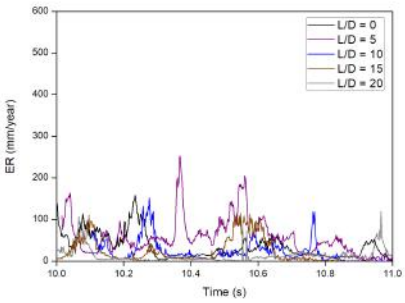

(b) Av. Erosion Rate in Elbow 2

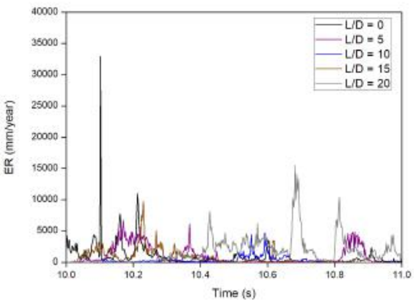

(c) Max. Erosion Rate in Elbow 1

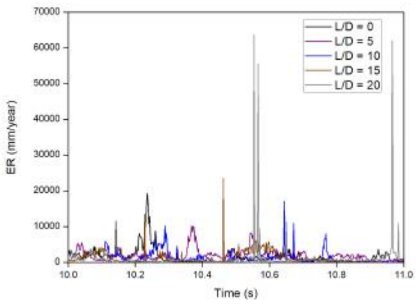

(d) Max. Erosion Rate in Elbow 2

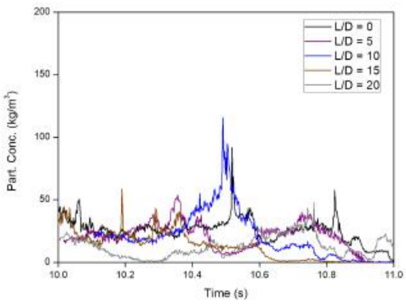

(e) Sand Concentration in Elbow 1

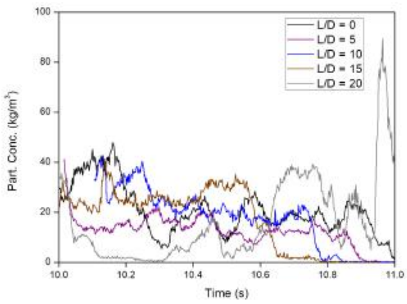

(f) Sand Concentration in Elbow 2

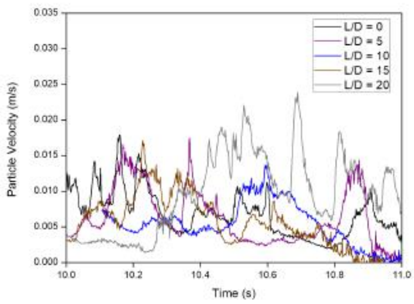

(g) Particle Impact Vel. in Elbow 1

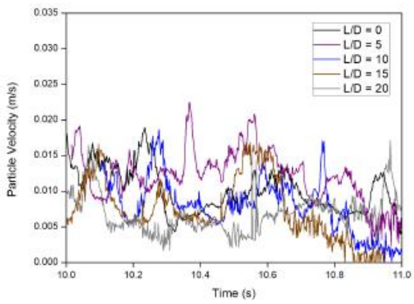

(h) Particle Impact Vel. in Elbow 2

Figure 5.41: Erosion rates, sand concentration and particle impact velocity in Churn Flow - Geometry 3

In slug flow, the peak average erosion rates in Elbows 1 and 2 of Geometry 1 (Figure 5.42) are observed to be between 2 mm/year at L/D of 5 and 7 mm/year at L/D of

15, and 0.1 mm/year at L/D of 20 and 1.6 mm/year at L/D of 5 in Elbows 1 and 2 respectively. Maximum erosion rates are predicted between 50 mm/year at L/D of 10 and 4200mm/year when the normalized separation distance is 0 in Elbow 1. In Elbow 2, it is predicted to be between 10 mm/year when L/D is 20 and 300 mm/year at L/D of 10. In Geometry 2, the peak average erosion rates in Elbows 1 and 2 are between 0.6 mm/year at L/D of 10 and 4000 mm/year at L/D of 5, and 0.3 mm/year at L/D of 10 and 600 mm/year at L/D of 5 respectively. While the maximum erosion rates in Elbow 1 are between 30 mm/year at L/D of 10 and 12000 mm/year at L/D of 5, and in Elbow 2 between 2×10^{-5} mm/year at L/D of 15 and 25000 mm/year at L/D of 5 (See Figure 5.43). In Geometry 3 (Figure 5.44), the peak average erosion rates in Elbows 1 and 2 are between 1 mm/year at L/D of 15 and 5 mm/year at L/D of 20 and 0.025 mm/year at L/D of 20 and 1.9 mm/year when L/D is 0 respectively. While the maximum erosion rates are between 70 mm/year at L/D of 10 and 125 mm/year at L/D of 20 in Elbow 1. In Elbow 2, the erosion rates are between 1.2 mm/year at L/D of 20 and 60 mm/year when L/D is 0.

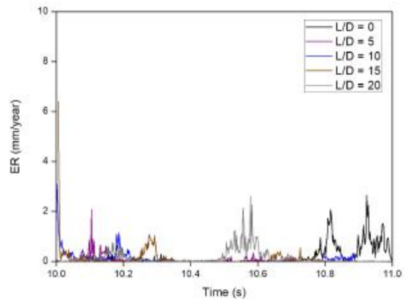

(a) Av. Erosion Rate in Elbow 1

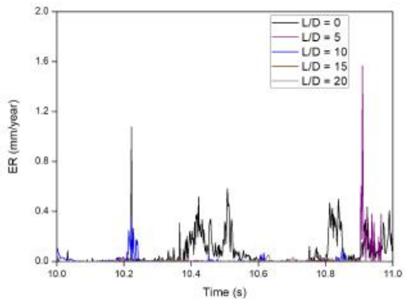

(b) Av. Erosion Rate in Elbow 2

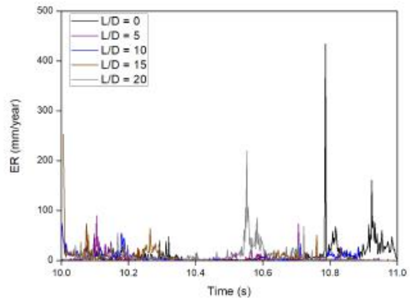

(c) Max. Erosion Rate in Elbow 1

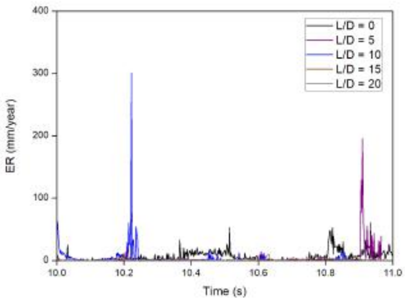

(d) Max. Erosion Rate in Elbow 2

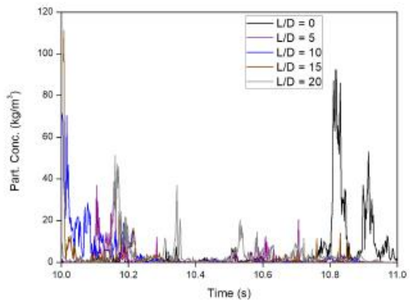

(e) Sand Concentration in Elbow 1

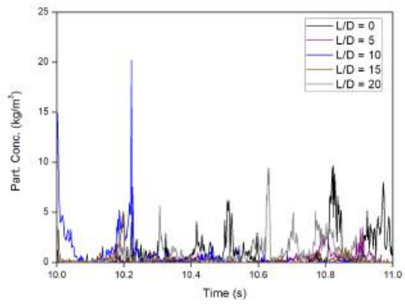

(f) Sand Concentration in Elbow 2

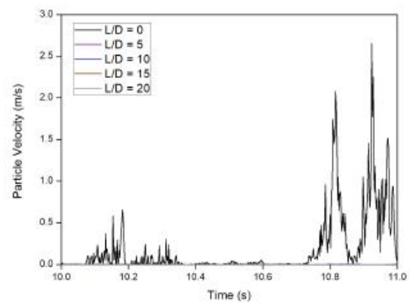

(g) Particle Impact Vel. in Elbow 1

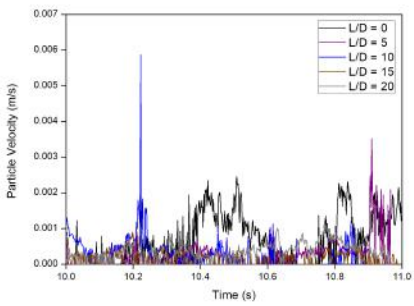

(h) Particle Impact Vel. in Elbow 2

Figure 5.42: Erosion rates, sand concentration and particle impact velocity in Slug Flow - Geometry 1

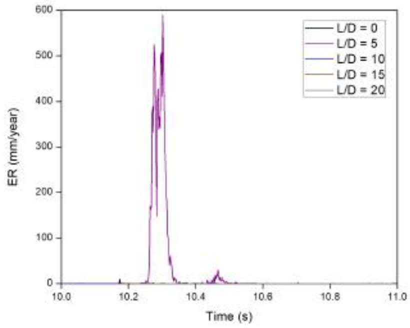

(a) Av. Erosion Rate in Elbow 1

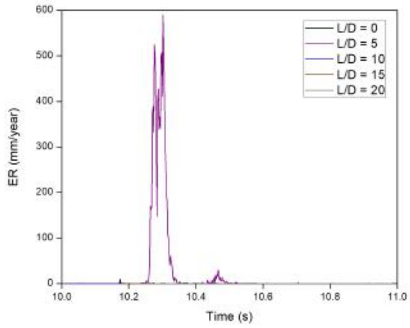

(b) Av. Erosion Rate in Elbow 2

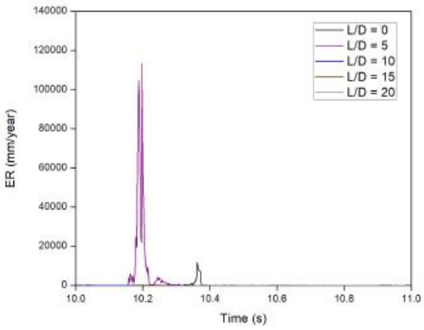

(c) Max. Erosion Rate in Elbow 1

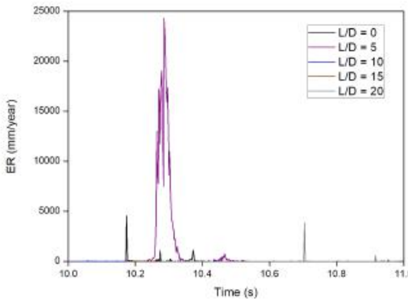

(d) Max. Erosion Rate in Elbow 2

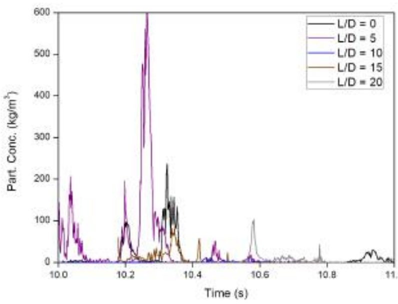

(e) Sand Concentration in Elbow 1

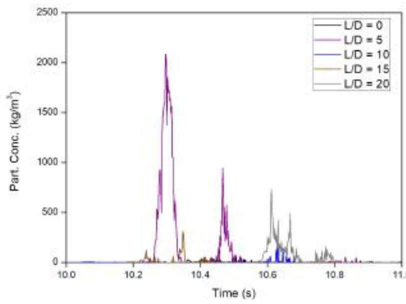

(f) Sand Concentration in Elbow 2

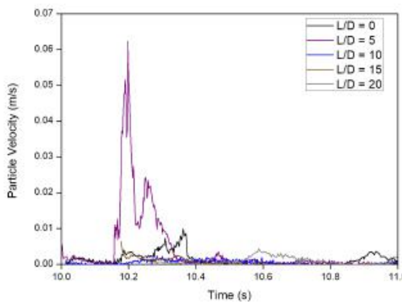

(g) Particle Impact Vel. in Elbow 1

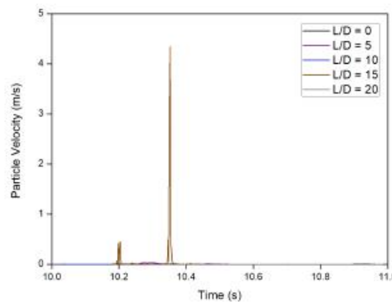

(h) Particle Impact Vel. in Elbow 2

Figure 5.43: Erosion rates, sand concentration and particle impact velocity in Slug Flow - Geometry 2

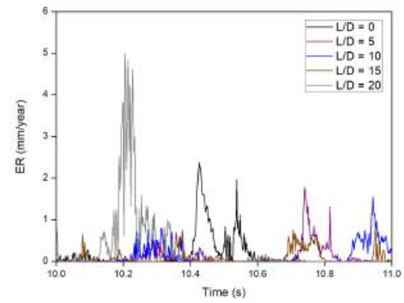

(a) Av. Erosion Rate in Elbow 1

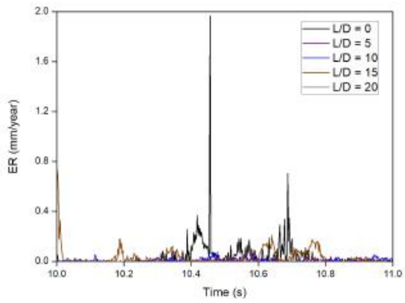

(b) Av. Erosion Rate in Elbow 2

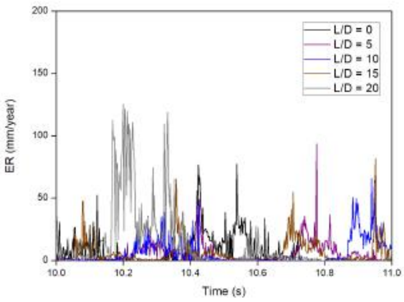

(c) Max. Erosion Rate in Elbow 1

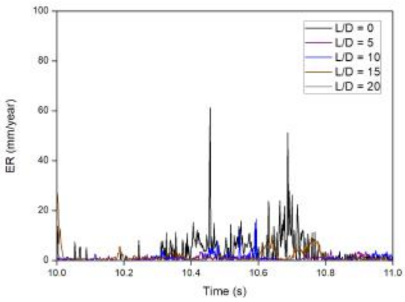

(d) Max. Erosion Rate in Elbow 2

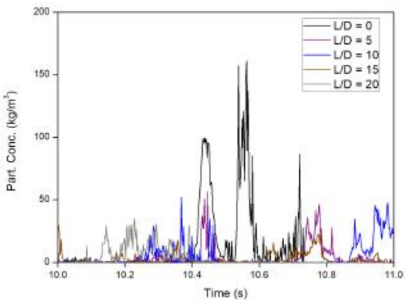

(e) Sand Concentration in Elbow 1

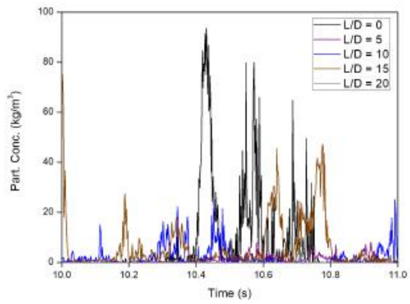

(f) Sand Concentration in Elbow 2

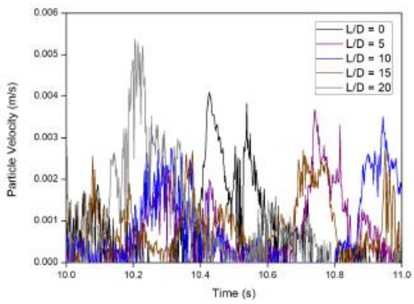

(g) Particle Impact Vel. in Elbow 1

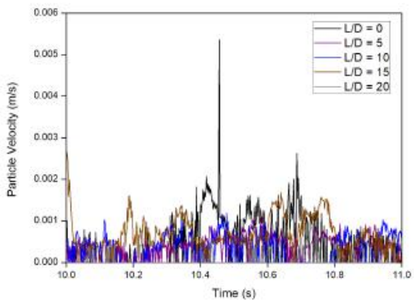

(h) Particle Impact Vel. in Elbow 2

Figure 5.44: Erosion rates, sand concentration and particle impact velocity in Slug Flow - Geometry 3

Furthermore, as observed in the flow analysis of churn flow that the volume fraction of the gas phase towards Elbow 2 is higher than that which flows into Elbow 1 in all cases studied, from Figures 5.39 to 5.41, erosion in Elbow 2 is predicted to be higher than that in Elbow 1. Therefore, the higher the gas(air) phase in the Elbow, the higher the magnitude of erosion. A similar observation is reported in the volume fraction of gas in slug flow towards Elbow 2, however, the erosion rates in Elbow 2 are predicted to be lower than Elbow 1 as can be seen in Figures 5.42 to 5.44. This is due to the fact that in slug flow, there is a huge accumulation of the liquid (water) phase towards Elbow 2 and this forms a thicker liquid film around the elbow as the fluid and particles drag through, hence reducing the rate, momentum and force at which the particles impinge on the pipe wall. At any instance when more gas will flow through the elbow, higher erosion rates should be expected.

With the different ranges of erosion rates observed in all cases investigated, a parametric study has been carried out to give a better understanding of the normalized distance at which the elbows are subjected to the most time averaged erosion rate (both average and maximum) as well as clearly highlight how the change in normalized separation distance affects the erosion rates, especially in Elbow 2 within the time frame employed (i.e between 10 s and 11 s).

5.5 Parametric Studies of the Time Averaged Erosion Rates

The time average of the instantaneous erosion rate (both average and maximum) for each of the cases studied is calculated, and this was related to the normalized separation distances to study the behaviour of the average and maximum erosion rates as the normalized separation distance (L/D) changes. These time averaged values have also been employed for the study of other flow and geometric parameters.

5.5.1 Effects of Change in Normalized Separation Distance "L/D" on the Time Averaged Erosion Rates

In this section, the effect of change in the normalized separation distance (L/D) on the time averaged erosion magnitudes and other parameters in Elbows 1 and 2 when the carrier fluid is in both the churn and slug flow conditions respectively.

Churn Flow

Figures 5.45 shows the effect of change in L/D on the time averaged erosion rates in Elbows 1 and 2 for all the cases studied under churn flow condition. In geometry 1 (Figures 5.45), as the normalized separation distance increased from 0 to 20, average and maximum erosion rates in Elbow 2 remained consistently higher than that in Elbow 1 after a normalized separation distance of about 2.5. This is due to the higher peaks of erosion rates predicted in Elbow 2 at all normalized separation distances except L/D of 0 (See Figure 5.39). In Elbow 1, the average erosion rates at L/D of 0 and 10 are within a considerable range of each other, this is also observed at L/D of 5 and 20. At a normalized separation distance of 15, Elbow 1 is subjected to the most erosion damage (both average and maximum) while Elbow 2 is subjected to the most erosion damage at L/D of 10. This implies that at a condition when L/D is greater than or equal to 10, and less than or equal to 15, the bends in geometry one will erode at a much faster rate than other conditions. After a normalized separation distance of 5, an increase in the average erosion rate in Elbow 1 results to a corresponding increase in the erosion rate in Elbow 2 as can be seen in Figure 5.45a.

In Geometry 2 as the normalized separation distance (L/D) increased from 0 to 20, there seems to be a linear relationship between the two bends (Elbows 1 and 2), the erosion rates dropped as L/D increases from 0 to 5 and increased as the normalized separation distance increased from 5 to 10. Furthermore, as L/D increased from 10 to 20, the erosion magnitudes in both elbows drops. The peak erosion magnitude in both elbows is observed at L/D of 10, this is as a result of the peak erosion magnitude recorded in the instantaneous average and maximum erosion rates at a flow time of about 10.61 s. The elbows are subjected to the least at a normalized separation distance of 20, Elbows 1 and 2 experienced the least peak in erosion rate at this L/D. As observed in Geometry 1, Elbow 2 is also subjected to more erosion damage than Elbow 1 in most normalized separation distances (10, 15 and 20).

In Geometry 3, as observed in Geometries 1 and 2, Elbow 2 is also subjected to more erosion damage than Elbow 1 in most cases. The reverse is however observed after L/D of 15, this is due to the increase in the peak average instantaneous erosion rate from 120 mm/year at L/D of 15 to 300 mm/year at L/D of 20 (Figure 5.41). The average erosion rate in Elbow 1 as the normalized separation distance increased from 0 to 15 remained within a considerable range. In Elbow 2 on the other hand, as L/D increases, the average and maximum erosion rates varies. Elbow 1 is subjected to the most average and maximum erosion at a normalized separation distance of 20 while elbow 2 is subjected to the most when L/D is 5. There is however no direct relationship between the erosion magnitudes in both Elbows.

In Figures 5.45 to 5.47, G1, G2 and G3 refer to Geometry 1, Geometry 2 and Geometry 3 respectively.

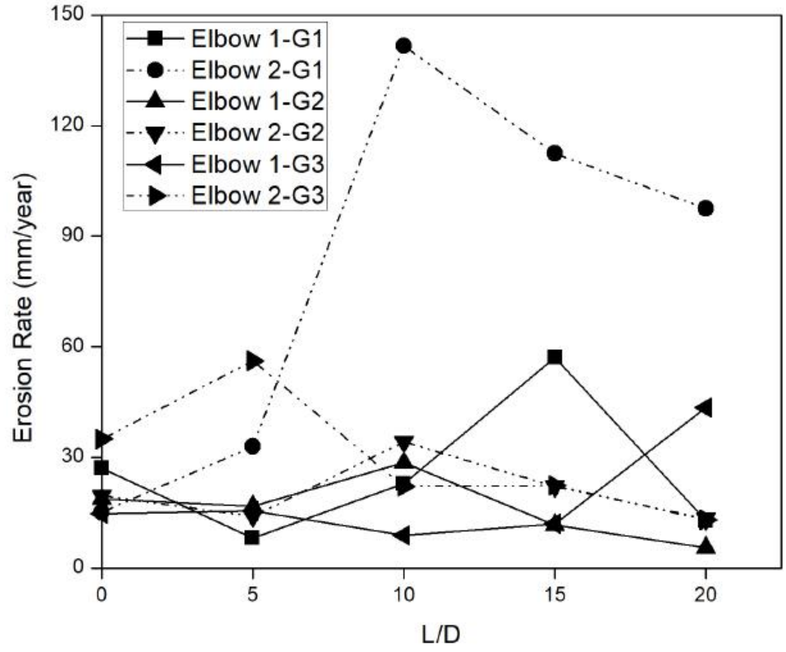

(a) Average Erosion Rates

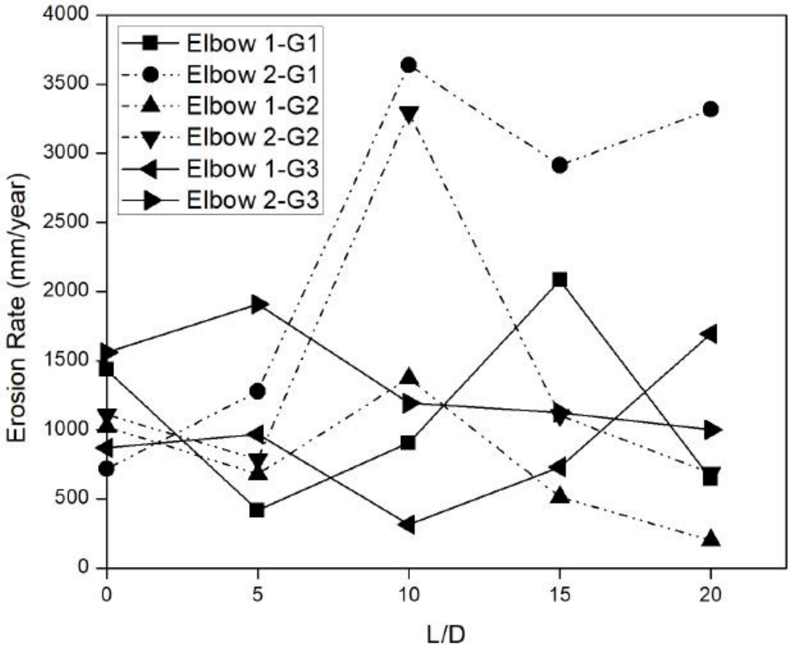

(b) Maximum Erosion Rates

Figure 5.45: Effects of L/D on Erosion Rates in Churn Flow

Slug Flow

Figure 5.46 shows the effect of change in L/D on the time averaged erosion rates in Elbows 1 and 2 for all the cases studied at low gas velocity, slug flow condition. In Geometry 1, the average and maximum erosion rates in Elbow 1 remained consistently higher than the erosion Elbow 2 is subjected to. This is because the peaks of the instantaneous average and maximum erosion rates in Elbow 1 are higher than the magnitudes predicted in Elbow 2 as shown in Figure 5.42. Also as the normalized separation distance (L/D) increased from 0 to 20, the amount of erosion damage Elbow 2 is subjected to reduces while in Elbow 1 on the other hand, after a normalized separation distance of 5, the average erosion rate in Elbow 1 remained on a steady rise within the time frame (1 s) considered for this investigation. This implies that in a pipe network system similar to the one under study, Elbow 1 will erode much faster than Elbow 2 within the time frame of interest, also an increase in the normalized separation distance will result in a drop in the erosion rate in Elbow 2.

A similar relationship as seen in Geometry 1 is observed in Geometry 2 (Erosion in Elbow 1 is consistently higher than that which Elbow 2 is subjected to). However, after a normalized separation distance of 10, the difference between the magnitude both elbows are subjected to is considerably low unlike the huge difference when the normalized separation distance is 5. At the normalized separation distance of 5, the peak of the instantaneous erosion rate is highest in both elbows. Also, the corresponding sand concentration and particle impact velocities are highest at this L/D. In Geometry 3, a similar observation to Geometries 1 and 2 is observed in the time averaged erosion rates with increase in the normalized separation distance.

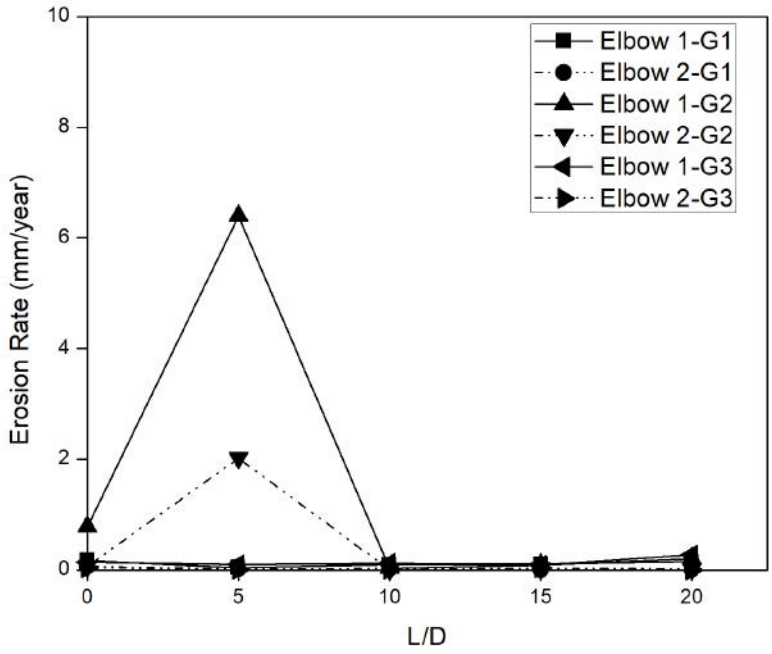

(a) Average Erosion Rates

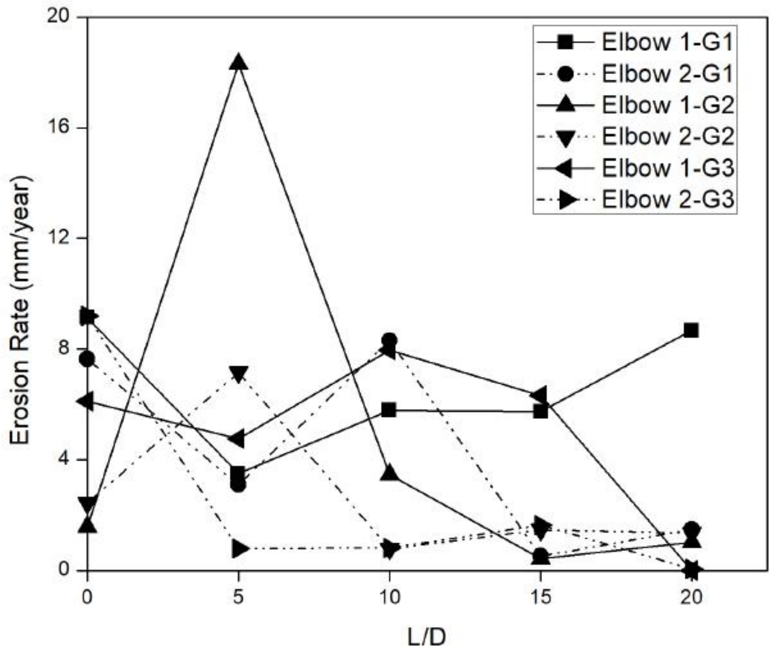

(b) Maximum Erosion Rates

Figure 5.46: Effects of L/D on Erosion Rates in Slug Flow

A change in the orientation of Elbow 2 also shows some significant influence on the magnitudes of average and maximum erosion rates in Elbows 1 and 2 at both flow conditions investigated. In churn flow, when L/D is 0, Elbow 2 is subjected to the most average erosion damage in Geometry 3 and the least in Geometry 1. At a normalized separation distance of 5, in Geometry 2 it is subjected to the least erosion damage while the magnitude in Geometry 3 remained the highest. Furthermore, between a normalized separation distance of 5 and 20, Elbow 2 became consistently subjected to the most erosion damage in Geometry 1. At L/D of 15 and 20 on the other hand, Elbow 2 is subjected to about the same magnitudes of average erosion in Geometry 2 and 3.

A similar trend as to that observed in the magnitudes of average erosion rates is observed in the maximum erosion rates, however, the magnitude of maximum erosion in Elbow 2 is much lower in Geometry 2 than Geometry 3 when the normalized separation distance (L/D) is 20. In view of these, Elbow 2 will be subjected to the most erosion damage (average and maximum) in Geometry 1 if mounted at a normalized separation distance greater than 5, while it is the least at a normalized separation distance (L/D) of 0. Although it is expected that the magnitude of both the average and maximum erosion in Elbow 1 should be independent of change in the orientation of Elbow 2, noticeable fluctuations have been recorded with this as well as with a change in the normalized separation distance. This is open to further research. In the present study, the least erosion magnitude in Elbow 1 is predicted in Geometry 3 between L/D of 0 and 15 while it is the highest at L/D of 15 in Geometry 1.

In slug flow, it can be seen that both elbows will be subjected to the most erosion damage in Geometry 2 when the normalized separation distance (L/D) is 5. At other separation distances, irrespective of elbow orientation, the erosion damage is within considerable range of each other. Unlike as predicted in Churn flow, erosion magnitude in Elbow 1 is independent of a change in the orientation of Elbow 2 except in Geometry 2 at L/D of 5. This is due to the high peak of the instantaneous erosion rate predicted within the time frame employed for this study.

5.5.2 Effects of change in flow conditions on the Time Averaged Erosion Rates

Erosion rates in the two different flow conditions (both high and low gas velocities) studied are compared in Figures 5.47. It is observed that in both elbows, all geometries and at every normalized separation distance of interest, erosion rate is of much higher magnitude in churn flow than slug flow. As it has been highlighted earlier that the particles in the gas phase accelerate faster thereby impinging on the pipe wall at a higher intensity it is expected they caused more erosion than if they are at a lower gas velocity. In view of this, in churn flow which is at a higher gas velocity, the particles tend to impinge on the pipe wall with much higher velocity and intensity than in slug flow where the gas phase is moving considerably slower. Also at the lower gas velocity in slug flow, there is a higher build up of liquid film at the pipe bends while the flow navigates the bends. The liquid film provides a cushion effect which reduces the intensity with which the accelerating sand particles impinge on the pipe wall. The sand particles have to cut through the liquid film before impinging and eroding the pipe wall. When there is a higher volume of liquid, the intensity of the particles will drop drastically before they get to impinge the pipe wall.

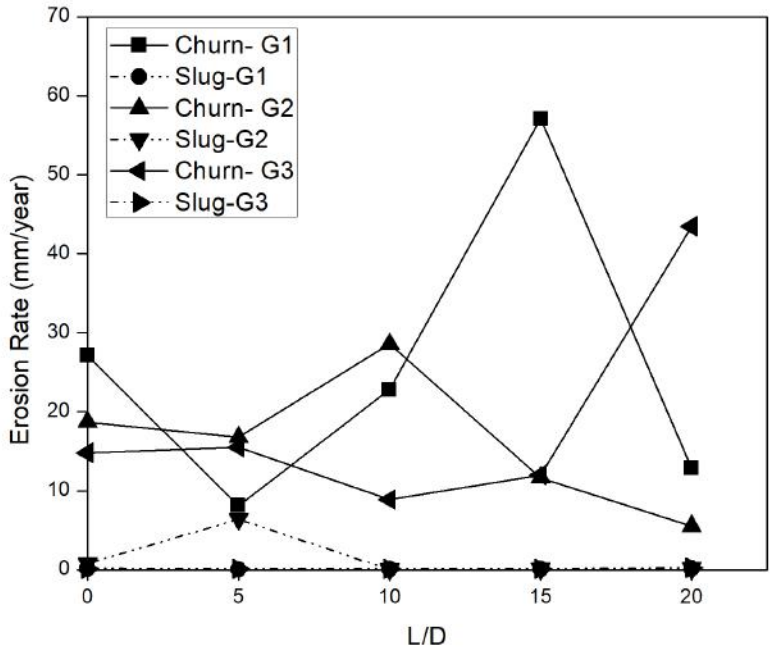

(a) Elbow 1

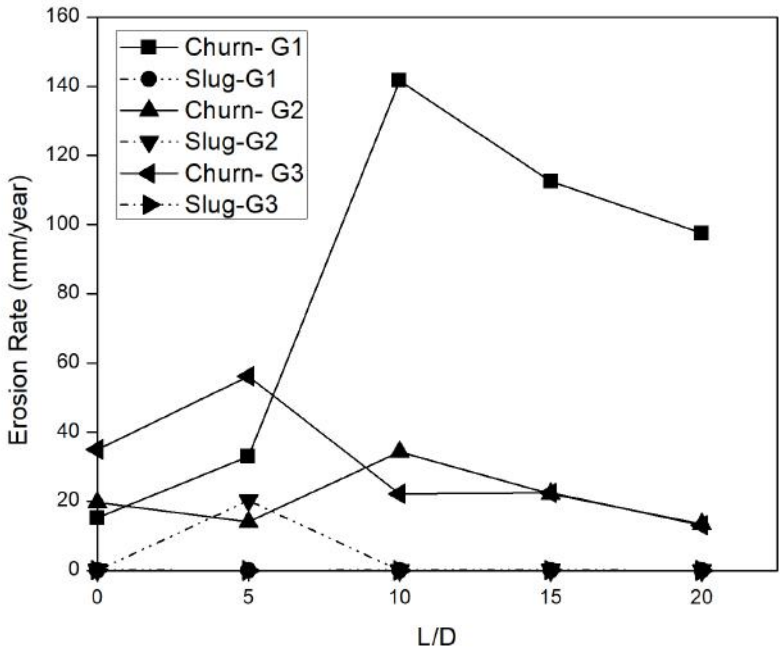

(b) Elbow 2

Figure 5.47: Effects of change in flow condition

5.6 Summary of Results

Multiphase flow modelling in elbows mounted in series was studied numerically at two different multiphase flow conditions (high and low gas velocities with a constant liquid velocity), sand particles were injected and tracked appropriately after flow development, the erosion damage on the pipe due the sand particle impact was analyzed. Based on the flow features observed and the distribution and behaviour of the phases in the flow domain, the flow pattern observed at the high has velocity is churn flow while slug flow was observed at the low gas velocity. The presence of the second bend (Elbow 2) shows a vital influence on the erosion rates in the first bend (Elbow 1) compared to the single bend geometry. Compared to the single bend, the peaks of the average erosion rates in Elbow 1 at churn flow condition are predicted to be about 115%, 50% and 88% higher in Geometries 1, 2 and 3 respectively.

It is further observed that erosion rate is higher in churn flow than slug flow. This is due to the higher velocity at which the gas phase moves in churn flow, resulting in the particles impinging on the pipe wall at much higher velocity and intensity than slug flow. In slug flow, the volume of liquid that would accumulate at the elbows will also be higher than that of churn, hence resulting in reduced erosion damage. It was also observed that based on the instantaneous flow dynamics in both flows, the erosion rate changes with a corresponding change in time and the concentration of sand particles at the elbows at the particular instance also plays a very significant role in the rate of erosion at the bend. The behaviour of the sand particle concentration is similar to that of the erosion rates in all cases investigated. In other words, the volume of sand at the elbow at a particular time could either enhance or reduce the erosion rate at the bend irrespective of the separation distance between the elbows. In slug flow with low gas velocity, there is more accumulation of fluid and sand particles at the elbows at any particular flow time than can be observed in churn flow. This accumulation of liquid results in a thicker liquid film at the elbow in slug flow than in churn flow, hence resulting in lower erosion rate as the sand particles that are been dragged through the bends would lose a lot more momentum while cutting through the liquid film in slug flows. There is as well a direct relationship between the particle impact velocity and the erosion rates. The inconsistency in the thickness of the liquid film around the elbows is one reason why it might be difficult to predict about the same erosion rates in Elbow 1.

It is important to note that there is an increase in the volume fraction of the gas phase (air) towards Elbow 2 compared to Elbow 1 in both churn and slug flows. Based on this a corresponding relationship is established between the erosion rates and the volume fraction. The higher the volume fraction of gas in the elbows the higher the erosion rates. This remained valid for the churn flow condition as the erosion rates predicted in Elbow 2 is higher compared to Elbow 1. However, in slug flow, erosion rates are higher in Elbow 1. This is because irrespective of the fact that the volume fraction of the gas phase is higher towards Elbow 2, there is equally a higher fraction of the liquid phase also flowing through the elbow which forms a thicker liquid film around Elbow 2 compared to Elbow 1. This film reduces the impacts of the sand particles on Elbow 2. Furthermore, based on the time average of the erosion rate within 1 s, the correlation between the erosion rates in both elbows at both flow conditions vary for both multiphase flow conditions. In churn flow, Elbow 2 is observed to be more erosive than Elbow 1 at most normalized separation distance while in slug flow the reverse is observed with Elbow 1 subjected to more erosion damage at most of the normalized separation distances investigated. At no separation distance and geometry is the erosion rates in both elbows expected to be equal as a change in flow direction from vertical to horizontal leads to changes in particle trajectory, distribution and angle, hence changes in erosion rates in Elbows 1 and 2.

The normalized separation distance (L/D) has a significant influence on the erosion rates in both Elbows 1 and 2. As the normalized separation distance increases, the erosion rate changes in all geometries and flow condition investigated. For churn flow, in Geometries 1 and 2, Elbow 2 is subjected to the most erosion damage when L/D is 10 and in Geometry 3 it is subjected the erosion rate is highest at L/D of 5. Hence for a pipe network similar to any of the geometries, the most erosion damage will be experienced between normalized separation distance of 5 and 10. Also in Geometry 3, L/D of 20 should be avoided at best in order to keep the erosion rate in Elbow 1 at minimum. At slug flow condition on the other hand, in Geometry 1 the lowest average erosion damage in Elbow 2 is experienced when L/D is 5 while it is the highest when L/D is 0. In Geometry 2, both Elbows are subjected to the most erosion damage when L/D is 5. While it will be safe to operate at L/D of 5 when the expected flow is slug and pipe network is similar to Geometry 1 based on the findings of this study, it will be hazardous to do the same when the pipe network is more like Geometry 2.

Overall, the best pipe operating condition for both elbows are Geometries 3 and 1 for churn and slug flows respectively.

Chapter 6

Sand Erosion in Elbows Mounted In Series Using A Pseudo Single-Phase Model

6.1 Flow conditions and description of geometries

Modelling the typical multiphase flows using the Eulerian-Eulerian Multifluid-VOF in CFD erosion analysis can be very computationally intensive because CFD utilizes the local multiphase flow properties to track the behaviour of particles. In view of this, a pseudo single-phase model that ignores the complex two-phase flow configuration has been employed to capture the average flow physics and properties of the air-water flow employed in this study. In this model, an approximation of the multiphase flow regimes with average velocity and other fluid properties were captured using a single-phase flow field and the multiphase flow particle tracking was also simplified. Hence, this chapter presents erosion study in double bend geometries using a pseudo single-phase model.

Properties such as velocities and densities of the air and water, for the multiphase flow conditions, were resolved into mixture properties using Equations (6.1), (6.2) and (6.3) for density, viscosity and velocity respectively. The resultant flow mixture properties of the slug and churn flow conditions are shown on Table 6.1. HGv and

LGv represents High Gas Velocity and Low Gas Velocity respectively. The Reynolds numbers of the resultant flow conditions were also obtained to ascertain if either falls in the laminar or turbulent category using Equation (6.4). The Reynolds numbers are shown on Table 6.2.

$$\rho_m = \rho_w H_w + \rho_a (1 - H_w) \tag{6.1}$$

$$\mu_m = \mu_w H_w + \mu_a (1 - H_w) \tag{6.2}$$

$$V_m = V_w + V_a \tag{6.3}$$

Where ρ_m, ρ_w and ρ_a are the mixture, water and air densities respectively. μ_m, μ_w and μ_a are mixture, water and air viscosities. V_m, V_w and V_a are mixture, water and air velocities respectively.

$$Re = \frac{\rho_m V_m D}{\mu_m} \tag{6.4}$$

Where Re is the Reynolds Number and D is the pipe diameter.

Table 6.1: Flow mixture properties

	V_{sl}	V_{sg}	ρ_l	ρ_g	$\mu_l(\times 10^{-3})$	$\mu_g(\times 10^{-5})$	V_m	ρ_m	μ_m
HGv	0.3	10.3	1000	1.225	1.003	1.789	10.6	29.188	4.50×10^{-5}
LGv	0.3	0.9	1000	1.225	1.003	1.789	1.2	250.92	2.644×10^{-4}

Table 6.2: Reynolds Number of Pseudo single phase

Flow Velocity	**Reynolds Number**
$10.6 m/s$	518,717.96
$1.2 m/s$	86,778.08

Based on the result presented on Table 6.2, the estimated Reynolds Numbers show that the flows are well in the turbulent flow category. Also, in this approach, the particle properties remain the same as that used in the multiphase flow analysis (i.e diameter of 300 μm and flow rate 0.0256 kgm^{-3}).

6.2 Results Analysis

6.2.1 Velocity Profile

Figure 6.1 shows the predicted velocity profiles across a plane 1m after the inlet of all the pipe geometries at the churn and slug flow conditions, hereafter referred to as the high and low gas velocity conditions. And as seen in the Reynolds numbers in Table 6.2, a qualitative observation of these velocity profiles show that both flow conditions are the turbulent flow region. This same observation (of the profile) has been reported for single phase turbulent flows by many researchers such as Metzner and Reed (1955), Dhawan and Narasimha (1958), Ghorai and Nigam (2006) and Yoon (2016) to mention a few. Figure 6.1 shows the normalized velocity profiles at both flow conditions studied, the maximum normalized velocity of the pseudo mixture at high gas velocity is 1.1 m/s, and at the low gas velocity, it is 0.13 m/s.

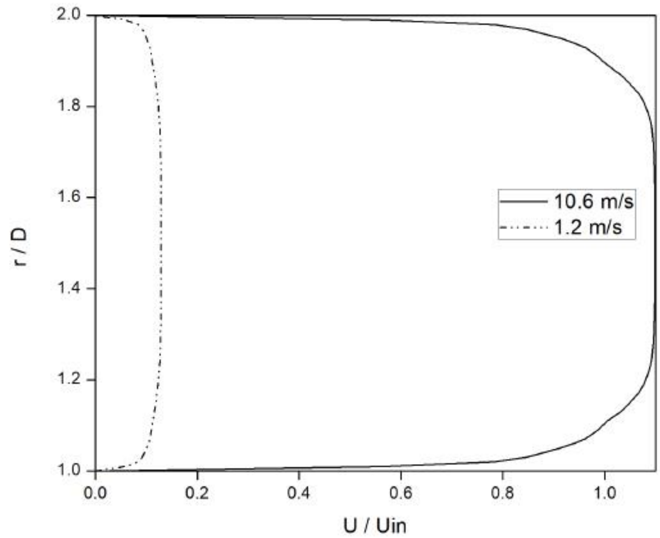

Figure 6.1: Velocity profiles of the pseudo single phase mixtures

It can be seen in Figure 6.1 that the region very close to the wall exhibits nearly linear velocity profile as seen in turbulent flow cases and it is completely dominated by the viscous effects in both flow conditions as reported by Kudela (2010). Furthermore, according to the power law verification of Newtonian fluids, described by Equation (6.5). The velocity distribution in the flow domain is described as a ratio of velocity

(u) and maximum velocity (U_{max}). More details about Equation (6.5) can be found in Cheng (2007).

$$\frac{u}{U_{max}} = (1 - \frac{r}{R})^{1/n} \tag{6.5}$$

Where, u is the time-mean flow velocity, U_{max} is the maximum flow velocity taken at free surface ($r = R$) and $1/n$ is the power-law exponent or index.
The empirical constant n increases with a corresponding increase in Re, hence an increase in Re will lead to a decrease in the power-law exponent, $1/n$. In Figure (6.1), the power-law exponent at flow velocity 1.2 m/s is evidently much high than that exhibited by 10.6 m/s due to the higher Re of the flow at the high mixture velocity.

6.2.2 Erosion Contours

Figures 6.2 to 6.7 show the erosion contour as a result of the sand particle impact in geometries 1, 2 and 3 respectively. The red patches indicate locations of the maximum erosion rates and the arrows show the direction of flow. The erosion pattern in Elbow 1, for both churn and slug conditions, remained consistent and independent of the normalized separation distance between the two elbows. This is observed for all three geometries. For churn flow conditions, the erosion pattern is concentrated on the elbow extrados, the maximum erosion occurred at about 45° into the elbow and spreads towards the elbow outlet. While erosion is concentrated at the intrados of Elbow 1 and spreads towards the outlet and sides of the elbow for the slug for condition. The maximum erosion occurred at the sides of the elbow. Researchers such as Felten (2014) and Asgharpour et al. (2017) have carried out erosion studies in elbows mounted in series with carrier fluid in single phase, they observed that the erosion location in standard single bends is similar to that of the first elbow. This is also the case when churn flow fluid properties were employed. The erosion contour and location of maximum erosion is in appropriate qualitative agreement when compared to the experimental and numerical erosion data reported by Parsi et al. (2015c) and Parsi et al. (2015b). Erosion in Elbow 1 is however under predicted by a factor of 1.8 compared to the available data. These results show the capability and accuracy of the model being used to predict the erosion for conditions under consideration. That of the pseudo single-phase flow at the low gas velocity could not be ascertained due to the unavailability of experimental and numerical data. However, the validity of the set up for the flow at high gas velocity is appropriate enough for it to be extended to other flow conditions.

In Elbow 2, the normalized separation distance and the orientation of Elbow 2 has significant influences on the erosion location, these are highlighted in the following sections. The erosion location and concentration changes as L/D is increased from 0 to 20 both at the high and low gas velocity condition across all geometries under study.

High Gas Velocity Mixture Condition

Figure 6.2 shows the behaviour of the erosion pattern in Geometry 1 as the normalized separation distance increased from 0 to 20 when the carrier fluid is resolved into churn flow mixture properties. At L/D of 0, the erosion occurred across the middle elbow extrados with the maximum erosion occurring towards the elbow outlet. However as L/D increases, the erosion pattern reduces and becomes more concentrated towards the elbow outlet. Location of maximum erosion remained more or less independent of L/D between normalized separation distances of 10 and 20. In Figures 6.2 to 6.7, E1 and E2 refers to Elbow 1 and Elbow 2 respectively.

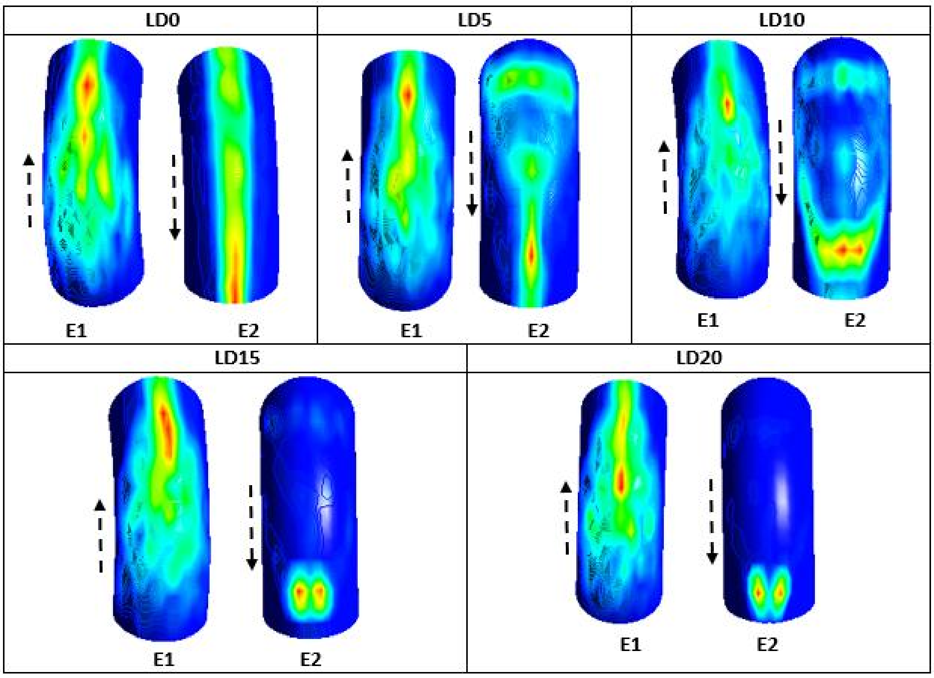

Figure 6.2: Erosion contour in Elbows 1 and 2 in Geometry 1 - High Gas Velocity

In Geometry 2 (Figure 6.3), although occurring more at the elbow extrados just like in the latter, erosion location and pattern changes as the normalized separation distance changes. When L/D is 0, the elbow outlet is subjected to more sand erosion compared to the other sections of the elbow, however as L/D increases, the elbow becomes subjected to more erosion damage as the erosion pattern spreads towards the sides of the elbow and outlet when L/D is between 5 and 20. At L/D of 15 and 20, the elbow inlet became more subjected to sand erosion damage. Due to the orientation of Elbow 2 in Geometry 3, the location of the erosion damage seems to be totally different from those of Geometries 1 and 2, however, the elbow extrados still remained subjected to a considerable magnitude of sand erosion damage than the other parts as can be seen in Figure 6.4. At normalized separation distances of 0, 5 and 10, the erosion pattern cuts across the elbow from the top to the bottom section, with location of maximum erosion location moving from the top of the elbow towards the elbow outlet at the bottom section. Erosion damage becomes more concentrated at the bottom section of the elbow when L/D is 15 and 20, and the location of maximum erosion remained towards the elbow outlet as well just in the case of Geometry 1.

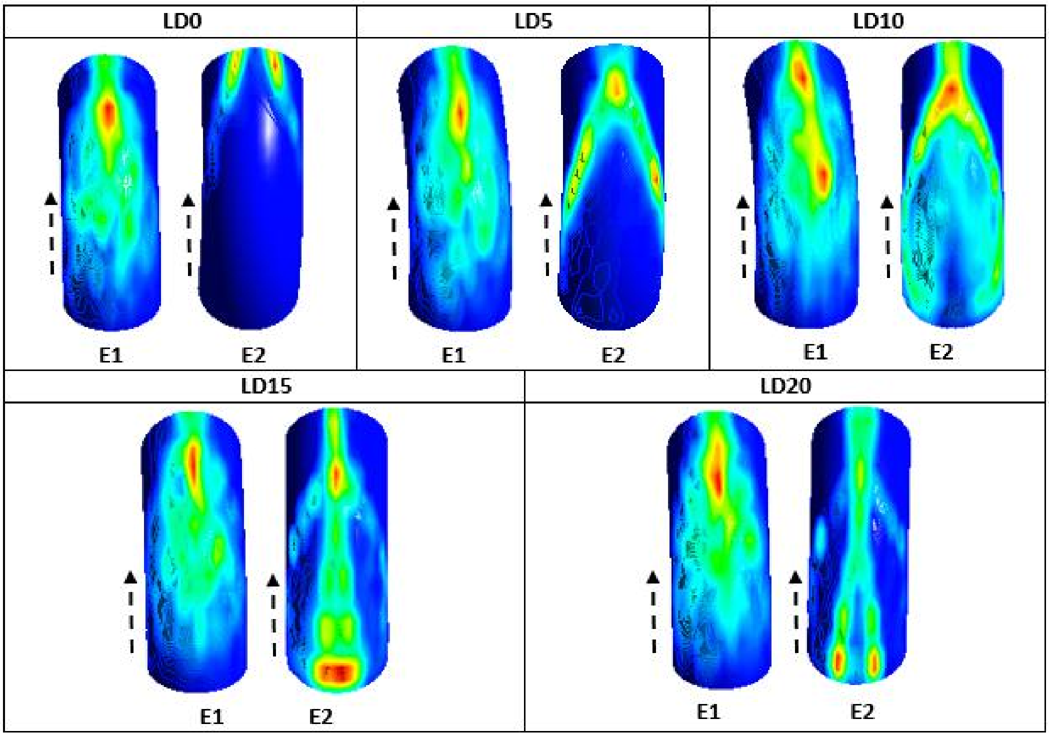

Figure 6.3: Erosion contour in Elbows 1 and 2 in Geometry 2 - High Gas Velocity

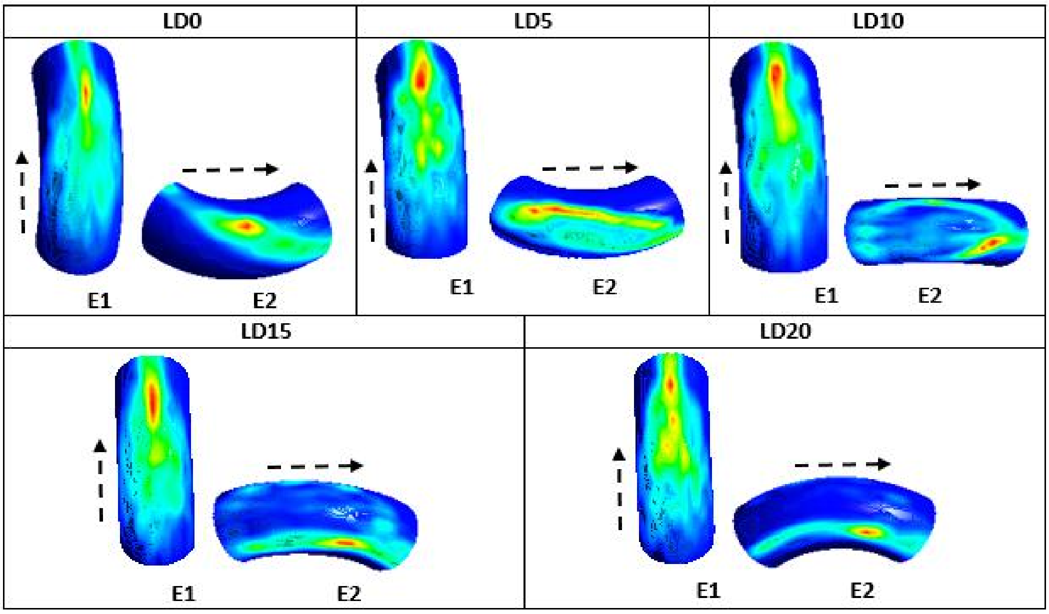

Figure 6.4: Erosion contour in Elbows 1 and 2 in Geometry 3 - High Gas Velocity

Low Gas Velocity Mixture Condition

When the carrier fluid is resolved with low gas velocity properties, the behaviour of the erosion location also changes in Elbow 2 as L/D and the elbow orientation changes. Figure 6.5 shows the erosion contour in Geometry 1, erosion is concentrated at the intrados of Elbow 2, this occurred just at the elbow inlet and remained independent of the normalized separation distance (L/D) of between 5 and 20. In Geometry 2, although erosion occurred on the elbow extrados across all normalized separation distances, a significant effect of L/D can be seen on the erosion location as shown in Figure 6.6. At L/D of 0, the elbow inlet is observed to have been eroded much more than any other part of the elbow and as L/D increases, the erosion pattern becomes more prominent and spreads across the middle of the elbow extrados up to the elbow outlet. This could be as a result of more sand particles getting dragged along the extrados as the normalized separation distance increases. However, the location of maximum erosion remained close to the elbow inlet for L/D of 5, 10 and 15, while an higher degree of erosion is observed from the elbow inlet up to about 47° into the elbow when L/D is 20.

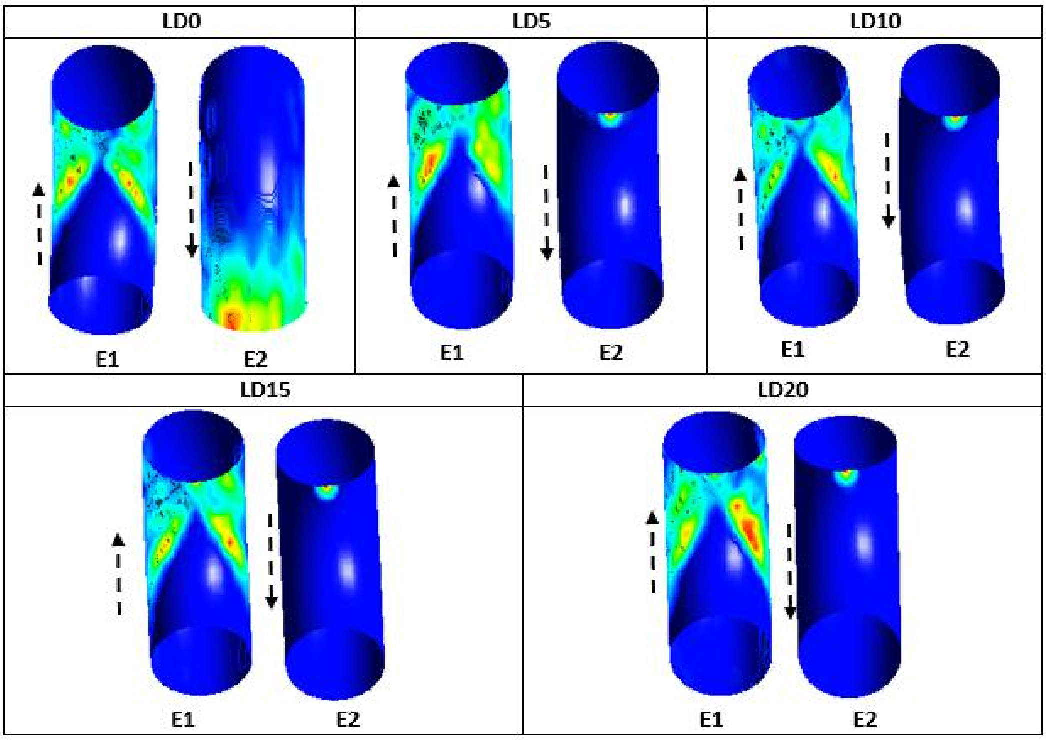

Figure 6.5: Erosion contour in Elbows 1 and 2 in Geometry 1 - Low Gas Velocity

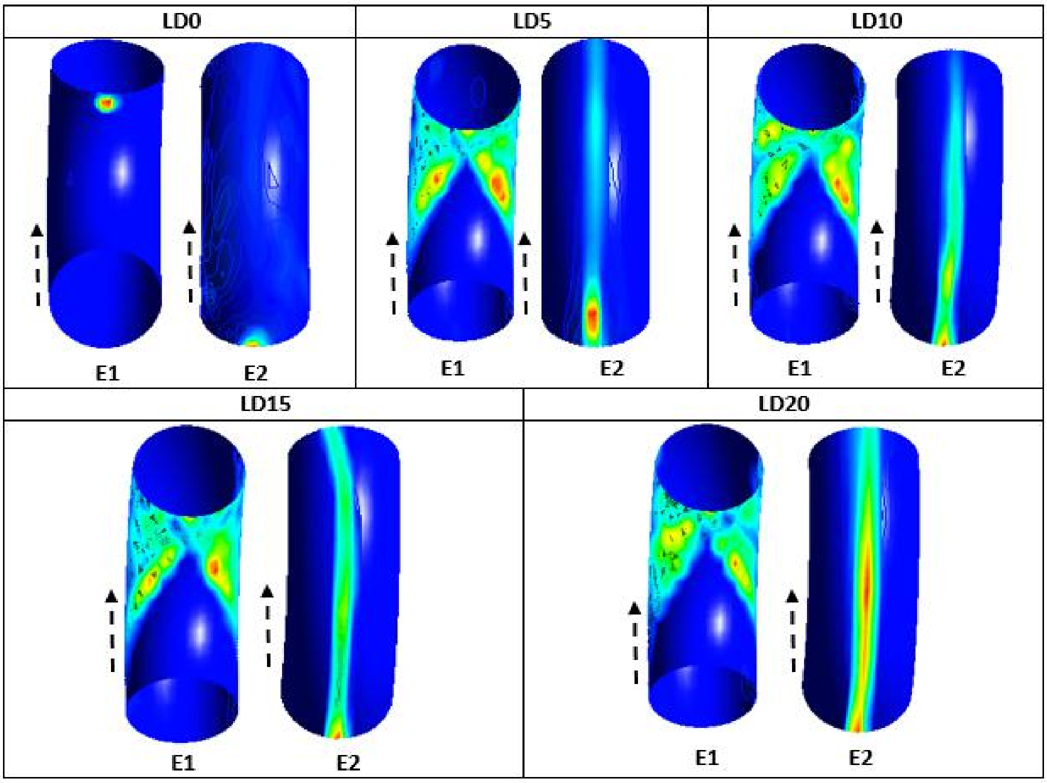

Figure 6.6: Erosion contour in Elbows 1 and 2 in Geometry 2 - Low Gas Velocity

Figure 6.7 shows the contours of erosion damage in Geometry 3 with carrier fluid resolved with low gas velocity, and an obvious influence of change in the normalized separation distance between Elbows 1 and 2 is noted on the erosion pattern and location. At L/D of 0, the erosion pattern spreads across the bottom section of the elbow from inlet to outlet, with the maximum erosion occurring close to elbow intrados. This can be attributed to the horizontal orientation of the elbow in this geometry and the effect of the force of gravity acting on the sand particles across the horizontal section of the geometry. As the normalized separation distance increases from 5 to 20, although the erosion location remained at the bottom section of Elbow 2 just as observed in L/D of 0, the area subjected to sand erosion narrowed down and extended towards the elbow intrados and elbow outlet. When L/D is 20, the location of maximum erosion location occurs at the middle of the erosion pattern, also spreading from the elbow inlet till about 50° into the elbow.

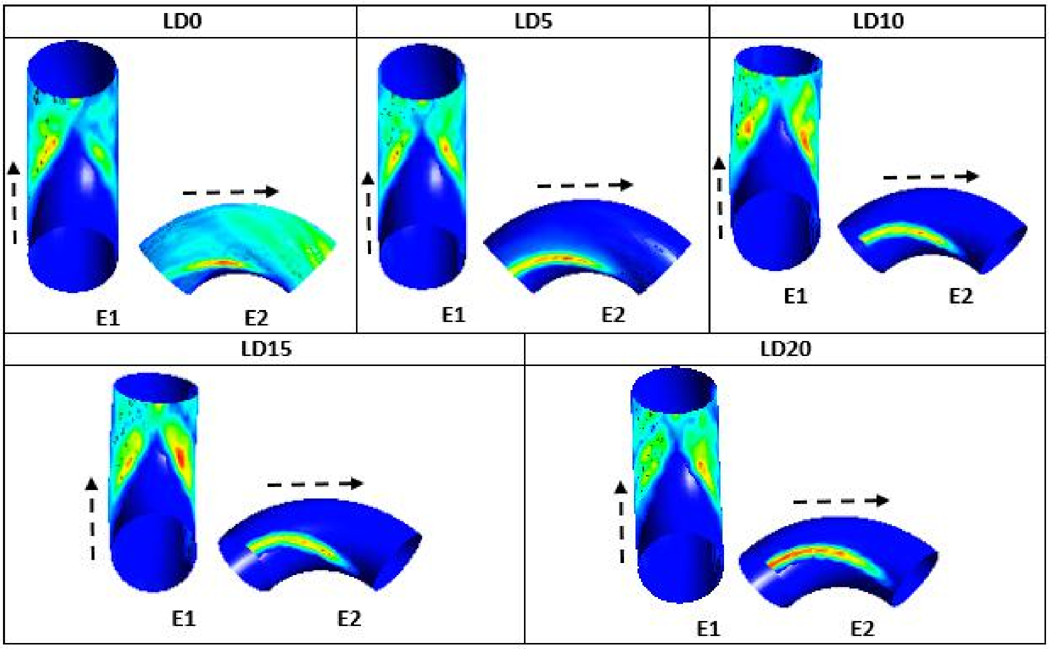

Figure 6.7: Erosion contour in Elbows 1 and 2 in Geometry 3 - Low Gas Velocity

6.2.3 Particle Tracks and Sand Particle Concentration

Figures 6.8 to 6.13 show the particle tracks in the geometries and cases studied. And a significant influence of the normalized separation distance (L/D) is observed downstream of Elbow 1 on the particle tracks as the fluid flows into Elbow 2 in both flow conditions. The normalized separation distance however has no significant influence on the path of particles upstream Elbow 1 across all geometries and flow conditions studied. Just as in the case of the erosion locations when L/D changes, the particle tracks change towards Elbow 2 as the normalized separation distance changes in both flow conditions studied. The sand particle tracks are represented in terms of their velocity magnitudes and the red streamlines in Figures 6.8 to 6.13 indicate where the velocity magnitude of the particles is highest.

High Gas Velocity Mixture Condition

In Geometry 1 (Figure 6.8), when the carried fluid has high gas velocity mixture properties, at L/D of 0, as the sand particles negotiate the bend (Elbow 2), the particles are more concentrated and are dragged across the elbow extrados. But as the normalized separation distance increases, the particles tend to spread / scatter across and settle at the bottom section of the horizontal section between Elbows 1 and 2 as more room becomes available for the flow to develop and attain equilibrium while the concentration at the extrados of Elbow 2 reduces. The settled sand particles at the bottom of the pipe cut across Elbow 2 to impinge on the elbow extrados towards the exit of the elbow. This point is observed to be the maximum erosion location as highlighted in the latter section (erosion contours). As L/D increases, more of the particles settle at the bottom section of the horizontal pipe section and more particles tend to impinge on the extrados of Elbow 2 towards the exit. This observation can be directly related to the change in erosion location as L/D changes in Elbow 2 for Geometry 1 at this flow condition.

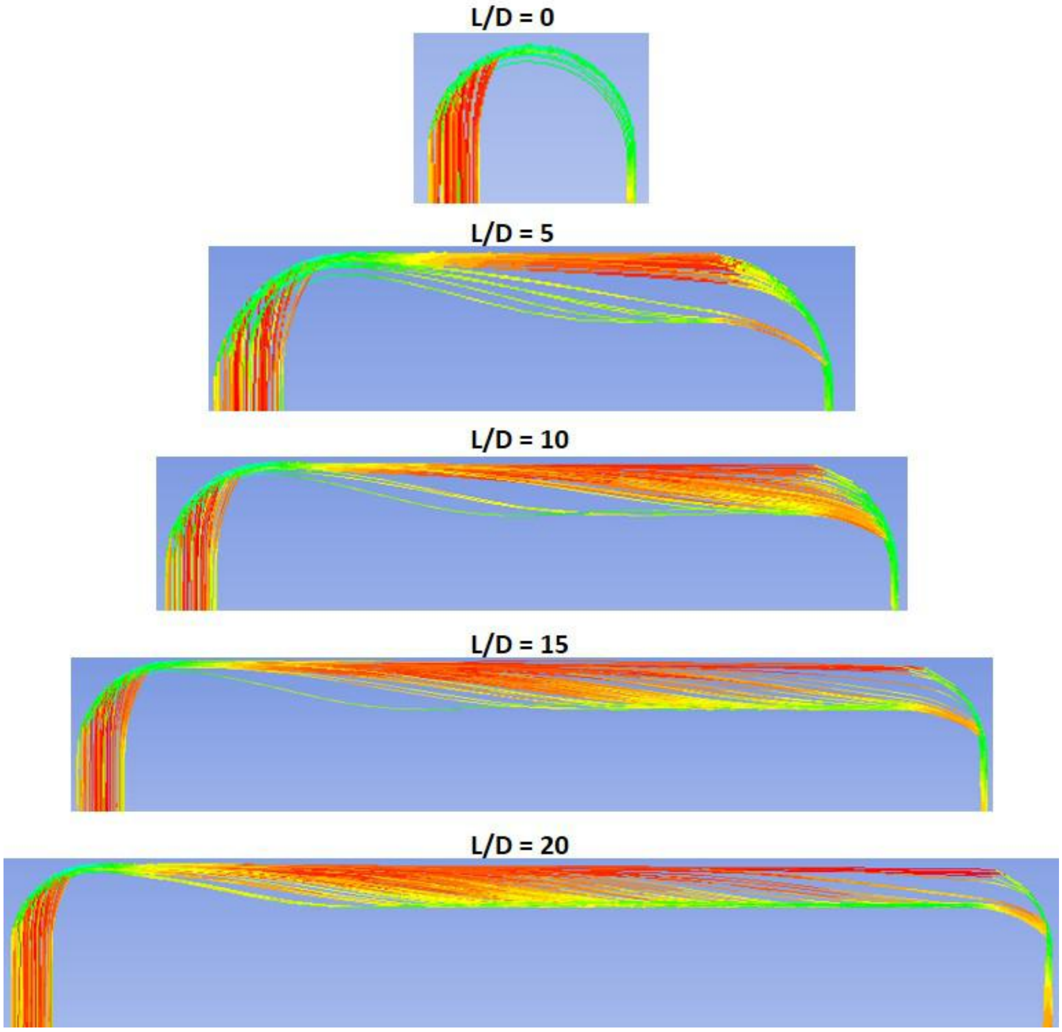

Figure 6.8: Particle Tracks in Geometry 1 - High Gas Velocity mixture condition

A similar behaviour observed in the particle tracks in Geometry 1 is seen in Geometry 2 as the normalized separation distance increases, and this can also be directly related to the erosion pattern in Elbow 2 in this case. Hence, the particle tracks plays a very vital role in the erosion pattern and location in pipelines. In Figure 6.9, the particles also settle more at the bottom of the horizontal section between Elbows 1 and 2 as L/D changes and the fluid develops and flows towards Elbow 2. The particles concentrate at the bottom of the pipe and negotiates the bend with more concentration at the elbow extrados and gets dragged across as they are lifted up against the force of gravity.

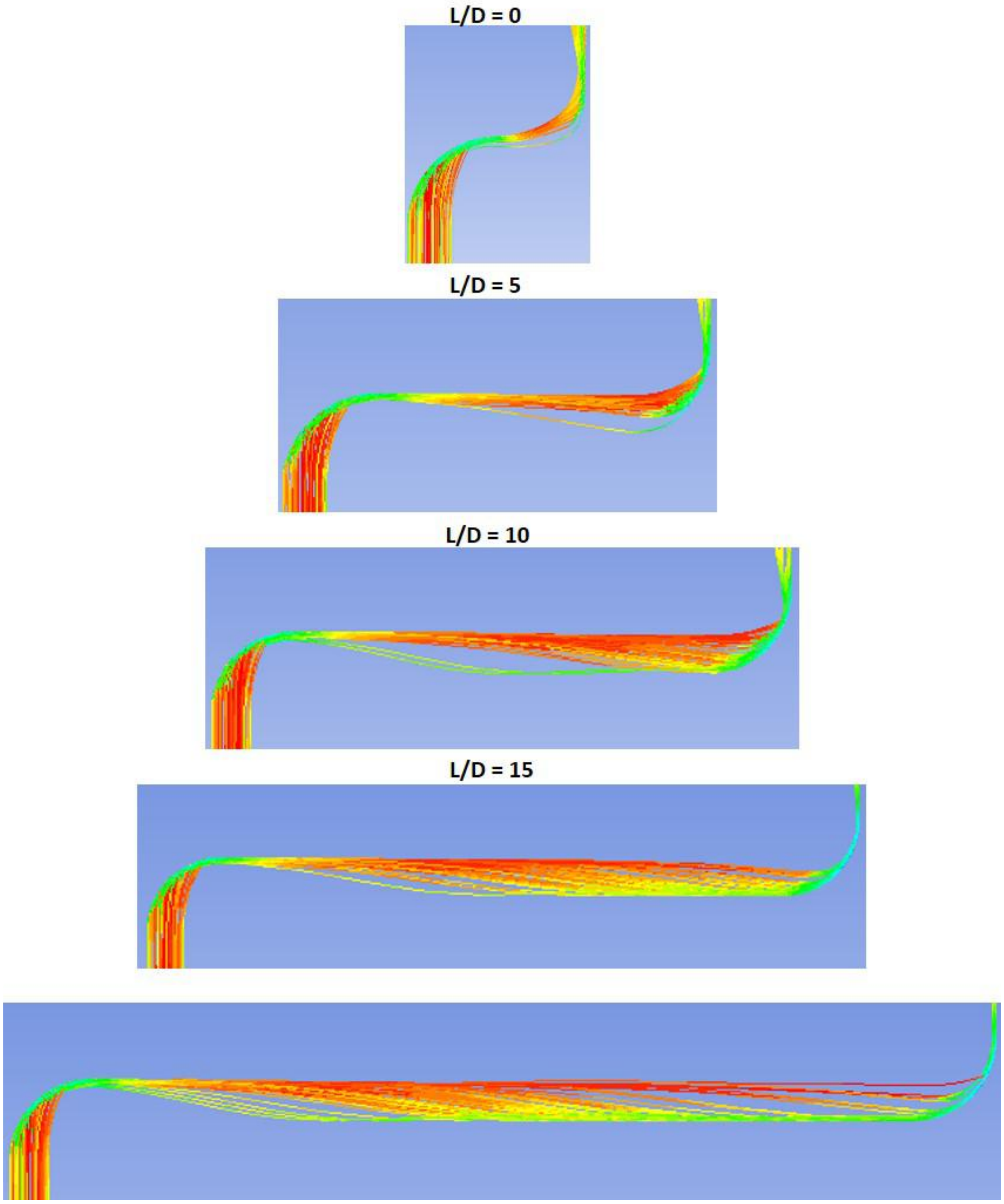

Figure 6.9: Particle Tracks in Geometry 2 - High Gas Velocity mixture condition

In Geometry 3 on the other hand (Figure 6.10), although a similar behaviour to the latter cases was observed in the particle tracks as L/D increases, however the path of the particles as they negotiate the bend is slightly different. Due to the orientation of Elbow 2, the particles get more concentrate more at the bottom of the the pipe section and Elbow 2. This can also be attributed to the force of gravity acting on the particles and the horizontal orientation of Elbow 2 in this geometry.

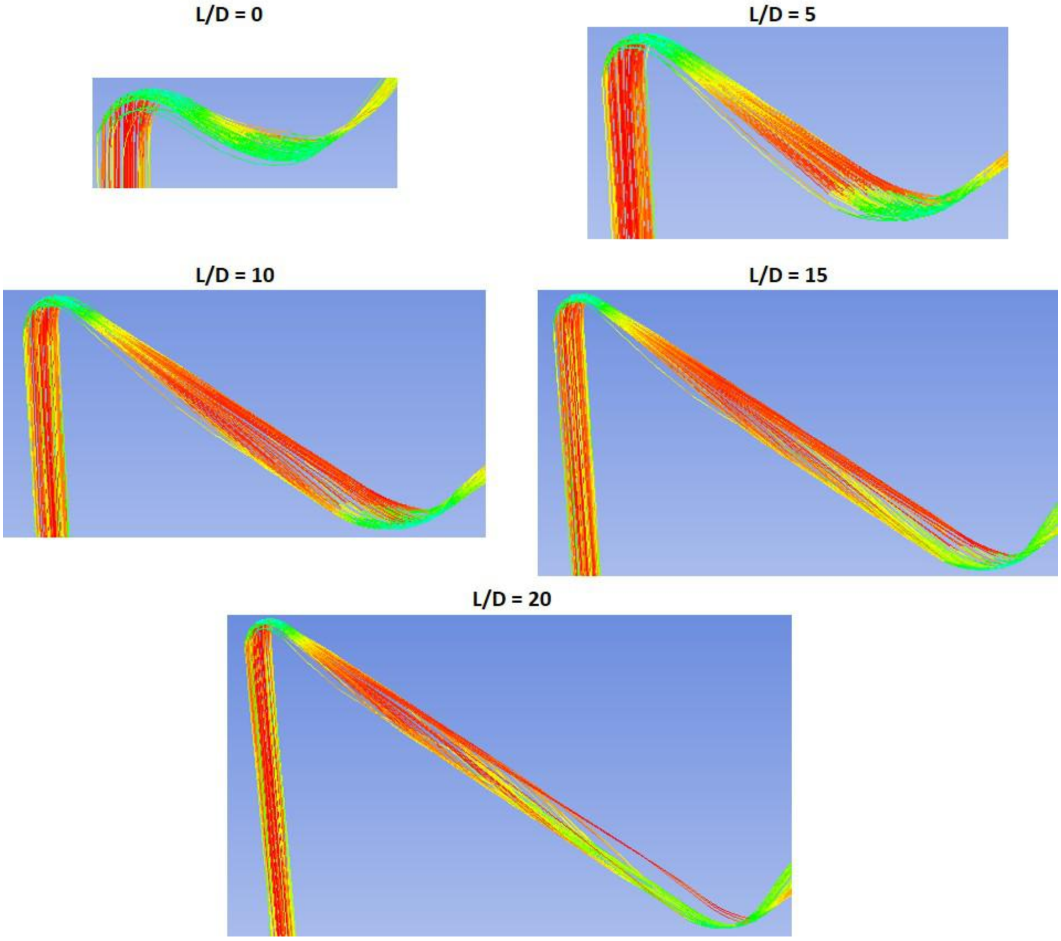

Figure 6.10: Particle Tracks in Geometry 3 - High Gas Velocity mixture condition

Low Gas Velocity Mixture Condition

When the carrier fluid has low gas velocity mixture properties, an equal influence of the normalized separation distance is obvious. A similar behaviour is observed in the particle tacks as the fluid flows towards Elbow 2 in Geometry 1 and 2 and L/D changes, see Figures 6.11 and 6.12. Although in Geometry 1, the sand particles tend to concentrate at the intrados of Elbow 2, this could be due to the high centripetal force acting on the particles while they are dragged via Elbow 2. The sand particles concentrate at the extrados of Geometry 2 as the fluid negotiates the bend. The centripetal force acting in Elbow 2 is much higher in Geometry 1 compared to Geometry 2. This observation hence informs the locations of erosion discussed for slug flow conditions in the previous section.

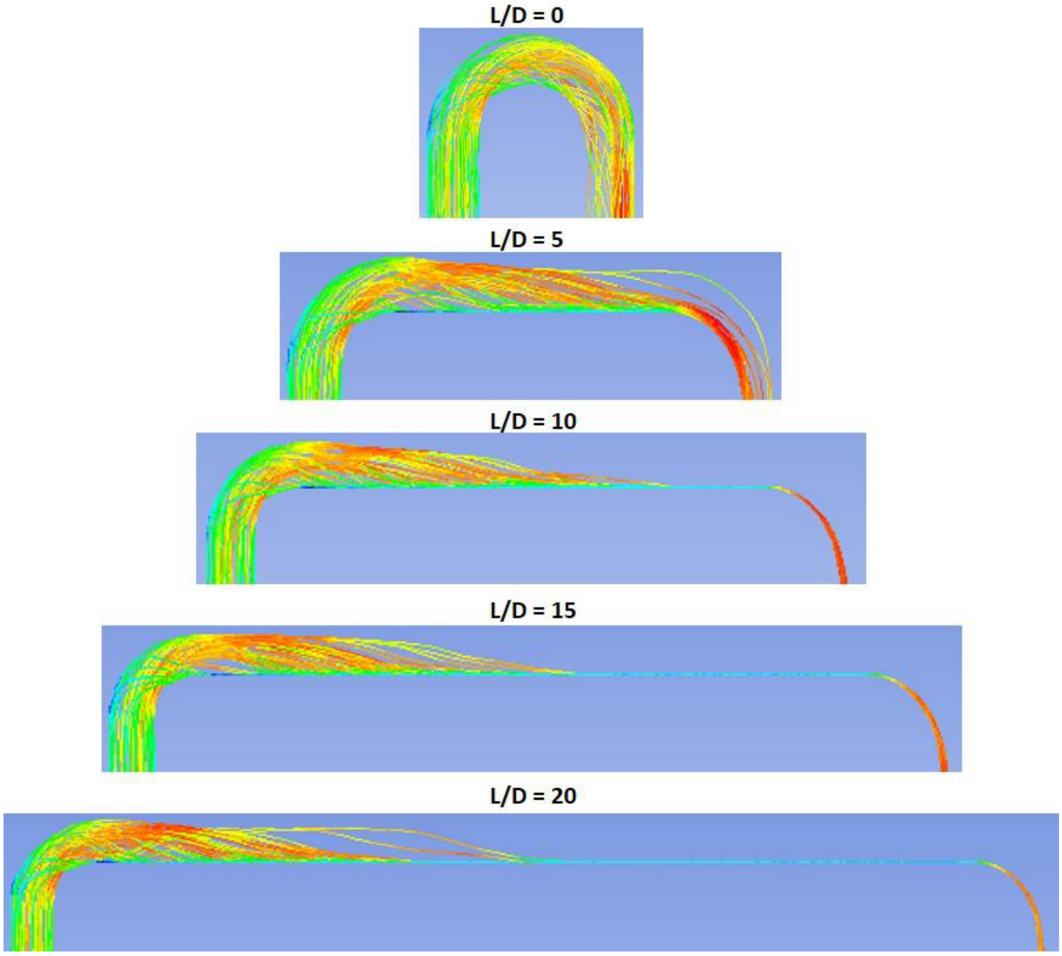

Figure 6.11: Particle Tracks in Geometry 1 - Low Gas Velocity mixture condition

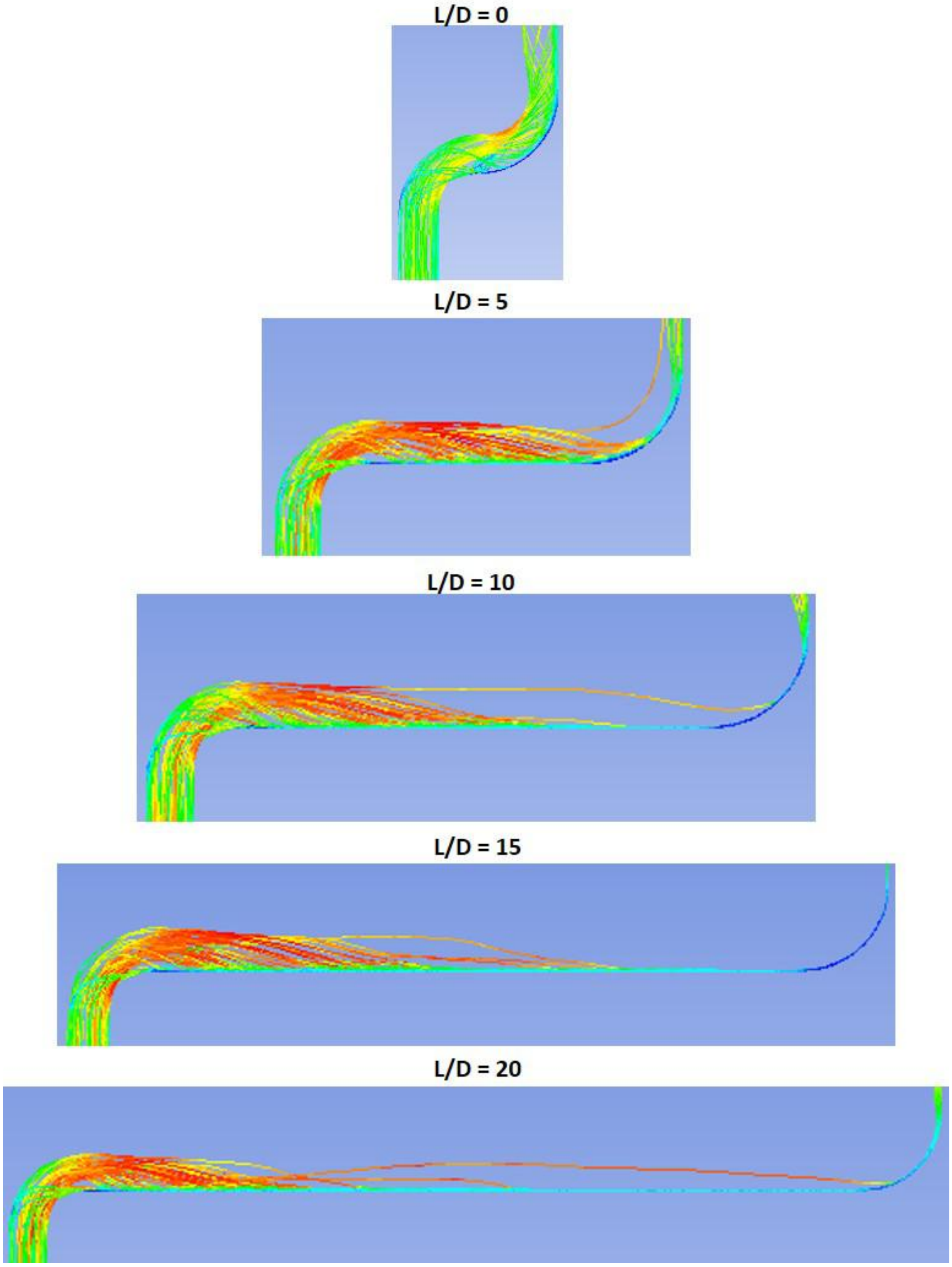

Figure 6.12: Particle Tracks in Geometry 2 - Low Gas Velocity mixture condition

Due to the orientation of Elbow 2 in Geometry 3, a behaviour similar to that observed at high gas velocity conditions is noticed in the particle tracks. The particle tracks however show a similar path to that of Geometry 1 and 2 in the horizontal section between Elbows 1 and 2 as the normalized separation distance increased from 0 to 20. Figure 6.14 shows the particle tracks in Geometry 3 when the carrier fluid has flow mixture properties with high gas velocity.

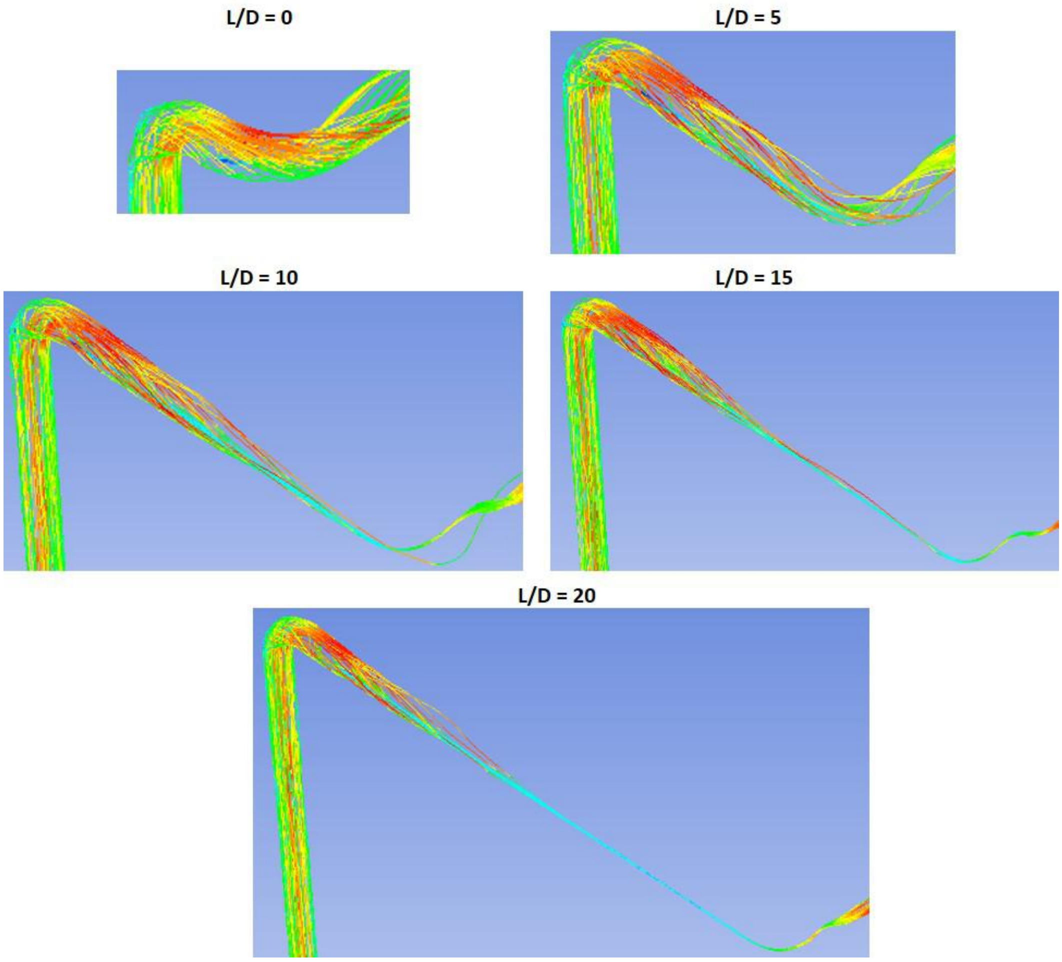

Figure 6.13: Particle Tracks in Geometry 3 - Low Gas Velocity mixture condition

Sand Concentration Profiles

The sand concentration profiles taken at slices along the normalized separation distance between Elbows 1 and 2 also ascertains the behaviour of the sand particles in the flow conditions and geometries under study. Figures 6.14 and 6.15 show the sand concentration profiles along L/D for Geometries 1, 2, 3 and both flow conditions. Cross-sectional planes have been created in the horizontal section between Elbows 1 and 2 at the outlet of Elbow 1 (EO), 0.2m after the outlet of Elbow 1 (AE1) and at 0.1m before Elbow 2 (BE2) to highlight the changes in particle tracks due to an increase in L/D. The most obvious change or influence is observed on the plane before Elbow 2. The cross-sectional profiles of the sand concentration for both flow conditions shows the same behaviour in all geometries, hence, the representation of all geometries in one flow conditions with one figure each. In Figures 6.14 and 6.15, the blue patches are indicative of when the sand particle concentration is lowest.

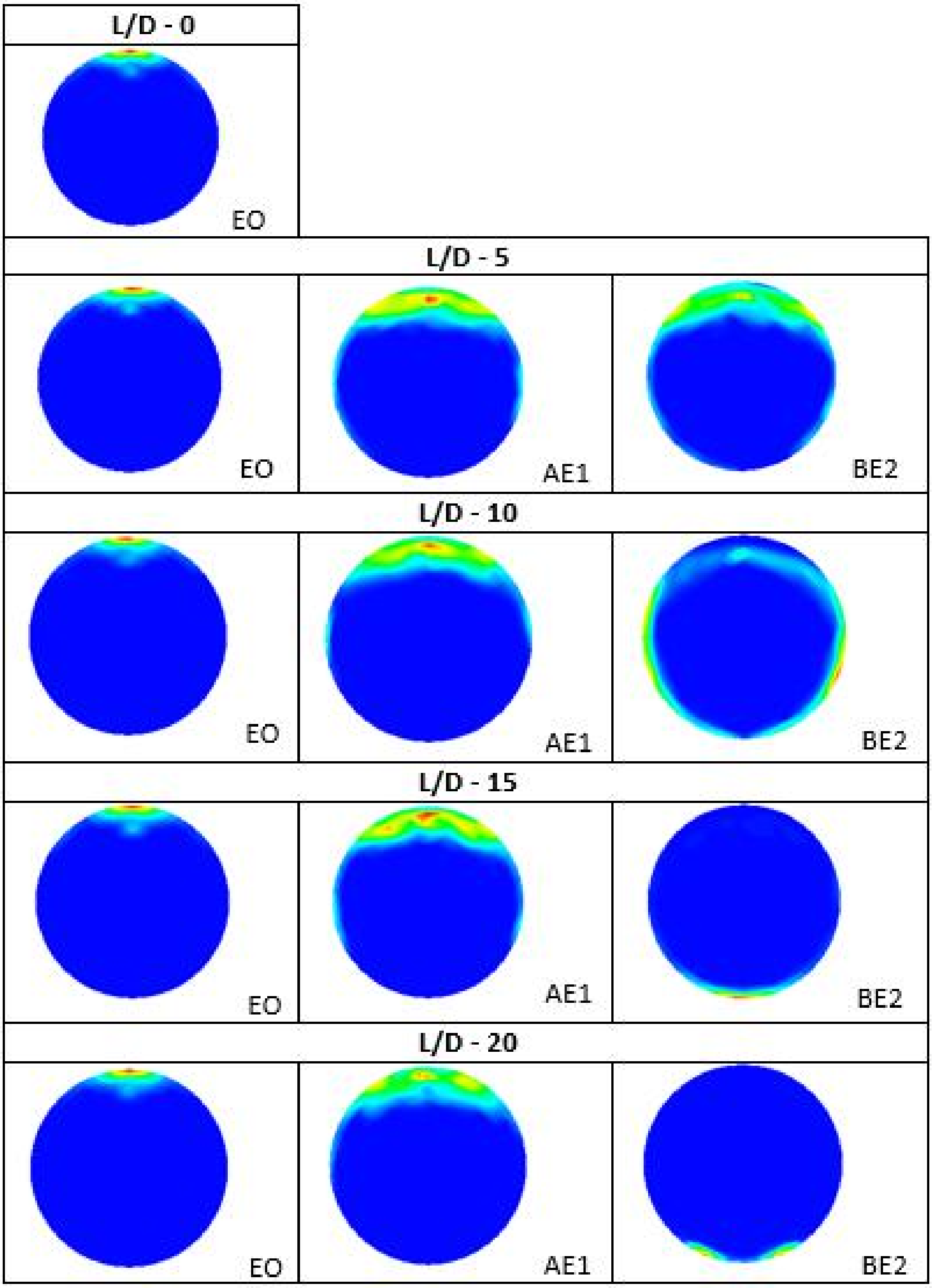

Figure 6.14: Sand Concentration Profiles - High gas velocity mixture condition

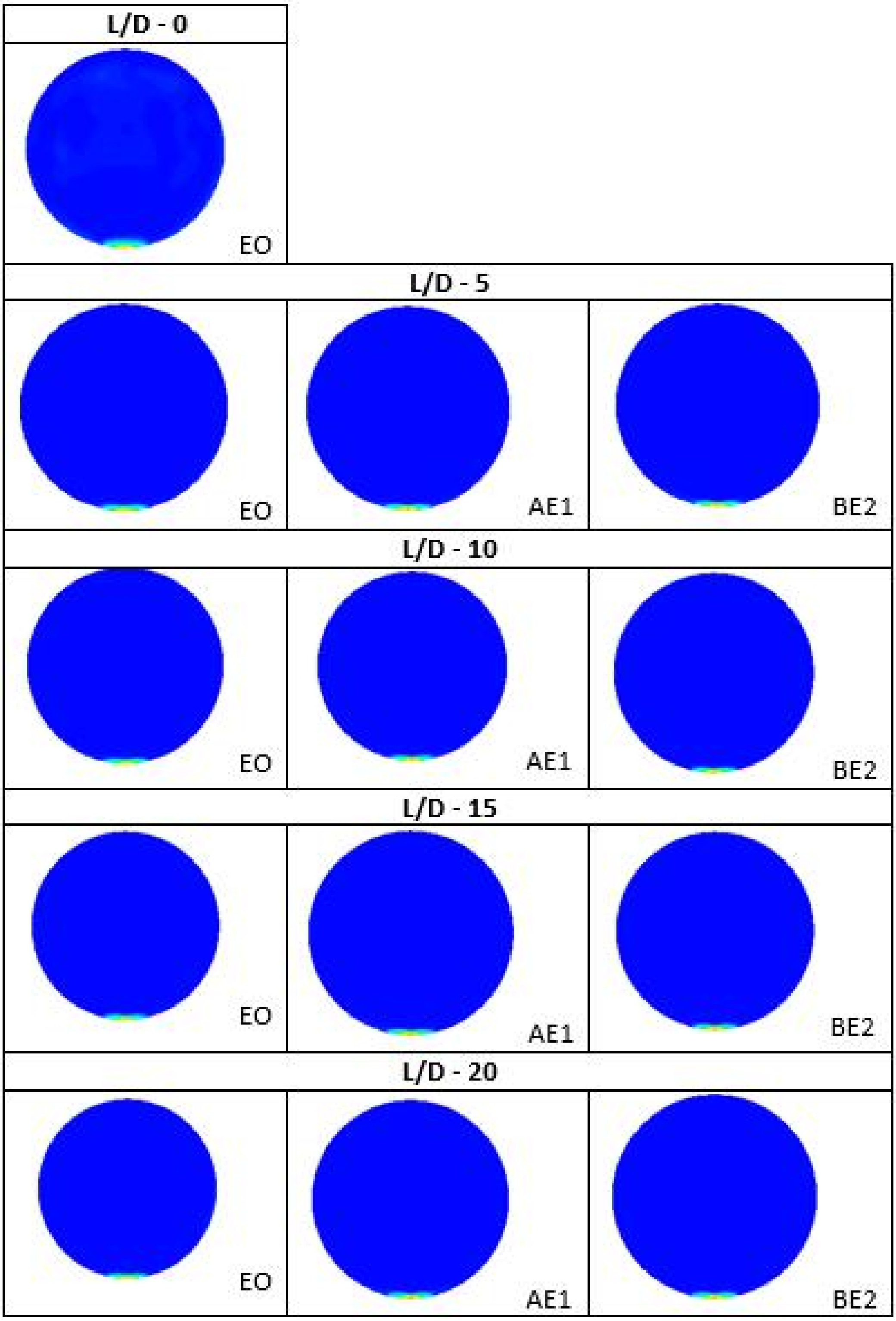

Figure 6.15: Sand Concentration Profiles - Low Gas Velocity mixture condition

6.3 Parametric Studies

6.3.1 Effects of Change in L/D on Erosion and Particle Concentration

Figures 6.16 and 6.17 show the effect of change in the normalized separation distance (L/D) on the erosion rates in Elbows 1 and 2 for the pseudo single phase conditions at high and low gas velocities flows respectively. For all cases under consideration, when the carrier fluid is in single phase both at high and low gas velocity conditions, average erosion rate in Elbow 1 remain independent of L/D. The magnitude of maximum erosion rates in Elbow 1 for both flow conditions also remained within a considerable range which just like the average erosion shows a negligible effect of the separation distance. However, in Elbow 2, a significant influence of the change in normalized separation distance is observed.

High Gas Velocity Mixture Condition

In Elbow 2, a significant effect of L/D on the magnitude of both the average and maximum erosion rates is visible. For mixture conditions with high gas velocity (Figures 6.16), as L/D increases, the magnitude of both the average and maximum erosion rates vary. From the results generated, irrespective of the orientation, Elbow 2 was subjected to the most erosion when the normalized separation distance, L/D, is 5. This is an indication that irrespective of the elbow orientation, a normalized separation distance of 5 must be avoided in order to ease flow operations and prevent gross erosive damage to Elbow 2.

The profile of the magnitude of average erosion rate in Elbow 2 shows the same behaviour across all geometries as L/D increased from 0 to 20, although more consistency is observed between L/D of 15 and 20 in Geometry 2 (Figure 6.16). And this further ascertains the importance of avoiding L/D of 5. Although, the magnitude of average erosion rates in Elbow 2 seems to be independent of that in Elbow 1, at some normalized separation distances (L/D), the erosion rate in both elbows should be of equal or similar magnitude. At a normalized separation distance of between 0 and 5, as well as between 5 and 10, the average erosion rates in Elbows 1 and 2 should be of similar magnitude while employing any of the three geometries studied, although that is not an established fact. Average erosion rate in Elbow 2 will however be minimum when the normalized separation distance (L/D) is 0 for Geometries 1 and 2, while it is minimum when the normalized separation distance is 20 for Geometry 3. It is also important to note that after a normalized separation distance of 10, the magnitude of average erosion in Elbow 2 become considerably lower than that of Elbow 1. And this drops consistently as L/D increased. In a situation like this, Elbow 1 will worn out due to sand particle erosion damage faster than Elbow 2. The magnitude of maximum erosion is highest when L/D is 20 in Geometry 1 while it is when L/D is 5 for Geometry 2. For Geometry 3, magnitude of maximum erosion is highest when L/D is 0. L/D of 5 therefore remains a black spot as it is further highlighted from the data generated for Geometry 2.

In Figures 6.16 to 6.19 G1, G2 and G3 represents Geometry 1, Geometry 2 and Geometry 3 respectively.

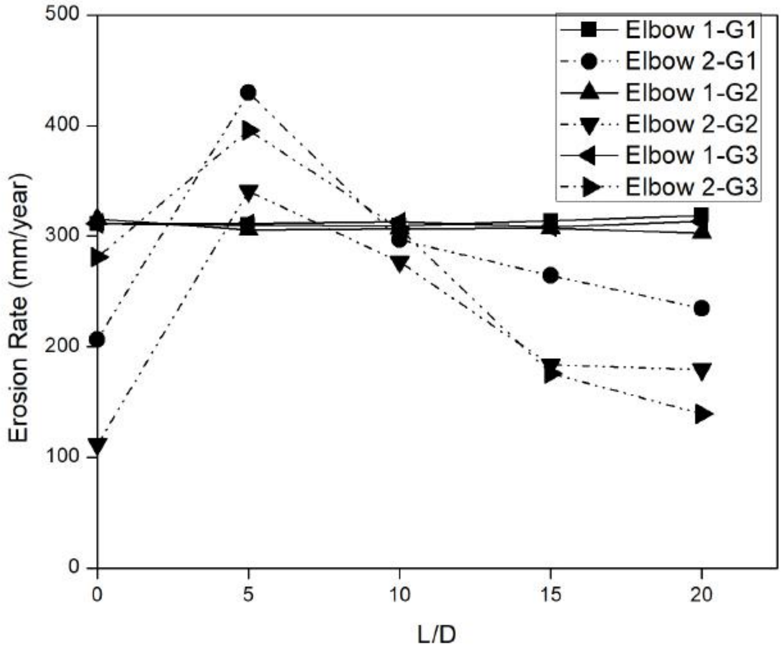

(a) Average Erosion Rates

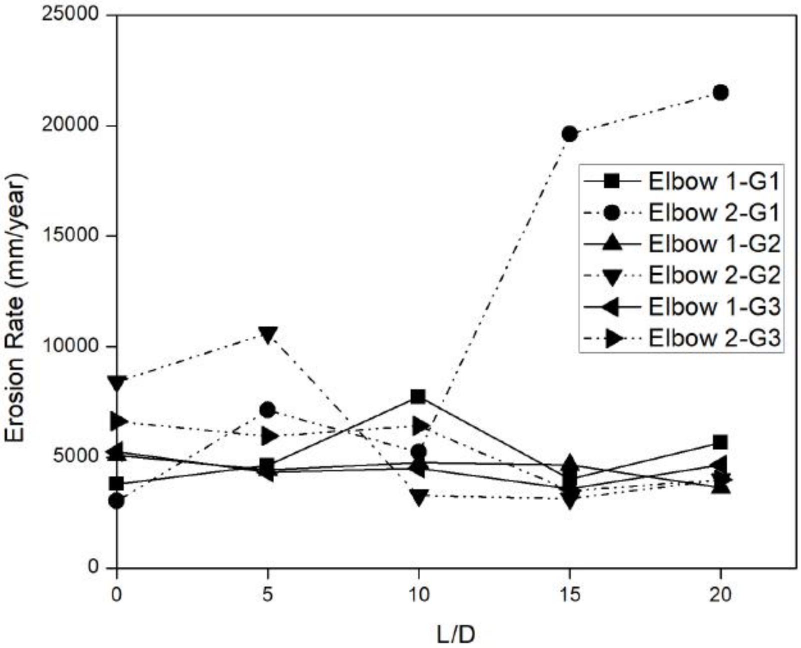

(b) Maximum Erosion Rates

Figure 6.16: Effects of L/D on Erosion Rates at high gas velocity

Low Gas Velocity Mixture Condition

For the pseudo single-phase flow at the low gas velocity, the effect of L/D on the magnitude of average and maximum erosion rates in Elbows 2 is also prominent (See Figure 6.17). Unlike for the flow condition at high gas velocity, the magnitude of average erosion rates in Elbow 2 shows varying behaviour as L/D changes across all geometries. In Geometry 1, the magnitude of average erosion rate became independent of the normalized separation distance after L/D of 5 with little or no variance till L/D of 20. The average erosion rate is highest when L/D is 0 and minimum when L/D is 5. A contrast to the observation in churn flow. The magnitude of maximum erosion however shows a direct inverse behaviour to that of the average erosion in Elbow 2, while the average erosion in elbow 2 remained consistently lower than that in Elbow 1 after L/D of about 1, the maximum erosion remained higher after L/D of 0.5.

For Geometry 2, the magnitude of average erosion rate changes continuously as L/D changes. After L/D of about 2, the average erosion rate in Elbow 2 remained consistently higher degree than that in Elbow 1. A direct relationship could also be observed between the two elbows between L/D of 0 and 10, as the average erosion rate reduces in Elbow 1, it also drops in Elbow 2, this communication breaks down after L/D of 10. Also, the magnitude of average and maximum erosion rates are minimum at L/D of 10 while the average erosion rate is maximum when the normalized separation distance is 20. Although the profiles vary, the magnitudes of maximum and average erosion rates are expected to be similar between normalized separation distances of 0 and 5.

The magnitudes of the average and maximum erosion rate are consistently higher in Elbow 2 than that of Elbow 1 in Geometry 3, and at no separation distance is the erosion in both elbows equal or expected to be equal. The average erosion rate is independent of the normalized separation distance between L/D of 0 and 5, and after it remained considerably on the rise as the normalized separation distance increased from 5 to 20. The average erosion rate is highest at L/D of 20. In Geometry 2 and

3, L/D of 20 should be avoided if the life span of Elbow 2 would be elongated when carried fluid has similar properties to that of slug flow studied.

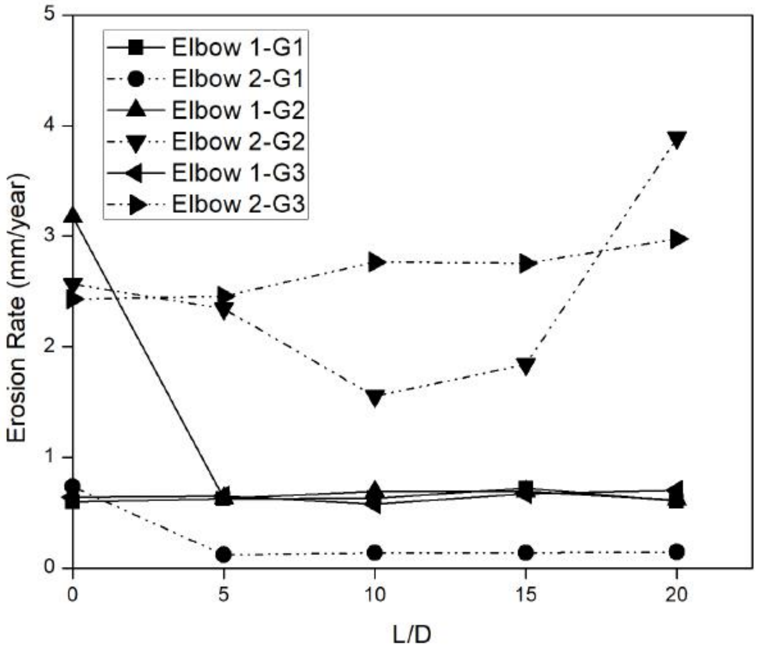

(a) Average Erosion Rates

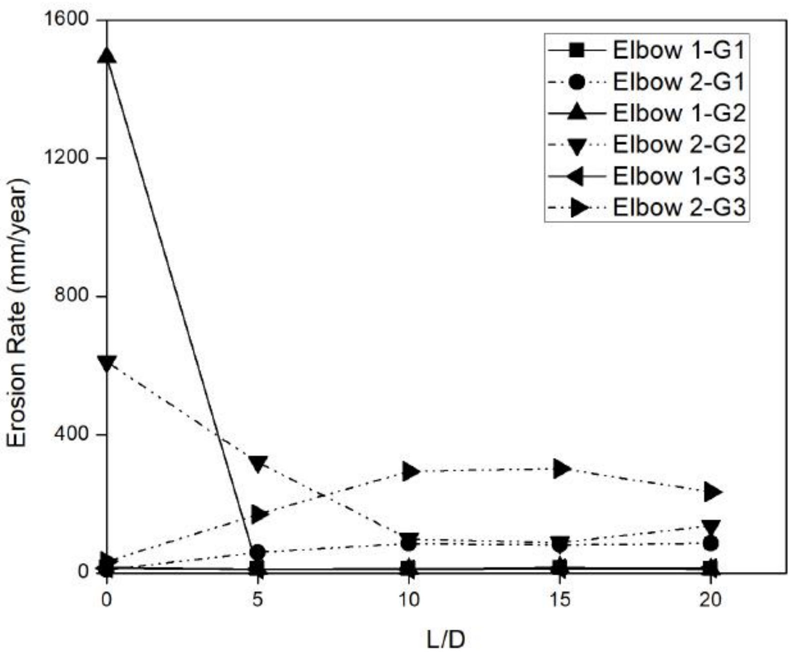

(b) Maximum Erosion Rates

Figure 6.17: Effects of L/D on Erosion Rates at low gas velocity

Sand Concentration

A change in the normalized separation distance also has a definite influence on the concentration of sand particles in both Elbows 1 and 2 for both the churn and slug flow conditions. Just as it was reported earlier in the case of the magnitude of erosion rates in Elbow 1, the sand particle concentration in Elbow 1 in all cases studied also remained fairly independent of L/D for both the slug and churn flow conditions. However, a telling influence in observed in Elbow 2.

For the pseudo single phase condition with high gas velocity, in Geometry 1, the effect of the change in the normalized separation distance is quite obvious. As L/D increases from 0 to 20, sand particle concentration reduces as shown in Figure 6.18. Between a normalized distance of 0 and 10, particle concentration is higher in Elbow 2 than that in Elbow 1, after L/D of 10, the concentration dropped below that in Elbow 1 continuously till L/D of 15. The concentration became more or less independent of L/D between 15 and 20, however, a further analysis of normalized separation distances greater than 20 can provide more insights on this.

In Geometry 2, a reverse of the behaviour of the sand particle concentration in Geometry 1 is observed, this could be attributed to the inverse relationship in the orientation of Elbow 2 in both geometries. The sand particle concentration increases as the normalized separation distance between Elbows 1 and 2 increases from 0 to 20 (Figure 6.18). However, a bit of consistency and reduced influence of L/D is also observed between L/D of 15 and 20. Particle concentration in both Elbows 1 and 2 is expected to have the same magnitude at a normalized separation distance of about 5. After L/D of 5, particle concentration in Elbow 2 remained consistently higher than that in Elbow 1. See Figure 6.18.

Unlike Geometry 1 and 2 that can be related, the behaviour of sand particle concentration in Elbow 2 of Geometry 3 is completely different. Although, just like the others, between the normalized separation distance of 15 and 20, the influence of L/D is observed to have reduced considerably. In some cases it might be considered negligible within that region. Between L/D of 0 and 15, the magnitude of sand concentration dropped from 10.29 kg/m^3 to 6.73 kg/m^3 at L/D of 5. And between L/D of 5 and 15, there is a rapid increase in the concentration sand particles in Elbow 2. At no point is the magnitude of the sand particle concentration in Elbows 1 and 2 expected to be the similar between the normalized separation distance of 0 and 20. But the particle concentration in Elbow 2 remained consistently higher than that in Elbow 1.

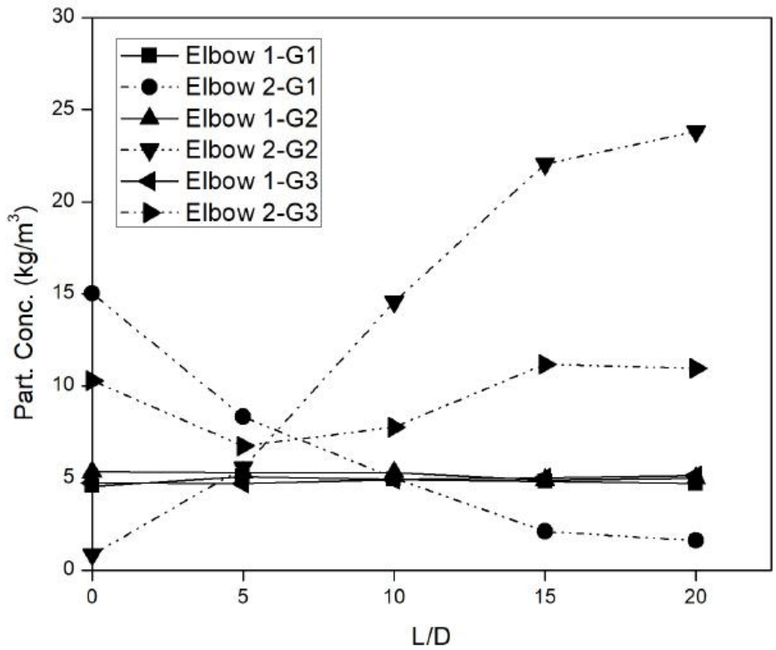

Figure 6.18: Sand Concentration at high gas velocity

Figures 6.19 shows the behaviour of the sand particle concentration in Geometries 1, 2 and 3 as the normalized separation distance changes at low gas velocity condition. In Geometry 1, the particle concentration dropped as the normalized separation distance (L/D) increased from 0 to 5 but a consistent increase in the sand accumulation at Elbow 2 is observed after L/D of 5 till 20. In other words, as L/D increases from 5 to 20, sand particle concentration Elbow 2 also increases. In Geometry 2 on the other hand, the sand particle concentration increased as L/D increased from 0 to 5, but a rapid drop occurred when L/D increased to 10. Between L/D of 10 and 20, the influence of the normalized separation distance on the particle concentration appears to have reduced considerably, there is however a slight drop in sand concentration when L/D is 20.

In Geometry 3, the sand particle concentration in Elbow 2 remained consistently higher than that in Elbow 1 between normalized separation distances of 0 and 20 just as observed when the carrier fluid has the churn flow mixture properties. And at no particular L/D is it expected that the particle concentrations in both elbows will be similar. Although the influence of L/D is not as pronounced as in the other geometries, a drop in observed as L/D increased from L/D of 0 to 5, between 5 and 15 there is a consistent increase in the particle concentration. And as L/D increased from 15 to 20, a drop occurred in the concentration of particles in Elbow2.
While it is not expected to record an equal magnitude of particle concentration in Elbows 1 and 2 for Geometries 1 and 3 between the normalized distances of 0 and 20, it is expected for it to be similar when L/D is 1.5 in Geometry 2.

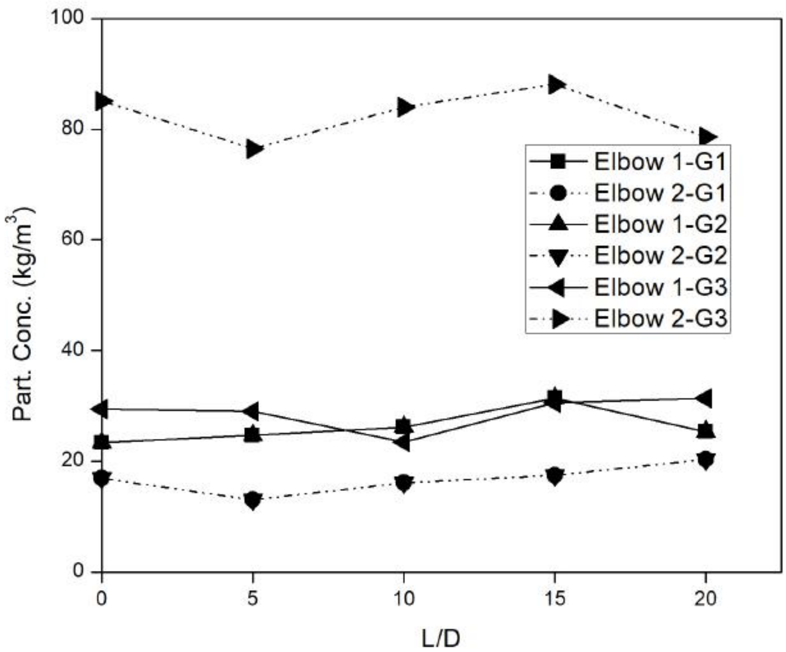

Figure 6.19: Sand Concentration at low gas velocity

6.3.2 Effects of change in orientation of Elbow 2 on Erosion

With the orientation of Elbow 1 kept constant, the change in the orientation of Elbow 2 has varying effects on the magnitudes of average and maximum erosion rates in Geometries 1, 2 and 3 investigated. Figures 6.20 and 6.21 show the profiles of the magnitude of the average and maximum erosion rates in Elbow 2 for Geometries 1, 2 and 3 for the high and low gas velocity flow conditions.

When the carrier fluid has the high gas velocity properties (Figure 6.20), and the normalized separation distance is less than 15, Elbow 2 of Geometry 2 is subjected to the least erosion damage. At L/D of 0, Elbow 2 is subjected to the most average erosion in Geometry 3 while the average erosion to Elbow 2 in Geometry 1 lies between that of Geometry 3 and 2. At L/D of 5, Elbow 2 of Geometry 1 becomes the most erosive with Geometry 2 remaining the least, this is maintained till the normalized separation distance of 20. The magnitude of average erosion in Elbow 2 of Geometry 3 dropped lower than the other two geometries with that of Geometry 2 observed as the second most erosive at L/D of 20. Comparing the magnitude of the maximum erosion rate further affirms the argument that Elbow 2 will be subjected to the most erosion damage in Geometry 1 if mounted at a normalized separation distance greater than 10. At a normalized separation distance (L/D) of 10, Elbow 2 is subjected to the most erosion damage due to sand particle impact in Geometry 3 and the least in Geometry 2.

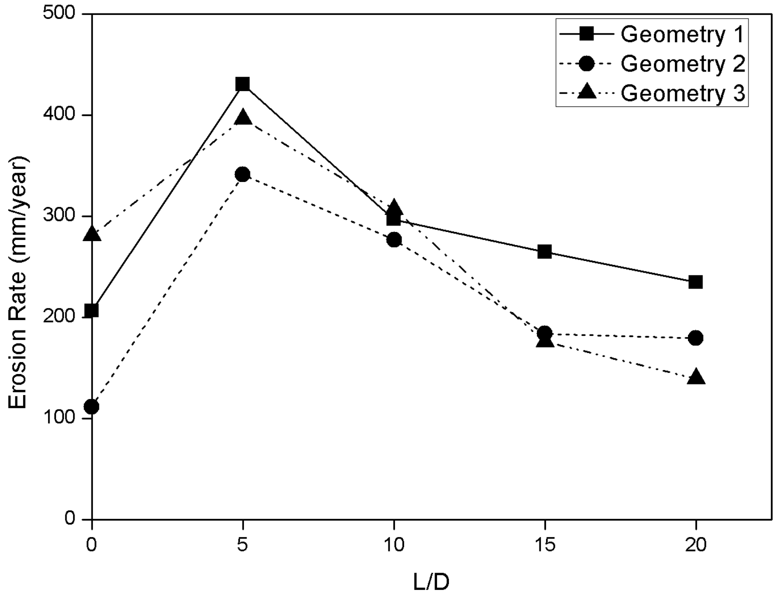

(a) Average Erosion Rates

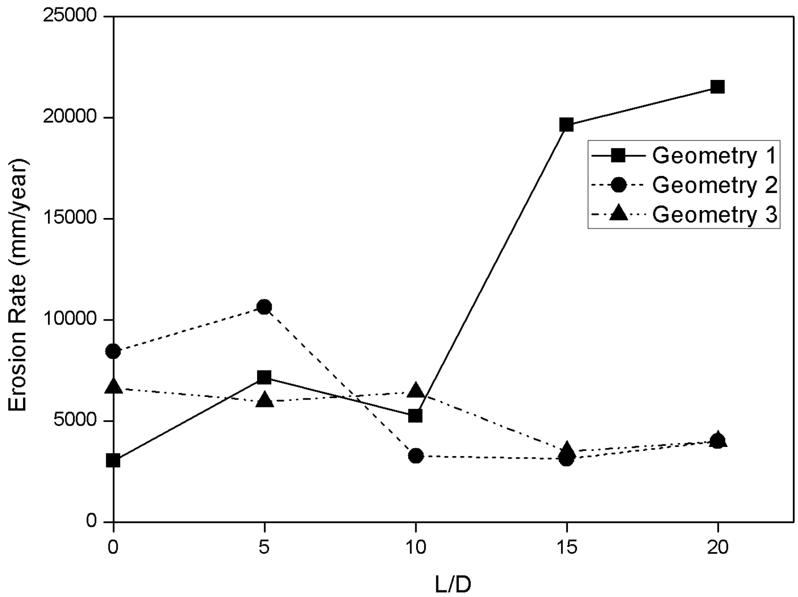

(b) Maximum Erosion Rates

Figure 6.20: Effects of change in orientation of Elbow 2 on erosion rate at high gas velocity

Figure 6.21 shows the comparison of the magnitude of erosion rates in Elbow 2 for Geometries 1, 2 and 3 when carrier fluid has low gas velocity properties. At a normalized separation distance (L/D) of 0, Elbow 2 is subjected to the most average erosion damage in Geometry 2 and the least in Geometry 1. Although the difference in magnitude between Geometries 2 and 3 is a handful. At L/D of 5, Elbow 2 becomes slightly more erosive in Geometry 3 than 2 while Geometry 1 remained the least erosive. As L/D increases, erosion damage in Elbow 2 of Geometry 2 dropped further and increased again after L/D of 10. At L/D of 20, Elbow 2 in Geometry 2 is prone to the most erosion damage. It is the least in Geometry 1 across all normalized separation distances studied.

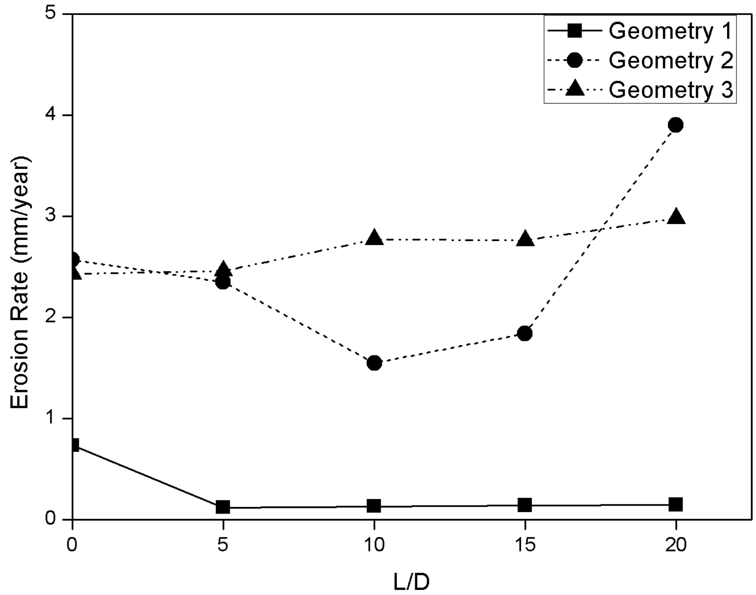

(a) Average Erosion Rates

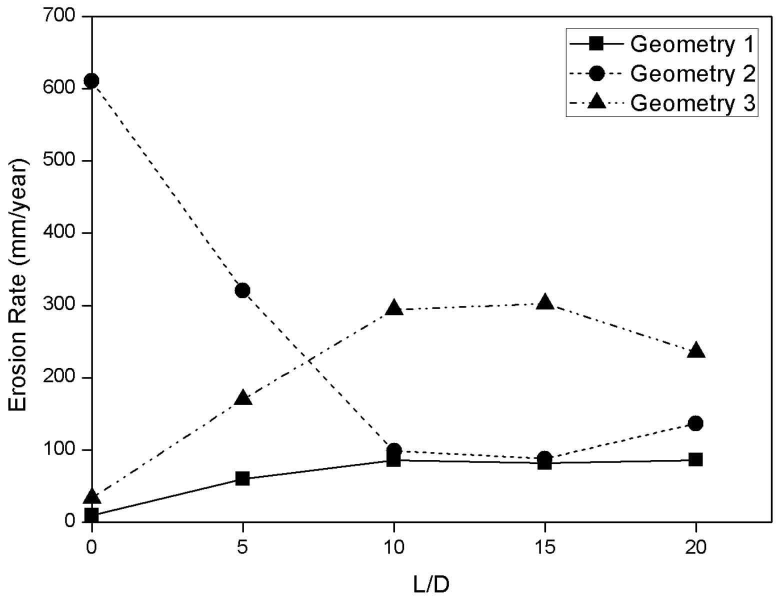

(b) Maximum Erosion Rates

Figure 6.21: Effects of change in orientation of Elbow 2 on erosion rate at low gas velocity

The concentration of the sand particles is also influenced by the orientation of Elbow 2 in both flow conditions under study. Figure 6.22 shows the comparison of the sand particle concentration in Elbow 2 of Geometries 1, 2 and 3 across all normalized separation distances. When the carrier fluid has high gas velocity properties (Figure 6.22a), sand particle concentration in Elbow 2 is highest in L/D of 0 in Geometry 1 and lowest in Geometry 2. A contrast of this is however observed after a normalized separation distance of 5, sand particle concentration dropped lower in Geometry 1 than that in Geometry 2. The volume of sand particle concentrated in Elbow 2 remained higher than the Geometries 2 and 3 in Geometry 2 till L/D of 7. Between L/D of 8 and 20, volume of sand particle in Elbow 2 is lowest in Geometry 1. The volume of sand in Elbow 2 of Geometry 3 remained in between that of Geometries 1 and 2 as the normalized separation distance changes.

Figure 6.22b shows the comparison of sand particle concentration in Elbow 2 when the carrier fluid has slug flow mixture properties. The volume of sand particle in Elbow 2 in Geometry 2 is clearly higher than the other geometries across all normalized separation distance under investigation. However, at L/D of 10, 15 and 20, the difference in the volume of particle concentration between Geometry 2 and Geometries 1 and 3 reduced considerably compared to at L/D of 5 of 0. Concentration of sand particles in Elbow 2 in Geometry 3 is also consistently higher than that in Geometry 1.

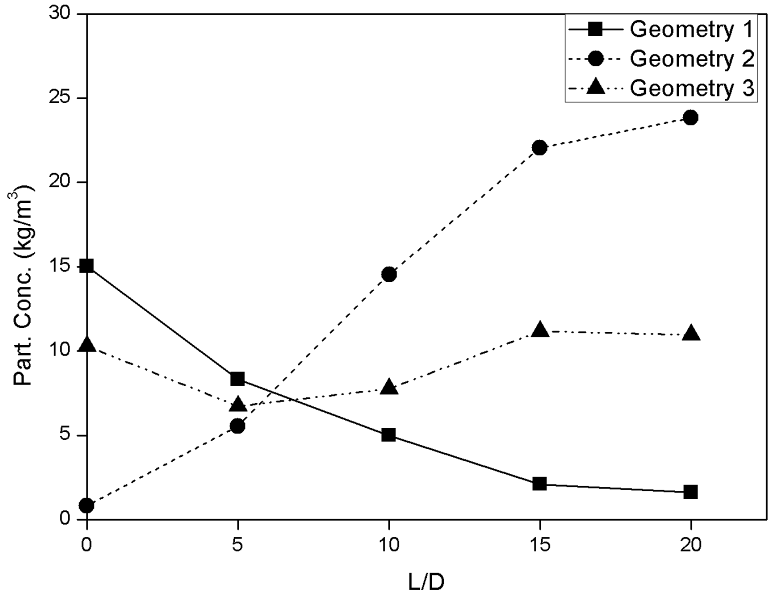

(a) High Gas Velocity

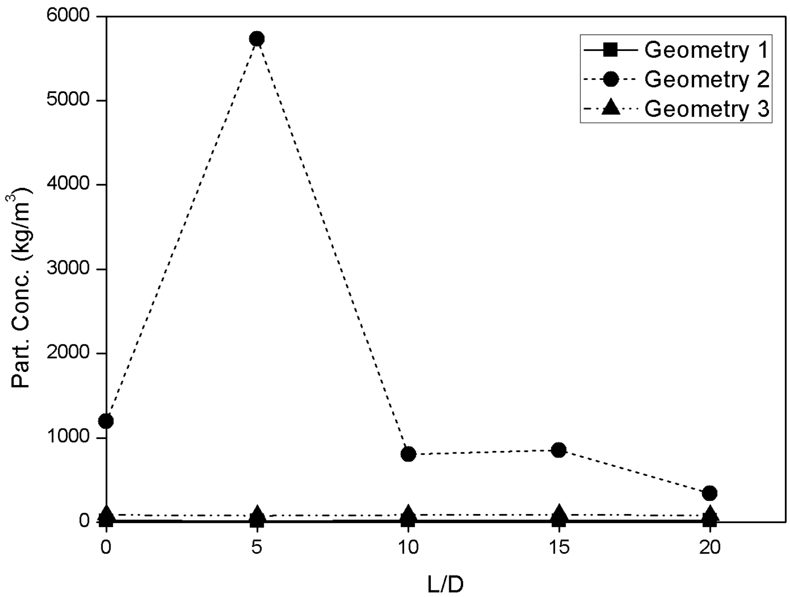

(b) Low Gas Velocity

Figure 6.22: Effects of change in orientation of Elbow 2 on sand concentration

6.3.3 Effects of change in Gas Velocity on Erosion Rates

Figures 6.23 to 6.25 show the comparison of the magnitude of average and maximum erosion rates in Elbows 1 and 2 when the carrier fluid has high and low gas properties.

Both Elbows 1 and 2 are observed to be subjected to much higher erosion rates, both average and maximum, when the flow properties are that of high gas velocity flow when compared to the flow with low gas velocity. For Geometry 1, the average erosion rates in Elbows 1 and 2 are higher when the mixture flow has high gas velocity than the low gas velocities with average factors of 500 and 950 respectively. In Geometry 2, they are higher by a factors of 260 and 90. While in Geometry 3, by 480 and 96 respectively.

This huge difference observed is as a result of the low gas velocity mixture condition forming a much heavier cushion effect at the pipe bends with a fluid density of 250.92 and also more more viscous effect, with a viscosity of 2.644×10^{-06}, compared to the high gas velocity mixture condition with a density and viscosity of 29.188×10^{-05} and 4.50×10^{-05} respectively. The fluid film formed around the elbow surface reduces the rate or intensity at which the sand particles impinges on the pipe surfaces when carrier fluid is in slug flow condition. Hence, more erosion damage to Elbows 1 and 2 when carrier fluid has high gas velocity mixture properties than at low gas velocity.

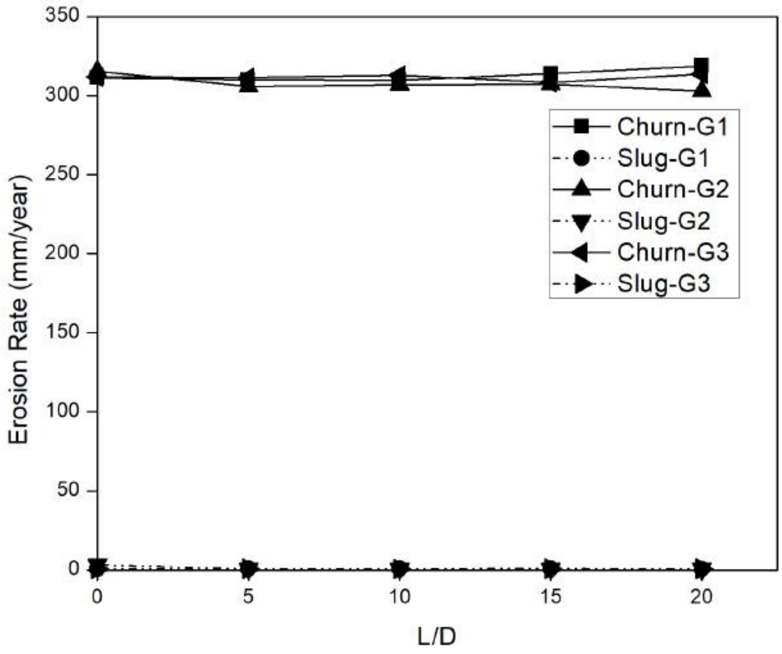

(a) Average Erosion Rates

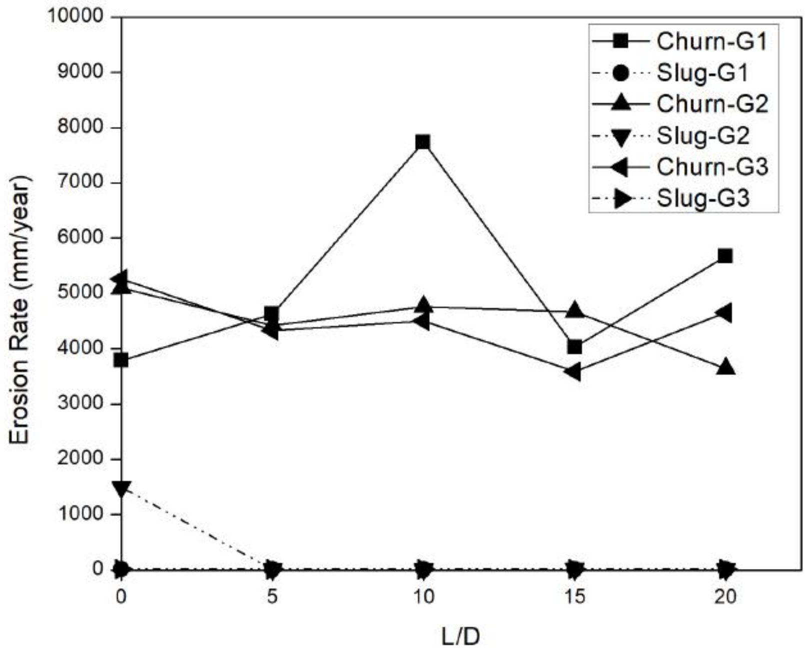

(b) Maximum Erosion Rates

Figure 6.23: Effects of change in flow velocity on Erosion Rates in Elbow 1

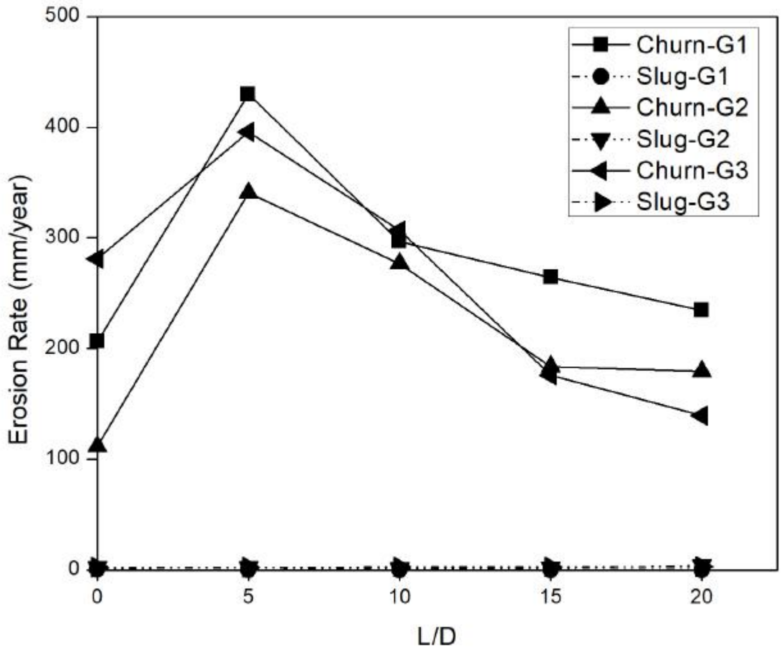

(a) Average Erosion Rates

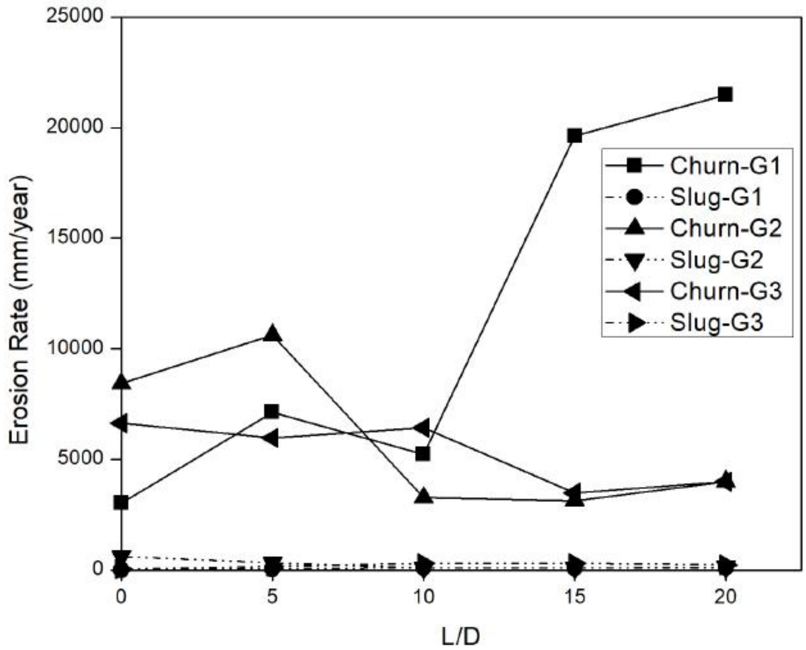

(b) Maximum Erosion Rates

Figure 6.24: Effects of change in flow velocity on Erosion Rates in Elbow 2

Figures 6.25 shows the comparison of the sand particle concentration in both flow conditions across the normalized separation distances under study. A change in flow velocity is also observed to have a significant influence on the volume of sand particles in Elbows 1 and 2. A contrast of the observation in the case of erosion rates explained earlier is observed. Here, the volume of sand particles concentrated in Elbows 1 and 2 in the low gas velocity condition is higher than that in the high gas velocity condition across all geometries. In Geometry 2 in particular, from a normalized separation distance (L/D) of 5 to 20, there is just a slight difference in the sand particle concentration in Elbow 1. Also in Elbow 2, from L/D of 10 to 20, the difference in sand particle concentration in the elbows between the flows is lower compared to when the normalized separation distance is 0 and 5. Sand concentration remained glaringly higher when the carrier fluid has low gas velocity mixture properties than when with high gas velocity. This behaviour of the sand particle concentration in the flows can also be attributed to the difference in the flow velocities and densities of the flow. For the lighter fluid with churn flow properties, flowing at a high velocity of 10.6 m/s compared to the low gas velocity of 1.2 m/s, at the elbow section, the flow with the high velocity would navigate the bend faster compared to the slow fluid. Hence, preventing the particles from settling at the pipe bend section irrespective of the particle density.

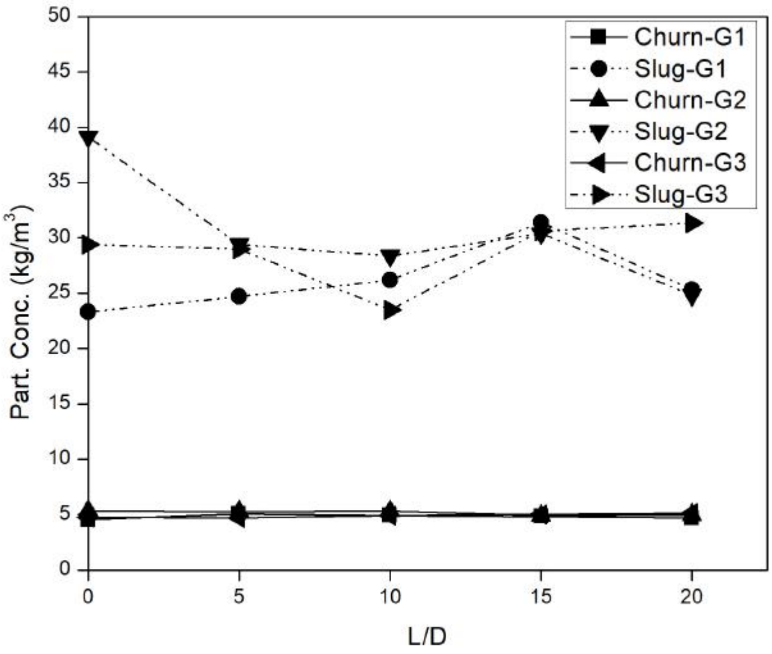

(a) Elbow 1

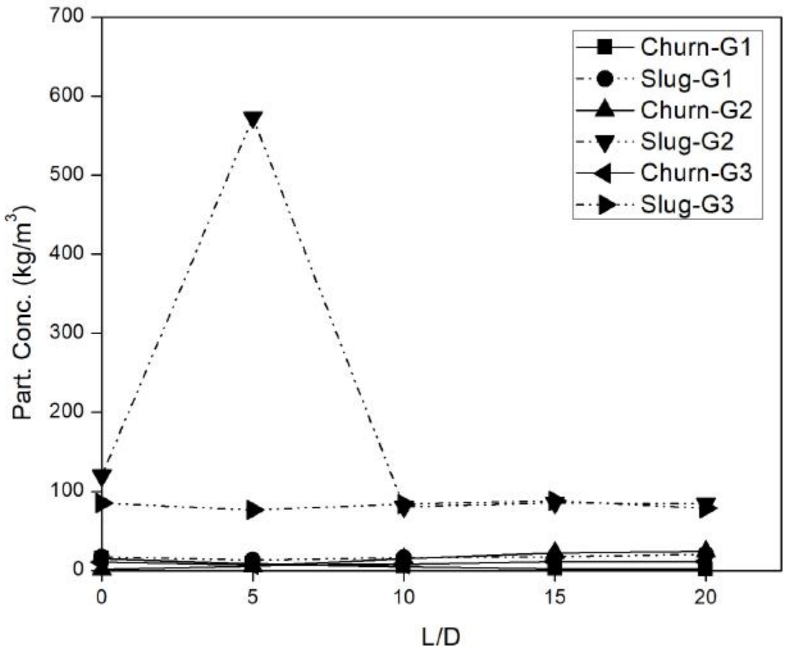

(b) Elbow 2

Figure 6.25: Effects of change in flow velocity on Sand Concentration

6.4 Summary of Results

Erosion behaviour in elbows mounted in series was studied numerically with complex multiphase carrier fluids resolved using a pseudo single-phase (mixture) modelling concept. Sand particles were injected and tracked appropriately, and the erosion damage on the pipe due the sand particle impact was analyzed. And the consistency of the erosion prediction (location and magnitude) for Elbow 1 in all of the geometries and flow conditions under study ascertains the accuracy and capability of the model setup employed for this study.

The single phase mixture at high gas velocity is found to be highly erosive compared to that at low gas velocity. This is as a result of the much higher mixture density and viscosity of the low gas velocity condition, as well as its low fluid velocity when compared to the flow with high gas velocity properties. The high density and viscosity results in high build up of fluid and formation of thick films at the pipe elbows as the fluid flows through, this reduces the intensity with which the particles impact on the pipe wall as well as their cutting effects, hence reducing the damage the bends are subjected to.

Erosion in Elbow 1 for both flow conditions remain independent of the geometry and normalized separation distance between the elbows. However, in Elbow 2, erosion rate is highly influenced by the normalized separation distance between the two elbows as varying behaviour is observed across all L/Ds and geometries. In the churn flow mixture condition, Elbow 2 is subjected to the most average erosion damage when the normalized separation distance is 5, hence at these conditions, the pipe network will worn out faster than others during service. While in slug flow mixture condition, it is subjected to the most sand erosion damage when the normalized separation distance (L/D) is 20 for both Geometries 2 and 3. In Geometry 1, it is subjected to most erosion damage when L/D is 0. The pipe network would therefore worn out faster at L/D of 20 in Geometries 2 and 3, and when L/D is 0 in Geometry 1. In general, the best operating condition for Elbow 2 in all geometries studied is; for churn flow -

after a normalized separation distance of 10. For slug flow condition, this varies as the orientation of Elbow 2 changes. For both elbows, Geometry 3 and Geometry 1 will be the best pipe network operating conditions for the high and low gas velocity flow conditions respectively.

When the carrier fluid has the high gas velocity mixture properties, at virtually no separation distance is a significant relationship observed between the erosion rates in Elbows 1 and 2. While with low gas velocity properties, a linear relationship is observed between the average erosion rates in Elbows 1 and 2 in geometries 1 and 3. In geometry 3, a relationship could not be properly ascertained for erosion magnitudes within the conditions studied.

Finally, the change in flow direction upstream of Elbow 1 and Upstream of Elbow 2 (Downstream Elbow 1), has a significant on the particle impact angle and intensity, based on this, it is difficult to expect the magnitude of erosion rate in Elbows 1 and 2 to be equal at any point, however in all geometries and flow conditions studied, similar magnitudes of erosion rates is expected at a few pipe network and flow conditions. According to the works of Frosell et al. (2015), Wang et al. (2017) and Shinde S. M et al. (2018), the target wall geometry and flow stream direction are also very important factors in erosion phenomenal. In the same flow geometry, the distribution of particles is different in either upstream or downstream flow, and this will result in different erosion patterns and magnitudes. Hence, the changes observed in the concentration of sand particles as the normalized separation distance and geometry changes.

On the average, Elbows 1 and 2 are more erosive in when the carrier fluid has the high gas velocity mixture properties than the low by a factor of 487 and 957 respectively in Geometry 1. In Geometry 2, 257 and 90 respectively, and 480 and 96 in Geometry 3. See Table 6.3 for more details. The average difference in Elbow 1 is similar for Geometries 1 and 3, and in Elbow 2, Geometry 3 is also similar to Geometry 2.

Table 6.3: Average Erosion Rates High and Low Gas Velocity Mixture Conditions across Geometries Studied

Geometry		**Av.ER - High**	**Av.ER - Low**
1	**Elbow 1**	312.0	0.64
	Elbow 2	287.0	0.30
2	**Elbow 1**	308.0	1.20
	Elbow 2	218.5	2.44
3	**Elbow 1**	312.0	0.65
	Elbow 2	260.0	2.70

Sand concentration remained consistent in Elbow 1 in all geometries and flow conditions studied, but varies in Elbow 2 as the normalized separation distance and flow condition changes. In Geometries 2 and 3, when the mixture has high gas velocity conditions, Elbow 2 is subjected to the least average and maximum erosion when sand concentration is at the highest while in Geometry 1, there is an almost direct relationship between the average erosion rate and sand concentration. Elbow 2 is subjected to the least average erosion at the lowest sand concentration but maximum erosion rate is highest. When the carrier fluid has low gas velocity mixture properties, the sand concentration at Elbow 2 in Geometries 2 and 3 remained consistently higher than that of Geometry 1 and this directly relates to the observation made with both the maximum and average erosion rates. However, it was lower than that of Elbow 1 in Geometry 1 just as seen in the average erosion rates as L/D changes from 0 to 20. In general, at both flow conditions, more frequent particle collisions will be expected in Elbow 2 at Geometries 2 and 3 compared to Geometry 1 due to the bend orientation.

6.5 Observations on Multiphase and Pseudo Single-phase analyses of Erosion in Double bend geometries

Detailed phase analysis is required where multiphase flow is expected as flow development and phase separation influence the motion and behaviour of particles in the pipeline. All of these peculiar features and characteristics such as different velocities of the phases and volume fractions to mention a few are lost when multiphase flow is analysed interms of it's mixture properties. Figure 6.26 and 6.27 are the contour plots of the multiphase and pseudo single-phase flows investigated in this study and a notable difference can be seen when the flows are analysed as typical multiphase flows and pseudo single-phase flows. In Figures 6.26 and 6.27 the pseudo single-phase shows velocity profiles showing no separation in the flow while the multiphase shows phase separation based on volume fractions as a result of the superficial velocities of the phases (red patch is the gas phase and blue patch is the liquid phase).

The change in the flow pattern in the horizontal section as stated earlier and the corresponding flow development as the normalized separation distance increases has been seen to play vital roles in the erosion rates in Elbow 2 because the fraction of either phases occupying the pipe bend at any instance has a stringent influence on the rate at which the elbow will erode at that particular time. All of these amongst other features are not captured in the mixture (properties) flow analyses.

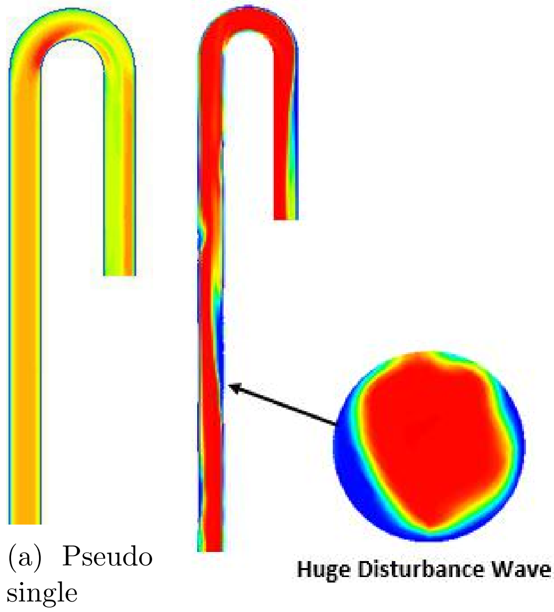

(a) Pseudo single phase

(b) Multiphase

Figure 6.26: Flow at high gas velocity (churn flow) at L/D of 0

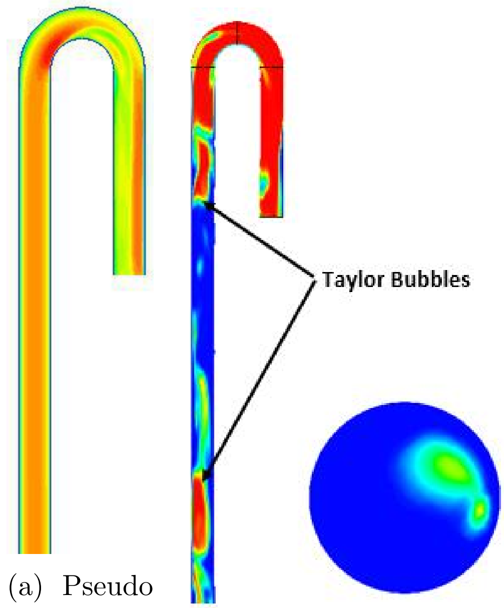

(a) Pseudo single phase

(b) Multiphase

Figure 6.27: Flow at low gas velocity (slug flow) at L/D of 0

At low gas velocity in the pseudo single-phase and slug flow, a similar prediction is observed for Elbows 1 and 2; Elbow 1 is subjected to more erosion than Elbow 2 irrespective of the normalized separation distance. For multiphase churn flow and the mixture flow at high gas velocity on the other hand, no similarities is observed between the behaviour of erosion in the elbows as L/D increases. Furthermore, location of average and maximum erosion are similar for both pseudo single-phase and multiphase flows, the erosion pattern in the pseudo single-phase flow spreads more to the sides of the pipe elbows. Pseudo single-phase model predicts much higher erosion rates than the multiphase flows. The best operating conditions for the pipe network predicted for both flow conditions using either modelling technique are however the same.

A comparison of the predicted erosion rates using the pseudo single phase and Eulerian-Multifluid VOF is shown in Figures 6.28. From this figure, it can be observed that there is more fluctuation in the predicted erosion rates in churn and high gas velocity flow condition than can be observed in slug and low gas velocity flow condition. The predicted erosion rates in slug and low gas velocity flow using either models are mostly within the same range and are less over-predicted compared to churn flow.

In summary even though the models have performed quite well, it can be seen that in many cases at the low gas velocity and slug flow conditions both models (pseudo and multiphase) generally predict similar erosion rates, therefore either model would provide reasonable results at this flow condition. While at high gas velocity and churn flow conditions, the predictions of both models do not correlate in most cases investigated. Detailed multiphase flow analysis is therefore recommended.

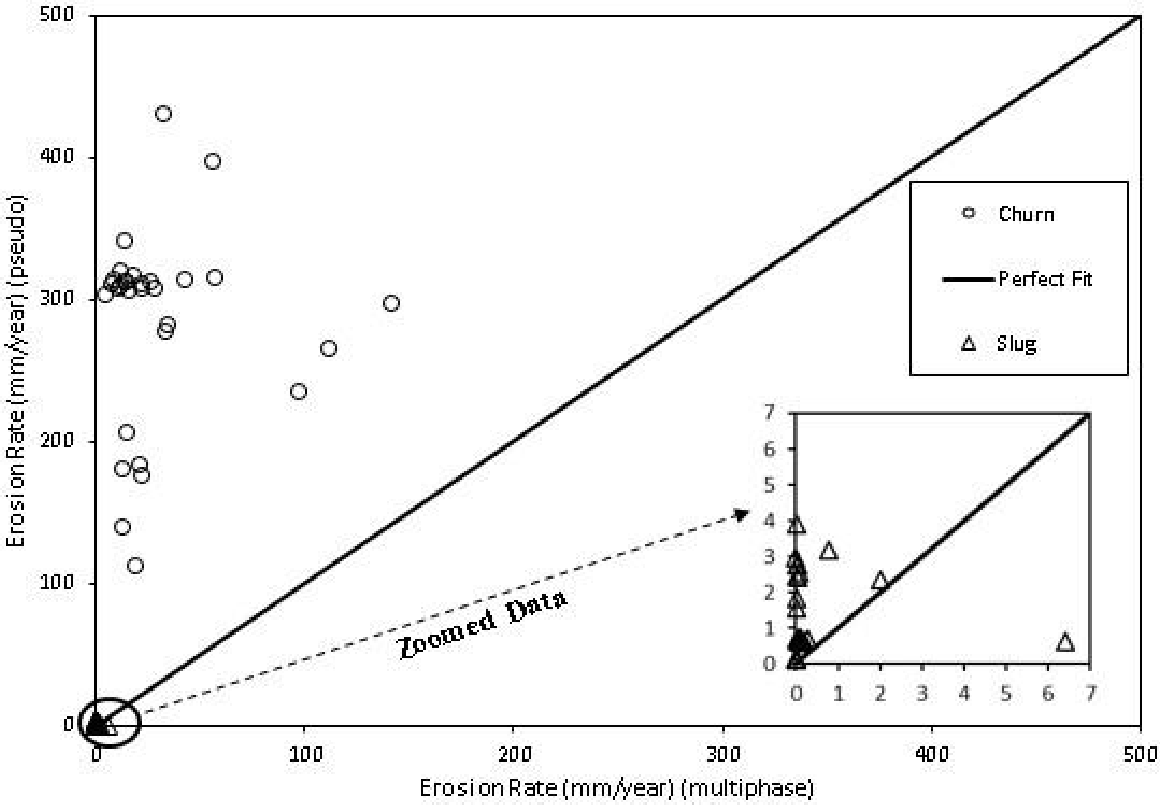

Figure 6.28: Comparison of the predicted erosion rates using the pseudo single-phase and multiphase models

Chapter 7

Conclusions and Recommendations for Future Work

7.1 Conclusions

Sand particle erosion remains one of the major bottlenecks for increased production in the oil and gas industry. Sand production results in the damage to the internal wall surfaces of pipelines and other line equipment in the oil and gas industry. It is therefore of paramount importance to predict the erosion rate of and identify the erosion location in the pipelines for possible leakage. Erosion risk becomes more significant in complex pipe networks and conditions where multiphase flows are expected. In view of this, Computational Fluid Dynamics (CFD) has been used to simulate air-water multiphase flow with the use of the Eulerian-Multifluid VOF model in a 76.2mm internal diameter pipe with a standard 90 degree elbow. Sand particles were injected into the flow domain and the particles were tracked within the lagrangian Discrete Phase Model (DPM) frame, erosion rate and location at the bend were accounted for by using the erosion model developed by Oka et al. (2005a). The CFD model was validated with published experimental data and results obtained showed appropriate agreement. The single bend geometry was redesigned to include a second elbow downstream of the first bend, and the validated single bend model was employed to carry out flow and erosion analyses in the double bend geometry. The separation distance between the two elbows was varied between 0 and 20, the orientation of the second elbow was also varied. Since modelling using Multifluid VOF is computationally expensive, the two-phase air-water flow was resolved into a mixture and also analyzed as a pseudo single-phase flow at both the high and low gas velocities using the mixture properties in other to speed up simulation. The liquid velocity remained unchanged for all cases in this study (single and multiphase). Particles with similar properties to the single bend validation were injected, tracked and the erosion damage the elbows were subjected to was analysed.

Based on the results from this study, the following conclusions have been drawn;

- The Eulerian-Multifluid VOF has the capability to produce multiphase flow features such as the time series of the local volume fractions, liquid and gas velocities and the flow patterns of air-water two-phase flows where the measurement maybe be impossible. Unlike the pseudo-single phase (mixture) analysis which does not give the actual flow representation as it ignores many flow parameters and features in double bends that would influence the erosion rates in complex multiphase flows. The coupled lagrangian Discrete Phase Model (DPM) also provides intricate understanding of the particle behaviours in the multiphase and mixture flow analyses. It provides particle characteristics such as the particle tracks as well as the concentration.

- Results show that at high gas velocity, churn flow is observed in the vertical pipe before Elbow 1 and this transitions into a wavy stratified flow in the horizontal section before Elbow 2. While at low gas velocity, slug flow is observed in the vertical section before Elbow 1, the flow pattern remained the same after the first bend but the Taylor bubble gets more aerated in the horizontal pipe section before Elbow 2. Increase in the normalized separation distance between the elbows aides the flow development and stability in the horizontal section irrespective of the pipe network and flow condition.

- The second bend (Elbow 2) has a significant influence on the erosion rates in the first bend (Elbow 1) when compared to the single bend geometry. The peak average erosion rates of Elbow 1 at churn flow condition are higher than that in the elbow in the single bend geometry in all Geometries studied.

- Elbow 2 is predicted to be subjected to more erosion than Elbow 1 in churn flow, while in slug flow, the reverse is observed for all cases investigated. Furthermore, both elbows are affected by the change in separation distance. An increase in the normalized separation distance after 10 leads to a drop in the erosion rate in both elbows in churn flow while in slug flow increase in normalized separation distance after 5 results a drop in the erosion rates in Elbow 2 and an increase in Elbow 1. The critical separation distance where the elbows are subjected to the most average erosion rates are normalized separation distance of 10 in Geometry 1 for churn flow and 5 in Geometry 2 for slug flow.

- Multiphase flow analyses provides the qualitative and quantitative criterion for the identification of these flow features and properties such as volume fractions and velocities of individual phases, all these were however ignored in the pseudo-single phase flow approach. Here, erosion rates in Elbow 1 remained independent of an increase in normalized separation distance while the change has significant effects on Elbow 2 in pseudo-single phase modelling. The normalized separation distances either side of 5 resulted in a corresponding drop in the erosion rates in Elbow 2 at high gas velocity, and at the low gas velocity, the erosion rate in Elbow 2 becomes independent of the normalized separation distance after 5 in Geometry 1 and increases in Geometries 2 and 3. This technique predicted higher erosion rates than the multiphase approach.

- Irrespective of modelling technique the best operating conditions for the pipe network are the same; Geometry 3 for churn and high gas velocity flow and Geometry 1 for slug and low gas velocity flow. The critical separation distance where both elbows are subjected to the most average erosion rates are normalized separation distance of 10 in Geometry 1 and 5 in Geometry 2 for churn and slug respectively in multiphase modelling. In pseudo single phase, it is a normalized separation distance of 5 at high gas velocity, and 20 for low gas velocity at

Geometries 2 and 3. It is L/D of 0 in Geometry 1.

- A change in the gas velocity also have a significant influence on the erosion rates in Elbows 1 and 2. A similar observation is made in both modelling techniques, at high gas velocity and Churn flow, the elbows are subjected to more erosion damage than at low gas velocity and slug flow.

Overall, it can be deduced from this study that an increase in the normalized separation distance between two elbows mounted in series will either enhance or reduce the erosion rates in the elbows when flow charateristics are properly captured. Therefore, the integrity of piping systems with double bends can be enhanced with proper analysis of the optimum distance between the elbows as well as the orientation of the elbows based on the findings highlighted in this study. It is also important to employ the right modeling technique to capture the flow features and particle behaviour where multiphase flows are expected.

7.2 Recommendations for Future work

- In this study, particles were treated in the Lagrangian Discrete Phase Model which does not take into account the particle-particle collisions. It is therefore recommended to investigate the effects of particle-particle interactions on the erosion rates at the elbows. The Discrete Element Method (DEM) is a modelling technique which has the capability to provide dynamic information of the individual particles and capture the effects of particle-particle interaction.
- The Eulerian Multifluid-VOF model is also known for its instability and convergence problems and the CPU run time. And increases as the number of mesh increases, hence further enhancing the level of uncertainties in the outcomes. However, it is recommended that the analysis be conducted with the use of a finer mesh to investigate the repeatability of the results.
- It is also assumed that the surface profile of the pipe wall is unchanged throughout the erosion analysis, this assumption ignores the effect of the instantaneous

change in erosion profiles during particle impingement. It also ignores its effect on the fluid flow. Hence, this factor could be a source of error in the prediction of erosion rates and location at the pipe bends.

- The liquid film around the elbows seems to have a very significant effect on the erosion rates as highlighted in this study. It is suggested to employ CFD techniques to study the behaviour of the film in and around the pipe bends.

- To further examine the accuracy of the erosion predictions in this study, it is suggested that proper experimental analysis be carried out with the same flow, particle and geometric parameters for further stability analysis.

References

Abdulla, A. (2011), 'Estimating erosion in oil and gas pipe line due to sand presence', *Masters Thesis, Department of Mechanical Engineering, Blekinge Institute of Technology, Karlskrona, Sweden* .

Al-Khayat, R. H., Al-Baghdadi, M. A. S., Neama, R. A. and Al-Waily, M. (2018), 'Optimization cfd study of erosion in 3d elbow during transportation of crude oil contaminated with sand particles', *International Journal of Engineering & Technology* **7**(3), 1420–1428.

Al-Rawahi, N. Z. (2009), Designing a multi-phase flow loop, *in* 'ICCES: International Conference on Computational & Experimental Engineering and Sciences', Vol. 9, pp. 97–98.

Alhajraf, S. (2000), 'Numerical simulation of drifting sand', *PhD Thesis, Cranfield University* .

Anderson, J. D. and Wendt, J. (1995), *Computational fluid dynamics*, Vol. 206, Springer.

Andersson, B., Andersson, R., Håkansson, L., Mortensen, M., Sudiyo, R. and Van Wachem, B. (2011), *Computational fluid dynamics for engineers*, Cambridge University Press.

Andrews, D. (1981), 'An analysis of solid particle erosion mechanisms', *Journal of Physics D: Applied Physics* **14**(11), 1979.

API (1981), '14e" recommended practice for design and installation of offshore production platform piping systems,”’, *American Petroleum Institute Recommended Practice RP* p. 22.

Arabnejad, H., Mansouri, A., Shirazi, S. and McLaury, B. (2015), ‘Development of mechanistic erosion equation for solid particles’, *Wear* **332**, 1044–1050.

Asgharpour, A., Zahedi, P., Arabnejad Khanouki, H., Shirazi, S. A. and McLaury, B. S. (2017), Experimental and numerical study on solid particle erosion in elbows mounted in series, *in* ‘ASME 2017 Fluids Engineering Division Summer Meeting’, American Society of Mechanical Engineers Digital Collection.

Asgharpour, A., Zahedi, P., Vieira, R., Parsi, M., Shirazi, S., McLaury, B. et al. (2018), Investigation of churn/annular and pseudo-slug flow characteristics before and after pipe elbows, *in* ‘11th North American Conference on Multiphase Production Technology’, BHR Group.

Ashrafizadeh, H. and Ashrafizadeh, F. (2012), ‘A numerical 3d simulation for prediction of wear caused by solid particle impact’, *Wear* **276**, 75–84.

Barnea, D. (1987), ‘A unified model for predicting flow-pattern transitions for the whole range of pipe inclinations’, *International Journal of Multiphase Flow* **13**(1), 1–12.

Benyahia, S., Syamlal, M. and O’Brien, T. J. (2005), ‘Evaluation of boundary conditions used to model dilute, turbulent gas/solids flows in a pipe’, *Powder Technology* **156**(2-3), 62–72.

Birchenough, P., Dawson, S., Lockett, T. and McCarthy, P. (1995), ‘Critical flow rates working party’, *AEA Technology, Harwell, UK, Report No. AEA-TSD-0348* .

Bitter, J. (1963), ‘A study of erosion phenomena part i’, *wear* **6**(1), 5–21.

Bitter, J. (1963b), ‘A study of erosion phenomena: Part ii’, *Wear* **6**(3), 169–190.

Bourgoyne Jr, A. et al. (1989), Experimental study of erosion in diverter systems due to sand production, *in* ‘SPE/IADC Drilling Conference’, Society of Petroleum Engineers.

Cerne, G., Petelin, S. and Tiselj, I. (2001), 'Coupling of the interface tracking and the two-fluid models for the simulation of incompressible two-phase flow', *Journal of computational physics* **171**(2), 776–804.

Chen, D., Sarumi, M., Al-Hassani, S., Gan, S. and Yin, Z. (1997), 'A model for erosion at normal impact', *Wear* **205**(1-2), 32–39.

Chen, J., Wang, Y., Li, X., He, R., Han, S. and Chen, Y. (2015), 'Reprint of "erosion prediction of liquid-particle two-phase flow in pipeline elbows via cfd–dem coupling method"', *Powder technology* **282**, 25–31.

Chen, X., McLaury, B. S. and Shirazi, S. A. (2004), 'Application and experimental validation of a computational fluid dynamics (cfd)-based erosion prediction model in elbows and plugged tees', *Computers & Fluids* **33**(10), 1251–1272.

Cheng, N.-S. (2007), 'Power-law index for velocity profiles in open channel flows', *Advances in water Resources* **30**(8), 1775–1784.

Chiesa, M., Mathiesen, V., Melheim, J. A. and Halvorsen, B. (2005), 'Numerical simulation of particulate flow by the eulerian–lagrangian and the eulerian–eulerian approach with application to a fluidized bed', *Computers & chemical engineering* **29**(2), 291–304.

Clark, H. M. (1991), 'On the impact rate and impact energy of particles in a slurry pot erosion tester', *Wear* **147**(1), 165–183.

Clark, H. M. (2002), 'Particle velocity and size effects in laboratory slurry erosion measurements or... do you know what your particles are doing?', *Tribology International* **35**(10), 617–624.

Costigan, G. and Whalley, P. (1997), 'Slug flow regime identification from dynamic void fraction measurements in vertical air-water flows', *International Journal of Multiphase Flow* **23**(2), 263–282.

Crowe, C., Troutt, T. and Chung, J. (1996), 'Numerical models for two-phase turbulent flows', *Annual review of fluid mechanics* **28**(1), 11–43.

Deen, N., Annaland, M. V. S., Van der Hoef, M. A. and Kuipers, J. (2007), 'Review of discrete particle modeling of fluidized beds', *Chemical engineering science* **62**(1-2), 28–44.

Deng, T., Patel, M., Hutchings, I. and Bradley, M. (2005), 'Effect of bend orientation on life and puncture point location due to solid particle erosion of a high concentration flow in pneumatic conveyors', *Wear* **258**(1-4), 426–433.

Dhawan, S. and Narasimha, R. (1958), 'Some properties of boundary layer flow during the transition from laminar to turbulent motion', *Journal of Fluid Mechanics* **3**(4), 418–436.

DNV (2007), 'O501 (revision 4.2)', *DNV recommended practice RP O501–erosion wear in piping systems* .

DNV (2007b), 'Recommended practice rp o501 erosive wear in piping systems', *DNV Recommended Practice* **4**.

Drew, D. A. (1983), 'Mathematical modeling of two-phase flow', *Annual review of fluid mechanics* **15**(1), 261–291.

Duarte, C. A. R., de Souza, F. J., de Vasconcelos Salvo, R. and dos Santos, V. F. (2017), 'The role of inter-particle collisions on elbow erosion', *International Journal of Multiphase Flow* **89**, 1–22.

Durst, F., Miloievic, D. and Schönung, B. (1984), 'Eulerian and lagrangian predictions of particulate two-phase flows: a numerical study', *Applied Mathematical Modelling* **8**(2), 101–115.

Ekambara, K., Sanders, R. S., Nandakumar, K. and Masliyah, J. H. (2009), 'Hydrodynamic simulation of horizontal slurry pipeline flow using ansys-cfx', *Industrial & Engineering Chemistry Research* **48**(17), 8159–8171.

Elghobashi, S. (1991), Particle-laden turbulent flows: direct simulation and closure models, *in* 'Computational fluid Dynamics for the Petrochemical Process Industry', Springer, pp. 91–104.

Enwald, H., Peirano, E. and Almstedt, A.-E. (1996), 'Eulerian two-phase flow theory applied to fluidization', *International Journal of Multiphase Flow* **22**, 21–66.

Evans, A. G., Gulden, M. and Rosenblatt, M. (1978), 'Impact damage in brittle materials in the elastic-plastic response regime', *Proceedings of the Royal Society of London. A. Mathematical and Physical Sciences* **361**(1706), 343–365.

Farokhipour, A., Saffar-Avval, M., Ahmadi, G. et al. (2018), 'Numerical modeling of sand particle erosion at return bends in gas-particle two-phase flow', *Scientia Iranica* **25**, 3231–3242.

Felten, F. N. (2014), Numerical prediction of solid particle erosion for elbows mounted in series, *in* 'ASME 2014 4th Joint US-European Fluids Engineering Division Summer Meeting collocated with the ASME 2014 12th International Conference on Nanochannels, Microchannels, and Minichannels', American Society of Mechanical Engineers, p. V01CT23A006.

Finnie, I. (1958), The mechanism of erosion of ductile metals, *in* '3rd US national congress of applied mechanics, ASME', pp. 527–532.

Finnie, I. (1960), 'Erosion of surfaces by solid particles', *wear* **3**(2), 87–103.

Finnie, I. (1972), 'Some observations on the erosion of ductile metals', *wear* **19**(1), 81–90.

Fluent, A. (2013), 'Ansys fluent theory guide 15.0', *ANSYS, Canonsburg, PA* .

Franca, F., Acikgoz, M., Lahey Jr, R. and Clausse, A. (1991), 'The use of fractal techniques for flow regime identification', *International Journal of Multiphase Flow* **17**(4), 545–552.

Frosell, T., Fripp, M. and Gutmark, E. (2015), 'Investigation of slurry concentration effects on solid particle erosion rate for an impinging jet', *Wear* **342**, 33–43.

Ghorai, S. and Nigam, K. (2006), 'Cfd modeling of flow profiles and interfacial phenomena in two-phase flow in pipes', *Chemical Engineering and Processing: Process Intensification* **45**(1), 55–65.

Gidaspow, D. (1994), *Multiphase flow and fluidization: continuum and kinetic theory descriptions*, Academic press.

Gosman, A. and Loannides, E. (1983), 'Aspects of computer simulation of liquid-fueled combustors', *Journal of energy* **7**(6), 482–490.

Graham, L., Lester, D. and Wu, J. (2009), Slurry erosion in complex flows: experiment and cfd, *in* 'Proceedings of the 7th International Conference on CFD in the Minerals and Process Industries', CSIR Melbourne, Australia, pp. 1–6.

Grant, G. and Tabakoff, W. (1975), 'Erosion prediction in turbomachinery resulting from environmental solid particles', *Journal of Aircraft* **12**(5), 471–478.

Hanafizadeh, P., Eshraghi, J., Taklifi, A. and Ghanbarzadeh, S. (2016), 'Experimental identification of flow regimes in gas–liquid two phase flow in a vertical pipe', *Meccanica* **51**(8), 1771–1782.

Hibiki, T. and Ishii, M. (2000), 'One-group interfacial area transport of bubbly flows in vertical round tubes', *International Journal of Heat and Mass Transfer* **43**(15), 2711–2726.

Huang, C., Chiovelli, S., Minev, P., Luo, J. and Nandakumar, K. (2008), 'A comprehensive phenomenological model for erosion of materials in jet flow', *Powder Technology* **187**(3), 273–279.

Hutchings, I. (1977), 'Deformation of metal surfaces by the oblique impact of square plates', *International Journal of Mechanical Sciences* **19**(1), 45–52.

Hutchings, I. (1981), 'A model for the erosion of metals by spherical particles at normal incidence', *Wear* **70**(3), 269–281.

Hutchings, I. and Winter, R. (1974), 'Particle erosion of ductile metals: a mechanism of material removal', *Wear* **27**(1), 121–128.

Hutchings, I., Winter, R. and Field, J. E. (1976), 'Solid particle erosion of metals: the removal of surface material by spherical projectiles', *Proceedings of the Royal Society of London. A. Mathematical and Physical Sciences* **348**(1654), 379–392.

Ishii, M. and Grolmes, M. (1975), ‘Inception criteria for droplet entrainment in two-phase concurrent film flow’, *AIChE Journal* **21**(2), 308–318.

Ishii, M. and Hibiki, T. (2010), *Thermo-fluid dynamics of two-phase flow*, Springer Science & Business Media.

Ishii, M. and Hibiki, T. (2011), *Thermo-fluid dynamics of two-phase flow*, Springer.

Ishii, M. and Mishima, K. (1989), ‘Droplet entrainment correlation in annular two-phase flow’, *International Journal of Heat and Mass Transfer* **32**(10), 1835–1846.

Islam, M. A. and Farhat, Z. N. (2014), ‘Effect of impact angle and velocity on erosion of api x42 pipeline steel under high abrasive feed rate’, *Wear* **311**(1-2), 180–190.

Jafari, M., Mansoori, Z., Avval, M. S. and Ahmadi, G. (2015), ‘The effects of wall roughness on erosion rate in gas–solid turbulent annular pipe flow’, *Powder technology* **271**, 248–254.

Jakobsen, H. A. (2014), *Chemical reactor modeling*, Springer.

Jennings, W. H., Head, W. J. and Manning Jr, C. R. (1976), ‘A mechanistic model for the prediction of ductile erosion’, *Wear* **40**(1), 93–112.

Johansson, S., Ericson, F. and Schweitz, J.-Å. (1987), ‘Solid particle erosion—a statistical method for evaluation of strength properties of semiconducting materials’, *Wear* **115**(1-2), 107–120.

Jordan, K. G. et al. (1998), Erosion in multiphase production of oil & gas, *in* ‘CORROSION 98’, NACE International, San Diego, California.

Kang, R. and Liu, H. (2019*a*), ‘A mechanistic model of predicting solid particle erosion on the symmetry plane of elbows for annular flow’, *Journal of Energy Resources Technology* **141**(3), 032907.

Kang, R. and Liu, H. (2019*b*), ‘A probability model of predicting the sand erosion in elbows for annular flow’, *Wear* **422**, 167–179.

Kaushal, D., Thinglas, T., Tomita, Y., Kuchii, S. and Tsukamoto, H. (2012), 'Cfd modeling for pipeline flow of fine particles at high concentration', *International Journal of Multiphase Flow* **43**, 85–100.

Kesana, N., Grubb, S., McLaury, B. and Shirazi, S. (2013a), 'Ultrasonic measurement of multiphase flow erosion patterns in a standard elbow', *Journal of Energy Resources Technology* **135**(3), 032905.

Kesana, N., Throneberry, J., McLaury, B., Shirazi, S. and Rybicki, E. (2012), Effect of particle size and viscosity on erosion in annular and slug flow, *in* 'ASME 2012 International Mechanical Engineering Congress and Exposition', American Society of Mechanical Engineers, pp. 2143–2154.

Kesana, N., Throneberry, J., McLaury, B., Shirazi, S. and Rybicki, E. (2014), 'Effect of particle size and liquid viscosity on erosion in annular and slug flow', *Journal of energy resources technology* **136**(1), 012901.

Kesana, N., Vieira, R., Schleicher, E., McLaury, B., Shirazi, S. and Hampel, U. (2013b), Experimental study of slug characteristics: implications to sand erosion, *in* 'ASME 2013 Fluids Engineering Division Summer Meeting', American Society of Mechanical Engineers.

Kim, H., Rao, P. S. C. and Annable, M. D. (1997), 'Determination of effective air-water interfacial area in partially saturated porous media using surfactant adsorption', *Water Resources Research* **33**(12), 2705–2711.

Kolev, N. I. and Kolev, N. (2005), *Multiphase flow dynamics*, Vol. 1, Springer.

Kudela, H. (2010), 'Lecture note on turbulent flow'.

Kumar, P. G., Smith, B. R., Vedapuri, D., Subramani, H. J., Rhyne, L. D. et al. (2014), Sand fines erosion in gas pipelines–experiments and cfd modeling, *in* 'CORROSION 2014', NACE International, San Antonio, Texas, USA.

Kvernvold, O. and Sandberg, R. (1993), "production rate limits in two-phase flow suystems: Erosion in piping systems for production of oil and gas', *Det Norske Veritas (DNV), Oslo, Norway, Report* (93-3252).

Launder, B. and Spalding, D. (1974), 'Computer methods', *Appl. Mech. Eng* **3**(2), 269–289.

Levy, A., Aghazadeh, M. and Hickey, G. (1986), 'The effect of test variables on the platelet mechanism of erosion', *Wear* **108**(1), 23–41.

Levy, A. V. (1986), 'The platelet mechanism of erosion of ductile metals', *Wear* **108**(1), 1–21.

Levy, A. V. (1995), *Solid particle erosion and erosion-corrosion of materials*, ASM International, Material Park, Ohio.

Li, A. and Ahmadi, G. (1992), 'Dispersion and deposition of spherical particles from point sources in a turbulent channel flow', *Aerosol science and technology* **16**(4), 209–226.

Liu, M., Liu, H. and Zhang, R. (2015), 'Numerical analyses of the solid particle erosion in elbows for annular flow', *Ocean Engineering* **105**, 186–195.

Liu, Y., Miwa, S., Hibiki, T., Ishii, M., Morita, H., Kondoh, Y. and Tanimoto, K. (2012), 'Experimental study of internal two-phase flow induced fluctuating force on a 90 elbow', *Chemical engineering science* **76**, 173–187.

Lowe, D. and Rezkallah, K. (1999), 'Flow regime identification in microgravity two-phase flows using void fraction signals', *International Journal of Multiphase Flow* **25**(3), 433–457.

Ma, D. and Ahmadi, G. (1990), 'A thermodynamical formulation for dispersed multiphase turbulent flows—ii: Simple shear flows for dense mixtures', *International Journal of Multiphase Flow* **16**(2), 341–351.

Mahdavi, M., Karimi, S., Shirazi, S. A. and McLaury, B. S. (2016), Parametric study of erosion under high concentrated slurry: Experimental and numerical analyses, *in* 'ASME 2016 Fluids Engineering Division Summer Meeting collocated with the ASME 2016 Heat Transfer Summer Conference and the ASME 2016 14th International Conference on Nanochannels, Microchannels, and Minichannels', American Society of Mechanical Engineers, p. V01AT06A002.

Mahdavimanesh, M., Noghrehabadi, A., Behbahaninejad, M., Ahmadi, G. and Dehghanian, M. (2013), 'Lagrangian particle tracking: model development', *Life Science Journal* **10**(8s), 34–41.

Mansouri, A. (2016), *A combined CFD-experimental method for developing an erosion equation for both gas-sand and liquid-sand flows*, The University of Tulsa, OK, USA.

Mazumder, Q. H. (2004), *Development and validation of a mechanistic model to predict erosion in single-phase and multiphase flow*, University of Tulsa, OK, USA.

Mazumder, Q. H. (2007), 'Prediction of erosion due to solid particle impact in single-phase and multiphase flows', *Journal of Pressure Vessel Technology* **129**(4), 576–582.

Mazumder, Q. H. (2014), Effect of particle size on magnitude and location of maximum erosion in s-bend, *in* 'ASME 2014 4th Joint US-European Fluids Engineering Division Summer Meeting collocated with the ASME 2014 12th International Conference on Nanochannels, Microchannels, and Minichannels', American Society of Mechanical Engineers, p. V01CT18A002.

Mazumder, Q. H., Santos, G., Shirazi, S. A. and McLaury, B. S. (2003), Effect of sand distribution on erosion in annular three-phase flow, *in* 'ASME/JSME 2003 4th Joint Fluids Summer Engineering Conference', American Society of Mechanical Engineers, pp. 871–880.

Mazumder, Q. H., Shirazi, S. A. and McLaury, B. (2008b), 'Experimental investigation of the location of maximum erosive wear damage in elbows', *Journal of Pressure Vessel Technology* **130**(1), 011303.

Mazumder, Q. H., Shirazi, S. A. and McLaury, B. S. (2008a), 'Prediction of solid particle erosive wear of elbows in multiphase annular flow-model development and experimental validations', *Journal of Energy Resources Technology* **130**(2), 023001.

Mazumder, Q. H., Shirazi, S. A., McLaury, B. S., Shadley, J. R. and Rybicki, E. F. (2005), 'Development and validation of a mechanistic model to predict solid particle erosion in multiphase flow', *Wear* **259**(1-6), 203–207.

McLaury, B. S., Rybicki, E. F., Shirazi, S. A., Shadley, J. R. et al. (1999), How operating and environmental conditions affect erosion, *in* 'CORROSION 99', NACE International, 25-30 April, San Antonio, Texas.

McLaury, B. S. and Shirazi, S. A. (2000), 'An alternate method to api rp 14e for predicting solids erosion in multiphase flow', *Journal of Energy Resources Technology* **122**(3), 115–122.

McLaury, B. S., Shirazi, S. A., Viswanathan, V., Mazumder, Q. H. and Santos, G. (2011), 'Distribution of sand particles in horizontal and vertical annular multiphase flow in pipes and the effects on sand erosion', *Journal of Energy Resources Technology* **133**(2), 023001.

McLaury, B., Wang, J., Shirazi, S., Shadley, J., Rybicki, E. et al. (1997), Solid particle erosion in long radius elbows and straight pipes, *in* 'SPE annual technical conference and exhibition', Society of Petroleum Engineers, San Antonio, Texas.

Meng, H. and Ludema, K. (1995), 'Wear models and predictive equations: their form and content', *Wear* **181**, 443–457.

Metzner, A. and Reed, J. (1955), 'Flow of non-newtonian fluids—correlation of the laminar, transition, and turbulent-flow regions', *Aiche journal* **1**(4), 434–440.

Morsi, S. and Alexander, A. (1972), 'An investigation of particle trajectories in two-phase flow systems', *Journal of Fluid mechanics* **55**(2), 193–208.

Neilson, J. and Gilchrist, A. (1968), 'Erosion by a stream of solid particles', *wear* **11**(2), 111–122.

Nguyen, V., Nguyen, Q., Liu, Z., Wan, S., Lim, C. and Zhang, Y. (2014), 'A combined numerical–experimental study on the effect of surface evolution on the water–

sand multiphase flow characteristics and the material erosion behavior', *Wear* **319**(1-2), 96–109.

Ogunsesan, O. A., Hossain, M., Iyi, D. and Dhroubi, M. G. (2018), Cfd modelling of pipe erosion due to sand transport, *in* 'Numerical Modelling in Engineering', Springer, pp. 274–289.

Oka, Y. I., Okamura, K. and Yoshida, T. (2005a), 'Practical estimation of erosion damage caused by solid particle impact: Part 1: Effects of impact parameters on a predictive equation', *Wear* **259**(1-6), 95–101.

Oka, Y., Ohnogi, H., Hosokawa, T. and Matsumura, M. (1997), 'The impact angle dependence of erosion damage caused by solid particle impact', *Wear* **203**, 573–579.

Oka, Y. and Yoshida, T. (2005b), 'Practical estimation of erosion damage caused by solid particle impact: Part 2: Mechanical properties of materials directly associated with erosion damage', *Wear* **259**(1-6), 102–109.

Oliveira, P. J. and Issa, R. I. (2003), 'Numerical aspects of an algorithm for the eulerian simulation of two-phase flows', *International Journal for Numerical Methods in Fluids* **43**(10-11), 1177–1198.

Orszag, S. A., Staroselsky, I., Flannery, W. and Zhang, Y. (1996), 'Introduction to renormalization group modeling of turbulence', *Simulation and Modelling of Turbulent Flows* pp. 155–183.

Orszag, S., Yakhot, V., Flannery, W., Boysan, F., Choudhury, D. and Maruzewski, J. (1993), Patel., b., 1993,"renormalization group modeling and turbulence simulations,", *in* 'International Conference on Near-Wall Turbulent Flows, Tempe, AZ'.

Parsi, M. (2015), *Sand Particle Erosion in Vertical Slug/Churn Flow*, The University of Tulsa, OK, USA.

Parsi, M., Agrawal, M., Srinivasan, V., Vieira, R. E., Torres, C. F., McLaury, B. S. and Shirazi, S. A. (2015b), 'Cfd simulation of sand particle erosion in gas-dominant multiphase flow', *Journal of Natural Gas Science and Engineering* **27**, 706–718.

Parsi, M., Agrawal, M., Srinivasan, V., Vieira, R. E., Torres, C. F., McLaury, B. S., Shirazi, S. A., Schleicher, E. and Hampel, U. (2016a), 'Assessment of a hybrid cfd model for simulation of complex vertical upward gas–liquid churn flow', *Chemical Engineering Research and Design* **105**, 71–84.

Parsi, M., Arabnejad, H., Al-Sarkhi, A., Zahedi, P., Vieira, R. E., Sharma, P., McLaury, B. S. et al. (2018), A new correlation for predicting solid particle erosion caused by gas-sand flow in elbows, *in* 'Offshore Technology Conference', Offshore Technology Conference, 30 April - 3 May, Houston, Texas, USA.

Parsi, M., Kara, M., Sharma, P., McLaury, B. S., Shirazi, S. A. et al. (2016b), Comparative study of different erosion model predictions for single-phase and multiphase flow conditions, *in* 'Offshore Technology Conference', Offshore Technology Conference, Houston, Texas, USA.

Parsi, M., Vieira, R., Agrawal, M., Srinivasan, V., Mclaury, B., Shirazi, S., Schleicher, E., Hampel, U. et al. (2015d), Computational fluid dynamics (cfd) simulation of multiphase flow and validating using wire mesh sensor, *in* '17th International Conference on Multiphase Production Technology', BHR Group.

Parsi, M., Vieira, R. E., Kesana, N., McLaury, B. S. and Shirazi, S. A. (2015a), 'Ultrasonic measurements of sand particle erosion in gas dominant multiphase churn flow in vertical pipes', *Wear* **328**, 401–413.

Parsi, M., Vieira, R. E., Torres, C. F., Kesana, N. R., McLaury, B. S., Shirazi, S. A., Schleicher, E. and Hampel, U. (2015c), 'Experimental investigation of interfacial structures within churn flow using a dual wire-mesh sensor', *International Journal of Multiphase Flow* **73**, 155–170.

Parsi, M., Vieira, R., Torres, C., Kesana, N., McLaury, B., Shirazi, S., Hampel, U. and Schleicher, E. (2014), Characterizing slug/churn flow using wire mesh sensor, *in* 'ASME 2014 4th Joint US-European Fluids Engineering Division Summer Meeting collocated with the ASME 2014 12th International Conference on Nanochannels, Microchannels, and Minichannels', American Society of Mechanical Engineers, p. V01DT32A009.

Pellacani, F., Macian, R., Chiva, S. and Pena, C. (2011), 'Implementation of a one-group interfacial area transport equation in a cfd code for the simulation of upward adiabatic bubbly flow'.

Peng Jr, D., Pak, A., Chinello, L., Wood, T., Low, A. et al. (2013), Advances in multiphase flow cfd erosion analysis, *in* 'Offshore Technology Conference', Offshore Technology Conference, Houston, Texas, USA.

Peng, W. and Cao, X. (2016), 'Numerical simulation of solid particle erosion in pipe bends for liquid–solid flow', *Powder technology* **294**, 266–279.

Pereyra, E. and Torres, C. (2005), 'Flopatn—flow pattern prediction and plotting computer code', *The University of Tulsa, Tulsa, OK, USA* .

Pletcher, R. H., Tannehill, J. C. and Anderson, D. (2012), *Computational fluid mechanics and heat transfer*, CRC press.

Pope, S. B. (2001), *Turbulent flows*, IOP Publishing.

Rabinowicz, E. (1979), The wear equation for erosion of metals by abrasive particles, *in* 'International Conference on Erosion by Liquid and Solid Impact, 5 th, Cambridge, England', pp. 38–1.

Saffman, P. (1968), 'Corrigendum to'the lift on a small sphere in a slow shear flow", *J. Fluid Mech.* **31**, 624.

Salama, M. (1998), a," an alternative to api 14e erosional velocity limits for sand laden fluids", offshore tech, *in* 'Conf, Houston, USA, May', pp. 4–7.

Salama, M. M. et al. (2000), 'An alternative to api 14e erosional velocity limits for sand laden fluids', *Transactions-American Society of Mechanical Engineers Journal Of Energy Resources Technology* **122**(2), 71–77.

Salama, M., Venkatesh, E. et al. (1983), Evaluation of api rp 14e erosional velocity limitations for offshore gas wells, *in* 'Offshore Technology Conference', Offshore Technology Conference, Houston, Texas.

Schiller, L. and Naumann, Z. (1935), 'Z.(1935)', *Ver. Deutsch. Ing* **77**, 318.

Sedrez, T. A., Rajkumar, Y. R., Shirazi, S. A., Khanouki, H. A. and McLaury, B. S. (2018), Cfd predictions and experiments of erosion of elbows in series in liquid dominated flows, *in* 'ASME 2018 5th Joint US-European Fluids Engineering Division Summer Meeting', American Society of Mechanical Engineers, p. V003T17A001.

Sedrez, T. A., Shirazi, S. A., Rajkumar, Y. R., Sambath, K. and Subramani, H. J. (2019), 'Experiments and cfd simulations of erosion of a 90 elbow in liquid-dominated liquid-solid and dispersed-bubble-solid flows', *Wear* **426**, 570–580.

Sheldon, G. (1970), 'Similarities and differences in the erosion behavior of materials', *Journal of Basic Engineering* **92**(3), 619–626.

Sheldon, G. and Kanhere, A. (1972), 'An investigation of impingement erosion using single particles', *Wear* **21**(1), 195–209.

Shirazi, S., McLaury, B., Arabnejad, H. et al. (2016), A semi-mechanistic model for predicting sand erosion threshold velocities in gas and multiphase flow production, *in* 'SPE Annual Technical Conference and Exhibition', Society of Petroleum Engineers, 26-28 September, Dubai, UAE.

Shirazi, S., McLaury, B., Shadley, J., Rybicki, E. et al. (1995b), 'Generalization of the api rp 14e guideline for erosive services', *Journal of Petroleum Technology* **47**(08), 693–698.

Shirazi, S., Shadley, J., McLaury, B. and Rybicki, E. (1995), 'A procedure to predict solid particle erosion in elbows and tees', *Journal of Pressure Vessel Technology* **117**(1), 45–52.

Shirolkar, J., Coimbra, C. and McQuay, M. Q. (1996), 'Fundamental aspects of modeling turbulent particle dispersion in dilute flows', *Progress in Energy and Combustion Science* **22**(4), 363–399.

Shoham, O. (2006), 'Mechanistic modeling of gas-liquid two-phase ow in pipes', *Richardson, TX: Society of Petroleum Engineers* .

Smith, L. M. and Reynolds, W. C. (1992), 'On the yakhot–orszag renormalization group method for deriving turbulence statistics and models', *Physics of Fluids A: Fluid Dynamics* **4**(2), 364–390.

Smith, L. M. and Woodruff, S. L. (1998), 'Renormalization-group analysis of turbulence', *Annual review of fluid mechanics* **30**(1), 275–310.

Sommerfeld, M. (2003), 'Analysis of collision effects for turbulent gas–particle flow in a horizontal channel: Part i. particle transport', *International journal of multiphase flow* **29**(4), 675–699.

Sommerfeld, M. and Kussin, J. (2003), 'Analysis of collision effects for turbulent gas-particle flow in a horizontal channel. part ii. integral properties and validation', *International journal of multiphase flow* **29**(4), 701–718.

Sooraj, V. and Radhakrishnan, V. (2013), 'Elastic impact of abrasives for controlled erosion in fine finishing of surfaces', *Journal of Manufacturing Science and Engineering* **135**(5), 051019.

Sundararajan, G. and Shewmon, P. (1983), 'A new model for the erosion of metals at normal incidence', *Wear* **84**(2), 237–258.

Svedeman, S. and Arnold, K. (1993), Criteria for sizing multiphase flow lines for erosive/corrosive services. spe 26569, *in* '68th Annual Technical Conference of the Society of Petroleum Engineers, Houston, Texas'.

Svendeman, S. and Arnold, K. (1994), "criteria for sizing multi-phase flow lines for erosive/corrosive services', *SPE Prod. Facil* **9**, 74–80.

Syamlal, M. and O'Brien, T. J. (1989), Computer simulation of bubbles in a fluidized bed, *in* 'AIChE Symp. Ser', Vol. 85, Publ by AIChE, pp. 22–31.

Syamlal, M., Rogers, W. and OBrien, T. J. (1993), Mfix documentation theory guide, Technical report, USDOE Morgantown Energy Technology Center, WV (United States).

Tabakoff, W., Kotwal, R. and Hamed, A. (1979), 'Erosion study of different materials affected by coal ash particles', *Wear* **52**(1), 161–173.

Talia, M., Lankarani, H. and Talia, J. (1999), 'New experimental technique for the study and analysis of solid particle erosion mechanisms', *Wear* **225**, 1070–1077.

Tebowei, R. (2016), 'Computational fluid dynamics (cfd) modelling of critical velocity for sand transport flow regimes in multiphase pipe bends.'.

Tilly, G. (1973), 'A two stage mechanism of ductile erosion', *Wear* **23**(1), 87–96.

Tomiyama, A. (1998), 'Struggle with computational bubble dynamics', *Multiphase Science and Technology* **10**(4), 369–405.

Tryggvason, G., Bunner, B., Esmaeeli, A., Juric, D., Al-Rawahi, N., Tauber, W., Han, J., Nas, S. and Jan, Y.-J. (2001), 'A front-tracking method for the computations of multiphase flow', *Journal of computational physics* **169**(2), 708–759.

Uzi, A., Ami, Y. B. and Levy, A. (2017), 'Erosion prediction of industrial conveying pipelines', *Powder technology* **309**, 49–60.

Vegendla, S. P., Heynderickx, G. J. and Marin, G. B. (2011), 'Comparison of eulerian–lagrangian and eulerian–eulerian method for dilute gas–solid flow with side inlet', *Computers & Chemical Engineering* **35**(7), 1192–1199.

Versteeg, H. K. and Malalasekera, W. (2007), *An introduction to computational fluid dynamics: the finite volume method*, Pearson education.

Vieira, R. E. (2014), *Sand erosion model improvement for elbows in gas production, multiphase annular and low-liquid flow*, The University of Tulsa, OK, USA.

Vieira, R. E., Mansouri, A., McLaury, B. S. and Shirazi, S. A. (2016), 'Experimental and computational study of erosion in elbows due to sand particles in air flow', *Powder technology* **288**, 339–353.

Vieira, R. E., Parsi, M., Zahedi, P., McLaury, B. S. and Shirazi, S. A. (2017a), 'Electrical resistance probe measurements of solid particle erosion in multiphase annular flow', *Wear* **382**, 15–28.

Vieira, R. E., Parsi, M., Zahedi, P., McLaury, B. S. and Shirazi, S. A. (2017b), 'Ultrasonic measurements of sand particle erosion under upward multiphase annular flow conditions in a vertical-horizontal bend', *International Journal of Multiphase Flow* **93**, 48–62.

Vieira, R. E., Parsi, M., Zahedi, P., McLaury, B. S. and Shirazi, S. A. (2017c), 'Sand erosion measurements under multiphase annular flow conditions in a horizontal-horizontal elbow', *Powder technology* **320**, 625–636.

Wang, K., Li, X., Wang, Y. and He, R. (2017), 'Numerical investigation of the erosion behavior in elbows of petroleum pipelines', *Powder technology* **314**, 490–499.

Weiner, P. D. and Tolle, G. (1976), *Condensed Version of Detection and Prevention of Sand Erosion of Production Equipment*, Texas A & M Research Foundation.

Wen, C. and Yu, Y. (1966), 'A generalized method for predicting the minimum fluidization velocity', *AIChE Journal* **12**(3), 610–612.

Wendt, J. and Anderson, J. (2009), 'Basic philosophy of cfd', *Computational Fluid Dynamics: An Introduction, Spinger Verlag, Berlin, Heidelberg* pp. 5–8.

Wu, Q., Kim, S., Ishii, M. and Beus, S. (1998), 'One-group interfacial area transport in vertical bubbly flow', *International Journal of Heat and Mass Transfer* **41**(8-9), 1103–1112.

Xu, L., Zhang, Q., Zheng, J. and Zhao, Y. (2016), 'Numerical prediction of erosion in elbow based on cfd-dem simulation', *Powder Technology* **302**, 236–246.

Xu, Y. and Subramaniam, S. (2010), 'Effect of particle clusters on carrier flow turbulence: A direct numerical simulation study', *Flow, Turbulence and Combustion* **85**(3-4), 735–761.

Ye, J. and Guo, L. (2013), 'Multiphase flow pattern recognition in pipeline–riser system by statistical feature clustering of pressure fluctuations', *Chemical Engineering Science* **102**, 486–501.

Yoon, G. H. (2016), 'Topology optimization for turbulent flow with spalart–allmaras model', *Computer Methods in Applied Mechanics and Engineering* **303**, 288–311.

Zahedi, P., Karimi, S., Mahdavi, M., McLaury, B. S. and Shirazi, S. A. (2016), Parametric analysis of erosion in 90 degree and long radius bends, *in* 'ASME 2016 Fluids Engineering Division Summer Meeting collocated with the ASME 2016 Heat Transfer Summer Conference and the ASME 2016 14th International Conference on Nanochannels, Microchannels, and Minichannels', American Society of Mechanical Engineers, p. V01AT06A003.

Zahedi, P., Zhang, J., Arabnejad, H., McLaury, B. S. and Shirazi, S. A. (2017), 'Cfd simulation of multiphase flows and erosion predictions under annular flow and low liquid loading conditions', *Wear* **376**, 1260–1270.

Zhang, H., Tan, Y., Yang, D., Trias, F. X., Jiang, S., Sheng, Y. and Oliva, A. (2012), 'Numerical investigation of the location of maximum erosive wear damage in elbow: Effect of slurry velocity, bend orientation and angle of elbow', *Powder Technology* **217**, 467–476.

Zhang, J., McLaury, B. S. and Shirazi, S. A. (2018), 'Modeling sand fines erosion in elbows mounted in series', *Wear* **402**, 196–206.

Zhang, Y., McLaury, B. S. and Shirazi, S. A. (2009), 'Improvements of particle near-wall velocity and erosion predictions using a commercial cfd code', *Journal of Fluids Engineering* **131**(3), 031303.

Zhang, Y., McLaury, B. S., Shirazi, S. A., Rybicki, E. F., Nesic, S. et al. (2011), Predicting sand erosion in slug flows using a two-dimensional mechanistic model, *in* 'CORROSION 2011', NACE International, 13-17 March, Houston, Texas.

Zhang, Y., McLaury, B. S., Shirazi, S. A., Rybicki, E. F. et al. (2010), A two-dimensional mechanistic model for sand erosion prediction including particle impact characteristics, *in* 'CORROSION 2010', NACE International, 14-18 March, San Antonio, Texas.

Zhang, Y., Reuterfors, E., McLaury, B. S., Shirazi, S. and Rybicki, E. (2007), 'Comparison of computed and measured particle velocities and erosion in water and air flows', *Wear* **263**(1-6), 330–338.

Zhu, H., Lin, Y., Zeng, D., Zhou, Y., Xie, J. and Wu, Y. (2012), 'Numerical analysis of flow erosion on drill pipe in gas drilling', *Engineering Failure Analysis* **22**, 83–91.

Zhu, H., Pan, Q., Zhang, W., Feng, G. and Li, X. (2014), 'Cfd simulations of flow erosion and flow-induced deformation of needle valve: Effects of operation, structure and fluid parameters', *Nuclear Engineering and Design* **273**, 396–411.

Zhu, H., Wang, J., Ba, B., Wu, Z. and Wang, W. (2015), 'Numerical investigation of flow erosion and flow induced displacement of gas well relief line', *Journal of Loss Prevention in the Process Industries* **37**, 19–32.

Appendix A

Conference Paper and Poster Presentation

A.1 Conference Paper

- Ogunsesan, O. A., Hossain, M., Iyi, D. and Dhroubi, M. G. (2018), Cfd modelling of pipe erosion due to sand transport, in 'Numerical Modelling in Engineering', Springer, pp. 274 - 289.

A.2 Poster Presentation

- Ogunsesan, O.A., Hossain, M. and Droubi, M.G., Sand Erosion Prediction in Complex Multiphase Flows in Double Bend Geometries.